Stability and optical diagnosis of laser wakefield accelerators

Claudia Camila Cobo Torres

PhD

Physics, Engineering and Technology
University of York

December 2023

Abstract

This thesis presents experimental and simulation work contributing to the stability and control of laser wakefield accelerators, as required for their successful use in further applications.

Experimental results of laser wakefield acceleration in a gas jet target with a density transition produced by a razor blade in the flow are reported. Modifications to the target setup are correlated with variations in the plasma density profile diagnosed via interferometry. The shot-to-shot fluctuations of the target plateau density, peak density and down-ramp position are characterised. Simulations of the effects of density profile variations reveal that peak density fluctuations independent of the plateau density dominate the variations in electron beam energy (15 %) and charge (9 %). The results suggest that blade motion is more detrimental to stability than gas pressure fluctuations, and that early focusing of the laser may improve stability. The injection dynamics are shown to be sensitive to the length scale of the density ramps even within the regime of sharp density transitions, as a result of transverse effects.

The post-interaction laser spectrum is measured as a proxy diagnostic for the electron dynamics in a laser wakefield accelerator using ionisation injection in a tailored gas cell. The unguided laser energy identified from the signal in the input wavelength range is indicative of laser-plasma coupling and the transmission below 900 nm is indicative of pump depletion and correlated with electron beam energy. The injection and acceleration dynamics are shown to be highly sensitive to the vacuum laser focus. Simulations reveal that the balance between self-focusing and geometric diffraction modifies the position of the peak a_0 and that the earliest position of effective focus results in the highest injected charge. The strength of the wakefield is shown to be determined by the time evolution of the laser a_0 and not by the instantaneous laser conditions.

Contents

List of Figures

List of Tables

Acknowledgements

My time doing my PhD in York has been the most stressed and overwhelmed I've ever been, but also a hugely rewarding experience.

Thanks to my CDT cohort (+ Adam) for making York feel so friendly and welcoming. Starting a PhD felt a lot less scary knowing we were all on the same page, and I have great memories of all our lectures and trips together (even if you all did move away in the end).

I am tremendously grateful to my supervisor, Chris Murphy, for being an incredible teacher; I have learnt so much about physics and being a physicist from you. Thank you for for all your guidance, positive feedback and words of encouragement about my work, as well as your understanding, empathy and support during the more difficult times. I could not have asked for a better mentor.

Thanks to all the people involved in the Gemini and Lund experiments, without whom the work in this thesis would not be possible. In particular, I'd like to extend my gratitude to Chris Arran and Matt Streeter for guiding me in my first high power laser experiment and being so helpful the numerous times I've reached out since. Also to Cornelia Gustafsson for all your kindness and support in Lund.

To Guille, thank you for putting up with me through this rollercoaster and trying to help out in any way you could. I really appreciate all the time you spent reading through this work and I'm really grateful for all your advice, care and encouragement.

Finally, I would like to thank my family for being okay with me living on the other side of the world to pursue this crazy stuff. I've missed so much but I always feel at home when we're together. Thank you for always supporting me and telling me I can achieve everything I want.

I dedicate this thesis to Mateo.

Declaration

I declare that this thesis is a presentation of original work and I am the sole author. This work has not previously been presented for a degree or other qualification at this University or elsewhere. All sources are acknowledged as references.

The work done on chapter 4 has been submitted for publication.

Role of the author

The experimental results in this thesis were obtained in three experimental campaigns, each of which were large international collaborations.

Chapter 4: The experiment was conducted by a large team from University of York, Imperial College London, Queen's University Belfast and the CLF; the author was involved in the setup and data collection. The analysis of the electron spectrometers was performed by C. Colgan (Imperial College London) and M. Streeter (Queen's University Belfast). Analysis of the interferometry measurements was done by the author. PIC simulations were performed by the author.

Chapter 5: The first experiment (2019) was conducted by a team from University of York, Imperial College London, Lund University, Universite Paris-Saclay, and ENEA. The author was not involved in the planning or data collection. The second experiment (2021) was conducted by a team including the author; the author was involved in the planning, setup and data collection. In both experiments, analysis of the electron spectrometer was performed by L. Dickson (Universite Paris-Saclay). The code for FROG retrieval was fully developed by the author, based on the known algorithms available in the literature. Analysis of the post-interaction laser measurements (spectrometer and FROG) was performed by the author. PIC simulations were performed by the author.

Chapter 1

Introduction

Laser wakefield acceleration (LWFA) is a process capable of generating gigaelectronvolt-energy electrons in centimetre-scale interaction lengths [1]. This is because of the use of plasma as the accelerating medium, which allows these devices to sustain acceleration gradients over a thousand times greater than those achieved in conventional linear accelerators. As a result, these plasma-based accelerators constitute promising compact sources of relativistic electrons and have the potential to revolutionise high-energy radiation sources by reducing their scale by many orders of magnitude. By making accelerator facilities cheaper and more accessible, this could drive impact in areas ranging from laboratory astrophysics [2] to biological imaging [3]. However, improvements in the stability, reliability and robustness of electron beam parameters are still required to develop the applications of LWFA beyond proof of principle [4].

1.1 Particle accelerators

Particle accelerators have enabled scientific discoveries ranging from the calculation of the size of an atomic nucleus [5] to the confirmation of the Higgs boson [6]. They are also used in more widespread applications to generate x-rays for biomedical imaging [7] and characterisation of materials [8]. Particle accelerators make use of large electric fields to accelerate charged particles to high energies. Typically, circular geometries are used, where the particles traverse the same accelerating region many times. However, a circular path requires the charged particles to emit synchrotron radiation with power $P \propto E^4/(m^4R^2)$, where E is the energy of the particle, m is its mass and R is the radius of its trajectory. Due to its strong mass dependence, synchrotron emission is the limiting factor to the circular acceleration of electrons. Therefore, conventional electron accelerators are instead linear devices based on superconducting radiofrequency (RF)

cavities. These provide average accelerating fields of $40\,\mathrm{MeV\,m^{-1}}$ to $50\,\mathrm{MeV\,m^{-1}}$. The fields are limited by electrical breakdown, whereby the walls of the device itself become ionised due to the strong field and the accelerator is severely damaged. As a result, these accelerators need to get progressively larger and more expensive in order to increase the achievable energy of the particles. Currently, the most powerful linear accelerator is the Stanford Linear Accelerator (SLAC), shown in figure 1.1. This device is capable of accelerating electrons to 50 GeV over a distance of 3.2 km.

Figure 1.1: Aerial view of the Stanford Linear Accelerator [9].

1.2 Plasma-based accelerators

A plasma is a quasi-neutral ensemble of charged particles which exhibits collective behaviour through electromagnetic interactions. It is created when electrons obtain sufficient energy to become free from the atoms to which they were bound. The potential of using plasma as an accelerating medium was first proposed by Veksler in 1956, who noted that plasma, being already ionised, is not constrained by breakdown and is therefore capable of sustaining significantly higher electric fields than other materials [10]. In 1979, Tajima and Dawson showed that a laser was capable of producing these electric fields, with magnitudes a thousand times greater than in conventional accelerators [1]. This would enable a dramatic reduction in the size and cost of particle accelerators.

Tajima and Dawson proposed the use of an ultra-high intensity laser to drive an electron plasma wave and accelerate electrons through a mechanism known as laser wakefield acceleration (LWFA). In this process, a laser pulse propagating through a plasma exerts a ponderomotive force on the plasma electrons. This force acts to sweep particles away from regions of high laser intensity. The electrons are moved predominantly, while the more massive ions are undisturbed in the timescale of the interaction. As a result, the electrons are accelerated back by the restoring force from the ions, thereby establishing plasma oscillations at the plasma frequency ω_p. As the laser pulse propagates through the plasma with a group velocity close to c, it is trailed by the

plasma oscillations, thereby generating an electron plasma wave in its wake. This is known as the wakefield, shown schematically in figure 1.2.

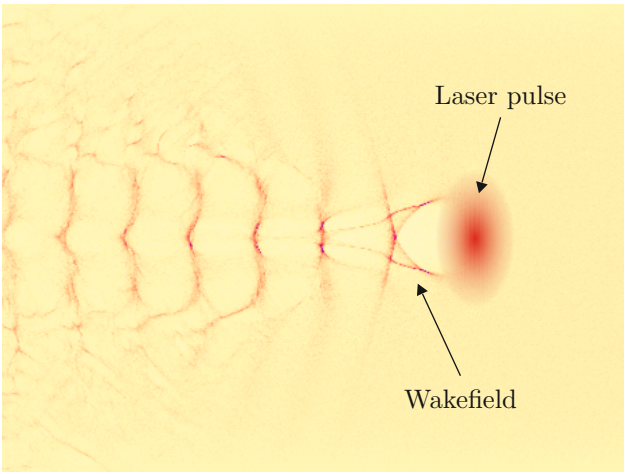

Figure 1.2: Simulation of a laser (red) driving a wakefield in a plasma. The colour map shows the electron density distribution.

The longitudinal electric field associated with the wakefield travels with a phase velocity approximately equal to the group velocity of the laser pulse. Therefore, electrons travelling with a velocity close to the plasma wave's will be trapped and continuously experience the same electric field. If they are in the accelerating phase of the wave, they will continuously gain kinetic energy. The energy gained by electrons in the plasma is limited as they eventually outrun the wave and enter a region of positive electric field, which decelerates them.

Efficient excitation of a wakefield requires the use of a laser pulse with a length comparable to half the wavelength of the plasma wave [1], which represents pulse durations of the order of 10 fs. Such ultra-short, ultra-high power lasers were unavailable at the time of Tajima and Dawson, so an alternative scheme known as plasma beat-wave acceleration (PBWA) was proposed [11]. This mechanism relies on the beating of two long pulses causing modulation at ω_p, leading to the resonance excitation of a large-amplitude plasma wave [12] able to accelerate externally-injected electrons [13]. While historically significant, the PBWA technique is limited due to the variation of the plasma frequency for strong wakefields, which causes the plasma wave to become out of phase with the laser beat wave. This breaks the resonance, thereby limiting the acceleration [11].

By taking advantage of non-linear optical effects, it is possible for the plasma to modulate a long laser pulse into a series of short pulses of width equal to the plasma wavelength [14], thereby maintaining resonance. This is an instability known as self-

modulation, and occurs due to the development of periodic regions of enhanced diffraction and focusing in the plasma wave [15]. This self-modulated laser wakefield (SM-LWFA) regime demonstrated the acceleration of electrons trapped from the plasma itself for the first time [16].

Developments of laser technology like the invention of chirped pulse amplification (CPA) [17] enabled the development of higher intensity and shorter duration laser pulses, such that the original LWFA scheme proposed by Tajima and Dawson eventually became possible. In 2004, experimental work from three groups demonstrated acceleration of self-trapped electrons resulting in quasi-monoenergetic electron beams [18–20]. In contrast to previous experiments, where the resulting beam was broad and close to Maxwellian, these studies demonstrated the potential of LWFA for generating high-quality electron beams.

1.2.1 State of the art

Since then, a considerable research effort has been dedicated to increasing the achievable electron energies and studying potential applications of the high-energy electron beams. Improvements in technology and understanding of LWFA have enabled the demonstration of nanocoulomb-class electron bunches [21] and energy gains up to 7.8 GeV [22]. These characteristics, combined with the femtosecond duration of these electron bunches [23–25], have led to extensive research into applications of LWFA. Many applications require the electrons to be stable and tunable, and achieving this requires further understanding of the electron trapping and acceleration dynamics. This is generally difficult to diagnose due to the ultra-fast timescales involved, so it is important that alternative diagnostic techniques continue to develop.

The state of the art parameters of LWFA are summarised in table 1.1. These can be compared with the state of the art of radio-frequency accelerators, which is summarised in table 1.2 as obtained at the 3.4 km long European XFEL. Excluding the orders of magnitude lower repetition rate that is currently achievable with LWFA, table 1.1 shows parameters that are becoming comparable to those of conventional accelerators. However, the current difficulty lies in achieving all of the optimal parameters simultaneously with LWFA. This indicates that stability remains an outstanding challenge.

1.3 Applications of LWFA

High energy electron beams obtained through LWFA have been successfully used to study strong-field quantum electrodynamics [2, 34], demonstrating their applicability

Electron beam parameter	State of the art value	Notes
Energy	8 GeV [22]	5 pC, 0.2 mrad
Charge	220 pC [21]	250 MeV, 7 mrad, $\delta E/E = 14\,\%$, ionisation injection
	1.1 nC [26]	334 MeV, 2.5 mrad, 18 % energy spread, density transition injection
	700 nC [27]	200 MeV, 100 % energy spread
Energy spread	0.2 % to 0.4 % RMS [28]	800 MeV density transition injection
Duration	1.4 fs [25]	
Emittance	0.2π mm mrad [29]	245 MeV
Repetition rate	1 Hz [30]	100,000 shots with 24 hour operation
	1 kHz [31]	15 MeV, 2.5 pC
Efficiency	9.6 % [26]	peaked energy spectrum
	11 % [27]	100 % energy spread

Table 1.1: Overview of state of the art parameters of LWFA; adapted from ref. [32].

Electron beam parameter	1.2 fs duration	80 fs duration
Energy (GeV	17.5	
Charge (nC)	0.02	1
Emittance (mm mrad)	0.32	0.97
Energy spread (MeV rms)	4.1	2
Repetition rate (GHz)	1.3	

Table 1.2: State of the art parameters of radio-frequency accelerators with 17.5 GeV energies; adapted from ref. [33].

in fundamental physics investigations. There is also interest in using them for linear particle colliders [35]. Moreover, they have been demonstrated as sources for electron diffraction [36], gamma rays [37] and positrons [38]. One key application of LWFA is its use as high energy x-ray sources, which can be generated through betatron oscillations [3, 39, 40], Compton scattering [41] and free-electron lasing [42, 43]. By using plasma-based accelerators, considerable reductions in size and cost can be achieved to make these electron beams and radiation sources more accessible.

1.3.1 High energy particle collider

A high energy particle (HEP) collider will likely require centre-of-mass energies $\gtrsim 1\,\mathrm{TeV}$ and luminosities $\gtrsim 1000\,\mathrm{cm}^{-2}\,\mathrm{s}^{-1}$ [35], which implies high charge $> 100\,\mathrm{pC}$, low normalised emittance $< 0.1\,\mu\mathrm{m}$ and low energy spread $< 1\,\%$ [44]. As shown in table 1.1, the required emittance, charge and energy spread have been achieved via LWFA, albeit not simultaneously. Reaching teraelectronvolt energies will require staging of multiple independently-driven laser-plasma accelerators [45,46]. While coupling of two stages has been demonstrated, only 3.5 % of the charge was captured in the second stage during optimal energy gain [45].

There are further limitations currently preventing the development of a HEP collider using LWFA, including acceleration of positrons, operation at kilohertz repetition rates and improvements in the wall-plug efficiency to achieve suitable luminosities [35, 47]. These critical issues need significant research and development efforts, including the development of new laser technologies.

1.3.2 Plasma-based free electron laser

X-ray free electron lasers (FELs) have revolutionised science by enabling single-shot high temporal and spatial resolution imaging [48]. Thus, the realisation of a compact FEL based on plasma acceleration has been identified as a key challenge for this decade [49]. Plasma based FELs will require electron beam energies between 1 GeV and 10 GeV [46], which makes them more accessible than linear collider applications as these energies are currently achievable with LWFA.

The performance requirements for FELs at x-ray energies require transverse emittances $< 0.1\,\mathrm{nm}$, peak currents of a few kiloampere [50] and energy spreads $< 1\,\%$ [49]. Given the required energy spread, it follows that the electron beam energies should be reproducible to at least the same degree. The experimental feasiblity of a FEL based on LWFA has been demonstrated at radiation wavelengths in the extreme-ultraviolet [42,43]. However, the robust operation of laser-plasma accelerators with these properties is challenging, and the absence of reproducible electron beams hinders this application. It is expected that this application is realistic at higher flux and photon energies, which are expected to be reached within five years [35, 48].

1.3.3 Medical applications

Obtaining x-rays from Compton scattering with LWFA electrons is challenging because of the precise temporal and spatial synchronisation required. Nevertheless, energies up

to 18 MeV have been obtained [37]. While the photon energies are competitive with sources from RF accelerators, the energy spread is still too high for use in precision applications [51].

Bremsstrahlung radiation has also been achieved with the use of electron beams from LWFA. Photons from these sources are found to be better collimated and have higher energies and lower emittances than those from direct irradiation of the target or other laser-plasma interactions. LWFA electron beams can produce high brightness tunable gamma ray beams [52, 53], albeit with photon doses smaller than the 10 Gy required to treat tumors. Radiobiology applications with significant irradiation dose can tolerate a 20 % charge stability [54] which can currently be achieved.

1.3.4 Betatron x-rays

Due to the transverse forces in a wakefield, the accelerated electrons perform betatron oscillations, thereby emitting betatron x-rays which can be used in single-shot phase-contrast imaging of micro-structures. Good quality images can be obtained with $\sim 10^7$ photons per shot with energies ranging from 4 keV to 15 keV at repetition rates of 0.3 Hz [55]. Betatron x-ray emission with these parameters have been extensively demonstrated [51, 56, 57] and used for imaging of bones [58] and shocks [59]. This application of LWFA is the most technologically ready. However, improvements in repetition rate and field of view are still required to make these sources competitive with conventional devices [57].

1.3.5 Future facilities

The revolutionary potential of compact plasma-based accelerators is leading to the development of new facilities around the world. In the UK, the Extreme Photonics Application Centre (EPAC) is due to come online in 2025 as an £82M facility aiming to develop and apply laser-based accelerators and particle sources [60]. By using laser wakefield acceleration to accelerate electrons to gigaelectronvolt energies, the facility promises bright x-rays with customisable energies ranging from a few keV to tens of MeV for radiography and computed tomography.

The EuPRAXIA project is a multi-million euro international collaboration which aims to build dedicated plasma accelerators with applications from nuclear physics to medical science [61]. In 2021, EuPRAXIA was accepted onto the ESFRI roadmap for strategically important research infrastructures which highlights it as a European priority. This new facility will provide users from many fields with high quality electron and photon beams for a range of applications including compact free-electron lasers and

tabletop sources for medical imaging.

As part of their objectives, EuPRAXIA aims to develop LWFA so that the accelerated electron beams satisfy the strict requirements that are outlined in the conceptual report [49]. These include a simultaneous high energy, high charge, low energy spread and stable shot-to-shot operation, comparable to those obtained in conventional RF accelerators. In particular, the design report highlights the need to characterise all sources of experimental parameter fluctuations in order to determine the required level of control and acceptable tolerances for a stable accelerator. Of these, the plasma density is highlighted as a key parameter in the stability of LWFA [62, 63], which currently lacks systematic stability studies [49]. In addition, controlled electron injection mechanisms are noted as requiring further study for improvements in stability and efficiency of laser-plasma accelerators. This includes studying the realisation and robustness of density transitions [49], as well as the control over the laser evolution [32]. The work done in this thesis addresses some of these ongoing issues, in an attempt to get closer to the stable, high quality electron beams needed for future applications.

1.4 Thesis outline

This thesis presents a combination of experimental and computational studies aiming to develop understanding of laser wakefield acceleration dynamics, in order to improve their stability and quality towards the standards required for further applications. Chapter 2 presents the theoretical background relevant to the work in this thesis. Chapter 3 describes the experimental, diagnostic and computational methods used for data collection and analysis. The two results chapters are outlined in the following.

Chapter 4. Stability of density transition injected electron beams: Density tailoring of the target is used in an attempt to generate stable laser wakefield accelerated electron beams. By characterising the shot-to-shot fluctuations of the target density profile, the sensitivity of the accelerated electrons to experimentally-relevant density fluctuations are studied through particle-in-cell simulations.

Chapter 5. Evolution of a laser driving wakefield acceleration: A laser-plasma injector for the EuPRAXIA project is tested. The modifications to the laser driver are studied by diagnosing the transmitted laser spectrum and shape and correlating this to the measured electron beam parameters. This is supplemented by particle-in-cell simulations of the longitudinal and transverse laser evolution.

Finally, chapter 6 summarises the main results and presents future prospects.

Chapter 2

Theory

2.1 Plasmas

A plasma is a quasi-neutral ensemble of charged particles which exhibits collective behaviour through electromagnetic interactions. As the electrons have much higher charge to mass ratios than the ions, they are more mobile and dominate the behaviour of the plasma at short timescales. Plasmas are characterised by the spatial and temporal scales over which exposed charges present an effect.

2.1.1 Plasma properties

Debye length

Quasi-neutrality in the definition of a plasma refers to the plasma's ability to shield an isolated charge over a given distance. This results in the plasma appearing neutral despite being made up of charged particles. The shielding length is known as the Debye length

$$\lambda_D = \frac{\epsilon_0 k_b T_e}{n_e e^2}\,, \tag{2.1}$$

where T_e and n_e are the electron temperature and density, respectively. λ_D defines the distance over which the electrostatic potential of the free charge decreases by a factor of $1/e$. A short Debye length relative to the size of the plasma is required for the plasma to exhibit collective behaviour.

Plasma frequency

Consider a slab of electrons with charge density $\rho_e = -en_e$ that is displaced by a distance δx from a background of static ions, as depicted in figure 2.1. Assuming the plasma is

Figure 2.1: A slab of electrons (green) is displaced by a distance δx from a background of static ions (blue), generating an electric field E.

fully ionised, infinite and uniform and neglecting thermal motion, Gauss's law gives

$$\begin{aligned} \frac{\mathrm{d}E}{\mathrm{d}x} &= \frac{-en_e}{\epsilon_0} \\ E &\approx \frac{-en_e}{\epsilon_0}\delta x\,. \end{aligned} \tag{2.2}$$

The Lorentz force on the electrons is then

$$m_e\frac{\mathrm{d}^2\delta x}{\mathrm{d}t^2} = \frac{e^2n_e}{\epsilon_0}\delta x\,, \tag{2.3}$$

which corresponds to simple harmonic motion at the plasma frequency

$$\omega_p = \sqrt{\frac{n_e e^2}{m_e\epsilon_0}}\,. \tag{2.4}$$

This is the characteristic frequency of collective electron motion. The typical electron response time is of the order of $1/\omega_p$, which is $\sqrt{m_e/m_i}$ shorter than that of an ion of mass m_i. Thus the assumption of a static ion background is justified.

Plasma dispersion relation

An electromagnetic wave propagating in the z direction can be described by

$$\mathbf{E} = E_0\exp\big(i(k_0z - \omega_0t)\big)\hat{x}\,. \tag{2.5}$$

The dispersion relation of a plasma is

$$\omega^2 = \omega_p^2 + k^2 c^2 \,. \tag{2.6}$$

As $\omega = ck\eta$, where η is the refractive index of the plasma,

$$\eta = \sqrt{1 - \frac{\omega_p^2}{\omega^2}} \,, \tag{2.7}$$

the phase velocity of the electromagnetic wave in a plasma is

$$v_\phi = \frac{\omega_0}{k_0} = \frac{c}{\sqrt{1 - \frac{\omega_p^2}{\omega_0^2}}} \,, \tag{2.8}$$

and its group velocity is

$$v_g = \frac{\mathrm{d}\omega_0}{\mathrm{d}k_0} = c\sqrt{1 - \frac{\omega_p^2}{\omega_0^2}} \,. \tag{2.9}$$

Using the dispersion relation, (2.5) can be rewritten as

$$E = E_0 \exp\left[i\left(\frac{\omega_0 \eta}{c} z - \omega_0 t\right)\right] . \tag{2.10}$$

When η is real, only the phase of the wave changes during propagation. When $\omega_0 \lesssim \omega_p$, the refractive index becomes imaginary and electromagnetic waves cease to propagate. This occurs at the electron density

$$n_c = \frac{m_e \epsilon_0 \omega_0^2}{e^2} \,, \tag{2.11}$$

which is known as the critical density. For an 800 nm laser, relevant to this thesis, $n_c = 1.75 \times 10^{21}\,\mathrm{cm}^{-3}$. Interactions with plasma densities $< n_c$ are underdense and the laser is transmitted. This is the regime in which LWFA occurs.

2.1.2 Single particle motion

Consider an infinite plane electromagnetic wave defined by

$$\begin{aligned} \mathbf{E} &= E_0 \cos(kz - \omega t)\hat{x} \\ \mathbf{B} &= B_0 \cos(kz - \omega t)\hat{y} \,. \end{aligned} \tag{2.12}$$

Using the dipole approximation, $kz - \omega t \approx -\omega t$, and assuming non-relativistic motion, $vB_0/c \ll E_0$, the electron responds only to the electric field $\mathbf{E} = E_0 \cos(\omega t)\hat{x}$. The motion of the electron in the x direction is then calculated from the Lorentz force as

$$\begin{aligned} \frac{\mathrm{d}^2 x}{\mathrm{d}t^2} &= -\frac{eE_0}{m_e}\cos(\omega t) \\ \frac{\mathrm{d}x}{\mathrm{d}t} &= -\frac{eE_0}{m_e\omega}\sin(\omega t) = a_0 c \sin(\omega t) \\ x &= -\frac{eE_0}{m\omega^2}\cos(\omega t)\,, \end{aligned} \tag{2.13}$$

where

$$a_0 \equiv \frac{eE_0}{m_e c\omega}\,. \tag{2.14}$$

(2.13) shows that the electron oscillates, or quivers, in the electric field of the wave.

The quiver motion of the electrons (2.13) causes the $-e\mathbf{v} \times \mathbf{B}$ force to become significant. The motion in the longitudinal direction is then

$$\begin{aligned} \frac{\mathrm{d}^2 z}{\mathrm{d}t^2} &= \frac{e^2 E_0^2}{m_e^2 \omega c}\sin(\omega t)\cos(\omega t) \\ \frac{\mathrm{d}z}{\mathrm{d}t} &= \frac{e^2 E_0}{2m^2\omega^2 c}\sin^2(\omega t) \\ z &= \frac{e^2 E_0^2}{8m^2\omega^3 c}\big(2\omega t - \sin(2\omega t)\big)\,, \end{aligned} \tag{2.15}$$

where $B_0 = E_0/c$ and the identity $2\sin^2\theta = 1 - \cos 2\theta$ have been used. The electron oscillates in the longitudinal direction at twice the frequency of the transverse motion, leading to a figure of eight motion while drifting in the z direction at a velocity $v_d = a_0^2 c/4$. This is shown in figure 2.2.

2.1.3 Laser strength parameter

Physically, a_0 (2.14) represents the normalised transverse momentum of plasma electrons in the electric field of an electromagnetic wave, $a_0 \equiv v_{\mathrm{osc}}/c$. Analogously, the electric field of the wave can be expressed in terms of the vector potential, $\mathbf{E} = -\partial\mathbf{A}/\partial t$, so $A_0 = E_0/\omega = m_e c a_0/e$ and a_0 also represents the normalised vector potential of the electromagnetic field. Thus, a_0 can be used to characterise the strength of a laser, and is also known as the laser strength parameter. a_0 can be related to the peak laser intensity I_0 and wavelength λ_0 through

$$a_0 \approx 0.855\,\lambda_0[\mu\mathrm{m}]\sqrt{I[10^{18}\,\mathrm{W\,cm^{-2}}]}\,, \tag{2.16}$$

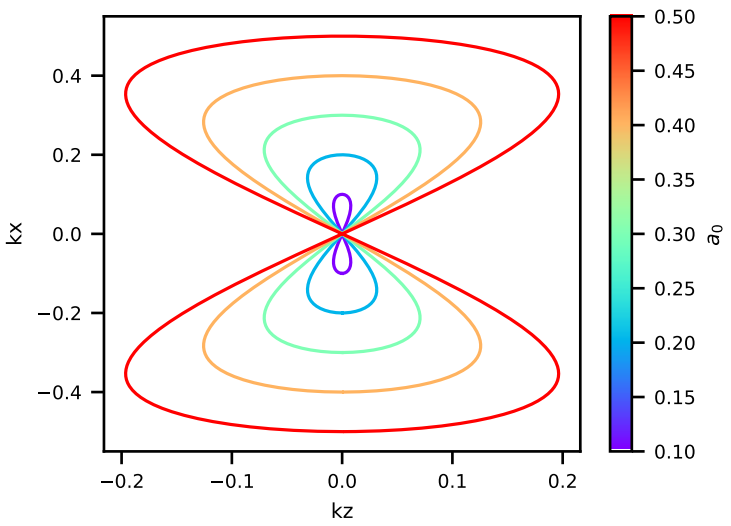

Figure 2.2: Electron trajectories (non-relativistic) in the presence of an electric field in the frame of reference of the drift velocity.

and is used to determine the regime of the interaction dynamics. When $a_0 > 1$, the electron transverse motion is relativistic and the laser-plasma interaction is non-linear. For a laser with $\lambda_0 = 800\,\text{nm}$, $a_0 = 1$ when $I_0 = 2 \times 10^{18}\,\text{W}\,\text{cm}^{-2}$. The relativistic regime requires $m_e \to \gamma m_e$, where

$$\gamma = \frac{1}{\sqrt{1 - \frac{v_e^2}{c^2}}} = \sqrt{1 + \frac{a_0^2}{2}} \tag{2.17}$$

is the Lorentz factor of the electrons. It decreases the plasma frequency (2.4) relative to the non-relativistic regime, which in turn affects the refractive index (2.7).

2.1.4 Ponderomotive force

The transverse, or quiver, motion of the electrons in the laser field constitutes a source of potential energy and therefore a potential field. The force associated with this potential field is known as the ponderomotive force [64], which is directed down the potential gradient. Consider the instantaneous kinetic energy of an electron characterised by (2.13),

$$U = \frac{1}{2} m_e a_0^2 c^2 \sin^2(\omega t)\,. \tag{2.18}$$

The average quiver energy over a laser cycle is

$$\langle U \rangle = \frac{1}{4} m_e a_0^2 c^2\,, \tag{2.19}$$

where $\langle \cos^2(\theta) \rangle = 1/2$ has been used. By taking the gradient of the quiver kinetic energy of the electrons, the ponderomotive force can be obtained as

$$\mathbf{F_p} = -\frac{m_e c^2}{4} \nabla a_0^2 \,, \tag{2.20}$$

in the linear regime.

A simplified derivation for the relativistic ponderomotive force is given here, which reproduces the result obtained in ref. [65] using a rigorous derivation. The relativistic equations of motion for a free electron in a plane wave,

$$\mathbf{A} = A_0 \cos(kz - \omega t)\hat{x} \,, \tag{2.21}$$

are

$$\begin{aligned} \frac{\mathrm{d}\mathbf{x}}{\mathrm{d}t} &= \frac{\mathbf{p}}{\gamma m_e} \\ \frac{\mathrm{d}\mathbf{p}}{\mathrm{d}t} &= -e(\mathbf{E} + \mathbf{v} \times \mathbf{B}) \,. \end{aligned} \tag{2.22}$$

The electric and magnetic fields are determined by the laser field, with the vector potential $\mathbf{A}$ defined as $\mathbf{E} = -\partial\mathbf{A}/\partial t$ and $\mathbf{B} = \nabla \times \mathbf{A}$. Using this, (2.22) can be rewritten as

$$\frac{\mathrm{d}\mathbf{p}}{\mathrm{d}t} = e\left(\frac{\partial \mathbf{A}}{\partial t} - \frac{\mathbf{p}}{\gamma m_e} \times (\nabla \times \mathbf{A}) \right) . \tag{2.23}$$

Using the vector identity $\mathbf{p} \times (\nabla \times \mathbf{A}) = (\nabla \mathbf{A}) \cdot \mathbf{p} - (\mathbf{p} \cdot \nabla)\mathbf{A}$ and the convective derivative $\mathrm{d}/\mathrm{d}t = \partial/\partial t + \mathbf{p} \cdot \nabla$, this becomes

$$\begin{aligned} \frac{\mathrm{d}\mathbf{p}}{\mathrm{d}t} &= e\left(\frac{\mathrm{d}\mathbf{A}}{\mathrm{d}t} - (\nabla \mathbf{A}) \cdot \frac{\mathbf{p}}{\gamma m_e} \right) \\ &= m_e c^2 \left(\frac{\mathrm{d}\mathbf{a}}{\mathrm{d}t} - (\nabla \mathbf{a}) \cdot \frac{\mathbf{p}}{\gamma m_e} \right) , \end{aligned} \tag{2.24}$$

where $\mathbf{a} = e\mathbf{A}/(m_e c)$. The transverse quiver motion of the electrons is by definition

$$\frac{\mathbf{p}}{\gamma m_e} = \frac{\mathbf{a} c}{\gamma} \,; \tag{2.25}$$

therefore,

$$\frac{\mathrm{d}\mathbf{p}}{\mathrm{d}t} = m_e c^2 \left(\frac{\mathrm{d}\mathbf{a}}{\mathrm{d}t} - (\nabla \mathbf{a}) \cdot \frac{\mathbf{a} c}{\gamma} \right) . \tag{2.26}$$

The ponderomotive force is then obtained by averaging over the fast oscillations in a

laser cycle

$$\mathbf{F_p} = -\frac{m_e c^2}{2\langle\gamma\rangle}\nabla\langle a^2\rangle\,, \tag{2.27}$$

where the identity $\nabla a^2 = 2a\nabla a$ has been used.

The ponderomotive force requires a gradient in the strength parameter, which occurs for inhomogeneous electromagnetic waves, such as a laser pulse. This works to expel charged particles from regions of high laser intensity. Due to the m^{-2} dependence of the ponderomotive acceleration, electrons will be swept predominantly, while the ions comprise a static neutralising background. This comprises the basis for laser wakefield acceleration.

2.2 Lasers

2.2.1 Pulse shape and phase

In the scalar approximation of the electric field of a laser pulse, the temporal features can be expressed by the complex amplitude

$$E(t) = \sqrt{I(t)}\exp\left(-i\phi(t)\right), \tag{2.28}$$

where $I(t)$ is the intensity and $\phi(t)$ is the temporal phase. This representation disregards the rapidly varying carrier wave $\exp\left(i\omega_0 t\right)$, where ω_0 is the carrier angular frequency. The instantaneous frequency of the pulse is given by

$$\omega_{\text{inst}}(t) = \omega_0 - \frac{\mathrm{d}\phi}{\mathrm{d}t}\,. \tag{2.29}$$

In the frequency domain, the electric field can be represented by the complex pulse

$$\tilde{E}(\omega) = \sqrt{S(\omega)}\exp\left(-i\varphi(\omega)\right), \tag{2.30}$$

where $S(\omega)$ is the spectrum and $\varphi(\omega)$ is the spectral phase. The spectral phase is the phase of each frequency in the waveform. $E(t)$ and $\tilde{E}(\omega)$ are related by the Fourier transform:

$$\tilde{E}(\omega) = \int_{-\infty}^{\infty} E(t)\exp\left(-i\omega t\right)\mathrm{d}t \tag{2.31}$$

$$E(t) = \frac{1}{2\pi}\int_{-\infty}^{\infty} \tilde{E}(\omega)\exp\left(i\omega t\right)\mathrm{d}\omega\,. \tag{2.32}$$

Therefore, it can be seen that the rapidly varying carrier wave term $\exp\left(i\omega_0 t\right)$ represents

a shift in the spectrum to centre it at ω_0 via the Fourier shift theorem. This term is disregarded for simplicity.

Consider a laser pulse with a Gaussian temporal profile and zero phase,

$$E(t) = E_0 \exp\left(-at^2\right). \tag{2.33}$$

The pulse can be represented in the frequency domain by performing the Fourier transform

$$\tilde{E}(\omega) = E_0 \int_{-\infty}^{\infty} \exp\left(-at^2 - i\omega t\right) \mathrm{d}t, \tag{2.34}$$

which can be solved by completing the square as

$$\tilde{E}(\omega) = E_0 \sqrt{\frac{\pi}{a}} \exp\left(-\frac{\omega^2}{4a}\right). \tag{2.35}$$

The spectrum is another Gaussian in frequency space centred at the carrier frequency ω_0. a is related to the pulse duration of a pulse with a flat phase

$$a = \left(\frac{1}{\tau_{1/e}}\right)^2, \tag{2.36}$$

where $\tau_{1/e}$ is the $1/e$ pulse duration of the laser relative to the electric field. For any spectrum, the shortest pulse occurs for a flat spectral phase; for any temporal intensity profile, the narrowest spectrum occurs for a flat temporal phase. This condition is the Fourier limited pulse, which has the smallest time-bandwidth product.

The temporal and spectral phases can be expressed as a Taylor series in t and ω, with each term representing a physical effect. In practice it is more common to expand the spectral phase, as it is difficult to measure the temporal laser intensity. Thus,

$$\varphi(\omega) = \varphi_0 + \varphi_1(\omega - \omega_0) + \frac{\varphi_2}{2}(\omega - \omega_0)^2 + \frac{\varphi_3}{6}(\omega - \omega_0)^3 + ... \tag{2.37}$$

The zeroth order phase $\varphi_0 = \phi_0$ is the carrier-envelope phase (CEP), which represents the phase offset between the plane wave and its amplitude. It is only relevant for single-cycle pulses. The first order spectral phase, φ_1, represents a shift in time, while the first order temporal phase, ϕ_1, represents a shift in frequency. These terms are typically neglected in time-frequency analysis of a laser pulse.

Higher order phases represent the pulse frequency varying in time. The second order temporal phase, ϕ_2, represents a linear chirp, and is positive when the frequency increases with time. In the spectral domain, φ_2 represents group delay dispersion (GDD),

whereby the pulse develops a frequency chirp due to the frequency dependence of the refractive index of a medium. These two representations are equivalent.

The cubic phase term corresponds to a quadratic group delay as a function of frequency, known as third order dispersion (TOD) and results in an asymmetric pulse shape in time. The central frequency arrives first, while frequencies $w_0 \pm \delta\omega$ arrive later. These cause beats in intensity, causing the pulse intensity profile to have oscillations after (before) the main pulse for positive (negative) φ_3.

2.2.2 Gaussian beam focusing

The spatial profile of a laser can be obtained by solving Maxwell's equations in cylindrical symmetry under the paraxial approximation,

$$\nabla^2 \vec{E} - \frac{\eta^2}{c^2} \frac{\partial^2 \vec{E}}{\partial t^2} = 0\,. \tag{2.38}$$

The solution (derivation in appendix A.1) is a Gaussian mode:

$$\begin{aligned} E(r,z,t) = E_0 \frac{w_0}{w(z)} &\exp\left(- \frac{r^2}{w^2(z)} \right) \\ &\times \exp\left(- i \frac{kr^2}{2R(z)} \right) \\ &\times \exp\left(- i \left[kz + \arctan\left(\frac{z}{z_R} \right) \right] \right) \\ &\times \exp\left(i\omega t \right), \end{aligned} \tag{2.39}$$

where each line corresponds to the amplitude, radial phase, longitudinal phase and temporal phase, respectively. The spatial variation of (2.39) is depicted in figure 2.3.

Gaussian modes retain their Gaussian spatial profile as they propagate and are characterised by the maximum electric field amplitude, E_0, and the minimum $1/e^2$ intensity radius of the beam, w_0. Both of these occur at the focus, here defined at $z = 0$. The beam width varies with distance from focus as

$$w^2(z) = w_0^2 \left[1 + \left(\frac{z}{z_R} \right)^2 \right], \tag{2.40}$$

where z_R is related to the physical parameter w_0 by

$$z_R = \frac{\eta \pi w_0^2}{\lambda}\,. \tag{2.41}$$

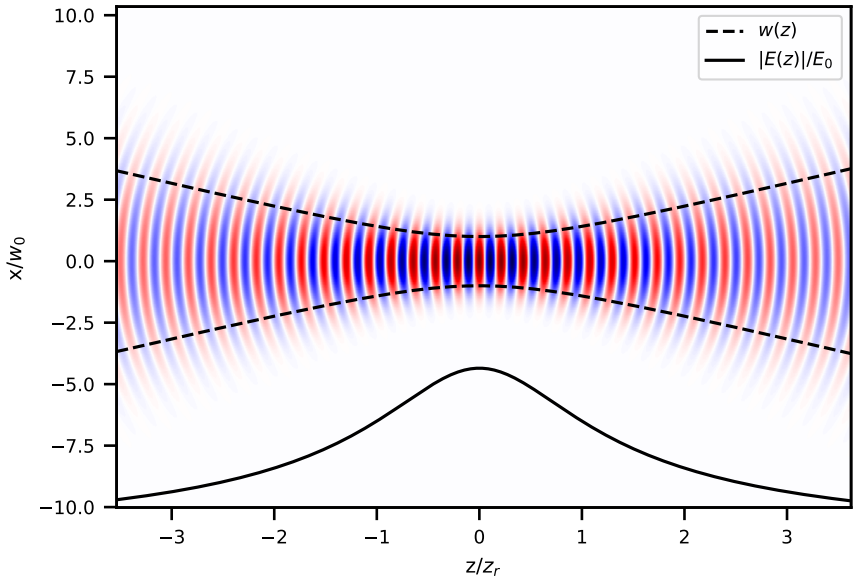

Figure 2.3: Spatial variation of the electric field of a Gaussian laser beam with $w_0 = 0.3\,\mu\text{m}$ and wavelength $\lambda = 800\,\text{nm}$ in the $y = 0$ plane.

z_R is known as the Rayleigh range, which is the distance from the focus over which the beam's electric field amplitude decreases to a factor of $1/e$ of the peak. Equivalently, it is the distance over which the area of the beam doubles compared to the waist at $z = 0$. It is often used to characterise the distance over which the laser intensity remains high.

The radius of curvature $R(z)$ is defined as

$$R(z) = z\left[1 + \left(\frac{z_R}{z}\right)^2\right]. \tag{2.42}$$

It corresponds to the wave picking up more phase farther off axis, which results in the wavefronts being curved parabolically. At the focus, $R(z = 0) = \infty$ and a plane wave is retrieved. At very large z, again $R \to \infty$, as the beam expands and the wavefronts appear locally planar.

Role of the Focusing Optics

The width $w(z)$ of a Gaussian mode (2.40) shows that at $z \gg z_R$, $w(z)$ varies linearly with z. Thus, the divergence angle of the beam can be calculated as

$$\theta = 2\frac{\mathrm{d}w}{\mathrm{d}z} = 2\frac{w_0}{z_R}. \tag{2.43}$$

Assuming θ is small, the beam radius at focus, w_0, can be obtained through geometric arguments relating θ to the focal length f of the focusing optic and the diameter D of the expanded beam as

$$w_0 = \frac{2\lambda}{n\pi}\frac{f}{D} = \frac{2\lambda}{n\pi}F_{\#}\,, \tag{2.44}$$

where the f-number $F_{\#}$ is defined as the ratio of the focal length of the optic to the expanded beam diameter. The f-number can also be used to characterise the Rayleigh range,

$$z_R = \frac{4\lambda}{n\pi}F_{\#}^2\,. \tag{2.45}$$

For a given laser pulse energy, reaching the high laser intensities required for LWFA requires a small beam radius at focus and therefore a focusing optic with a low f-number would be desirable. However, (2.45) implies that a tightly focused laser has a smaller Rayleigh range, which restricts the interaction length in which the laser remains intense enough to drive the wakefield. While the non-linear optics of plasmas can counteract the natural beam diffraction (section 2.5.3), this becomes difficult for tightly focused beams due to their stronger diffractive power. A compromise is required and typically a powerful (> 1 TW) laser is used along with an optic with a large f-number between 20 and 40 to obtain a larger spot, a longer Rayleigh range and a slow focus.

2.3 Plasma formation

The Coulomb potential well of electrons in an atom can be modified in the presence of a strong electric field E_0, such as that from an intense laser pulse, as

$$V(r) = -\frac{Ze^2}{4\pi\epsilon_0 r} - eE_0 r\,, \tag{2.46}$$

where Z is the charge of the ion. This is illustrated in figure 2.4.

At sufficiently high fields, the potential barrier is completely suppressed, enabling electrons to ionise without requiring additional energy. This is known as barrier suppression ionisation (BSI). The BSI threshold intensity in a linearly polarised laser is [66]

$$I_{\text{th}}[\text{W cm}^{-2}] = 4\times10^9\frac{E_{\text{ion}}^4[\text{eV}]}{Z^2}\,, \tag{2.47}$$

where E_{ion} is the electron binding energy. Table 2.1 lists ionisation potentials and intensity thresholds relevant to the work in this thesis.

At lower fields, the deformation may not be sufficient to fully suppress the potential

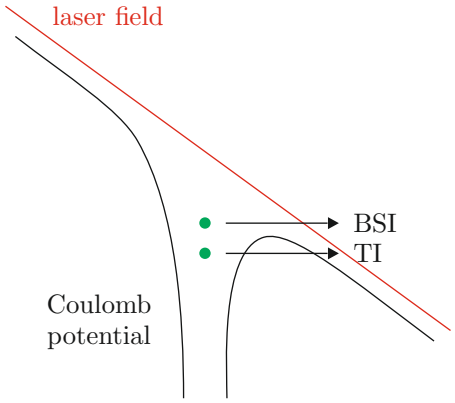

Figure 2.4: Distortion of the Coulomb potential by a strong electric field. An electron (green) can ionise through quantum tunnelling or barrier suppression.

Ion	E_{ion}(eV)	I_{th}(W cm^{-2})
H^+	13.6	1.4×10^{14}
He^+	24.6	1.5×10^{15}
He^{2+}	54.4	8.8×10^{15}
N^{5+}	97.9	1.5×10^{16}
N^{6+}	552.1	1.0×10^{19}
N^{7+}	667.0	1.6×10^{19}

Table 2.1: Ionisation potentials [67] and corresponding laser intensity thresholds for barrier suppression ionisation of elements used as plasma targets.

barrier, but electrons may still be able to become free via quantum tunnelling. This is known as tunnelling ionisation (TI). The most accurate tunnelling ionisation theory is the Ammosov-Delone-Krainov (ADK) tunneling theory [68], which is often implemented in PIC codes.

Typical laser wakefield acceleration experiments use intensities $\gtrsim 1 \times 10^{18}\,\text{W cm}^{-2}$. This means that ionisation of hydrogen and helium occurs instantaneously by the leading edge of the pulse, and the plasma can be considered to be fully ionised when the bulk of the pulse arrives.

2.4 Laser wakefield acceleration

The ponderomotive force of a high intensity ultrashort laser pulse is able to expel electrons from its vicinity, leaving a static ion background behind. This sets up plasma oscillations at the plasma frequency which propagate along with the laser at relativistic velocities; this comprises the wakefield. The longitudinal electric field associated with the wakefield enables particles to accelerate forwards or backwards depending on their

position. Particles which have velocities close to the phase velocity of the wakefield can propagate along with the accelerating field without leaving the accelerating gradient, thereby being able to accelerate to high energies over long distances.

2.4.1 Linear wake

In the linear regime, wakefield generation can be examined by considering the cold fluid equations. The fluid momentum equation, the continuity equation and Gauss's law are, respectively,

$$m_e \frac{\mathrm{d}\mathbf{v}}{\mathrm{d}t} = m_e \left(\frac{\partial \mathbf{v}}{\partial t} + (\mathbf{v} \cdot \nabla)\mathbf{v} \right) = -e(\mathbf{E} + \mathbf{v} \times \mathbf{B}) \tag{2.48}$$

$$\frac{\partial n_e}{\partial t} + \nabla \cdot (n_e \mathbf{v}) = 0 \tag{2.49}$$

$$\nabla \cdot \mathbf{E} = -e \frac{n_e - n_i}{\epsilon_0} \,. \tag{2.50}$$

The quantity $\mathbf{p}_\perp - e\mathbf{A}$ is conserved, meaning that $\mathbf{p} = e\mathbf{A}$ and $\mathbf{v} = e/m_e\mathbf{A}$. Then, grouping the non-linear terms in the right hand side and using $\mathbf{B} = \nabla \times \mathbf{A}$ and the vector identity $(\mathbf{A} \cdot \nabla)\mathbf{A} + \mathbf{A} \times (\nabla \times \mathbf{A}) = \nabla(\mathbf{A} \cdot \mathbf{A})/2$, (2.51) can be rewritten as

$$\begin{aligned} m_e \frac{\partial \mathbf{v}}{\partial t} + e\mathbf{E} &= -e(\mathbf{v} \times \mathbf{B}) - m_e(\mathbf{v} \cdot \nabla)\mathbf{v} \\ &= -\frac{e^2}{m_e}(\mathbf{A} \times \nabla \times \mathbf{A}) - \frac{e^2}{m_e}(\mathbf{A} \cdot \nabla)\mathbf{A} \\ &= -\frac{e^2}{2m_e}\nabla|\mathbf{A}|^2 \\ &= -\frac{m_e c^2}{2}\nabla|\mathbf{a}|^2 \,, \end{aligned} \tag{2.51}$$

which is the non-relativistic ponderomotive force.

The fluid equations can be linearised assuming a small density perturbation, $n_e = n_0 + \delta n$ where $\delta n/n_0 \ll 1$, and an equilibrium $\mathbf{E} = 0$ and $\mathbf{v} = 0$. Then, taking $\partial/\partial z$ of (2.51) and $\partial/\partial t$ of (2.49) and rewriting in 1D:

$$m_e \frac{\partial^2 v}{\partial z \partial t} - e\frac{\partial E}{\partial z} = -\frac{m_e c^2}{2}\frac{\partial^2 a^2}{\partial z^2} \tag{2.52}$$

$$\frac{\partial^2 v}{\partial t \partial z} = -\frac{1}{n_0}\frac{\partial^2 \delta n}{\partial t^2} \tag{2.53}$$

$$\frac{\partial E}{\partial z} = -\frac{e}{\epsilon_0}\delta n \,, \tag{2.54}$$

Substituting (2.53) and (2.54) into (2.52):

$$\left(\frac{\partial}{\partial t^2} + \omega_p^2\right)\delta n = \frac{n_0 c^2}{2}\frac{\partial^2 a^2}{\partial z^2}\,, \tag{2.55}$$

or, transforming to $\zeta = z - v_p t$, $\tau = t$, using the quasistatic approximation such that $\partial/\partial t \to -v_p \partial/\partial\zeta$ and $\partial/\partial z \to \partial/\partial\zeta$,

$$\left(\frac{\partial^2}{\partial \zeta^2} + k_p^2\right)\delta n = \frac{n_0}{2}\frac{\partial^2 a^2}{\partial \zeta^2}\,, \tag{2.56}$$

where $k_p = \omega_p/v_p$ and $v_p \approx c$. The solution to (2.56) is a sinusoidal wave with phase velocity v_p equal to the group velocity of the laser. The wake follows simple harmonic motion oscillations at the plasma frequency driven by the ponderomotive force. By Gauss's law (2.54), the electric field is also sinusoidal with frequency ω_p. The density modulation and corresponding electric field for a 1D linear wake are shown on the left column of figure 2.5. This derivation assumes a nonevolving laser driver.

The maximum attainable accelerating field in a cold non-relativistic plasma wave is [69]

$$E_0 = \frac{m_e c \omega_p}{e}\,. \tag{2.57}$$

E_0 scales with density as $n_e^{1/2}$, so for $n_e = 1 \times 10^{18}\,\mathrm{cm}^{-3}$ it is around $100\,\mathrm{GV\,m}^{-1}$. This shows that a plasma can sustain acceleration gradients three to four orders of magnitude larger than conventional linear accelerators. Such a maximum exists in this regime because the above analysis assumes that electron trajectories do not cross [69]. Above this limit, a singularity would develop in the electron density and the fluid approximation would break down.

2.4.2 Nonlinear wake

When $a_0 \geq 1$, δn becomes large; the accelerating fields $> E_0$, the approximations of (2.56) break down and the plasma wave becomes nonlinear. In this case, the wake is described by the differential equation [70, 71]

$$\frac{\partial^2 \phi}{\partial \zeta^2} = \gamma_p^2 k_p^2 \left(\beta_p \left[1 - \frac{1 + a_0^2}{\gamma_p^2 (1+\phi)^2}\right]^{-\frac{1}{2}} - 1\right), \tag{2.58}$$

where the wake potential $\Phi(\zeta)$, defined as $E = -\nabla\Phi$, has been normalised as $\phi = \Phi e/(m_e c^2)$, $\gamma_p = (1 - \beta_p^2)^{-1/2}$ and $\beta_p = v_p/c$ is the phase velocity of the wake. Analysis of (2.58) shows that the electric field departs from a linear sinusoidal form and develops

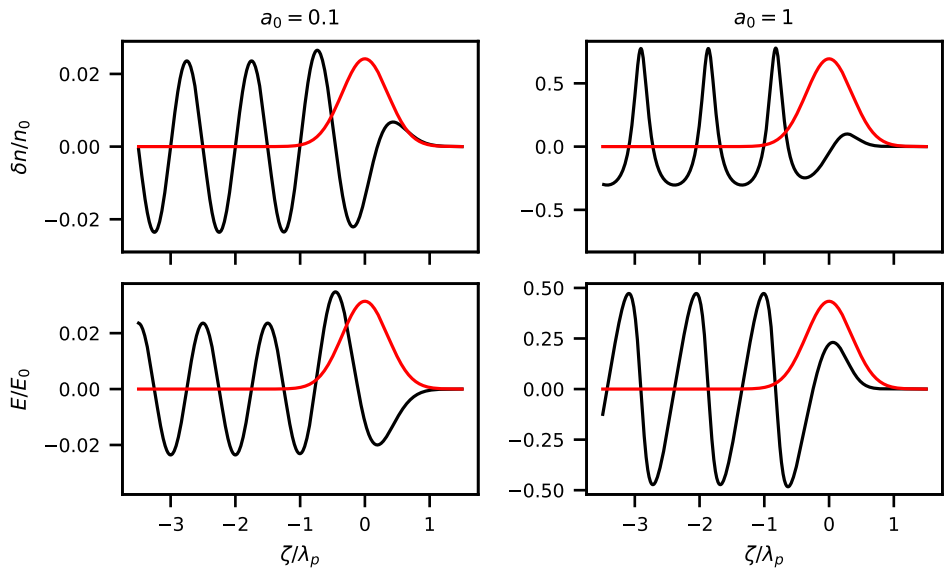

Figure 2.5: Numerical solutions to the density perturbation (top black) and electric field (bottom black) driven by lasers (red) with different strength parameters.

a sawtooth profile associated with wave steepening and period lengthening, as shown on the right column of figure 2.5.

The maximum electric field is now

$$E_{\max} = E_0 \frac{a_0^2}{\sqrt{1 + \frac{a_0^2}{2}}}, \tag{2.59}$$

which scales with a_0 at high intensity.

As nonlinear wakefields occur in the relativistic regime, the plasma wavelength increases by a factor of γ, which depends on a_0 as per (2.17). In three dimensions, the laser driver has a peaked transverse a_0 profile, meaning that the plasma wavelength is longer on axis. This causes the wavefronts of the wakefield to become curved.

2.4.3 Bubble regime

In three dimensions, ultra high intensity lasers are able to completely expel all electrons from the region of the pulse, due to the radial effect of the ponderomotove force, generating an ion cavity that is approximately spherical. This is known as the bubble regime [72]. Assuming a perfectly spherical bubble moving relativistically, the fields

within it are [73]

$$\begin{aligned} E_z &\simeq \frac{k_p \zeta}{2} E_0 \\ E_r &\simeq \frac{k_p r}{4} E_0 \\ B_\theta &\simeq -\frac{k_p r}{4} E_0 \,, \end{aligned} \tag{2.60}$$

where the terms of order γ_p^{-2} have been neglected. The accelerating fields are constant with radius and the focusing fields are linear with radius, which is beneficial for acceleration. They all vary $\sim \sqrt{a_0}$. The radius of the bubble can be estimated by balancing the outward ponderomotive force (2.27) and the inward Lorentz force of the electron sheath on the plasma (2.60). It is given by [74]

$$r_b \approx 2\sqrt{a_0}\frac{c}{\omega_p} \,. \tag{2.61}$$

The bubble regime typically requires high $a_0 \gtrsim 4$. For smaller $a_0 > 1$, complete cavitation does not occur but the wakefield develops a similar structure. The bubble regime is still a good approximation, but the structure deviates from a perfect sphere, becoming more elongated [74].

2.4.4 Acceleration dynamics

The nonlinear behaviour of an electron in a 1D plasma wave is analysed using Hamiltonian dynamics following ref. [75]. The energy gain of the electron in the wake potential $\Phi(\zeta)$ is

$$m_e c^2 \delta\gamma = -eE_z \delta z = e\frac{\partial \Phi}{\partial z}\delta z \,; \tag{2.62}$$

therefore,

$$\frac{\mathrm{d}\gamma}{\mathrm{d}z} = \frac{e}{m_e c^2}\frac{\partial \Phi}{\partial z} = \frac{\partial \phi}{\partial \zeta} \,, \tag{2.63}$$

where the potential has been normalised, $\phi = \Phi e/(m_e c^2)$ and $\partial/\partial\zeta = \partial/\partial z$ has been used.

Assuming that the drive laser pulse is nonevolving means it is a function of the ζ coordinate only. Therefore, by applying the quasistatic approximation, the plasma fluid quantities can also be assumed to be functions of ζ only. By keeping z as an independent parameter, ζ and γ can be considered to be the generalised position and momentum of

the electron. Hamilton's equations of motion are then

$$\frac{\partial \mathcal{H}}{\partial \zeta} = -\frac{\mathrm{d}\gamma}{\mathrm{d}z} = -\frac{\partial \phi}{\partial \zeta} \tag{2.64}$$

$$\frac{\partial \mathcal{H}}{\partial \gamma} = \frac{\mathrm{d}\zeta}{\mathrm{d}z} = 1 - \frac{\beta_p}{\beta}\,, \tag{2.65}$$

where $\mathcal{H}(\zeta, \gamma)$ is the Hamiltonian, which is conserved; (2.63) has been substituted into the first equation and the definition of ζ has been used in the second equation. The Hamiltonian can be found by integrating (2.64) as $\mathcal{H} = -\phi(\zeta) + f(\gamma)$ and (2.65) as $\mathcal{H} = \gamma - \beta_p\sqrt{\gamma^2 - 1} + g(\zeta)$, such that

$$\mathcal{H}(\zeta, \gamma) = \gamma\big(1 - \beta_z\beta_p\big) - \Phi(\zeta)\,. \tag{2.66}$$

The Hamiltonian is conserved in a nonevolving wake. Therefore, the path in phase space of an electron with initial momentum γ_0 before entering the wake is determined by (2.66). A set of trajectories is shown schematically in figure 2.6.

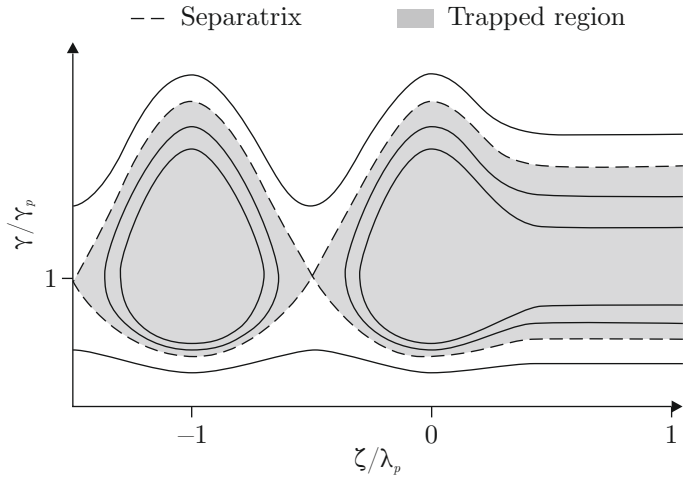

Figure 2.6: Schematic diagram of the electron phase space trajectories in a wakefield. The dashed line denotes the separatrix, which denotes the limit between trapped and passing particles. The shaded region denotes trajectories that are trapped within the accelerating structure.

Electrons with low or high initial Lorentz factor relative to γ_p are periodically accelerated forwards and backwards while not gaining any net energy from the interaction. These electrons make up the oscillating structure which comprises the wakefield. In contrast, electrons with similar γ to the wakefield are trapped by the wake potential. They travel along with the wakefield structure, where they can be accelerated to very high energies. This occurs for electrons with γ exceeding the potential minimum of the

wakefield, $\gamma_{\min}$, defined by the separatrix. Thus, acceleration requires electrons to be in the correct phase space position to be trapped. This process is known as injection and is discussed further in section 2.6.

2.4.5 Limits on acceleration

Diffraction

The propagation of the laser is determined by the focusing geometries, as discussed in section 2.2.2. This causes the beam to diverge at an angle $2w_0/z_R$. In practice, the laser remains focused over many Rayleigh lengths because diffraction can be overcome by relativistic self-focusing and plasma wave guiding. This is discussed in section 2.5.3.

Pump depletion

The laser transfers energy to the plasma until it is no longer able to excite a plasma wave. This process is known as depletion. At ultra high intensities, there is local energy depletion at the front of the laser pulse, causing the leading edge of the pulse to erode. Decker *et al.* calculate the energy lost in driving the wakefield and derive a pulse-front etching model for pump depletion. The front of the laser pulse is eroded with an etching velocity [76]

$$v_{\text{etch}} = \left(\frac{\omega_p}{\omega_0}\right)^2 c\,. \tag{2.67}$$

This causes the velocity of the leading edge to slow down to $v_g - v_{\text{etch}}$. The front of the laser moves back through the laser pulse and the energy ahead of this is depleted. The depletion length for the laser is then

$$L_{\text{pd}} = \left(\frac{\omega_0}{\omega_p}\right)^2 c\tau = \frac{n_c}{n_e} c\tau\,. \tag{2.68}$$

L_{pd} characterises the length scale over which the laser loses energy and changes frequency and intensity.

Dephasing

The phase diagram in figure 2.6 shows that trapped electrons undergo periodic acceleration and deceleration. This is because electrons continuously gain energy from the wakefield and eventually travel at close to c. However, the plasma wave travels at $v_p \approx v_{gl} < c$, where v_{gl} is the group velocity of the laser. This means that the electrons can outrun the wakefield, and eventually reach the decelerating phase of the wave.

In the linear regime, the dephasing length can be calculated as the propagation distance in which an electron slips forward by half a wavelength relative to the wake. In the lab frame, this corresponds to a distance $\lambda_p c/2(c - v_p)$, assuming the electron travels at approximately c. The dephasing length is then [71]

$$L_d = \frac{\lambda_0}{2}\left(\frac{n_c}{n_e}\right)^{3/2} . \tag{2.69}$$

2.4.6 Beam-loading

The electrons that are trapped and accelerated will modify the accelerating fields of the wakefield as a result of their own Coulomb field and the wakefield that the bunch itself produces [77]. These modifications can limit the energy gain of the electron bunch, but can also be beneficial in restricting the beam energy spread and improving beam quality [78]. This is because beam loading can flatten the accelerating fields, thereby reducing the chirp of the electron beam. However, taking advantage of beam loading for increased beam quality requires precise knowledge and control of the electron beam shape.

In 1D, the wakefield generated by the electron bunch is given by [77]

$$\frac{E_b}{E_0} \approx k_p L_b \frac{n_b}{n_0} , \tag{2.70}$$

where L_b is the length of the bunch and n_b is the trapped bunch density. This assumes that electron injection occurs within a single wakefield period, $k_p L_b \leq 1$, and that $E_b/E_0 < 1$ so that there is no wavebreaking (section 2.6.1) of the electron-driven wave.

2.5 Non-linear plasma optics

At the high intensities used in LWFA, the laser driver responds non-linearly to the plasma modulations it drives as a result of the variations in the refractive index of the plasma. This leads to various pulse modification processes [79]. Recalling the refractive index (2.7) with relativistic correction

$$\eta = \sqrt{1 - \frac{\omega_p^2}{\gamma\omega_0^2}} ,$$

where $\omega_p \propto n_e^{1/2}$ and $\gamma = (1 + a_0^2/2)^{1/2}$, it can be seen that the refractive index can be modified by changes of the plasma density, laser strength parameter or laser frequency.

This causes changes in the group and phase velocities of the laser.

The classical action (photon number) is conserved during laser propagation in a plasma [79]:

$$\langle a^2 \rangle \omega_0 w_0^2 L = \text{constant}, \tag{2.71}$$

where a is the normalised vector potential, ω_0 is the laser frequency, w_0 is the laser spot size and $L = c\tau_0$ is the pulse length. This means that the laser vector potential can be modified by varying ω_0, w_0 or L. All of these variations occur in LWFA because the laser co-propagates with gradients in the refractive index generated by the electron density wave.

2.5.1 Photon acceleration

A short laser pulse in a wakefield witnesses a longitudinal density gradient, meaning that the local density at the position of successive wavefronts is different. Consider a laser pulse in an increasing density gradient as illustrated in figure 2.7. A given wavefront is in a region of higher plasma density than the wavefront immediately behind it; therefore, the phase velocity of the leading wavefront, $v_{\phi 2}$, is higher than that of the trailing wavefront, $v_{\phi 1}$. The wavefronts move farther apart causing a decrease in laser frequency.

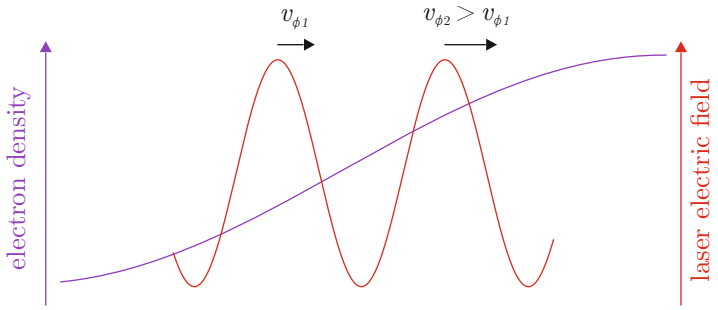

Figure 2.7: Schematic diagram of photon deceleration induced by a longitudinal density gradient.

In a time Δt, the wavefronts have moved such that the spacing between them is

$$\Delta z = \lambda_0 + (v_{\phi 1} - v_{\phi 2})\Delta t\,, \tag{2.72}$$

which defines the modified wavelength $\Delta z = \lambda$. Since $\Delta v = v_{\phi 2} - v_{\phi 1}$ is small relative to Δz, this can be rewritten as

$$\Delta\lambda = \Delta t \lambda_0 \frac{\partial v_\phi}{\partial z}\,. \tag{2.73}$$

Therefore, changing to the speed of light frame with $\psi = t - z/c$ and $t = \tau$

$$\frac{\partial \lambda}{\partial t} = -\frac{\lambda}{c}\frac{\partial v_\phi}{d\psi}\,, \tag{2.74}$$

or in terms of frequency

$$\frac{\partial \omega}{\partial \tau} = \frac{\omega}{c}\frac{\partial v_\phi}{\partial \psi} = -\frac{\omega}{c}\eta^{-2}\frac{\partial \eta}{\partial \psi}\,. \tag{2.75}$$

The scenario in figure 2.7 represents the excitation of a wakefield, where the pulse experiences a redshift. As $E = \hbar\omega$, this frequency shift is consistent with energy transfer from the laser to the plasma wave. Due to the periodicity of the refractive index, the back of a pulse longer than $\lambda_p/2$ will undergo blueshift, which diminishes wakefield generation. Energy gain of the laser via blueshifting is known as photon acceleration [80], by analogy to electron acceleration, as the group velocity dispersion in plasma implies higher v_{gl} at higher frequencies.

Photon deceleration at the front of the pulse is the mechanism through which pump depletion occurs. This local pump depletion causes steepening of the leading edge of the pulse, as the redshifted light has a lower group velocity and slips back. When $a_0 > 1$, the region of energy depletion becomes shorter [76].

Ionisation blueshift

The laser ionises the gas target as it propagates. This means that the laser co-propagates with a moving ionisation front in which the electron density increases from 0 to large values of order $10^{18}\,\mathrm{cm}^{-3}$. While not strictly photon acceleration as the photon number varies [79], this $\mathrm{d}n/\mathrm{d}t$ results in an increase of the frequency of light in this region [81,82]. However, because of the high intensities used to drive LWFA which are three orders of magnitude higher than typical ionisation thresholds (section 2.3), ionisation of the target typically occurs far from the peak of the laser pulse. Therefore, ionisation blueshift is expected to be an insignificant effect.

2.5.2 Longitudinal bunching of laser energy

The longitudinal refractive index variations also drive changes in the laser group velocity. Consider a laser pulse co-propagating with an increasing density gradient, as shown in figure 2.8. The front of the laser pulse travels at a group velocity, v_{g2}, smaller than the group velocity of the rear, v_{g1}. Therefore, after a time Δt, the pulse length will have changed by

$$\Delta l = (v_{g2} - v_{g1})\Delta t \approx l\frac{\partial v_g}{\partial z}\Delta t = -\frac{l}{c}\frac{\partial v_g}{\partial \psi}\Delta t\,, \tag{2.76}$$

where $\partial/\partial z = -(1/c)\partial/\partial\psi$ was used. Therefore,

$$\frac{\partial l}{\partial \tau} = -\frac{l}{c}\frac{\partial v_g}{\partial \psi}\,, \tag{2.77}$$

and disregarding relativistic effects, so that the group velocity variation arises from variations in the plasma density,

$$\frac{\partial l}{\partial \tau} = -l\frac{\partial \eta}{\partial \psi}\,. \tag{2.78}$$

In practice, photon acceleration causes a chirp to develop in the laser, and the group velocity dispersion of the plasma enhances the pulse compression as the redshifted light at the front travels more slowly than the blueshifted light at the rear.

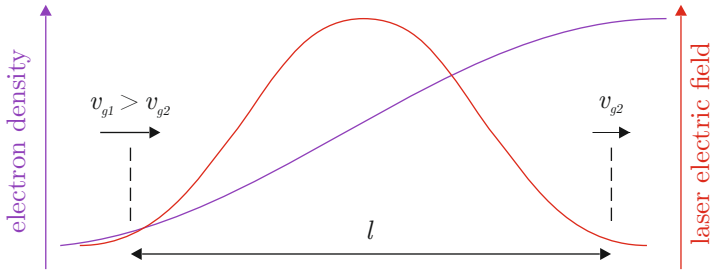

Figure 2.8: Schematic diagram of longitudinal bunching of laser energy caused by an inhomogeneous plasma density.

Pulse compression is smaller in non-linear wakes because at very high a_0, the strong blowout of electrons means the laser effectively travels in a vacuum, so the relative phase slippage is smaller [74, 83].

2.5.3 Transverse focusing of laser energy

Transverse variations of the refractive index can change the curvature of laser wavefronts so as to modify the beam's focusing or diffracting behaviour. Enhanced focusing requires $\partial\eta/\partial r < 0$, such that the phase velocity of light, $v_\phi = \omega_0/k_z \approx c\eta^{-1}$, is higher at large r than along the propagation axis. This causes the direction of the Poynting vector to change so that the energy flows inwards.

Consider an initially flat wavefront propagating through a radially varying refractive index. After a time Δt, the region off-axis has moved a longer distance than the region on axis, as shown in figure 2.9. The angle at which the wavefront bends is given by

$$\tan\theta = \frac{v_{\phi r} - v_{\phi 0}}{w_0}\Delta t\,, \tag{2.79}$$

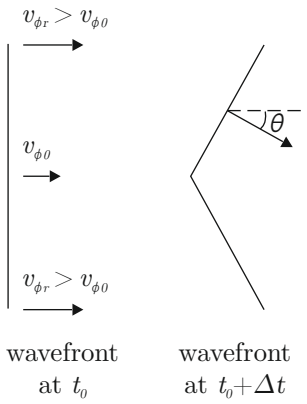

Figure 2.9: Schematic diagram of transverse focusing of laser energy. A wavefront travels to the right over a time Δt and transverse variations of the local phase velocity cause a focusing effect.

which, assuming a small θ, can be generalised to

$$\theta = \frac{\partial w_0}{\partial z} = \frac{\partial v_\phi}{\partial r}\Delta t\,. \tag{2.80}$$

The rate at which the energy flows inwards is then given by

$$v_{\text{in}} = \frac{\partial w_0}{\partial \tau} = -c\theta = -c\frac{\partial v_\phi}{\partial r}\Delta t\,, \tag{2.81}$$

or

$$\frac{\partial^2 w_0}{\partial \tau^2} = -c\frac{\partial v_\phi}{\partial r}\,. \tag{2.82}$$

This is a general result to characterise the rate of focusing for a given phase velocity distribution. The source can be a radial density profile (external guiding) or a laser intensity profile with a peak on axis (relativistic self-focusing).

Relativistic self-focusing

A laser intensity profile with a peak on axis has $\partial a^2/\partial r < 0$, leading to refractive guiding of light. This occurs because the increased quiver motion of electrons on axis causes an effective decrease in the plasma frequency, leading to an increased refractive index on axis. Neglecting changes in density, and assuming small changes in a_0, the refractive index can be approximated by a binomial expansion

$$\eta^{-1} \approx 1 + \frac{2}{2}\frac{\omega_p^2}{\gamma\omega_0^2} \approx 1 + \frac{1}{2}\frac{\omega_p^2}{\omega_0^2}\left(1 + \frac{a_0^2}{4}\right), \tag{2.83}$$

where $\eta^{-1} = v_\phi/c$ has been considered. Then (2.83) can be used to rewrite the transverse focusing (2.82) as

$$\frac{\partial^2 w}{\partial \tau^2} = -c^2 \frac{\partial\left(\eta^{-1}\right)}{\partial r} \approx -\frac{c^2}{8}\frac{n_e}{n_c}\frac{\partial a^2}{\partial r}\,. \tag{2.84}$$

This relativistic effect counteracts the natural Gaussian beam diffraction given by (2.40). Differentiating (2.40) twice gives

$$\frac{\mathrm{d}^2 w}{\mathrm{d}z^2} = \frac{4c^2}{w_0^3\omega_0^2}\,, \tag{2.85}$$

or, using $\mathrm{d}/\mathrm{d}\tau = c\,\mathrm{d}/\mathrm{d}z$,

$$\frac{\mathrm{d}^2 w}{\mathrm{d}\tau^2} = \frac{4c^4}{w_0^3\omega_0^2}\,. \tag{2.86}$$

Approximating $\partial a^2/\partial r \approx a^2/w_0$ in (2.84) and equating it to (2.86) gives

$$a_0^2 w_0^2 = \frac{32c^2}{\omega_p^2}\,, \tag{2.87}$$

which represents the condition on the pulse power $a_0^2 w_0^2$ for relativistic self-focusing to dominate over geometric diffraction. It can be expressed as [84]

$$P_c[\mathrm{GW}] \approx 17.4\left(\frac{n_c}{n_e}\right)^2, \tag{2.88}$$

where P_c is the critical power for relativistic self-focusing. The laser is found to diffract for $P < P_c$ and remain guided or matched for $P = P_c$. For relativistic lasers, $a_0 \gtrsim 1$, $P > P_c$ corresponds to a beam with a width that oscillates around its matched value [85].

At the front of the laser, the ponderomotive force causes a density compression associated with a decrease in the refractive index which cancels the relativistic self-focusing and the laser should still diffract [86]. This is because changes to the refractive index occur on the plasma frequency time scale, not the laser frequency timescale. However, the front of the laser pump depletes before diffracting, meaning that the pulse can still be considered to self-focus to a degree even when $L \lesssim \lambda_p$ [76]. This occurs because the leading edge of the laser is photon decelerated, and these redshifted photons slip back to a region where guiding is effective. The condition for depletion to dominate over diffraction is [76]

$$w_0^2 > 2\frac{\omega_0}{\omega_p}\frac{c^2}{\omega_p^2}\,, \tag{2.89}$$

where w_0 is the Gaussian spot size.

Plasma guiding

A wakefield with sufficiently large amplitude can additionally guide the laser that drives it. If the plasma wave has a form $\delta n(r)\sin(k_p\zeta)$, with $\delta n(r) > 0$ and $\mathrm{d}\delta n/\mathrm{d}r < 0$, then the plasma wave acts to focus the laser in regions where $\sin(k_p\zeta) < 0$. A pulse will be guided by a wakefield provided that [85]

$$\delta n_0 \geq \frac{1}{\pi r_e w_0^2}\,, \tag{2.90}$$

where $r_e = e^2/mc^2$ is the classical electron radius and w_0 is the laser spot size.

In the bubble regime (section 2.4.3), $\delta n_0 \sim 1$ and the electron density drops to zero within the bubble radius r_b. In this case, there is no laser focusing structure within r_b and the laser pulse is guided by the edges of the bubble, $w_0 \approx r_b$. This comprises the matched condition [74]

$$w_0 \approx w_m = \frac{2\sqrt{a_0}}{k_p}\,. \tag{2.91}$$

This self-guided propagation means that the pulse profile does not exhibit significant variations over the interaction distance. Guiding is only effective if $w_0 \geq w_m$; if the laser is focused to $\lesssim \lambda_p$, the pulse breaks down into filaments [87]. Guiding is stronger for higher P/P_c and $\delta n/n_e$ [88].

External guiding methods

Relativistic self-focusing and plasma guiding are self-guiding mechanisms that occur at high densities and intensities. They are easy to implement practically but are dependent on the laser parameters and therefore rely on reliable laser performance. This may be problematic in terms of the reproducibility and control of the interaction.

External guiding methods use a radial density profile as a guiding structure for the laser. This decouples the focusing of the drive laser beam from its parameters, thereby enabling better control and stability. Examples of external guiding methods include capillary discharge waveguides [22, 89] and hydrodynamic optical field ionised (HOFI) channels [90–92]. These are able to operate at lower plasma densities where relativistic self-focusing is less efficient and allow longer guiding distances. However, their implementation requires high voltage systems or an additional laser, which may pose practical difficulties.

2.6 Electron injection and trapping

For an electron to reach high energies, it must be separated from the coherent motion that forms the plasma wave in a process known as injection. Various injection schemes have been proposed.

2.6.1 Self-injection

The dynamics of a Langmuir wave in the framework of cold electron hydrodynamics is considered as in ref. [93] using the Lagrange coordinates (z_0, t). The position of an element of the electron fluid is given by the Euler coordinate

$$z = z_0 + \xi(z_0, t)\,, \tag{2.92}$$

where $\xi(z_0, t)$ is the displacement of an electron fluid element from its initial position z_0 at time t.

The electron density is given by

$$n_e(z, t) = \frac{n_0(z_0)}{J}\,, \tag{2.93}$$

where

$$J \equiv \left|\frac{\partial z}{\partial z_0}\right| = \left|1 + \frac{\partial \xi(z_0, t)}{\partial z_0}\right| \tag{2.94}$$

is the Jacobian of the transformation from Euler to Lagrange coordinates. Wave-breaking occurs when the Jacobian vanishes,

$$\frac{\partial \xi(z_0, t)}{\partial z_0} = -1\,, \tag{2.95}$$

as a singularity in the electron density arises here. This condition corresponds to electron oscillation amplitudes of order λ_p. Wave-breaking refers to the catastrophic event in which the entire wakefield structure is destroyed [94] due to the loss of wave coherence and breakdown of the fluid approximations. However, this term is also often used more generally to refer to the development of the electron density singularity and subsequent self-injection of electrons [95]. In this case, few fast electrons on the sharp density structure leave the plasma wave; these can become trapped in the accelerating phase and reach high energies. Self-injection typically requires high intensity lasers with $a_0 > 3/8$ [96, 97].

In the bubble regime, injection is associated with temporal expansion of the bubble

[98]. Electrons in the plasma wave interact with the bubble as they slip backwards during a time t_{slip}. If the bubble expands sufficiently during t_{slip}, the electrons can gain sufficient energy to satisfy the injection condition

$$\gamma_e \geq \gamma_p \,, \tag{2.96}$$

where γ_e and γ_p are the relativistic factors of the electrons and plasma wave (phase velocity), respectively.

Schroeder *et al.* attribute the injection in a growing plasma wavelength to the decrease in the wakefield phase velocity. These changes to the nonlinear plasma wavelength, λ_{Np}, are attributed to laser evolution via redshifting and steepening. The contribution of the evolution of λ_{Np} to the wakefield phase velocity $v_p = \beta_p c$ is then given by [99]

$$\begin{aligned} \delta\beta_p &\approx \zeta_p \lambda_{Np}^{-1} \frac{\partial \lambda_{Np}}{\partial E_m} \frac{\partial E_m}{\partial ct} \\ &\approx \zeta_p \lambda_{Np}^{-1} \frac{\partial \lambda_{Np}}{\partial a_0} \frac{\partial a_0}{\partial ct} \,, \end{aligned} \tag{2.97}$$

where $E_m = E_{\max}/E_0$ is the peak accelerating field behind the laser, and $E_m = E_m(a_0)$ has been used. This shows that laser pulse modifications (section 2.5) can drive self-injection; not by reaching the threshold wakefield strength $a_0 > 4$ but by the time evolution of the driver modifying the wakefield dynamics. Due to the non-linearity of the laser evolution, self-injection is difficult to predict and control, leading to low electron beam stability and tunability, as well as electron beams with large energy spread and divergence [71].

Transverse effects

The transverse structure of the wakefield comprises curved phase fronts, as a result of the transverse a_0 variation which causes an increased plasma wavelength on axis. The curvature of the phase fronts also increases farther behind the laser driver. Trapping of particles can occur when the curvature of the phase front is of the order of the electron fluid displacement, as this causes the regular wakefield structure to be destroyed [95]. This process is known as transverse wave-breaking, and is a $\geq$2D effect. It generally occurs below the thresholds for self-injection in 1D, which means that self-injection may occur earlier than expected from 1D theory.

2.6.2 Density transition injection

Injection of electrons into a wakefield by a density inhomogeneity was first proposed by Bulanov *et al.* [93], whose theoretical and computational work showed a locally reduced non-linear injection threshold at a gentle decreasing density transition. Suk *et al.* [100] theorised the improved localised trapping of electrons by a sharp density transition, which has been realised in the literature via the production of a shock in a gas flow target [101]. The gentle $L \gg \lambda_p$ and sharp $L < \lambda_p$ density transitions are fundamentally different regimes, driving injection through different dynamics.

Gentle transition length $L \gg \lambda_p$

The dynamics of a Langmuir wave in the framework of cold electron hydrodynamics is considered as in ref. [93, 102, 103] using the Lagrange coordinates (z_0, t).

Consider small-amplitude Langmuir oscillations in a density inhomogeneity $n_e = n_e(z_0)$. The displacement ξ is approximated by $\xi(z_0, t) = \xi_1 \cos(k_p z_0 - \omega_p t)$; i.e. the oscillations are harmonic. The injection condition (2.95) occurs when $k_p \xi_1 = 1$, which is equivalent to $v_e = v_p$, where $v_e \equiv \partial z/\partial t$ is the electron velocity and $v_p \equiv \omega_p/k_p$ is the phase velocity of the wave. Given that a Langmuir wave in an inhomogeneous density follows [93]

$$\frac{\partial k_p}{\partial t} = -\frac{\partial \omega_p}{\partial z}\,, \tag{2.98}$$

where $\omega_p = \omega_p(z_0)$ is the plasma frequency which varies due to its density dependence, the wavenumber k_p increases with time and the wave breaks even when the initial wake amplitude is below the wavebreaking threshold.

The phase position of an electron element in the plasma wave is given by

$$\psi(z_0, t) \equiv k_p(z_0)\big(z_0 - v_{gl} t\big),$$

where $k_p = k_p(z_0)$ and v_{gl} is the group velocity of the laser driver. Consider a plasma wave propagating through a longitudinal density profile $n_e = n_e(z_0)$. The phase position of an electron then varies as

$$\frac{\mathrm{d}\psi}{\mathrm{d}z_0} = k_p(z_0)\left(1 - \frac{v_{gl}}{v_e}\right) + \frac{\psi}{2n}\frac{\mathrm{d}n_e}{\mathrm{d}z_0}\,, \tag{2.99}$$

where it has been used that $k_p \propto n_e^{1/2}$, so that $\mathrm{d}k_p/\mathrm{d}z_0 = k_p/2n_e \times \mathrm{d}n_e/\mathrm{d}z_0$.

An electron at z_0 travelling at the phase velocity of the plasma wave, $v_e = v_p$, will

obey $\mathrm{d}\psi/\mathrm{d}z_0 = 0$, such that

$$v_p = v_{gl}\left(1 + \frac{\zeta}{2n_e}\frac{\mathrm{d}n_e}{\mathrm{d}z_0}\right)^{-1}, \tag{2.100}$$

where $\zeta(z_0, t) \equiv z_0 - v_{gl}t \equiv \psi/k_p$ is the position of the electron relative to the laser driver. Since $\zeta < 0$ behind the laser pulse, the phase velocity of the plasma wave decreases on the density downramp, where $\mathrm{d}n_e/\mathrm{d}z_0 < 0$. This local decrease in v_p accommodates the increase in plasma wavelength. Figure 2.10 depicts the phase velocity variation of a laser-driven plasma wake in a density downramp. The phase velocity at a given z_0 decreases with time, allowing for the increasing shift in ζ of subsequent wake periods.

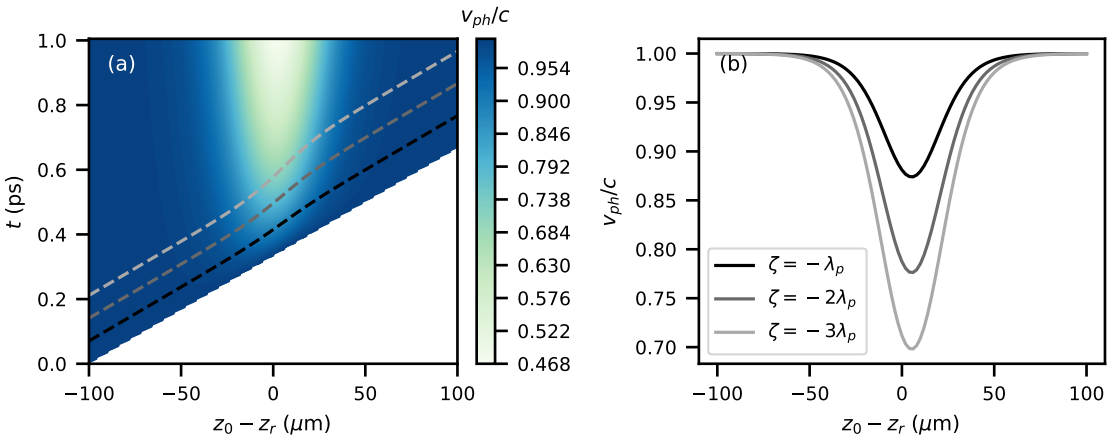

Figure 2.10: Phase velocity of a plasma wave in a decreasing density transition centred at z_r. (a) v_p as a function of distance from the middle of the density ramp $z_0 - z_r$ and time $t = (z_0 - \zeta)/v_{gl}$. The dashed lines show $\zeta = -(1, 2, 3)\lambda_p$, which correspond to the trajectory of the back of the first three plasma buckets, where injection could take place. (b) v_p along the dashed lines in (a).

Combining (2.99) and (2.100) gives the phase shift of a plasma electron in a density transition as

$$\frac{\mathrm{d}\psi}{\mathrm{d}z_0} = k_p v_{gl}\left(\frac{1}{v_p} - \frac{1}{v_e}\right). \tag{2.101}$$

Electrons with $v_e(z_0) = v_p(z_0)$ are locked in phase, while those with $v_e(z_0) > v_p(z_0)$ advance in phase. Both of these cases correspond to electrons being trapped in the wakefield, as they do not leave the accelerating region of the corresponding wake period. All electrons involved in wave-breaking are injected in this regime.

The injection condition $v_e \geq v_p$ can be expressed as [102]

$$\gamma_e \geq \frac{v_p\tau + c}{\sqrt{(v_p\tau + c)^2 - v_p^2}}, \tag{2.102}$$

where γ_e is the Lorentz factor of the electrons, $\tau = ct\Delta\omega_p/w_p\Delta z$, Δz is the scale length of the inhomogeneity and $\Delta\omega_p$ is the change in the plasma frequency in the transition region. In a homogeneous plasma, $\tau = 0$ and (2.102) reduces to the usual $\gamma_e \geq \gamma_{ph}$ wave-breaking threshold.

Sharp transition length $L \lesssim \lambda_p$

When the length of the density transition region is shorter than the plasma wavelength, electrons in the wakefield cannot adapt to the change in density in the same way as when traversing a gentle ramp. In this case, the amplitude of electron oscillations is large enough that electrons can move between high and low density regions within a single oscillation. Electron injection at a sharp density transition is caused by phase mixing in the first bucket [104].

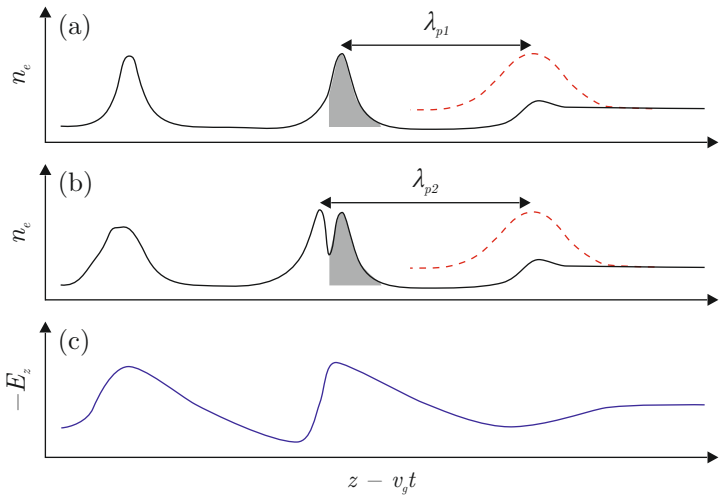

Figure 2.11: Schematic diagram of phase mixing in a sharp density transition. Electron density (a) before and (b) after the density transition; the laser pulse is shown as the dashed red line and the shaded area represents the same electron bunch. (c) Longitudinal electric field at the timestep in (b).

Electrons originating in the high density region oscillate with plasma wavelength λ_{p1}. As the density transition is sharp, these electrons can cross to the low density region during their oscillation, remaining at $\zeta = -\lambda_{p1}$. Meanwhile, electrons originating in the low density region oscillate with $\lambda_{p2} > \lambda_{p1}$, forming a new peak at $\zeta = -\lambda_{p2}$ as shown

in figure 2.11. As a result, the bunch at λ_{p1} finds itself advanced in phase space, where acceleration may occur [105].

In contrast to injection through a gentle density ramp, where all electrons are injected, trapping of electrons at a sharp density transition is not guaranteed [102]. Figure 2.12 shows the phase space trajectories of electrons at either side of a sharp density ramp. Trapped particles move along closed orbits, and the separatrix denotes the boundary between trapped and free electrons. The transition from higher to lower density results in a decrease of the minimum momentum required for trapping. Therefore, free particles in open trajectories can access closed trajectories through the density transition, meaning that they become trapped.

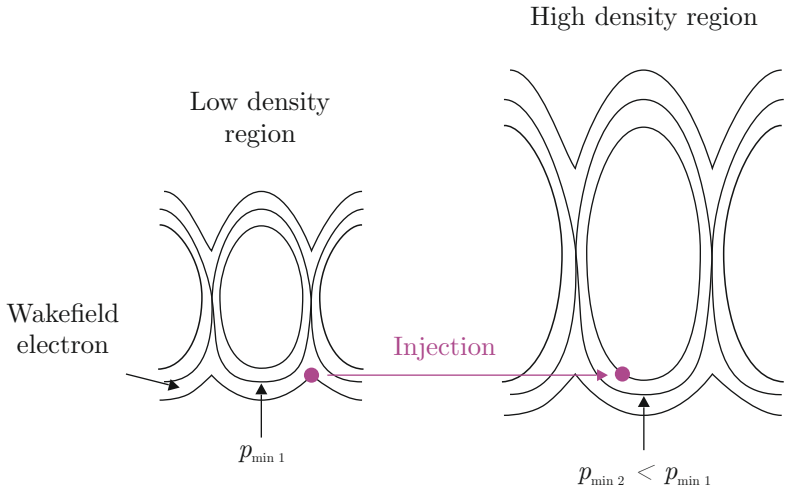

Figure 2.12: Electron phase space corresponding to the Hamiltonian of a wakefield in the high and low density regions at either side of a sharp transition. The bottom curves represent the motion of the electron fluid in the wakefield. Adapted from ref. [102].

2.6.3 Ionisation injection

Ionisation injection is the process whereby deeply bound electrons of high Z gases are ionised in a pre-existing wakefield, enabling them to be trapped. It typically relies on the use of trace amounts of nitrogen in hydrogen or helium gas. This was initially achieved by using multiple laser pulses [106, 107].

A single intense laser pulse can also be used to drive ionisation injection [108, 109]. The leading edge of the laser can ionise most of the gas (section 2.3) and drive a wakefield with these electrons lying on the untrapped, cold fluid orbits that constitute the plasma wave oscillation. The electric field of the laser is strong enough to enable tunnelling ionisation of the inner shell electrons of the dopant gas only near the peak of the pulse.

These electrons ionise when the wakefield is already present and are therefore released in the middle of the bubble, dephased from the plasma wave oscillations. The electrons are ionised at rest, so they travel backwards through the interior of the bubble where they are accelerated. If their velocities surpass the wakefield phase velocity, $v_e > v_p$, before they reach the back of the bubble, they are able to inject. Assuming a static wakefield, this requires [108, 110]

$$\Delta\phi \geq 1, \tag{2.103}$$

where $\Delta\phi$ is the difference between the normalised ($\phi = e\Phi/(m_e c^2)$) potentials at the injection position ϕ_i and at the back of the wave bucket ϕ_f. Ionisation injection requires a laser $a_0 > 1.6$ [108], compared to self-injection which requires laser $a_0 > 3.8$ [96, 97].

Ionisation injection drives electron beams with a large energy spread because injection occurs continuously while the laser intensity remains above the ionisation threshold of the inner nitrogen electrons. Plasma density tailoring [111] was proposed to reduce the energy spread by controlling the trapping, which was first achieved in staged accelerators composed of multiple gas jet targets [112–114]. Shock assisted ionisation injection was proposed to further improve the energy spread of the electron beams by operating at lower laser intensities and restricting the injection to a density down-ramp [115], similarly to the density transition injection described in section 2.6.2. Another proposed method of reducing the energy spread of ionisation-injected electrons is to take advantage of the self-focusing of the laser driver [116]. By using an unmatched laser pulse, propagation through the plasma can increase the intensity to beyond the ionisation threshold via self-focusing only in a restricted region. Alternatively, the self-truncated ionisation injection regime relies on laser pulse evolution causing an increase of the wake amplitude, such that Ψ_f is increased and condition (2.103) is no longer satisfied [117]. Low energy spread electron beams have been demonstrated using this method in gas jet targets [118, 119].

Chapter 3

Methods

3.1 Gemini laser

The Gemini laser at the Central Laser Facility is a two-beam petawatt-class laser system. It uses titanium-sapphire as the gain medium and employs chirped pulse amplification (CPA) [17]. The layout of the laser system is shown in figure 3.1. It is capable of producing laser pulses with energies up to 15 J in a pulse duration of 40 fs at a central wavelength of 800 nm. The laser has a repetition rate of one shot every 20 s in full power mode, which is limited by the heating of the pump laser [120]. Various off-axis parabolic mirrors from $f/1$ to $f/40$ are available to focus the laser, which allows laser intensities of order $10^{18}\,\mathrm{W\,cm^{-2}}$ to $10^{21}\,\mathrm{W\,cm^{-2}}$ to be achieved.

3.2 Lund laser

The High Power Laser at the Lund Laser Centre, University of Lund, is a 50 TW laser system. It also uses titanium-sapphire as the gain medium and employs CPA. The system uses four amplification stages to produces laser pulses with energies around 1 J in a pulse duration of 38 fs. The schematic diagram of the laser is shown in figure 3.2; more details are described in ref. [121].

3.3 Interferometry

The low density plasma used in LWFA is transparent to low intensity optical light, but will impart a phase on a beam that traverses it due to its refractive index. Therefore, an imaging system that is sensitive to the phase of the light is required in order to diagnose the density profile of a LWFA target. Interferometry is a technique whereby a probe

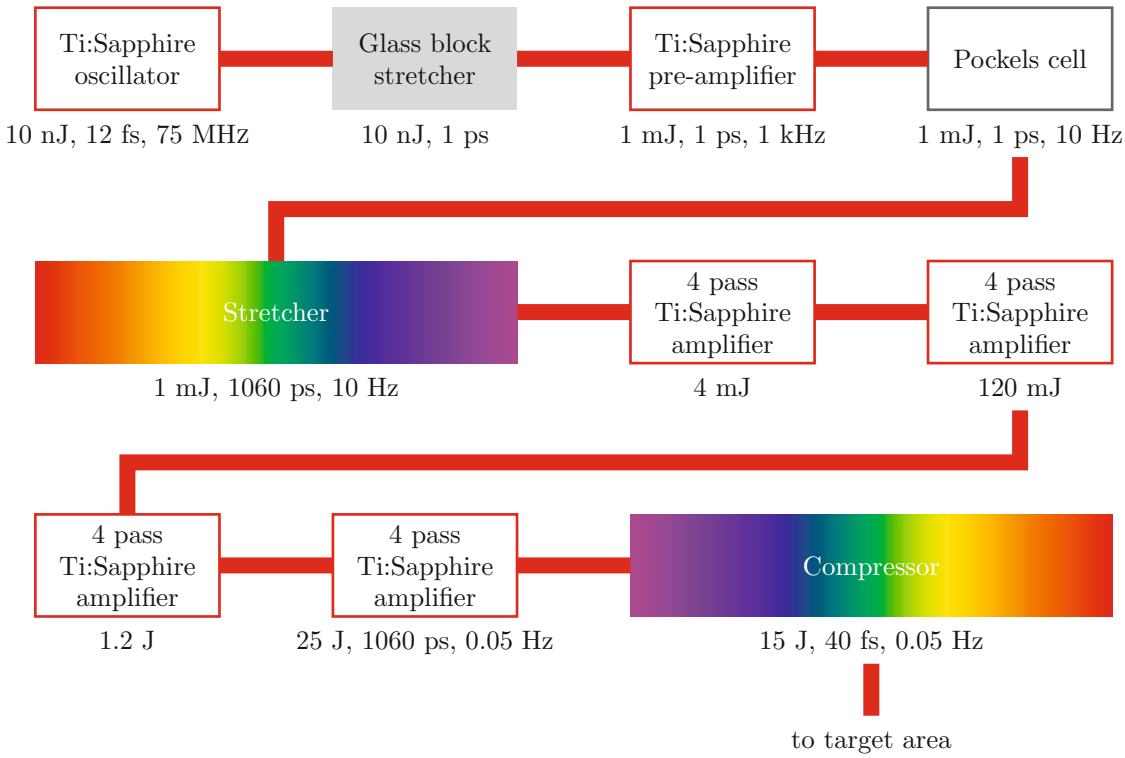

Figure 3.1: Schematic diagram of the Gemini laser system.

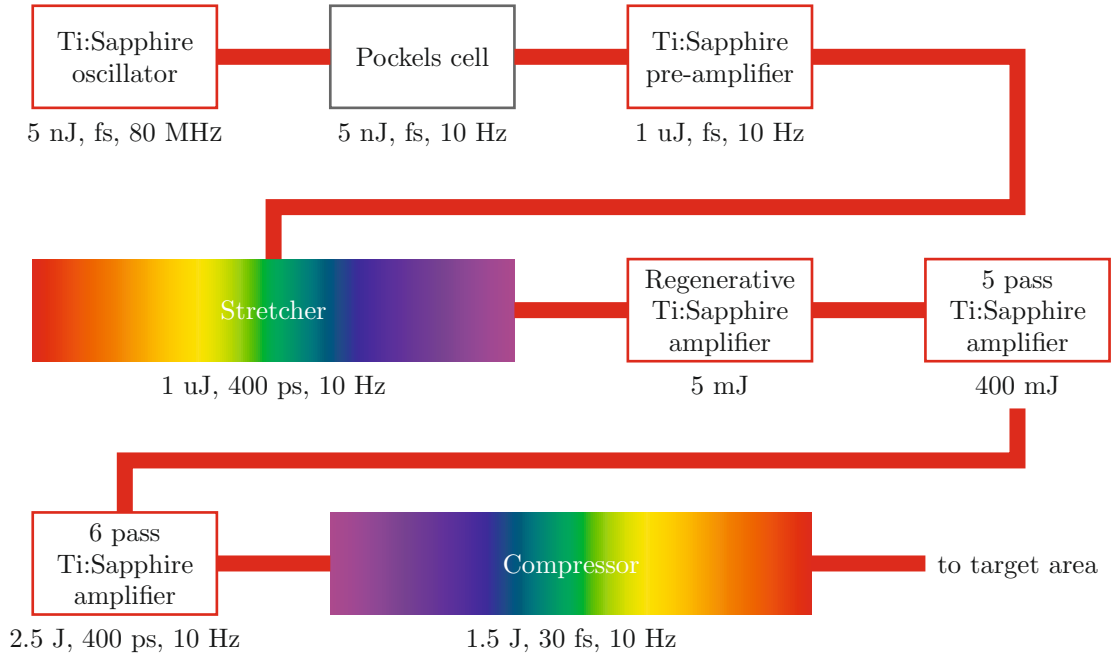

Figure 3.2: Schematic diagram of the Lund multi-terawatt laser system.

beam, which propagates through the plasma, is overlapped with a second reference beam which is undisturbed, creating an interference pattern. The phase accumulated by the probe beam relative to a reference beam is given by

$$\Delta\phi(y,z) = \frac{2\pi}{\lambda_0}\int \big(\eta(x,y,z) - 1\big)\,\mathrm{d}x\,, \tag{3.1}$$

where the beam is a plane wave with wavelength λ_0 propagating in the x-direction. Recalling that the refractive index of a plasma is

$$\eta(x,y,z) = \sqrt{1 - \left(\frac{\omega_p}{\omega_0}\right)^2}\,,$$

the fact that the plasma is underdense in LWFA, $\omega_p \ll \omega_0$, means that it can be rewritten as

$$\eta(x,y,z) \approx 1 - \frac{1}{2}\frac{n_e}{n_c}\,, \tag{3.2}$$

where the critical density is $n_c = \omega_0^2 m_e \epsilon_0 / e^2$. Thus the phase shift is given by

$$\Delta\phi(y,z) \approx \frac{\lambda_0 e^2}{4\pi c^2 m_e \epsilon_0}\int n_e(x,y,z)\,\mathrm{d}x\,. \tag{3.3}$$

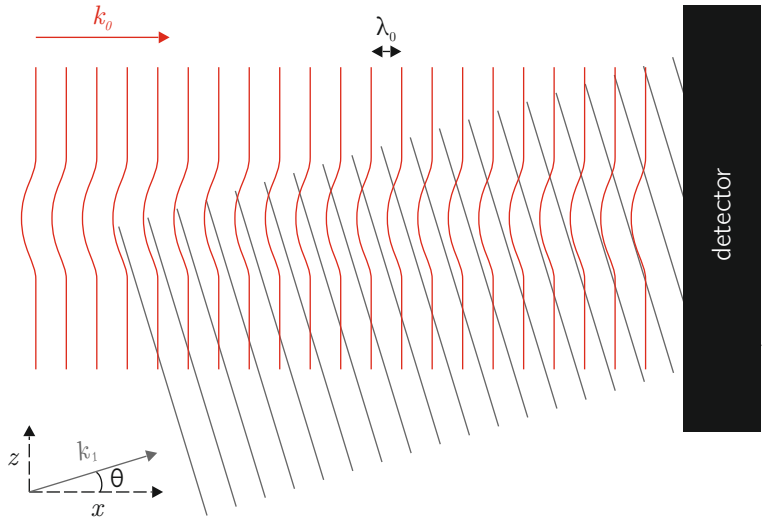

Figure 3.3: Schematic of a probe beam (red) interfering with a reference beam (grey) at an angle θ.

In order to measure $\Delta\phi$, a small angle θ is introduced between the probe and reference beams as shown in figure 3.3. Excluding the temporal component, the probe beam

can be described by

$$E_{\text{probe}}(x, y, z) = E_0 \exp\left(i(k_0 x + \Delta\phi(y, z))\right), \tag{3.4}$$

and the reference beam is given by

$$E_{\text{ref}}(x, y, z) = E_0 \exp\left(i(k_0 x \cos\theta + k_0 z \sin\theta)\right). \tag{3.5}$$

Therefore, the signal measured by the detector at $x = 0$ is

$$\begin{aligned} I(y, z) &\propto |E_{\text{probe}} + E_{\text{ref}}|^2 \\ &\propto 1 + \cos\left(k_0 z \sin\theta - \Delta\phi(y, z)\right). \end{aligned} \tag{3.6}$$

The inclusion of the temporal envelopes of E_{probe} and E_{ref} modifies the cosine term in (3.6) by a visibility function $V(z)$, which varies slowly relative to the cosine oscillations [122].

When no plasma is present, $\Delta\phi = 0$ and the detector measures interference fringes in the z-direction with a spacing

$$\lambda_f = \frac{\lambda_0}{\sin\theta}. \tag{3.7}$$

The presence of the plasma causes the fringes to shift in the z-direction.

As the phase information is encoded in the spatial position of the fringes, the diagnostic's sensitivity to space and phase are linked. When λ_f is larger, the phase (and therefore density) resolution is higher, but structures of order smaller than λ_f cannot be resolved.

3.3.1 Phase retrieval

Fourier transform phase retrieval

Computational analysis of interferograms can be performed through the use of Fourier transform techniques [123]. The interferogram has a form given by (3.6). Modifying this to include noisy terms for the background $g_{bg}(y, z)$ and plasma $g_p(y, z)$, the signal becomes

$$\begin{aligned} I(y, z) &= g_{\text{bg}}(y, z) + g_p(y, z) \cos\left(k_f z - \Delta\phi(y, z)\right), \\ &= g_{\text{bg}} + \frac{1}{2}\left(e^{ik_f z} f(y, z) + e^{-ik_f z} f^*(y, z)\right) \end{aligned} \tag{3.8}$$

where $k_f = 2\pi/\lambda_f$ and $f(y,z) = g_p \exp(i\Delta\phi)$. Performing a two-dimensional Fourier transform from the (y,z) plane to the (u,v) plane and denoting the transforms by capitals, $\mathcal{F}[f(y,z)] = F(u,v)$,

$$\mathcal{F}[I(y,z)](u,v) = G_{\text{bg}} + \frac{1}{2}F(u+k_f,v) + \frac{1}{2}F^*(u-k_f,v)\,. \tag{3.9}$$

The Fourier transform of I is shown in figure 3.4(b). The first term in (3.9) comprises a peak at the centre of the image, while copies of the Fourier transform of $f(y,z)$ are translated by $\pm k_f$. Thus, the transformation to Fourier space enables the separation of the phase information from the noisy background by placing these contributions in different regions of the $u-v$ plane. A mask was chosen around $F(u+k_f,v)$, such that everything outside the mask was set to zero and $\mathcal{F}[I_{\text{mask}}] = F(u+k_f,v)/2$. An inverse Fourier transform then retrieves

$$I_{\text{mask}}(y,z) = \frac{g_p}{2}\exp\left(i(k_f z + \Delta\phi)\right), \tag{3.10}$$

which no longer contains the background noise but does contain the effect of the fringes. Performing the same procedure on a reference interferogram with $\Delta\phi = 0$ gives $I^{\text{ref}}_{\text{mask}} = \exp(ik_f z)/2$. Therefore, the phase can be calculated as

$$\Delta\phi(y,z) = \arg\left(\frac{I_{\text{mask}}(y,z)}{I^{\text{ref}}_{\text{mask}}(y,z)}\right). \tag{3.11}$$

The retrieval process is shown in figure 3.4.

The FFT technique for phase retrieval has been reported to allow improved recovery for interferograms with highly curved fringes in short processing times [122].

Hilbert transform phase retrieval

The Hilbert transform is an integral transform typically used in signal processing. It is defined as

$$\mathcal{H}[f(z)] = f(z) * \frac{1}{\pi z}\,. \tag{3.12}$$

The Hilbert transform is easier to understand in the frequency domain:

$$\mathcal{F}[\mathcal{H}[f(z)]] = \sigma(u)\mathcal{F}[f(z)]\,, \tag{3.13}$$

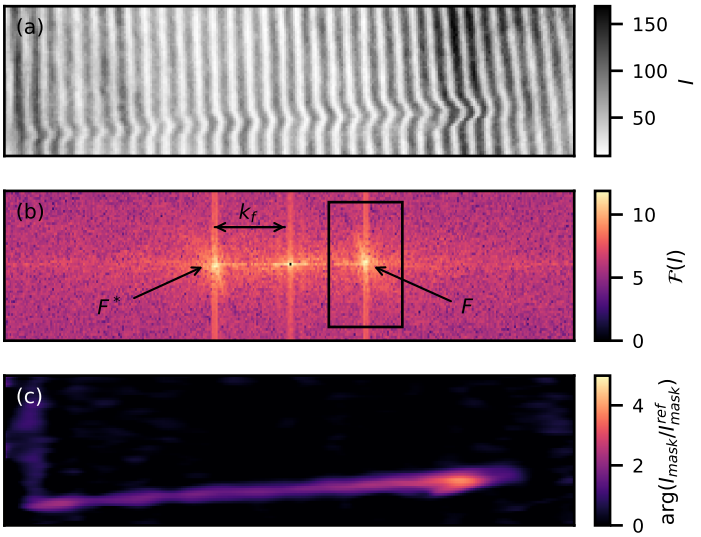

Figure 3.4: Phase retrieval using Fourier transform method. (a) Raw interferogram. (b) 2D FFT of the interferogram; the mask is depicted by the black rectangle. (c) Retrieved phase map after unwrapping.

where

$$\sigma(u) = \begin{cases} i & u < 0\,; \\ -i & u > 0\,. \end{cases} \tag{3.14}$$

Thus, the Hilbert transform shifts positive frequencies by a $-\pi/2$ phase and negative frequencies by a $\pi/2$ phase. This is useful in defining the analytic signal of a function $f(x)$ as

$$f_a(x) = f(x) + i\mathcal{H}[f(x)]\,. \tag{3.15}$$

The analytic signal discards the negative frequency components of a signal by converting it into a complex function. This facilitates many mathematical manipulations and interpretations.

Consider a 1D lineout of the interferogram (3.8):

$$I(z) = g_{\text{bg}}(z) + g_p(z)\cos\big(k_f z - \Delta\phi(z)\big). \tag{3.16}$$

Taking a moving average of the signal and subtracting it from $I(z)$ yields an oscillatory signal centred at zero. Its analytic signal is then

$$\begin{aligned} I_a(z) &= g_p(z)\cos\big(k_f z - \Delta\phi(z)\big) - ig_p(z)\sin\big(k_f z + \Delta\phi(z)\big) \\ &= g_p(z)\exp\big(i(k_f z + \Delta\phi)\big)\,. \end{aligned} \tag{3.17}$$

where $\cos(\theta - \pi/2) = -\sin\theta$ has been used. The equivalent analysis to a lineout of a reference interferogram gives $I_a^{\text{ref}} = \exp(ik_f z)$, such that the phase shift can be obtained through

$$\Delta\phi(z) = \arg\left(\frac{I_a(z)}{I_a^{\text{ref}}(z)}\right), \tag{3.18}$$

as depicted in figure 3.5. The full phase map can be built up by repeating this process line by line [124].

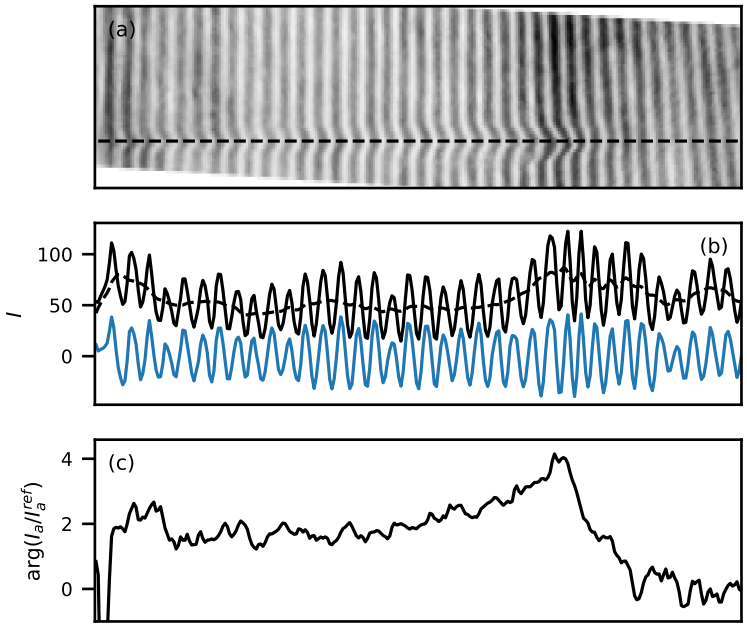

Figure 3.5: Phase retrieval using Hilbert transform method. (a) Raw interferogram. The lineout along the black line is plotted in black in (b), along with its moving average (dashed black) and the centred signal. (c) Retrieved phase profile after unwrapping.

Both of the phase retrieval methods discussed return a wrapped phase, $-\pi < \Delta\phi \leq \pi$. A 2D phase unwrapping [125] was performed using the Scikit-Image package in python.

3.3.2 Density retrieval

The phase shift (3.3) is proportional to the line integrated plasma density, thereby representing a projection of the perturbation in the $(y-z)$ plane. The full structure can be reconstructed from a set projections at different angles via the process of tomographic reconstruction [126, 127].

Abel inversion

In LWFA experiments, the laser produces a plasma channel that can be assumed to be cylindrically symmetric around the laser axis. Structures that exhibit cylindrical symmetry present the advantage that the full three-dimensional map of the plasma can be deduced from a single projection measurement via the Abel inversion. This is a transformation that changes an axial distribution into a radial one.

The Abel transform of a radially symmetric function $f(r)$ represents its projection onto the y-axis and is defined as

$$f_{\mathrm{Abel}}(y) = 2\int_y^R \frac{rf(r)}{\sqrt{r^2-y^2}}\,\mathrm{d}r\,. \tag{3.19}$$

The Abel inversion is then [128]

$$f(r) = \frac{1}{\pi}\int_r^\infty \frac{\mathrm{d}f_{\mathrm{Abel}}(y)}{\mathrm{d}y}\frac{1}{\sqrt{y^2-r^2}}\,\mathrm{d}y\,, \tag{3.20}$$

and, using $\Delta\phi(y,z)$ as the projection of the radially symmetric $\Delta\phi(r,z)$ and (3.3),

$$n(r,z) = \frac{4\pi c^2 m_e \epsilon_0}{\lambda_0 e^2}\Delta\phi(r,z)\,. \tag{3.21}$$

The Abel inversion of the 2D phase map was obtained using the PyAbel package in python. This provides multiple transform methods, but direct integration of (3.20) was employed in this work. This direct method includes a correction to account for the singularity at $r = y$ [129].

3.3.3 Implementation

The interferometry analysis was implemented in python. In practice, the reference was often chosen from the same probe images, cropped to a region with no plasma present. The analysis was then done by averaging multiple references in order to account for the shot-to-shot fluctuations in the probe beam. While this allowed a more accurate measurement of k_f, the use of a different section of the image could cause a non-zero background, due to a systematic translation of the probe and reference fringes. To account for this, a channel mask was defined as the area of the image which contained the plasma channel. A background subtraction was then performed on the phase maps by subtracting the average value outside the channel mask.

The Abel inversion is very sensitive to the choice of symmetry axis of the projection.

Due to fluctuations of laser pointing shot-to-shot, the unwrapped phase maps had to be rotated. The angle of the plasma channel was calculated by identifying the vertical position with the maximum phase shift at every horizontal position. Once the plasma channel was horizontal, the axis of symmetry was found as the centre of a Gaussian fit to the phase map integrated over the horizontal axis.

PyAbel works in quadrants, so performing the Abel inversion outputs a 2D slice of the 3D map that has two distinct halves. The two regions are averaged to find the on-axis density profile, while the difference between the regions provides a measure of the uncertainty in the density. This uncertainty corresponds to the assumption of cylindrical symmetry. An additional source of uncertainty comes from the background noise. This was characterised as the standard deviation of the (Gaussian) distribution of values obtained outside the channel mask.

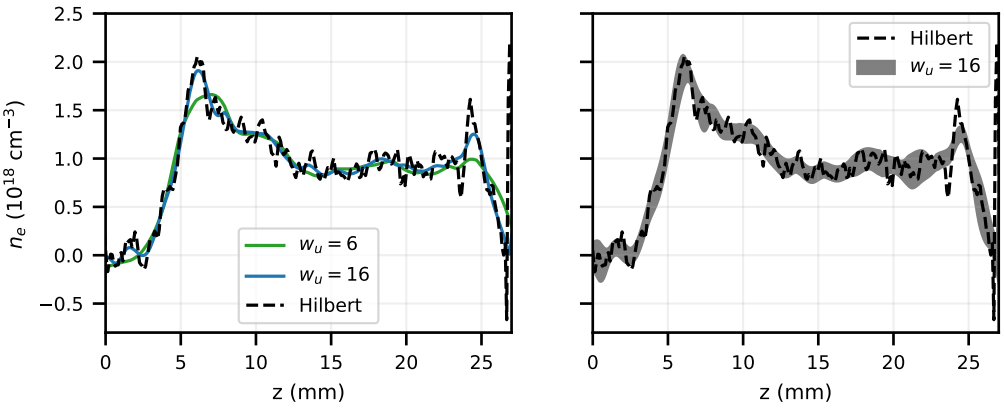

Figure 3.6: Comparison of Fourier and Hilbert phase retrieval methods.

While the Fourier transform methods can reduce the noise, the choice of filtering mask is crucial to avoid over-smoothing the signal. Figure 3.6 compares the density profiles retrieved using the Hilbert transform phase retrieval and the Fourier transform phase retrieval with two different sized filtering masks. The result from the Hilbert method can be considered the most faithful reconstruction of the raw image, but it could not be reproduced by a Fourier technique with a large mask. Instead, a smaller mask whose phase retrieval captured the results from the Hilbert method within the uncertainties (from noise) was employed. For the data in this thesis, the mask was chosen to have a transverse size of $w_u = 16$ pixels.

3.4 Electron spectrometer

The high energy electrons obtained via LWFA are characterised by an electron spectrometer, which comprises a permanent magnet and a scintillating screen. Consider an electron with velocity $\mathbf{v} = v\hat{\mathbf{z}}$ and Lorentz factor γ travelling through a magnet of length L_m with uniform magnetic field $\mathbf{B} = B\hat{\mathbf{x}}$. The electron experiences a Lorentz force

$$\frac{\mathrm{d}\gamma m_e \mathbf{v}}{\mathrm{d}t} = -e(\mathbf{E} + \mathbf{v} \times \mathbf{B}) \,, \tag{3.22}$$

and performs circular orbits at the cyclotron frequency $\omega_C = eB/\gamma m_e$ with radius $R_C = v/\omega_C$. Assuming high electron energies, R_C is sufficiently large that the electron exits the magnet from the opposite side to where it entered, as shown in figure 3.7. Therefore, the electron exits the magnet at an angle $\sin\theta = L_m/R_C$ and a perpendicular distance $\Delta y = R_C(1 - \cos\theta)$. The intersection point to the detector is then

$$l = \Delta y + L_s \tan\theta \,. \tag{3.23}$$

Taking $E = (\gamma - 1)m_e c^2$ and assuming γ is large,

$$\gamma m_e v \approx \frac{E}{c} \,, \tag{3.24}$$

and $\sin\theta \approx L_m eBc/E$. Assuming high energies so $L_m \ll R_C$, $\sin\theta \approx \theta$ as the angle is small and

$$l = \frac{L_m eBc}{E}\left(\frac{R_c}{2} + L_s\right) . \tag{3.25}$$

This means that the dispersion of the spectrometer $\mathrm{d}l/\mathrm{d}E \sim E^{-2}$; the resolution worsens rapidly at increasing energies. Tilting the detector towards the optical axis can improve the resolution as the dispersion stays nearly constant for $E < L_m cBe/\tan\alpha$, where α is the angle between the optical axis and the detector [122]. In practice, achieving a constant dispersion would require an unfeasibly large detector, so that the low resolution at high energy remains.

The detector consists of a scintillating Lanex screen (Gd_2O_2S:Tb) which emits light at 546 nm [130] with a decay lifetime of 600 µs. For electrons with energies $\gtrsim 1\,\mathrm{MeV}$, the energy deposited on the screen per electron is constant, meaning that the emitted light is proportional to the incident electron charge [131].

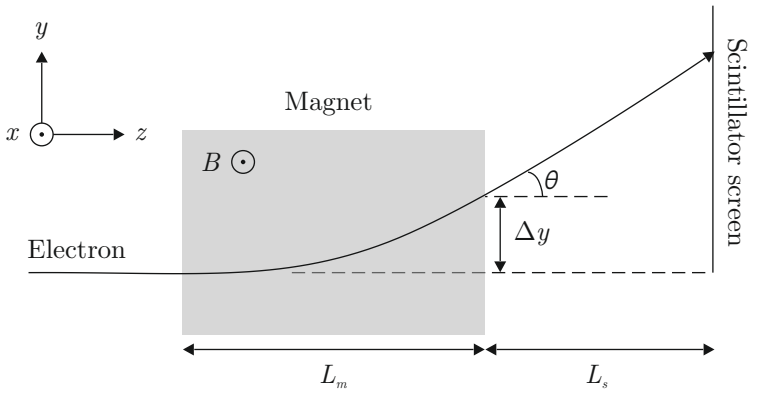

Figure 3.7: Schematic diagram of the electron spectrometer.

3.5 Frequency-resolved optical gating

Frequency-resolved optical gating (FROG) is a diagnostic used to measure the complete temporal information of an ultra-short laser pulse: its intensity $I(t)$ and phase $\phi(t)$ [132]. This enables the characterisation of the pulse length of ultra-short lasers. The principle behind FROG is that the femtosecond pulse is the only available reference with which to measure itself. Using FROG as a diagnostic of the transmitted laser after driving wakefield acceleration can provide insights into the modifications to the laser spectrum and temporal profile that result from the interaction (section 2.5).

FROG relies on non-linear optical processes which modify the polarisation of a material traversed by high intensity waves. In this thesis, second harmonic generation (SHG) is employed, which modifies the laser pulse with electric field $E(t)$ through a term

$$E_{2\omega}(t) \propto E^2(t) \exp\left(2i(\omega t - \mathbf{k}\cdot\mathbf{r})\right). \tag{3.26}$$

The SHG crystal produces light at twice the frequency of the input light. Crossing two pulses, E_1 and E_2, in the SHG medium results in three second harmonic waves: one wave for E_1, one wave for E_2 and the cross-correlation, given by

$$E_{\mathrm{SHG}}(t) \propto E_1(t)E_2(t) \exp\left(i[(\omega_1 - \omega_2)t - (\mathbf{k_1} - \mathbf{k_2})\cdot\mathbf{r}]\right). \tag{3.27}$$

For pulse measurement, the laser pulse is split into two beams and a relative delay τ is introduced between them before spatially overlapping them in the SHG crystal. Therefore, the generated signal field will be of the form

$$E_{\mathrm{sig}}(t,\tau) = E_{\mathrm{SHG}}(t,\tau) \propto E(t)E(t-\tau), \tag{3.28}$$

By varying the delay τ between the two beams, a profile can be generated which is known as the intensity autocorrelation. By mapping the delay onto a transverse position, the autocorrelation can be measured in a single shot. This requires a smooth beam spatial profile. A cylindrical lens is used to overlap the two large beams at a large angle in the non-linear medium, as shown in figure 3.8. An intensity autocorrelator can be used as a diagnostic for the laser pulse duration. However, it is impossible to uniquely determine $I(t)$ from the autocorrelation, so a particular pulse shape must be assumed to get an accurate pulse duration measurement from it.

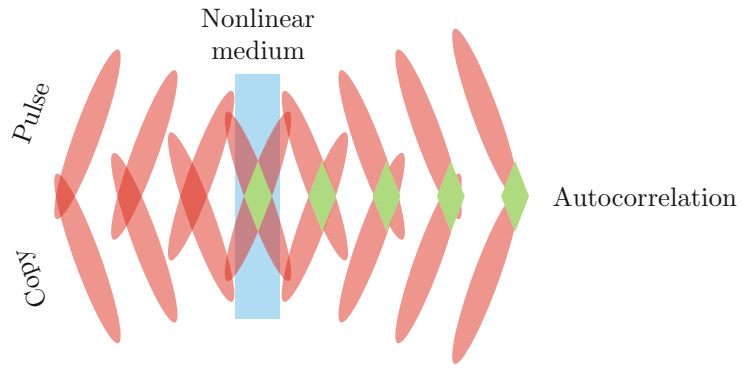

Figure 3.8: Schematic diagram of the experimental setup for a single-shot autocorrelator. On the top, the pulse arrives earlier than the copy, $\tau < 0$, while on the bottom, the copy arrives earlier than the pulse, $\tau > 0$.

FROG goes on to spectrally resolve the autocorrelation signal, producing a SHG FROG trace given by

$$I_{\mathrm{FROG}}(\omega, \tau) = \left| \int_{-\infty}^{\infty} E(t)E(t-\tau)e^{-i\omega t}\,\mathrm{d}t \right|^2 . \tag{3.29}$$

The resulting image has delay and frequency as the axes. Note that $E(t)$ and $E(-t)$ produce the same FROG measurement. As opposed to FROG schemes using third-order optical non-linearities, which directly produce a spectrogram of the pulse, SHG FROG produces an unintuitive trace that is symmetrical with respect to delay. Thus, it has an ambiguity in the time direction. This means that even-order phase distortions (odd-order frequency distortions) such as linear chirp appear as a widening of the trace in frequency, as shown in figure 3.9, rather than as the acquisition of a slope in other types of FROG [133]. While less intuitive to interpret without analysis, SHG FROG is preferred due to its increased sensitivity and dynamic range. Moreover, the time ambiguity can be removed with additional information about the chirp of the pulse [134].

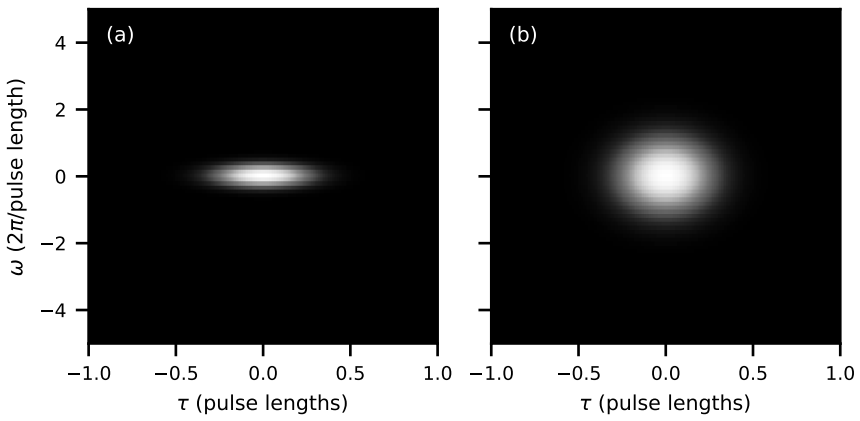

Figure 3.9: Synthetic SHG FROG measurements for (a) a transform limited pulse and (b) a pulse with linear chirp.

3.5.1 Marginals

The delay marginal is the integral of the FROG trace with respect to frequency, which for SHG FROG gives the intensity autocorrelation [133],

$$M_\tau(\tau) = \int_{-\infty}^{\infty} I(t)I(t-\tau)\,\mathrm{d}\tau\,. \tag{3.30}$$

The frequency marginal is the integral of the FROG trace with respect to delay, which is given by [133]

$$M_\omega(\omega) = 2I(\omega) * I(\omega) \tag{3.31}$$

for SHG FROG.

3.5.2 Retrieval algorithm

There is no function that enables $E(t)$ to be calculated from the FROG trace (3.29). Instead, an iterative retrieval algorithm is employed [135], in which the FROG trace produced by a given $E^{(k)}(t)$ is compared to the measured image and iteratively improved until a good fit is found. The difference between the measured and calculated FROG traces is quantified by the FROG error,

$$G^{(k)} = \sqrt{\frac{1}{N^2}\sum_{i,j}^{N}\left|I_{\mathrm{FROG}}(\omega_i,\tau_j) - I^{(k)}_{\mathrm{FROG}}(\omega_i,\tau_j)\right|^2}\,, \tag{3.32}$$

where I_{FROG} is the measurement, $I^{(k)}_{\mathrm{FROG}}$ is the FROG trace calculated from the k$^{\mathrm{th}}$ iteration of the electric field and N is the number of pixels in each image.

2D Phase Retrieval Problem

Starting from the definition of the FROG trace,

$$\begin{aligned} I_{\mathrm{FROG}} &= \left| \int_{-\infty}^{\infty} E_{\mathrm{SHG}}(t,\tau) e^{-i\omega t}\, \mathrm{d}t \right|^2 \\ &= \left| \int_{-\infty}^{\infty}\int_{\infty}^{\infty} E_{\mathrm{sig}}(t,\Omega) e^{-i\omega t - i\Omega t}\, \mathrm{d}\Omega \mathrm{d}t \right|^2, \end{aligned} \tag{3.33}$$

where τ and Ω are conjugate pairs. Therefore, the FROG trace constitutes a two-dimensional phase retrieval problem. As opposed to a one-dimensional phase retrieval problem, such as the autocorrelation, the FROG trace can uniquely determine the intensity and phase of a short pulse. FROG retrieval methods are based on iterative Fourier transform algorithms used in phase retrieval.

Mathematical and Data Constraints

Inverting a FROG trace requires the use of constraints for convergence. The known mathematical form of the signal electric field yields the mathematical constraint [135]:

$$\begin{aligned} \int_{-\infty}^{\infty} E_{\mathrm{sig}}(t,\tau)\, \mathrm{d}\tau &\propto \int_{-\infty}^{\infty} E(t) E(t-\tau)\, \mathrm{d}\tau \\ \Rightarrow E(t) &\propto \int_{-\infty}^{\infty} E_{\mathrm{sig}}(t,\tau)\ \mathrm{d}\tau\,, \end{aligned} \tag{3.34}$$

where the constant of proportionality is given by the reciprocal of $\int_{-\infty}^{\infty} E(t-\tau)\,\mathrm{d}\tau = \int_{-\infty}^{\infty} E(\tau')\,\mathrm{d}\tau'$, which is independent of t. The constant of proportionality is disregarded, so $=$ is used instead of $\propto$ in the following. This constraint is applied in the time domain.

Using the mathematical constraint, the $(k+1)$th iteration for $E(t)$ is obtained from the kth iteration $E^{(k)}_{\mathrm{sig}}$:

$$E^{(k+1)}(t) = \int_{-\infty}^{\infty} E^{(k)}_{\mathrm{sig}}(t,\tau)\, \mathrm{d}\tau\,. \tag{3.35}$$

Then, this can be used in the definition of $E_{\mathrm{sig}}(t,\tau)$ to find the $E^{(k+1)}_{\mathrm{sig}}$.

In addition to the mathematical constraint, it follows from the definition of the FROG trace (3.29) that the FROG trace is equal to the magnitude squared of the

Fourier transform of $E_{\text{sig}}(t,\tau)$. This yields the data constraint,

$$\tilde{E}_{\text{sig}}(\omega,\tau) = \sqrt{I_{\text{FROG}}}\,, \tag{3.36}$$

which is applied in the frequency domain and where $\tilde{E}$ is the Fourier transform of E with respect to t. Using the data constraint on the $(k+1)$th iteration means replacing its magnitude with the measurement

$$\tilde{E}_{\text{sig}}^{(k+1)}(\omega,\tau) = \frac{\tilde{E}_{\text{sig}}^{(k)}(\omega,\tau)}{|\tilde{E}_{\text{sig}}^{(k)}(\omega,\tau)|}\sqrt{I_{\text{FROG}}}\,. \tag{3.37}$$

An inverse Fourier transform retrieves $E_{\text{sig}}^{(k+1)}$, and the process is repeated for the next iteration. The process is summarised in figure 3.10.

Principal Components Generalised Projections

The application of the mathematical and data constraints can be improved through the use of generalised projections (GP). This means that the next iteration $E^{(k+1)}$ is found as that which is closest to the previous guess.

The principal components generalised projections (PCGP) [136] constructs the FROG trace from the outer product of two vectors: the pulse $E^{(k)}(t)$ and the gate $G^{(k)}(t)$ (= $E^{(k)}(t)$ for SHG FROG) with t and τ discretised. By rotating and rearranging the elements of $O^{(k)} = E^{(k)} \otimes G^{(k)}$, the signal field $E^{(k)}(t)G^{(k)}(t-\tau)$ can be retrieved; this comprises a reversible transformation. A 1D Fourier transform then produces $\tilde{E}_{\text{sig}}^{(k)}(\omega,\tau)$. The process is shown in figure 3.11.

In the PCGP algorithm, the data constraint is applied as in (3.37), and an inverse Fourier transform retrieves $E_{\text{sig}}^{(k+1)}(t,\tau)$. Next, the rearranging and row rotation are reversed to form a matrix that should be of outer product form. Consider the singular value decomposition (SVD) of O into three matrices:

$$O = E \times W \times G^T\,, \tag{3.38}$$

where E and G^T are orthogonal square matrices and W is a square diagonal matrix. The columns of E, $\{E_1, ...E_N\}$ and the rows of G^T, $\{G_1, ...G_N\}$ are the left and right eigenvectors of O, while the diagonal values of W, $\lambda_i = W_{ii}$, are the eigenvalues, whose values determine the contribution of each outer product to O. Therefore, O can be

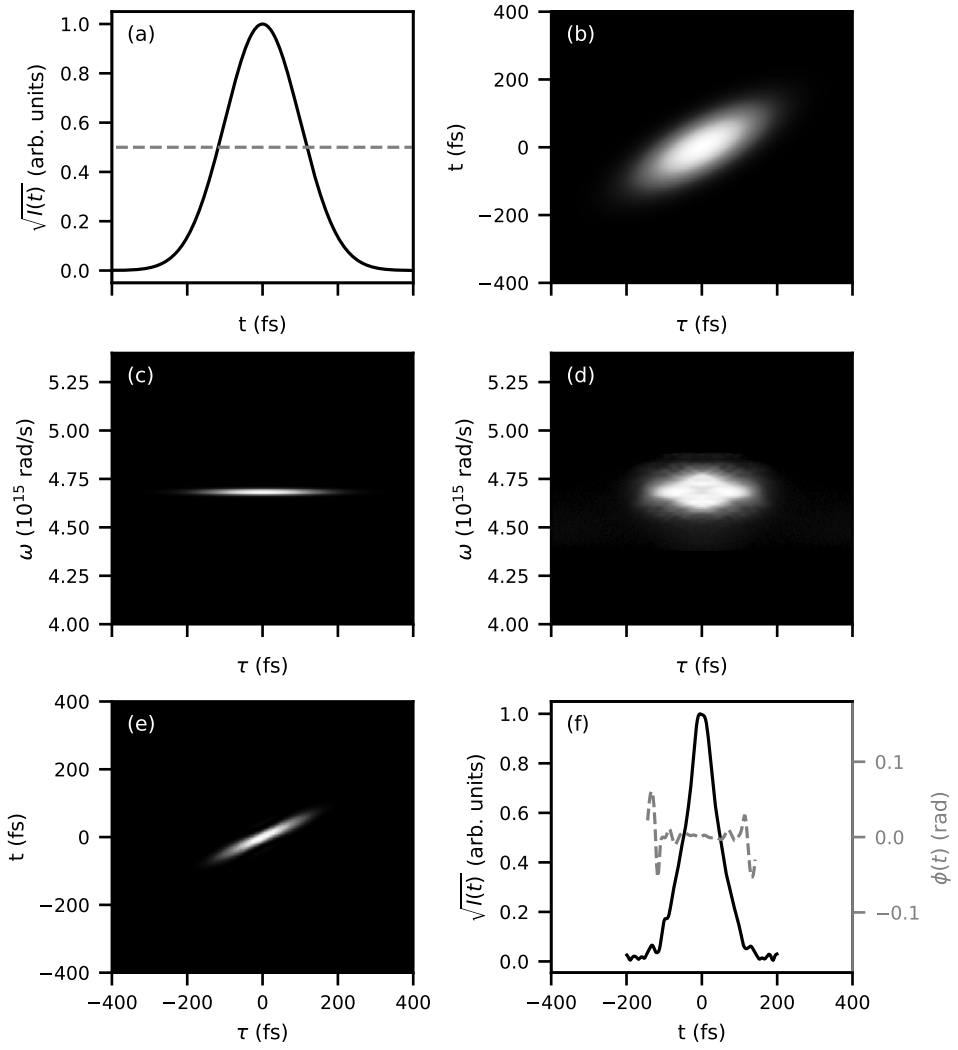

Figure 3.10: Basic FROG retrieval algorithm using the data and mathematical constraints. (a) Initial guess. (b) SHG signal field. (c) FFT of the signal field with respect to t. (d) Application of the data constraint. (e) Inverse FFT with respect to ω. (f) Next iteration.

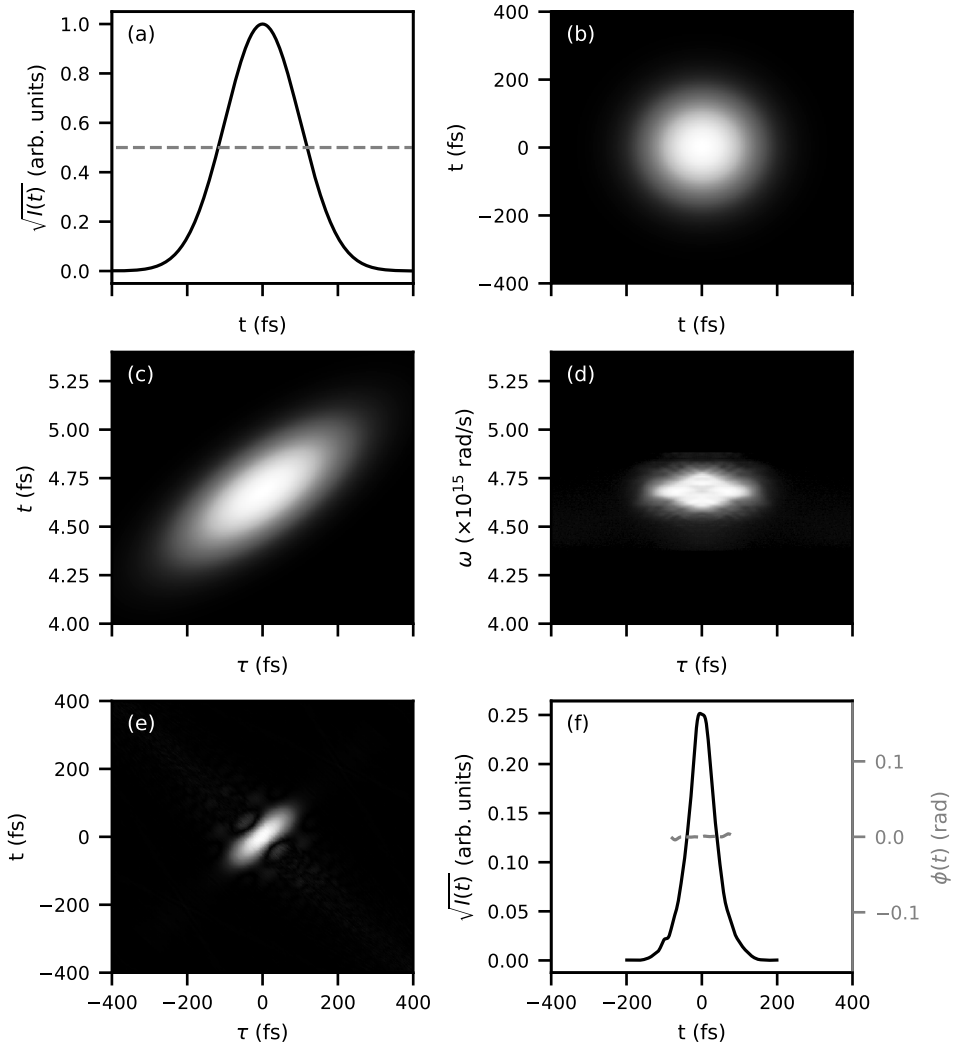

Figure 3.11: PCGP retrieval algorithm. (a) Initial guess. (b) Outer product form. (c) Signal field obtained via row rotation and shifting. (d) Application of the data constraint in the frequency domain. (e) Inverse FFT with respect to ω followed by reverse transformation to outer product form. (f) Principal component.

constructed as

$$O = \sum_{i}^{r} \sqrt{\lambda_i} E_i G_i^T \,, \tag{3.39}$$

where $r \leq N$ is the rank of O.

A matrix of outer product form $E \otimes G$ has one nonzero eigenvalue, with one right eigenvector and one left eigenvector describing the pulse and gate, respectively [137]. However, $O^{(k+1)}$ is unlikely to be of outer product form before convergence, meaning that it will have $r > 1$. The pulse $E^{(k+1)}$ and gate $G^{(k+1)}$ for the next iteration are taken to be the principal components of O; i.e. the outer product pair with the largest contribution to O (largest λ_i). This is equivalent to minimisation of the function

$$\epsilon = \sum_{i,j=1}^{N} |O_{i,j} - E_i G_j|^2 \,, \tag{3.40}$$

which comprises a generalised projection.

Singular value decomposition (SVD) is implemented in python to directly decompose O into r eigenvalues and eigenvectors and find the principal components. Alternatively, the power method [136] can be employed to save computational time and resources. E_i and G_i satisfy

$$\begin{aligned} OO^T E_i &= \lambda_i E_i \\ O^T O G_i &= \lambda_i G_i \,. \end{aligned} \tag{3.41}$$

Consider

$$OO^T x_0 = \sum_{i=1}^{r} k_i \lambda_i E_i \,, \tag{3.42}$$

where E_i are the eigenvectors of OO^T, x_0 is an arbitrary nonzero vector and k_i are a set of constants. Then, multiplying (3.42) by $(OO^T)^{p-1}$ gives

$$(OO^T)^p x_0 = \sum_{i=1}^{r} k_i \lambda_i^p E_i \,. \tag{3.43}$$

As p increases, the largest eigenvalue λ_l dominates the sum, so that

$$(OO^T)^p x_0 \approx k_l \lambda_l^p E_l \,, \tag{3.44}$$

meaning that the next iteration for the pulse $E^{(k+1)}$ is found by multiplying the previous guess by OO^T (one iteration has been found to be adequate in practice [136]).

3.5.3 Implementation

The FROG retrieval and analysis was performed in python. Implementation of the iterative Fourier transform algorithm requires that the delay increment and frequency spacing of points are related by

$$\delta\omega = \frac{2\pi}{N\delta t}\,, \tag{3.45}$$

where the FROG trace is in an $N \times N$ grid. In practice, the FROG trace was measured as a function of wavelength and delay. Therefore, satisfying this relation required remapping the FROG trace into a linear frequency axis, via a 2D interpolation. Complex pulses require large N. For the data in this thesis, $N = 2048$ was chosen with $\delta t = 1\,\text{fs}$. The $\tau = 0$ axis was identified as the axis of symmetry of the image, because systematic intensity asymmetries skewed the image's centre of mass.

The performance of the basic and PCGP algorithms are compared in figure 3.12 for test data provided by Lund Laser Centre. The basic algorithm saturates quickly at a trace with moderate error that is visually very different to the measurement; this algorithm was originally proposed for polarisation-gate FROG and found to be less effective when applied to SHG [133]. In contrast, both PCGP algorithms result in faithful reconstructions in $\lesssim 100$ iterations. The marginals of the FROG measurement were compared to those calculated from the retrieved pulse using (3.30) and (3.31) to check for systematic errors in the FROG processing and retrieval.

Retrieved pulse analysis

The FROG retrieval algorithm yields the complex $E(t)$ that most accurately describes the measured laser pulse. A polynomial fit to the phase (temporal or spectral) enabled the dominant terms to be identified (see section 2.2.1). The instantaneous frequency (2.29) was also calculated. Since the pulse develops a negative chirp while driving wakefield acceleration (section 2.5.1), the solution with a positive chirp can be discarded. This removes the time ambiguity of the measurement. However, transmission through dielectric materials can alter the measurement due to group velocity dispersion.

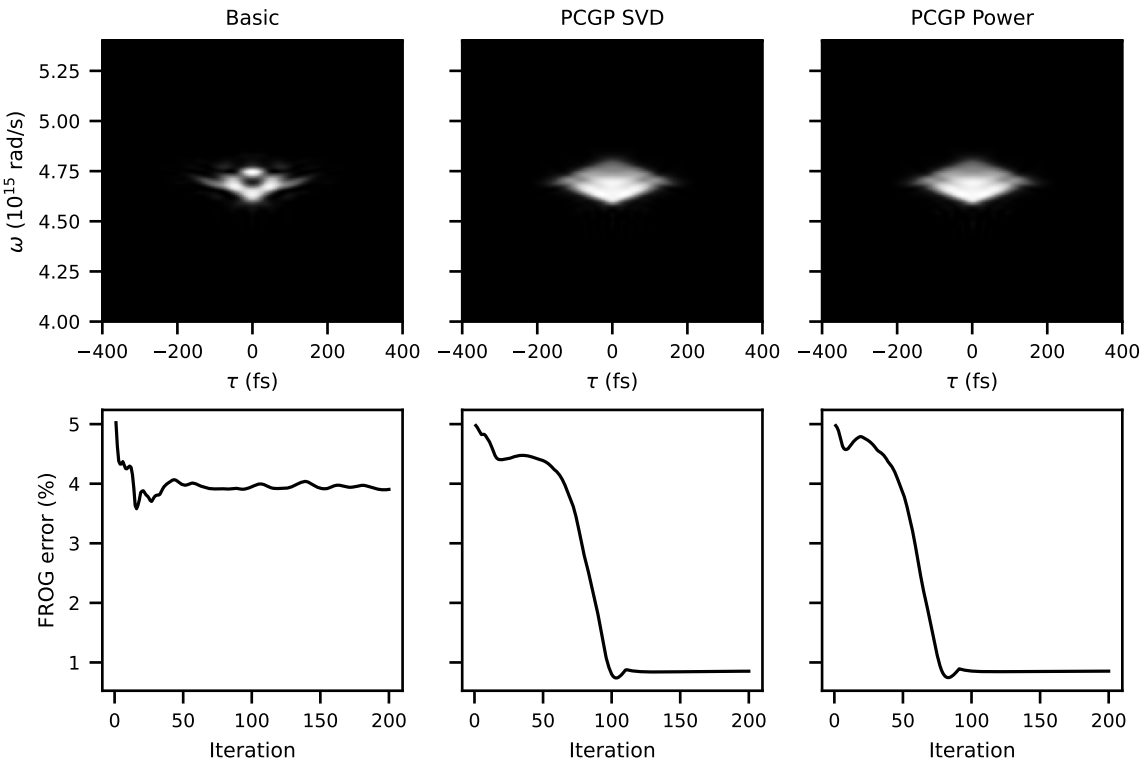

Figure 3.12: The top row shows the FROG reconstruction after 200 iterations of the basic (left), PCGP with SVD (middle) and PCGP with power method (right) retrieval algorithms. The bottom row shows the FROG error of the retrieval through the iterations.

3.6 Particle-in-cell simulations

Numerical simulations have been a vital part of LWFA research since its onset [1]. Accurate representation of the laser evolution and electron injection and acceleration dynamics requires evolving the electromagnetic fields according to Maxwell's equations and tracking the trajectories of all particles in these fields. Particle-in-cell (PIC) codes are used to simplify these simulations and make them computationally feasible. The simulations presented in this thesis used EPOCH [138], which is an MPI-parallelised relativistic PIC code. The simulations were performed on the Viking cluster, which is a high performance computing facility provided by the University of York.

PIC codes use a small number of macroparticles to represent groups of physical particles. The electromagnetic fields generated by the motion of these macroparticles are calculated using Maxwell's equations on a discrete grid using a finite difference time domain method. The fields are then interpolated to the position of the macroparticles and the Lorentz force is used to push them to their new positions. Such an algorithm

is capable of reproducing all the classical dynamics of a collection of charged particles.

Simulating LWFA is a complicated process due to the range of scales involved; it is necessary to simultaneously resolve both the short laser wavelength and the long propagation lengths. A moving window is employed, which travels along with the laser at the laser group velocity. This allows the important dynamics, which take place immediately behind the laser pulse, to be simulated efficiently while discarding the unimportant information in front of the laser and farther behind.

3.6.1 Resolution constraints

The simulation is constrained by the Courant-Friedrichs-Lewy (CFL) condition on the simulation timestep Δt:

$$c\Delta t < \frac{1}{\sqrt{\frac{1}{\Delta x^2} + \frac{1}{\Delta y^2}}}\,, \tag{3.46}$$

where Δx and Δy are the longitudinal and transverse grid sizes, respectively. This condition represents the requirement that information cannot travel to an adjacent grid point in under Δt.

The discretisation of space and time in PIC codes causes issues with Maxwell's equations, as it is found that the speed of light $< c$. The numerical dispersion relation for a plane wave is [139]

$$\frac{1}{c^2\Delta t^2}\sin\left(\frac{\omega\Delta t}{2}\right)^2 = \frac{1}{\Delta x^2}\sin\left(\frac{k_x\Delta x}{2}\right)^2 + \frac{1}{\Delta y^2}\sin\left(\frac{k_y\Delta y}{2}\right)^2, \tag{3.47}$$

giving the numerical group velocity in the x-direction

$$\frac{\partial\omega}{\partial k_x} = v_g = c\frac{\cos\left(k_x\Delta x/2\right)}{\sqrt{1-\frac{c^2\Delta t^2}{\Delta x^2}\sin^2\left(k_x\Delta x/2\right)}}\,. \tag{3.48}$$

Numerical dispersion is minimised when $\Delta x \ll \lambda_x$, where $v_g \to c$. The effect of the transverse resolution Δy was studied by running simulations of vacuum laser propagation with different Δx and Δy. The numerical dispersion is depicted in figure 3.13. A simultaneous decrease of Δx and increase of Δy is required in order to resolve light propagation as accurately as possible. However, arbitrarily reducing the transverse resolution may worsen the accuracy of 2D effects such as self-focusing and transverse wavebreaking. The simulations in this thesis used $\Delta x = \lambda_0/60$. Thus, the ratio $\Delta x/\Delta y = 1/3$ was chosen, as it is found to resolve the speed of light to better than 0.1 %.

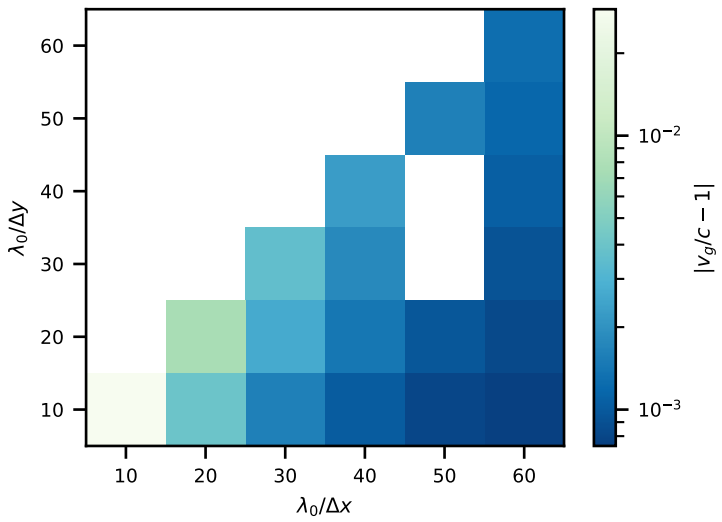

Figure 3.13: Simulation results of the propagation of a laser in vacuum for different grid sizes. Numerical dispersion effects are shown as the deviation of the simulated speed of light from c.

3.6.2 Laser analysis

A laser in EPOCH is driven using $\sin(\omega t + \phi)$ where ϕ is the phase parameter. Phase may be a function of both space and time. Spatial phases are used to define a focusing laser pulse, while temporal phases shape the time intensity and spectrum of the pulse.

EPOCH defines the laser with respect to the electric field. A Gaussian shape is assumed for the transverse and temporal profiles as

$$E = E_0 \exp\left(-\frac{x^2}{w_E^2}\right) \tag{3.49}$$

where w_E is the $1/e$ width relative to the electric field. As experimental measurements of the laser are typically done with respect to the intensity profile

$$I = I_0 \exp\left(-\frac{x^2}{w_I^2}\right) \propto \exp\left(-\frac{2x^2}{w_E^2}\right) \tag{3.50}$$

the widths are related by $w_E = \sqrt{2} w_I$. As $\mathrm{FWHM_I} = 2\sqrt{\ln 2}\mathrm{w_I}$,

$$w_E = \frac{\mathrm{FWHM_I}}{\sqrt{2\ln 2}} \tag{3.51}$$

Chapter 4

Stability of density transition injected electron beams

In laser wakefield accelerators, small fluctuations in the experimental conditions can cause significant shot-to-shot variations of the electron beam parameters. This is because the electron injection and acceleration dynamics are determined by the non-linear evolution of the laser driver as it traverses the plasma. The need to maintain good density stability to minimise shot-to-shot fluctuations of electron beam energy and charge has been demonstrated for self-injection in a steady-state gas cell [140]. Similarly, non-uniformities in the density profile have been shown to cause variations in electron energy gain [141]. Controlled mechanisms of injection have demonstrated improved short-term stability compared to self-injection through the use of colliding laser pulses [142] or plasma density tailoring [105]. Recently, long term stability over $\sim 100,000$ shots at high repetition rate has been investigated through high statistics experimental approaches, using ionisation injection. These have shown strong correlations of electron beam parameters with fluctuations of laser energy [30] and plasma density [143], and conclude that stable ionisation injection requires tight constraints on the reproducibility of the interaction. The shot-to-shot fluctuations in the electron bunches accelerated via laser wakefield accelerators thus constitute a main limitation preventing their successful use in applications. Improvements in the stability, reliability and robustness of electron beam parameters are still required to expand the applications beyond proof of principle [4, 49].

Density transition injection (section 2.6.2) is a mechanism of controlled injection aiming to improve electron beam stability, which uses a tailored target with a decreasing density ramp. Along with ionisation injection, it is one of the controlled mechanisms considered for EuPRAXIA. By avoiding very high laser intensities and target densities

to limit self-injection, the dependence of the electron trapping process on the laser-plasma coupling should weaken. Density transition injection in the long-scale ramp regime has been realised experimentally by using the falling edge of a gas jet as a ramp, achieving low electron beam energy spread [144] in line with numerical studies [102,145]. These beams were later demonstrated to have energy tunability by incorporating an additional acceleration region after injection at the edge of the gas jet with a capillary discharge [146] or additional gas jet [147]. More recent experimental realisations have utilised a razor blade [101] or wire [148] inserted in a supersonic gas jet target, producing tunable low energy spread electron beams [149, 150]. The densities at either side of the shock produced by this setup have been shown to depend on height of the interaction above the blade [151, 152], while the peak density and length scale of the shock have further been shown to vary with gas pressure and blade coverage [153].

Due to the range of density profiles available with a blade in a gas jet setup, extensive simulation work has examined the dependence of electron beam parameters on the down-ramp profile. The effect of the transition length, ranging from the sharp to the gentle regime has been studied [154]. The effect of both transition length and height for sharp transitions has also been investigated [155] and later extended to include laser energy effects [156]. The influence of ramp steepness on electron beam quality has also been examined [157]. However, the density profile in experiments fluctuates over time and between shots, thereby reducing the stability of the electron beam charge and energy. No dedicated investigations have looked at these fluctuations, which include coupled variations of the peak and plateau densities, as well as variations of the down-ramp position relative to the laser focus. Studies of the source of these fluctuations, which indicate the robustness of the density-tailoring technique, are similarly lacking.

This chapter presents experimental results of parameter scans used to tailor the target density profile in a laser wakefield accelerator and optimise density transition-injected electron beams for radiation reaction applications [2]. The shot-to-shot fluctuations of the target density profile and the electron energy spectrum are characterised for self-injection and density down-ramp injection. The sensitivity of the accelerated electrons to the experimentally-measured density fluctuations are studied through particle-in-cell simulations. These investigations reveal the relative importance of different aspects of the density profile and the limitations to the density tailoring setup.

4.1 Experimental setup

An experiment was conducted at the Central Laser Facility of the Rutherford Appleton Laboratory. The experimental setup is shown in figure 4.1. An $f/40$ off-axis parabolic mirror focused the beam to a $(50 \pm 2) \times (45 \pm 2)$ µm spot into a supersonic gas jet target to produce a plasma wakefield. The Gemini laser pulse delivered (6.6 ± 0.5) J to the target in a duration of ≈ 50 fs with a central wavelength of 800 nm. The setup drives a laser with a Rayleigh range > 4.44 mm .

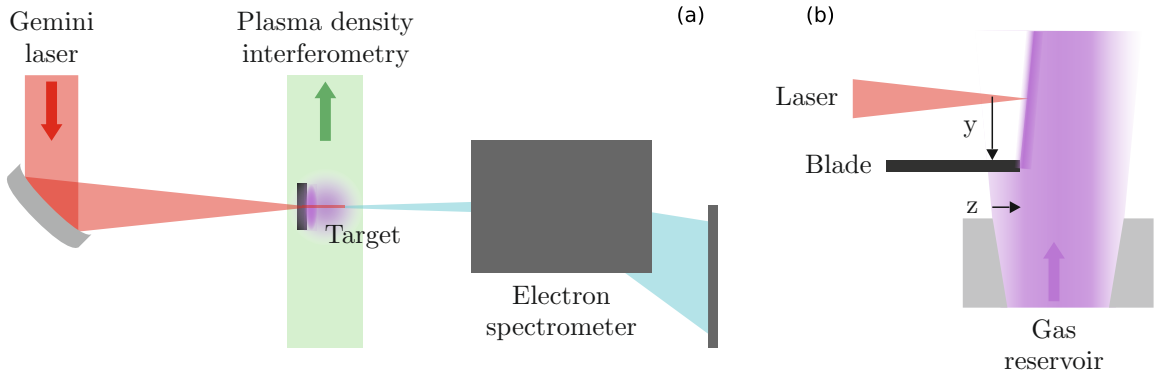

Figure 4.1: Schematic diagram of the (a) experimental setup and (b) target for density transition injection.

A 15 mm diameter conical nozzle of the type in ref. [158] was used to generate a supersonic helium gas jet target, which produced plasma electron densities of order $10^{18}\,\mathrm{cm}^{-3}$ when fully ionised. The setup provided a density plateau region between approximately linear density ramps to vacuum. A razor blade inserted into the flow was used to tailor the longitudinal density profile of the target [101] so as to have a decreasing density gradient for density transition injection. The blade constitutes an obstruction to the supersonic flow, thereby producing a hydrodynamic shock which comprises a density build-up followed by a lower density plateau region. The complex hydrodynamics of the target means that the density profile of the interaction region is dependent on the position of the blade relative to the nozzle and the height of the laser relative to the blade [153]. The density transition width can range from sub-ten micrometres (sharp regime) [101] to hundreds of micrometres (gentle regime) [149, 150] with this setup.

The steel single edge razor blade had dimensions 40 mm × 10 mm × 230 µm and was mounted in the chamber independently of the nozzle as shown in figure 4.2. This allowed the blade to be moved in y, z and angle θ to the $x - z$ plane. The blade was held on the custom mount with two bolts on either end and positioned transversely over the

gas jet. This was expected to reduce any blade motion or damage induced by the high pressure gas jets and improve the robustness of the setup.

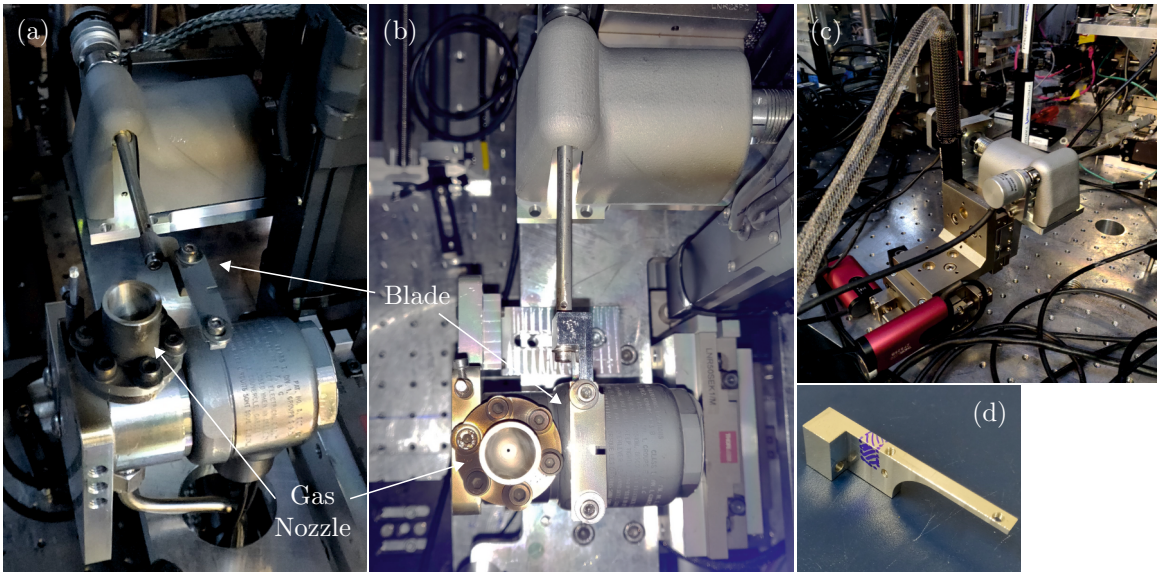

Figure 4.2: Photographs of the target setup with the razor blade: (a) oblique view, (b) top view, (c) blade mount on translation stages, (d) blade mount.

A millijoule energy probe beam with $\sim 90\,\mathrm{fs}$ pulse duration was directed transversely to the main beam to diagnose the plasma density profile via interferometry. A shadowgraphy diagnostic using the same probe also allowed the nozzle and blade position to be identified. The electron energy spectra were measured using an electron spectrometer. Electrons were dispersed by a magnetic dipole ($\int B\,\mathrm{d}z = 0.35\,\mathrm{T\,m}$) onto two scintillating Lanex screens. The scintillation was measured by a 16 bit camera, filtered to eliminate laser and ambient light. The images on the screens were energy-calibrated by numerical tracking of electron trajectories in the magnetic field, and measured electrons with energies between $0.3\,\mathrm{GeV}$ and $2.5\,\mathrm{GeV}$. The typical peak electron beam energies reached $\sim 1\,\mathrm{GeV}$. Calibration and processing of the raw data from the spectrometer was performed using analysis scripts by M. Streeter and C. Colgan, as detailed in ref. [159].

4.2 Transverse interferometry

An example interferogram is displayed in figure 4.3 along with the retrieved phase shift and axial density profile. The electron plasma density was measured using a folded Mach-Zehnder interferometry setup, such that a single probe beam passed through the target and was split into the measurement and reference beams outside the target chamber. This is possible because the change in refractive index of the plasma channel

comprising the interaction region dominates over the change in refractive index of the neutral gas target. Thus, only the small region of the target that is ionised by the laser is probed, and the region comprising the neutral gas can be used as reference. This results in the interferogram having two copies of the measurement, with opposite phases. Only the top measurement is considered and analysed, because of inconsistencies in the reconstruction of the bottom measurement for many shots. In contrast to a Normaski interferometer, the folded Mach-Zehnder setup allows the interference fringes to be parallel to the angle of the beam split, which is necessary for measurement of the plasma.

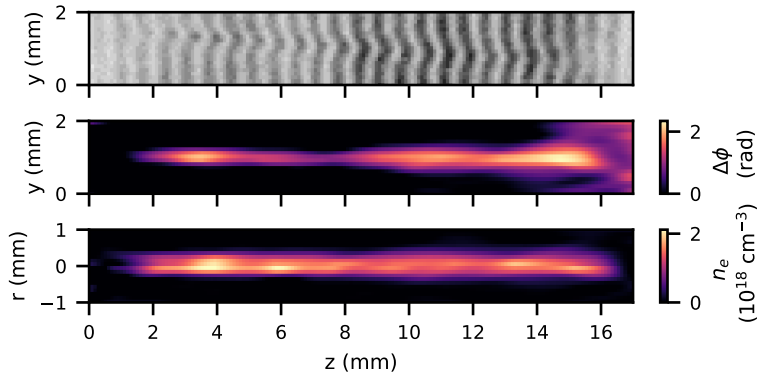

Figure 4.3: An interferometry image of a low density plasma channel on the top, with its phase retrieval in the middle and density retrieval from Abel inversion on the bottom. The drive pulse is propagating from left to right.

The imaging system had a field of view of 23 mm × 23 mm and a resolution of 100.1 µm limited by the pixel size. This allowed the entire length of the plasma channel to be probed, at the expense of spatial resolution. The transverse profile of the plasma channel can be approximated by a Gaussian with $1/e$ width $2w = (610 \pm 20)$ µm which is significantly larger than the laser focal spot. This means the laser is sufficiently intense to ionise helium away from focus.

The density was retrieved via Abel inversion, under the assumption that the shock produced by the blade is cylindrically symmetric within the plasma channel. This assumption is valid where the shock is perpendicular to the probe beam. However, Abel inversion is still used when the shocks are oblique (see section 4.2.2). In these cases, it can still provide accurate measurements of the region away from the shock. In order to measure the on-axis density profile, the average of the two central pixels of the image is taken, as this is the region of the intense laser-plasma interaction. The uncertainty on the density profile is taken from the noise in the density map and the error on the Abel inversion, calculated from the range of values in the pixels considered in the average.

4.2.1 Plateau density profile for self-injection

The gas jet was employed without the blade to produce a plateau density profile capable of generating GeV electrons via self-injection. An example of the plasma density profile retrieved from the interferometry data is shown in figure 4.4(a). The plateau density profile was characterised with a fit

$$n_e(z) = \frac{n}{2}\left[\tanh\left(\frac{z - z_u}{w_u}\right) - \tanh\left(\frac{z - z_d}{w_d}\right)\right], \tag{4.1}$$

where the meaning of the parameters is shown in figure 4.4(a). This kind of density profile is characterised by two parameters of interest: the plateau density n_0 and the acceleration length $L = z_d - z_u$. The length scales of the rising and falling edges of the target, w_u and w_d, can also be characterised but their effect will not be discussed. While they varied with distance from the nozzle, this was of secondary importance compared to variations of n and L which also took place in these scans.

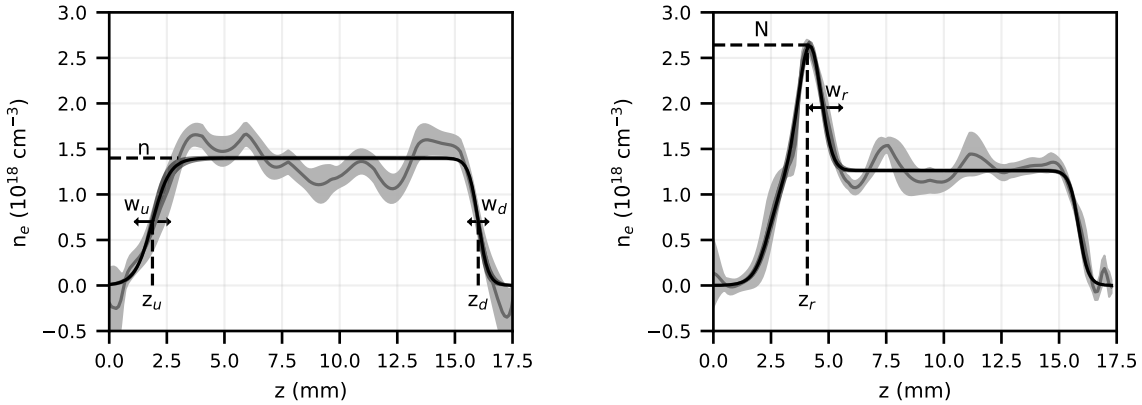

(a) Target with the blade out for a shot with a backing pressure of 100 bar.

(b) Target with the blade in for a shot with 90 bar backing pressure and blade 9 mm below the laser axis and 3.2 mm into the gas jet.

Figure 4.4: Representative density profile along the laser axis of the targets used in the experiment. The grey line shows the retrieved density profile for a single measurement; the shaded region represents the uncertainty in the measurement (1σ), which takes into account the noise in each density map and the error on the Abel inversion. The black solid line depicts the fit applied to characterise the density parameters.

Figure 4.4(a) shows the presence of non-uniformities in the plateau region of the density profile. These are likely caused by internal shocks produced within the conical nozzle employed in the experiment. The discontinuity at the throat of these kinds of nozzles produces shocks in the flow, which reflect at the nozzle walls and produce

the density fluctuations [160, 161]. Note that the resolved length scales of the non-uniformities are affected by the filtering mask used in the interferometry analysis, as discussed in section 3.3.3.

Figure 4.5(a) shows a 2D density map of the gas jet produced at 100 bar backing pressure. The laser propagates from left to right. The measured gas jet appears asymmetric as the falling edge of the density profile lies at a constant (within 0.15 mm) horizontal position for all heights above the nozzle. This is unphysical for a supersonic jet flowing into vacuum, which comprises an under-expanded flow that expands radially to the lower ambient pressure. Such an expansion causes a smoothing of the density profile farther from the nozzle [158, 162, 163]. This observation suggests that the timing of the probe beam did not allow for measurement of the full plasma channel; the falling edge in density corresponds to the distance reached by the laser at the time of probing and not to the falling edge of the target. Therefore, the acceleration length is not discussed further. Online analysis of a target height scan during the experiment would prevent these issues in the future.

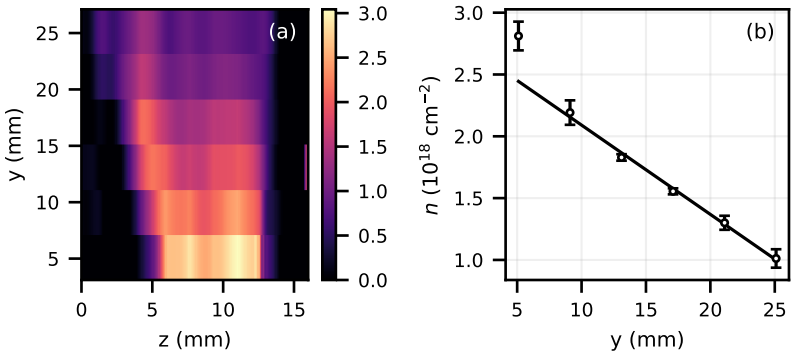

Figure 4.5: (a) 2D density map of the target produced by a supersonic gas flow at 100 bar backing pressure. Each horizontal lineout corresponds to the average of the density profile retrieved from interferometry of three to five shots at the same height. (b) Average plateau density as a function of height.

The average density as a function of distance from the nozzle is plotted in figure 4.5(b). The results from ≥ 9 mm away show that the density decreases farther from the nozzle approximately linearly at a rate of $(-0.072 \pm 0.003) \times 10^{18}\,\mathrm{cm}^{-3}\,\mathrm{mm}^{-1}$. Configurations with interaction regions far from the nozzle were preferred in the experiment in order to suppress self-injection while maintaining a long channel length. These were expected to produce high energy, low energy spread electron bunches upon density tailoring with the blade.

4.2.2 Tailored density profile for density transition injection

Inserting a blade into the supersonic gas jet target tailors the density profile by producing a peaked region prior to the density plateau. An example of such a tailored density profile retrieved from the interferometry data is shown in figure 4.4(b). This density profile was characterised with a fit

$$n_e(z) = \frac{n}{2}\left[\tanh\left(\frac{z-z_u}{w_u}\right) - \tanh\left(\frac{z-z_d}{w_d}\right)\right] + (N-n)\exp\left[-\left(\frac{z-z_r}{w_r}\right)^2\right], \quad (4.2)$$

where the first term is identical to the plateau density profile fit, the second term is a peak corresponding to the high density region and the meaning of the parameters is shown in figure 4.4(b). This kind of density profile is characterised by five parameters of interest: the plateau density n, the peak density N, the position of the peak z_r, the density transition length w_r and the acceleration length $L = z_d - z_r$. Again, the length scales of the rising and falling edges of the target, w_u and w_d, will not be discussed.

The transition length w_r is measured on the order 1 mm, which is one to two orders of magnitude larger than expected for a ~ 100 bar gas jet striking a razor blade [153]. In addition to the assumption of cylindrical symmetry of the ramp within the interaction region and the 100 µm pixel size of the camera, resolving the density ramp relies on perfect simultaneous alignment of the probe beam parallel to the shock and transverse to the drive laser. Any misalignments, which are likely due to the motion of the blade during electron beam optimisation scans, would lead to an overestimated transition length, as observed. Therefore, the density ramp is taken as inaccurate, and will not be considered further in the context of the experimental results.

Figure 4.6 shows three density maps in the $z - y$ plane of the target produced with different blade coverages and backing pressures. Each plot corresponds to the results of a single scan where the vertical position of the blade was varied between the gas nozzle and the laser axis. In all cases, the density ramp is observed to move outwards as the blade is moved farther below the laser axis, representing an outwards shock. This is inconsistent with the sharp, shallow bow shock formed by the interaction of the supersonic gas with the thin blade, as it would require the unphysical expansion of the flow into the shock [164]. Instead, it is likely representative of the intercepting shock which develops due to the re-expansion of the subsonic region behind the bow shock. The blade and the bow shock form a secondary virtual nozzle, and the coalescence of compression waves results in an intercepting shock [153]. This type of fluid structure has a transition length larger than the mean free path of the gas, representing a gentle density ramp.

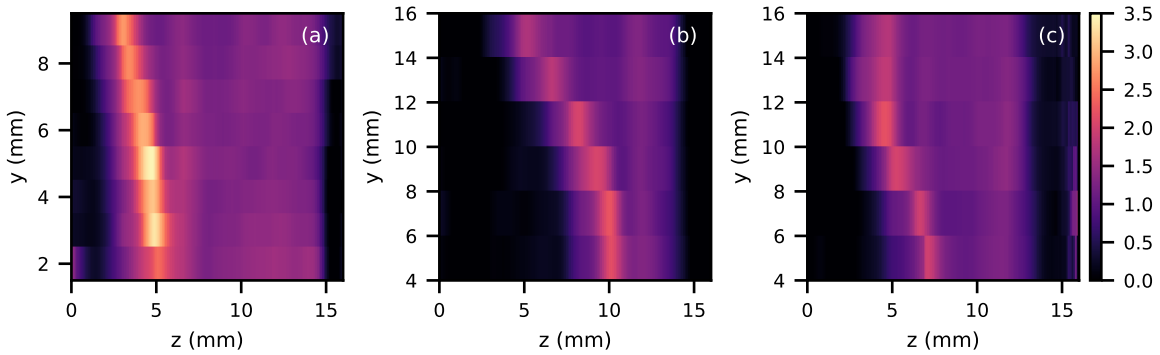

Figure 4.6: 2D density maps of the target produced by a blade in a gas jet. The y axis corresponds to the vertical distance between the tip of the blade and the interaction region. Each horizontal lineout corresponds to the average of the density profile retrieved from interferometry of three to five shots at the same height. (a) Scan at 90 bar, 3.2 mm blade z, 18 mm gas y. (b) Scan at 100 bar, 3.5 mm blade z, 21 mm gas y. (c) Scan at 100 bar, 2.7 mm blade z, 21 mm gas y.

The variation of shock angle with target setup complicates the reconstruction of the ramp, as the deviation from the cylindrical symmetry assumed in the Abel inversion is not systematic. This constitutes further justification for disregarding the measured ramp lengths. The position of the falling edge of the target density remains approximately constant within the heights explored, but this is likely due to incorrect probe timing as in 4.2.1.

The data discussed in this thesis was taken over four days and comprised ~ 1500 shots taken at repetition rates < 0.05 Hz. The same razor blade was used to produce the density ramp in all shots. No damage to the blade was noted, and no decline of the density profile quality or stability over time was measured. However, due to the low number of shots and repetition rates used, compared to the > 20 Hz expected in future facilities [49], no strong conclusions can be drawn regarding the lifetime and longevity of the setup. This is still an important issue that requires further investigation.

4.2.3 Density scans

To investigate the dependence of the target density profile on input target parameters, the backing pressure of the gas jet and the vertical and horizontal positions of the blade were scanned, with three to five shots taken at each set of initial conditions. The gas pressure was varied between 50 bar and 100 bar; the blade was moved vertically between 2 mm and 16 mm below the laser axis and horizontally between 0 mm and 11 mm coverage of the gas jet. The data presented here constitutes a representative

sample of the scans taken. From them it is possible to identify representative trends, though they may not cover the entire parameter space explored in the experiment.

The measured density characteristics are plotted in figure 4.7. Figure 4.7(a) shows that changes in the backing pressure between 55 and 95 bar result in approximately linear variations of both the peak and plateau densities, maintaining a constant peak: plateau ratio of 2.4 ± 0.3. The correlation coefficient between peak and plateau densities is $r = 0.95$ for the pressure scan. In contrast, scanning the vertical blade position between 7 and 15 mm below the laser breaks the correlation between peak and plateau densities, as shown in figure 4.7(b). Increasing the distance between the blade and the laser axis (higher blade y) causes a decrease in the peak density with an anomalous result for the lowest blade position; this is likely due to the curvature of the shock and so will be disregarded when considering the trends here. The plateau density remains approximately constant. Therefore, the correlation coefficient between peak and plateau densities is $r = 0.38$ when the blade height is varied (disregarding the anomalous result). Changing the horizontal position of the blade has an erratic effect on the peak and plateau densities, as shown in figure 4.7(c). A negative correlation is observed for blade coverages under 3 mm, but this trend inverts for larger blade coverages. Changes in the plateau density due to blade position are a signature of an intercepting shock [153], which is consistent with the findings of section 4.2.2. These results suggest that correlated peak and plateau densities are indicative of a change in gas backing pressure, while a lack of correlation between the densities implies motion of the blade in the gas.

The position of the density down-ramp is found to be strongly affected by the position of the blade in the gas jet, as shown in the right panel of figure 4.7(b) and figure 4.7(c). The ramp position is most sensitive to longitudinal motion of the ramp, varying at a rate $(3.7 \pm 0.8)\,\mathrm{mm\,mm^{-1}}$. This control over the shock position is what enables the electron beam energy to be tuned [146, 149, 157], assuming the density profile is unperturbed after the shock. Figure 4.7(a) shows that the gas pressure has a weak effect on the ramp position, but still comparable to or larger than the shot-to-shot fluctuations for pressure variations of order 10 bar.

4.2.4 Shot-to-shot density fluctuations

The experiment produced data from numerous parameter scans with three to five repeats, which cover a broad range of potential targets for LWFA. From these, a measure of the shot-to-shot fluctuations of the density characteristics can be obtained by considering the repeat shots at the same nominal initial conditions to be a sample, and using

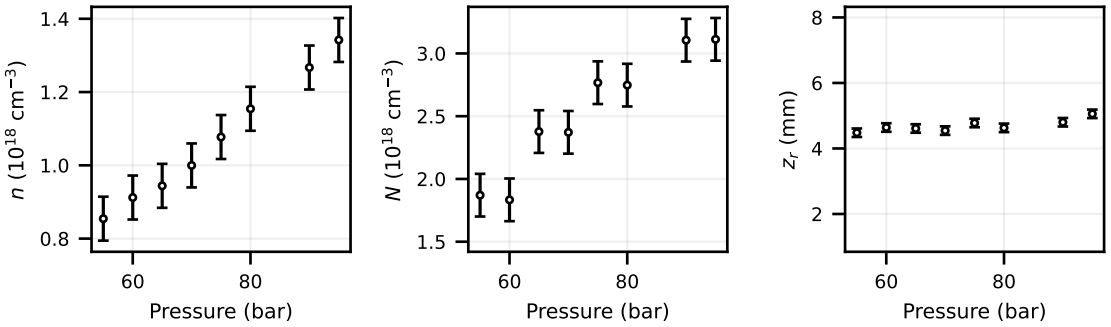

(a) Backing pressure scan. The laser axis was 18 mm above the nozzle and 6.5 mm above the blade; the blade coverage was 3.2 mm.

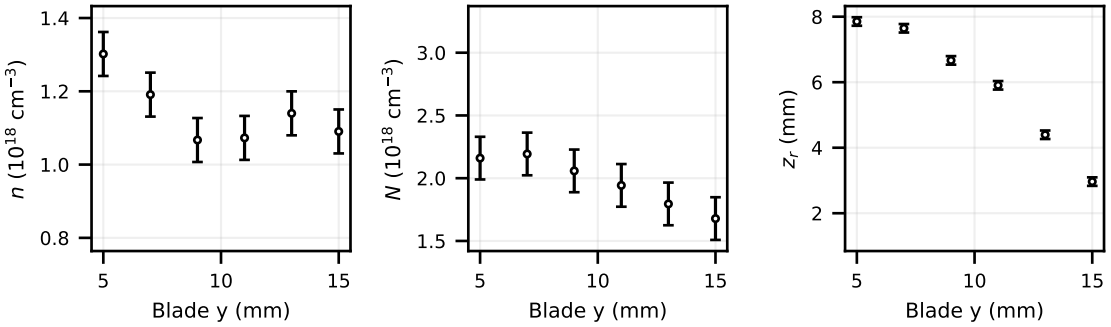

(b) Blade height scan. The laser axis was 18 mm above the nozzle and 6.5 mm above the blade; the blade coverage was 3.2 mm.

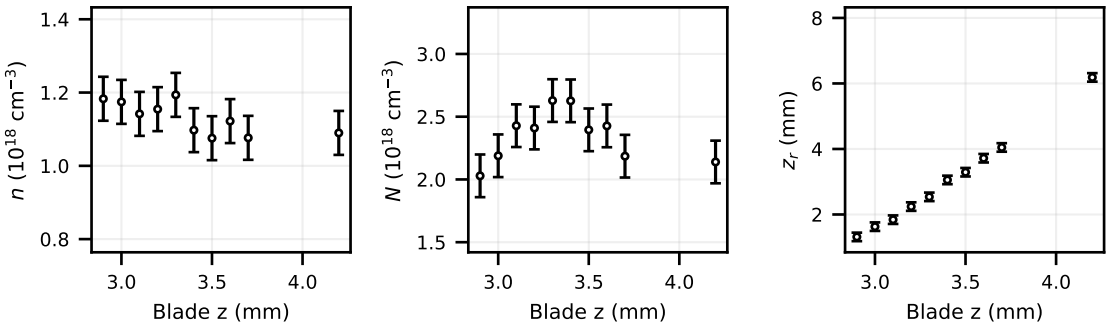

(c) Blade coverage scan. The backing pressure was 100 bar, the laser axis was 21 mm above the nozzle and 12 mm above the blade.

Figure 4.7: Each row shows the response of (left to right) plateau density, peak density, down-ramp position and acceleration length to changes in the target setup. Each point is the average of three to five shots and the error bars represent the shot to shot fluctuations ($\pm 1\sigma$) discussed in section 4.2.4.

many samples to estimate the true spread. The distribution of the density characteristics measured from repeat shots at the same nominal initial conditions have a spread characterised by the standard deviation σ. Due to the small number of repeats, σ may not accurately represent the standard deviation of the parameters but it is an estimator of the fluctuations. σ is made artificially large in order to make a conservative estimate of the distribution spread:

$$\sigma = \sqrt{\sum_{i=0}^{n} (X_i - \bar{x})^2 \frac{n}{n-1}}\,, \tag{4.3}$$

where

$$\bar{x} = \frac{\sum_{i=0}^{n} X_i w_i}{\sum_{i=0}^{n} w_i} \tag{4.4}$$

is the weighted mean, n is the number of measurements and the weights w are calculated as inversely proportional to the square of the measurement uncertainties.

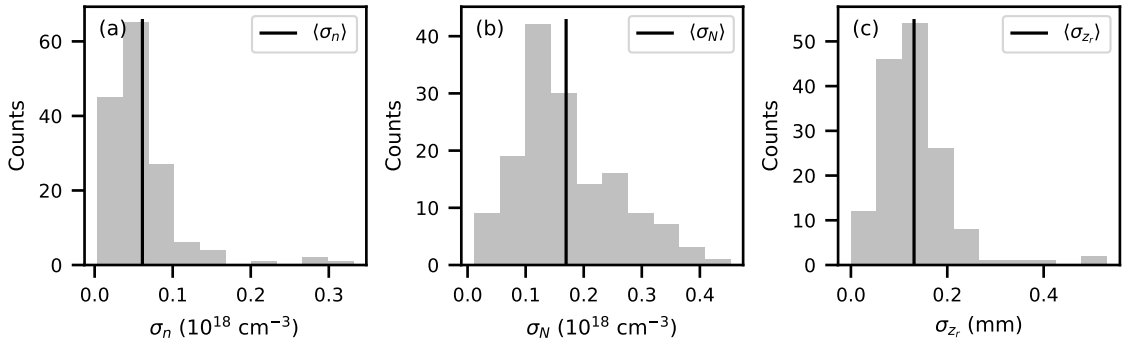

Figure 4.8: Distribution of sample standard deviations for (a) plateau density, (b) peak density and (c) down-ramp position. The black line denotes the average of the distribution, which corresponds to the population standard deviation.

By measuring the standard deviation σ_j for every set of shots j, it is possible to build a distribution of the measured fluctuations, as shown in figure 4.8. Here there are 145 samples from 628 shots taken over two days. The average of the set of standard deviations, $\langle\sigma\rangle$, is expected to accurately represent the spread of possible density values obtained with the same setup, which are taken to comprise the shot-to-shot fluctuations. This assumes that the fluctuations are independent of the absolute density values. Each measured standard deviation is weakly correlated with the mean for the plateau density ($r = 0.03$) and peak density ($r = 0.24$), suggesting that this assumption is valid for the range of density profiles used in the experiment.

Thus, the shot-to-shot fluctuations can be characterised by the spread $2\langle\sigma\rangle$, which

represents 68 % of the possible density values obtained. These are $2\langle\sigma_n\rangle = 0.12 \times 10^{18}\,\mathrm{cm}^{-3}$ for the plateau density, $2\langle\sigma_N\rangle = 0.34 \times 10^{18}\,\mathrm{cm}^{-3}$ for the peak density and $2\langle\sigma_{z_r}\rangle = 260\,\mu\mathrm{m}$ for the ramp position.

Fluctuations in the peak density are 2.8 times higher than those in the plateau density because the plateau density is mainly affected by the backing pressure, whereas the peak density depends strongly on both the backing pressure and blade position. Fluctuations in the ramp position are $\sim 260\,\mu\mathrm{m}$, which is small compared to the focusing geometry of the laser (Rayleigh range $> 4.44\,\mathrm{mm}$). Zhang *et al.* measured $\sim 100\,\mu\mathrm{m}$ fluctuation of shock position experimentally [165]. While the experiment was not designed as a stability study, the data provides accurate estimates of the shot-to-shot target fluctuations that are relevant to a wide range of target profiles used in LWFA.

4.3 Shot-to-shot electron fluctuations

44 shots were taken at nominally identical initial conditions, at backing pressure 70 bar, blade coverage 0.5 mm and with the laser axis 13 mm above the blade and 18 mm above the gas nozzle. The distributions of the measured density parameters in this run are presented in figure 4.9. Their means and standard deviations are $n = (0.86 \pm 0.07) \times 10^{18}\,\mathrm{cm}^{-3}$, $N = (1.83 \pm 0.18) \times 10^{18}\,\mathrm{cm}^{-3}$ and $z_r = (2.46 \pm 0.11)\,\mathrm{mm}$. The shot-to-shot fluctuations 2σ of the peak density, plateau density and ramp position measured in this run are in agreement with those estimated in section 4.2.4, proving the validity of the method used. The peak and plateau densities were weakly correlated ($r = 0.3$), suggesting that erratic blade motion was the dominant source of density fluctuations rather than any fluctuation in gas jet pressure, as identified in section 4.2.3. This suggests that the way in which the blade was mounted on the target (figure 4.2) was not sufficiently rigid. The long arm attaching the mount to the translation stages may not have been sufficiently robust to the $\sim 100\,\mathrm{bar}$ gas jets hitting the blade at its end. Offline characterisation of the blade motion in this setup should inform future mount designs.

Automated edge detection was employed on the electron spectra in divergence-energy space to measure the maximum electron beam energy for every shot. The total charge was measured by integrating the signal in the electron spectrometer. The fluctuations of these parameters are presented in figure 4.10 as a function of the measured plateau density, and peak density and ramp position. Injection was observed in 42 out of 44 shots (95 %).

The correlations with ramp position are weak and limited by the resolution of the

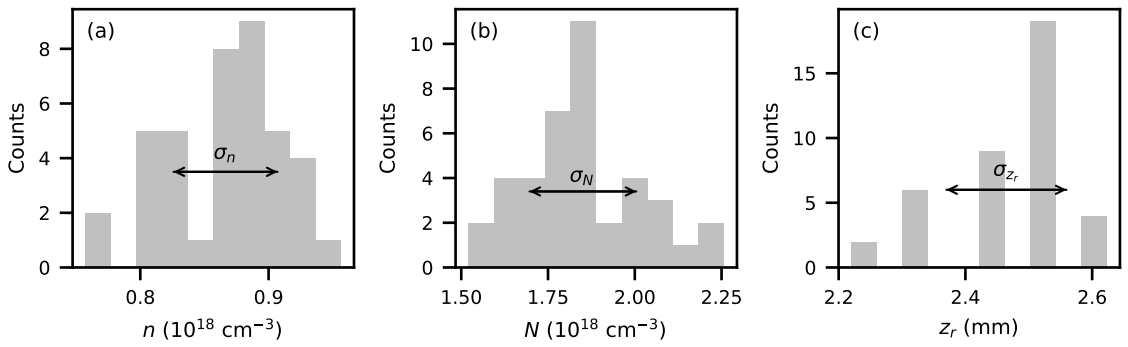

Figure 4.9: Experimental data from 44 shots at the same nominal initial conditions. Distribution of (a) plateau density, (b) peak density and (c) ramp position.

measurements. Figure 4.10(a)-(b) show that the maximum electron beam energy is strongly correlated with the peak density while the correlation with the measured plateau density is very weak. However, the plateau density is of known importance to the acceleration dynamics present in the experiment, as it determines the wakefield amplitude and therefore the accelerating fields, $E_z \propto n_e^{1/2}$. The lack of correlation may be attributed to the small variations and non-uniformities in the plasma density profile after the ramp. The values of n presented constitute the average of the plateau region, but may not capture the full effect of the extended density profile on the acceleration dynamics. Non-uniform densities change λ_p erratically, leading to variations in the accelerating phase of the electrons. This has been shown to affect electron beam energy in self-injection [141]. The non-uniformities in the density profile were characterised as the RMS deviation of the retrieved profile to n in the plateau region and for this run were $(0.28 \pm 0.02) \times 10^{18}\,\mathrm{cm}^{-3}$. These correspond to 32 % of the plateau density. No correlations were found between electron beam parameters and density non-uniformities, suggesting that their effect is nuanced and requires further investigation. The maximum electron energy is found to be $(860 \pm 150)\,\mathrm{MeV}$, where the uncertainty $\sigma = 150\,\mathrm{MeV} \approx 17\,\%$ is the standard deviation.

Figure 4.10(d)-(e) display a strong correlation between the total charge and the peak density, while the correlation with plateau density is weak. Thus, the injected charge is primarily set by the peak density. The injected charge observed in the experiment is (6400 ± 3000) arbitrary units. The 1σ variation of the injected charge observed is thus 45 %. This low degree of stability is evident in the electron spectra, which varied between comprising single electron bunches, multiple bright bunches separated in energy, or an approximately constant charge density beam spreading over a wide energy range. Multiple electron bunches may be caused by injection in successive periods of the

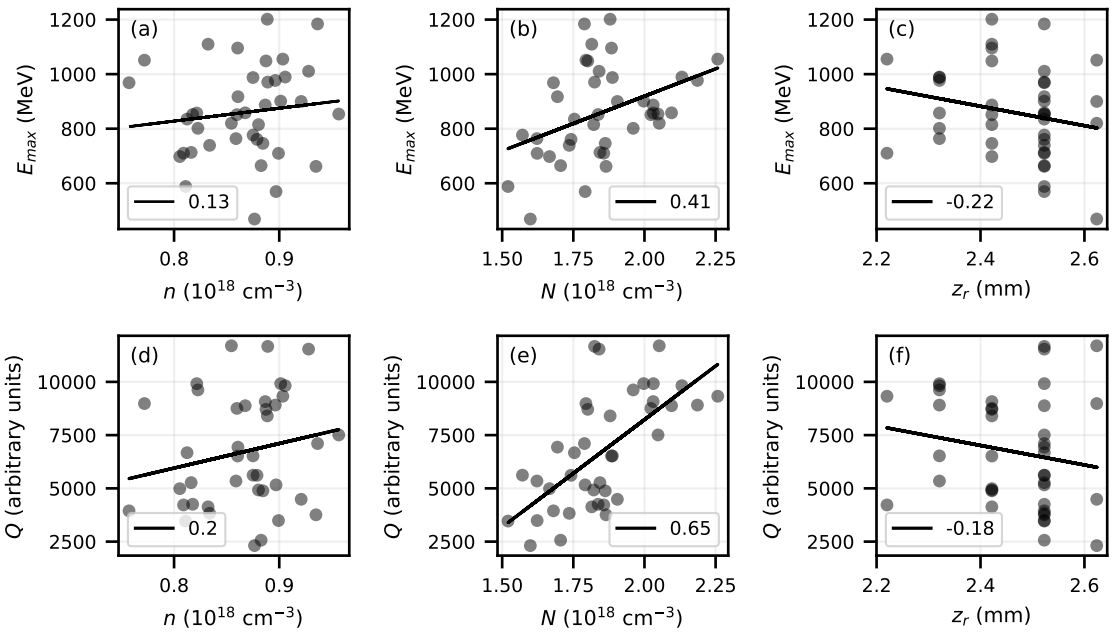

Figure 4.10: Experimental data from 50 shots at the same nominal initial conditions. Correlations of maximum electron beam energy with (a) plateau density, (b) peak density and (c) ramp position. (d)-(f) show correlations of the injected charge with the density parameters in (a)-(c). The labels denote the Pearson's correlation coefficient.

wakefield [102], while a dark current likely comprises electron injection after the ramp, suggesting that the experimental conditions are close to the self-injection threshold. Laser evolution in the $\sim$ 20 mm long plasma can cause a decrease of the wakefield phase velocity, thereby relaxing the injection threshold in the acceleration region [99]. Moreover, small-scale density ripples with $\Delta n_e/\lambda_p > 0.4\,\%$ can stimulate self-injection [166], leading to many uncontrolled separate injection events in gas jet targets with random inhomogeneities [167]. Note that the charge is calculated as $\int_{300\,\mathrm{MeV}}^{2.5\,\mathrm{GeV}} N_e \,\mathrm{d}E$, meaning that the low energy electrons are disregarded from the calculation and the charge is underestimated. Due to the varying structure of the electron spectra, instances of continuous injection are likely more underestimated than electron beams with peaked spectra. These differences may worsen the measured charge correlations.

4.4 Simulations of LWFA stability

PIC simulations were performed to examine the effect of shot-to-shot fluctuations on LWFA, with a focus on density transition injection. These simulations are not meant to model the full experimental results, but to allow estimates of the fluctuations of charge and energy to be investigated. The 2D simulations were run in a window of size 64 µm × 112 µm in the laser propagation and transverse directions, respectively, which moved along the laser direction at the linear group velocity as calculated for the plateau density when the laser reached 2/3 of the window. The spatial resolution was 60 cells per wavelength in the longitudinal direction and 20 cells per wavelength in the transverse direction (following section 3.6.1) and 8 electrons per cell were used. The laser pulse was polarised out of the plane of the window. The laser pulse was modelled as a Gaussian with a duration of 50 fs, focused to a 46 µm diameter focal spot and a peak intensity $I_0 = 1.97 \times 10^{19}\,\mathrm{W\,cm^{-2}}$.

Figure 4.11 shows the plasma density profile used to simulate density transition injection. The target comprised a pre-ionised plasma with a 360 µm rising edge from vacuum up to a peak density N. This was followed by a $\tanh\left((z - z_r)/r\right)$ down-ramp with characteristic length $r = 20\,\mu\mathrm{m}$ onto a plateau region at density n up to a total propagation distance of 1.2 mm. The functional form of the ramp was chosen arbitrarily as a smooth transition between two densities. r corresponds to a density transition length $\approx 80\,\mu\mathrm{m}$, which is in the gentle regime for the plasma wavelength $\lambda_p \approx 25\,\mu\mathrm{m}$. The simulations are limited to 1.2 mm propagation compared to > 15 mm in the experiment in order to limit computational costs while still capturing the important injection dynamics. The time evolution of the electrons suggests that these short simulations sufficiently capture the effect of density fluctuations on the acceleration before approaching the dephasing limit.

A baseline simulation (denoted by subscript 0) comprised the basis for comparison of the effect of laser and density fluctuations. The baseline peak density is $N_0 = 2.82{\times}10^{18}\,\mathrm{cm^{-3}}$, the baseline plateau density is $n_0 = 1.2{\times}10^{18}\,\mathrm{cm^{-3}}$ ($N_0/n_0 = k_0 = 2.35$) and the vacuum laser focus is set to the middle of the down-ramp, $z_l = z_{r0} = 400\,\mu\mathrm{m}$. n_0 represents the average plateau density used in the experiment. Simulations performed with no down-ramp at plateau densities n_0 and N_0 show that a non-linear wakefield is produced but no self-injection occurs in the first wakefield period.

Three sets of simulations were run, based on the experimentally measured trends of density characteristics with target inputs, each of which isolated one kind of density fluctuation. Simulation set I varied the peak density only, $n = n_0$; simulation set II varied the plateau and peak densities at a constant ratio, $N/n = k_0$; simulation set III

varied the laser focus z_l relative to the position of the ramp. Based on the findings of section 4.2.3, simulation set II represent fluctuations of the backing pressure, while simulation sets I and III represent independent effects of blade position fluctuations. Within each set, four simulations were run at $\pm 1\sigma$ and $\pm 2\sigma$ away from the baseline relevant density parameter, where 2σ represent the experimental shot-to-shot fluctuations measured in section 4.2.4. In addition, a set of simulations was run to study the effect of laser energy fluctuations for reference. The deviations of injected charge from the baseline, ΔQ, and the deviations of maximum electron energy from the baseline, $\Delta(E_{\max})$, are calculated at the end of the simulation (4 ps) and given as a percentage of the baseline quantity. Only the electrons in the first wakefield period are considered. The electron energy is calculated from the relativistic longitudinal momentum of the electrons only, neglecting transverse motion. The energy spectra depict a sharp cut-off in a log-scale at both high and low energies. The high-energy cut-off $E_{\max}$ was identified by fitting the distribution function in energy to a $\tanh\left((E - E_{\max})/w_E\right)$ function, with the length scale of the step w_E taken as the measurement uncertainty. The simulations show that injection occurs only at the ramp.

Supplementary simulations were also run without the density down-ramp, to compare the shot-to-shot fluctuations that would arise when relying on self-injection. For these, the plasma density profile comprised a similar rising edge from vacuum to a constant density n_p up to a total simulation length of 1.2 mm. The baseline density was $n_p = 4 \times 10^{18}\,\mathrm{cm}^{-3}$, and this was varied consistently with simulation set II. n_p is significantly higher than the densities used in the experiment, which were comparable for both plateau and tailored targets. This is because the simulation only takes into account the first two periods of the wakefield, while injection becomes more likely at further periods due to the increased wavefront curvature. In addition, the longer interaction lengths in the experiment allow for sufficient laser evolution to drive injection [99]. Thus, the higher density in the plateau simulation is used in order to observe injection within a short propagation distance, while maintaining the same intensity as for the simulations with a tailored density profile for comparison. The results are presented throughout but discussed in section 4.4.5.

4.4.1 Baseline simulation

The density profile used for the baseline simulation is shown in figure 4.11, along with the evolution of the energy distribution of the injected electrons. The laser drives a nonlinear wakefield and the bubble elongates from 24 µm at the peak density to 37 µm at the bottom of the ramp. The phase velocity decrease associated with this elongation causes

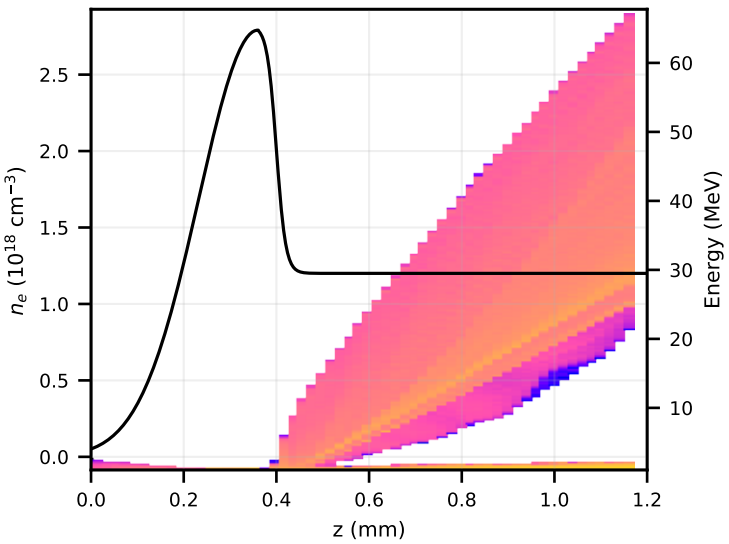

Figure 4.11: Density profile of the baseline simulation with a density down-ramp in black. The energy spectra of electrons in the first wakefield period throughout the simulation is overlaid on a log colour scale.

electrons to inject in the region where $v_e > v_p$. At the time of injection, the electrons that inject are located at the back of the bubble, at a position $\zeta = -\lambda_p(z)$ behind the laser, where the plasma wavelength $\lambda_p \sim n_e^{-1/2}$ varies in z in the density ramp. Therefore, electrons injected earlier in time are positioned closer to the laser pulse, while those injected later are located farther behind. This results in an electron bunch spanning approximately 15 µm in the wakefield, which corresponds to a bunch duration of around 50 fs. The spatial extent of the electron beam can be seen in figure 4.12, which shows the electron $z - p_z$ distribution as a colour map. No injection is observed in the first wakefield period after the density down-ramp. The injected electrons are accelerated to energies between 23 MeV and 68 MeV after 1.2 mm of laser propagation. The energy spread of the bunch increases over time due to the quick acceleration of the leading electrons.

Figure 4.12 also shows the longitudinal electric field of the wakefield in the final timestep of the simulation, compared to the unloaded field depicted by the dashed line, which was obtained from a simulation with no density down-ramp at the same plateau density. The strengthening of the wakefield amplitude (evident around 1.185 mm) compared to the unloaded case can be attributed to the stronger laser evolution in the high density region at the beginning of the target. The presence of electrons between 1.14 µm and 1.17 µm disturbs the wakefield structure, due to the beam loading caused by the space charge of the injected bunch and the wake the bunch generates out of phase with

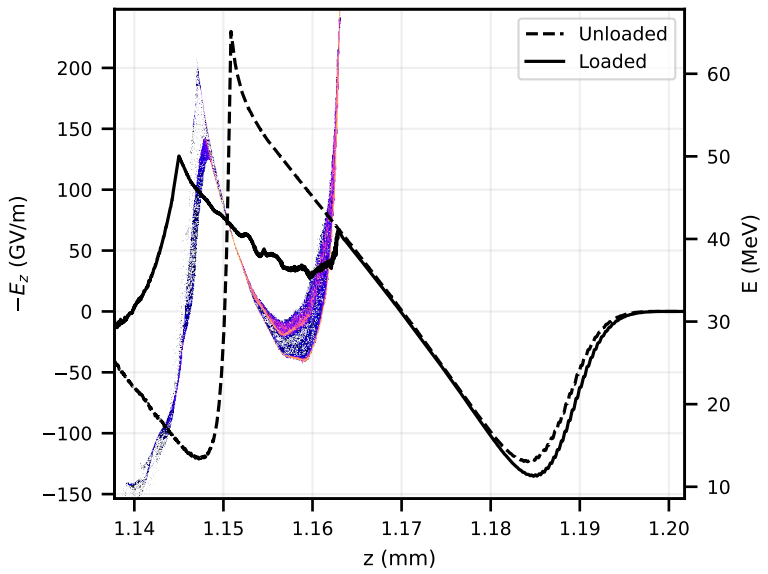

Figure 4.12: Accelerating field after 4 ps. The dashed line shows the unloaded wakefield, obtained from a simulation at n_0 without a density down-ramp. The electron distribution in $z - p_z$ space is overlaid in the colour map.

the laser-driven field. This causes a 6 µm elongation of the bubble, with the rear fields significantly suppressed compared to the unloaded case.

Figure 4.13 depicts the evolution of the laser intensity, a_0, pulse spot size and average wavevector. The latter was measured by averaging the FFT of the laser electric field, while the former were determined by removing the rapid oscillations from the electric field and measuring the peak and FWHM in the transverse direction. Self-focusing causes the laser width to decrease beyond the expected spot size at the vacuum focus of 400 µm, reaching 23 µm at the end of the simulation. This self-focusing is associated with an increase in laser intensity of up to 3.1×10^{19} W cm^{-2} at the end of the simulation, which is 1.55 times larger than the vacuum result. The evolution of the laser wavevector shows a steady redshift of the laser, which indicates energy being transferred to the wakefield. The laser evolution within the ramp is found to be slow relative to the effect of the density gradient, meaning that the effect of pulse evolution on the wakefield phase velocity can be neglected in the ramp.

A simulation using neutral helium as the target was run to simulate the effect of ionisation. This simulation resulted in identical wakefield generation, injection and acceleration dynamics. The maximum electron energies agreed within the uncertainties with those in the simulation using a pre-ionised plasma; the injected charge differed by under 0.8 %. This justifies the use of a pre-ionised plasma for the sensitivity study.

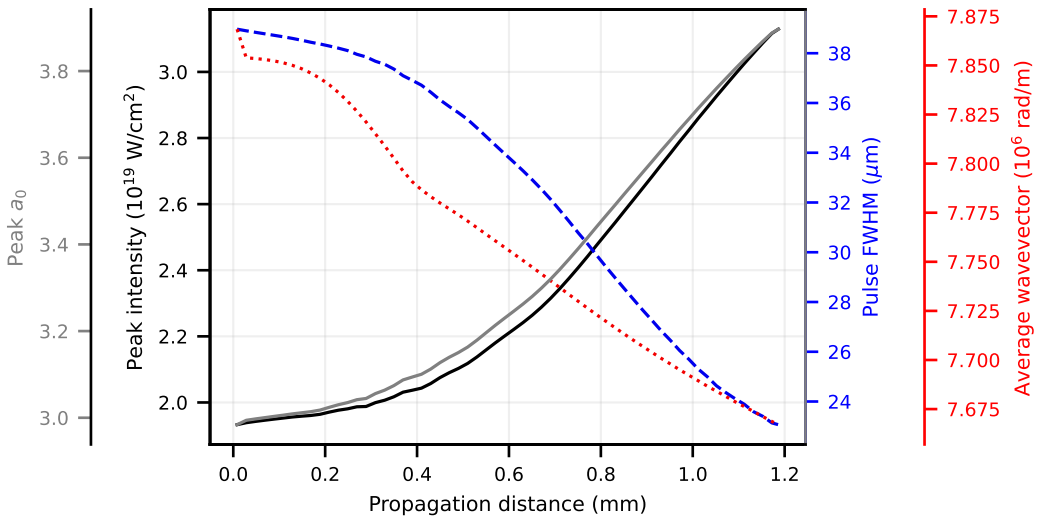

Figure 4.13: Evolution of laser parameters throughout the simulation: peak laser intensity in black, FWHM of the laser pulse in red, average wavevector of the laser in blue.

4.4.2 Sensitivity to laser fluctuations

A series of simulations were run with the laser energy varying by ±5 % and 10 % relative to the baseline simulation with $E_L = 8.3\,\mathrm{J}$. These variations are comparable to the experimental laser fluctuations ±7.5 %. The pulse duration and vacuum spot size were kept constant, such that these variations correspond to a vacuum intensity range between $I = 1.8 \times 10^{18}\,\mathrm{W\,cm^{-3}}$ and $2.2 \times 10^{18}\,\mathrm{W\,cm^{-3}}$. The measured laser intensities throughout the simulations with a density ramp are shown in figure 4.14; the evolution of the pulse width and average wavevector remained identical in all simulations. The evolution of the intensity remains similar up to approximately 0.8 mm into the plasma, after which the different rates of pulse conditioning drive deviations larger than the input 5 % and 10 % as seen in figure 4.14(b). The resulting electron beam deviations are shown as the orange triangles in figure 4.15.

Figure 4.15(a) shows that increasing the laser energy results in an increased injected charge. As the density profile of the target remains constant, the reduction of the phase velocity due to bubble expansion in the ramp is the same for all simulations; a 10 % intensity variation causes a $< 1\,\mu\mathrm{m}$ change in the non-linear plasma wavelength, which is neglected. However, the varying a_0 represents a change in the maximum velocity reached by the electrons during their wakefield oscillations. This means that more electrons satisfy the injection condition, $v_e > v_p$, at higher laser intensities, leading to the observed increase in injected charge. This is investigated further in section 4.6.4. Within the density down-ramp, the baseline laser intensity reaches $2.08 \times 10^{18}\,\mathrm{W\,cm^{-2}}$

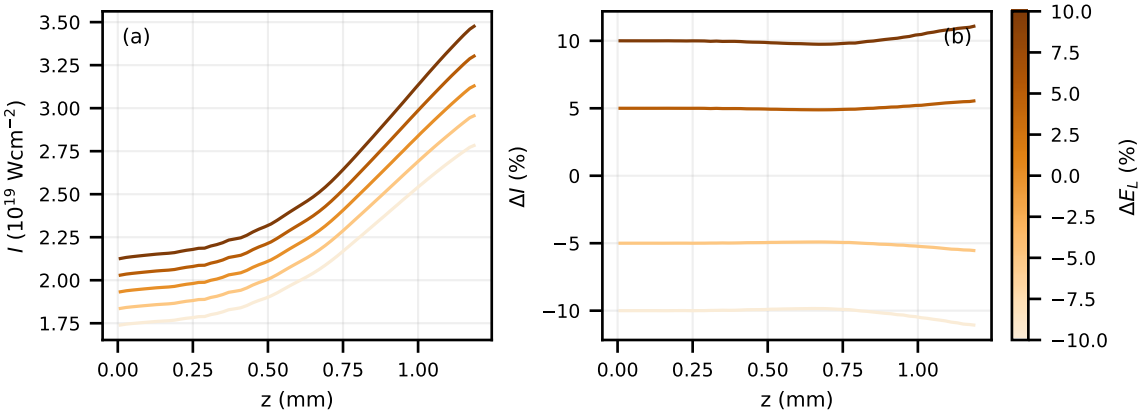

Figure 4.14: Simulation results of the laser intensity evolution in a density ramp for different laser energies. (a) Maximum laser intensity. (b) Deviation of maximum laser intensity from the baseline.

and varies by −9.93 %, −4.96 %, 4.96 % and 9.90 % for increasing laser energy. These represent a_0 of 2.94, 3.02, 3.10, 3.17, and 3.25. Previous numerical studies of laser energy effects on density transition injection reported the bunch charge to increase from 10 pC to 60 pC to 130 pC when a_0 increased from 2.16 to 2.50 to 2.79 in a 50 µm ramp with $N/n = 1.7$ [156]. The improved stability presented here may be attributed to the lower plasma density, smoother density profile and larger spot size which combine to yield a slower laser evolution.

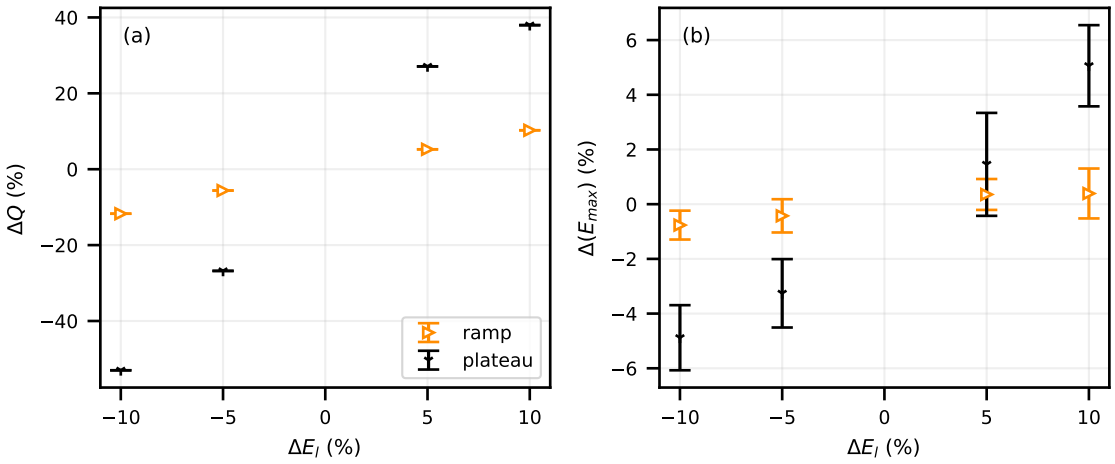

Figure 4.15: Results from the simulations of laser energy fluctuations in a tailored plasma target after 4 ps. (a) Deviations of injected charge. (b) Deviations of maximum electron energy.

The injected electrons are accelerated to higher energies by higher-energy lasers, as shown in figure 4.15(b). In the bubble regime, the accelerating field of a laser-driven

wakefield varies with laser intensity as $E_z \sim \sqrt{a_0}$. The evolution of the laser wavevector is indistinguishable, so the variation of a_0 is dominated by the intensity variations. This trend would correspond to variations in the accelerating fields of $\pm 3\,\%$ and $\pm 2\,\%$. However, the laser energy fluctuations of $5\,\%$ and $10\,\%$ result in very small variations of the maximum electron energy of $< 1\,\%$ after 1.2 mm. This is likely due to beam-loading by a higher injected charge with higher laser energies. Previous studies reported a negative trend of mean electron beam energy with laser energy [156] due to the beam-loading effect. As the injected charge deviations are smaller here, beam-loading does not fully compensate for the increase in the strength of the laser-driven wakefield, so a weak positive trend remains.

Summary

- The effect of laser energy fluctuations on electron beam energy and charge provides a reference to which the effect of density fluctuations can be compared.
- 2σ laser energy fluctuations produce fractional charge deviations of similar level.
- The effect on maximum energy is sub-1 %.

4.4.3 Sensitivity to absolute density fluctuations

Two types of absolute density fluctuations of the tailored density profile are investigated: independent variations of the peak density at a constant plateau density and coupled variations of peak and plateau densities.

Peak density fluctuations

The density profiles used for simulation set I are shown in figure 4.16(a). The peak density variations correspond to peak:plateau ratios of 2.07, 2.21, 2.35, 2.49 and 2.63. The injection dynamics in these simulations can be understood through the relaxation of the phase velocity of the wakefield. Thus the evolution of v_p at the back of the bubble, $\zeta = -\lambda_p$, is plotted in figure 4.16(b) for the simulated density ramps, based on the analytic expression (2.100). The effect of the laser evolution on v_p is neglected as mentioned in section 4.4.1. The charge and maximum energy deviations from the baseline caused by these density fluctuations are summarised in figure 4.17 as the blue circles.

In figure 4.17(a), the injected charge is observed to increase with an increase in peak density, indicating that the number of electrons available in the injection region affects

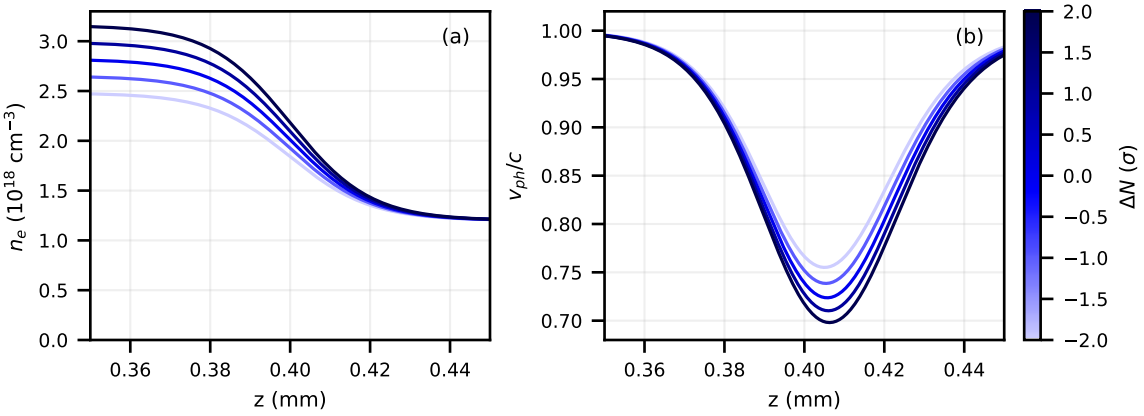

Figure 4.16: Simulations with peak density varying at a constant plateau density. (a) Simulated density profiles in the vicinity of the down-ramp. (b) Analytic evolution of the wakefield phase velocity at the back of the bubble.

the injected charge. This is in line with previous studies [155–157]. An additional effect drives further differences in the injection dynamics in these simulations. The electron velocities are similar, as the laser intensities and wavevectors are constant to within $< 1\,\%$ in the ramp. However, the wakefield phase velocity varies as shown in figure 4.16(b), because steeper ramps necessitate a faster rate of phase velocity decrease to accommodate a larger change in plasma wavelength over the same distance. This means that the injection region, where $v_p < v_e$, is larger for steeper ramps. This compounds with the lower minimum v_p reached for higher peak densities to drive the observed charge fluctuations. The combination of these effects results in the non-linear trend of injected charge with peak density: the deviations are measured to be $+6\,\%$ when increasing the peak density but 2σ but $-8\,\%$ when decreasing it by the same factor.

The maximum electron beam energy is observed to decrease with increasing peak density in figure 4.17(b). While the accelerating fields should be constant at constant plateau density, beam-loading may partially explain the variation. However, the phase at which electrons are injected also plays a significant role. Due to the extended injection region at higher peak densities, injection begins earlier, leading to electrons located at an advanced phase ψ in the wake, but also terminates later, resulting in a more elongated bunch in the longitudinal direction, as evidenced in the beam-loaded fields in figure 4.18.

Figure 4.18(a) depicts the accelerating fields after 4 ps. The local maximum $-E_z$ in the inset coincides with the position of the leading high energy electrons, denoted by the triangles. This shows their separation in $\zeta \propto \psi$ as a result of the varying injection dynamics with peak density. The accelerating fields behind this point are suppressed

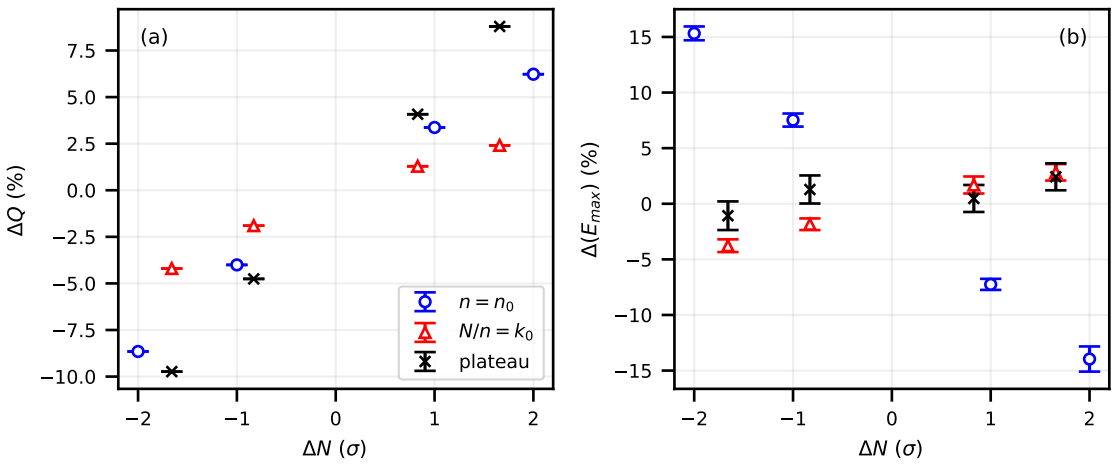

Figure 4.17: Results from the simulations of absolute density fluctuations in a tailored plasma target after 4 ps. Deviations of (a) injected charge and (b) maximum electron energy. The blue circles correspond to variations of the peak density at a constant plateau density, while the red triangles correspond to coupled variations of the peak and plateau densities at a constant ratio.

by beam-loading. The leading electrons from higher density simulations witness lower accelerating fields than those from lower density simulations. This is because of the advanced phase of electrons injected from higher peak density targets, which is associated with a lower accelerating field from the laser-driven wakefield. This is illustrated schematically in figure 4.19. After 4 ps, the leading electrons are located at phase positions $\psi = -3.87\,\text{rad}$, $-3.74\,\text{rad}$, $-3.60\,\text{rad}$, $-3.51\,\text{rad}$ and $-3.40\,\text{rad}$ for increasing peak densities, where the plasma wavelength $\lambda_p = 37\,\mu\text{m}$ at $n = 1.2 \times 10^{18}\,\text{cm}^{-3}$. This positional effect compounds with beam-loading, which is more significant for the higher charge injected with higher peak densities. Beam-loading modifies the electric field at the back of the electron bunch, causing the effective plasma wavelength to appear longer for higher densities. This is due to the trailing electrons being advanced in ζ at lower densities, as a result of the shorter injection at lower N.

The electron energies at a given propagation distance z are determined by the work done per unit charge, $W_e = e\int_{z_\text{inj}}^{z} -E_z \text{d}z'$, where z_inj is the injection location. The deviation of this quantity from the baseline is plotted in figure 4.18(b) for the ζ of the leading electrons, neglecting differences in z_inj. Quantitative agreement is found between the deviations of W_e and $\Delta(E_\text{max})$ after 4 ps, which reach 15 % for 2σ density fluctuations. The results are consistent with previous studies [155] which report a 14 % decrease in mean electron beam energy when the transition height is increased by 15 %. The variations in the mean energy of the electron beam have been reported to become

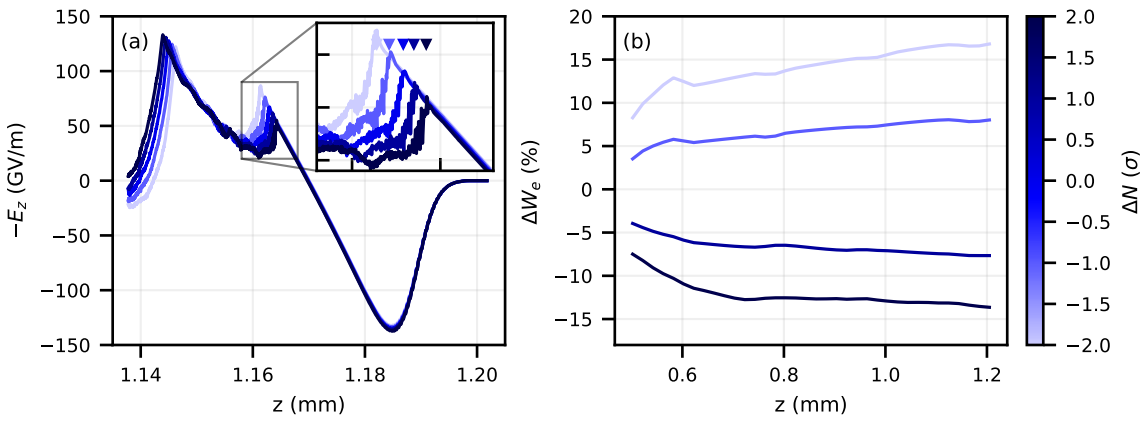

Figure 4.18: (a) Accelerating fields for simulations varying only the peak density after 4 ps. The inset shows the vicinity of the leading high energy electrons, whose position is shown by the triangles. (b) Deviations in the spatially integrated accelerating fields witnessed by the leading electrons.

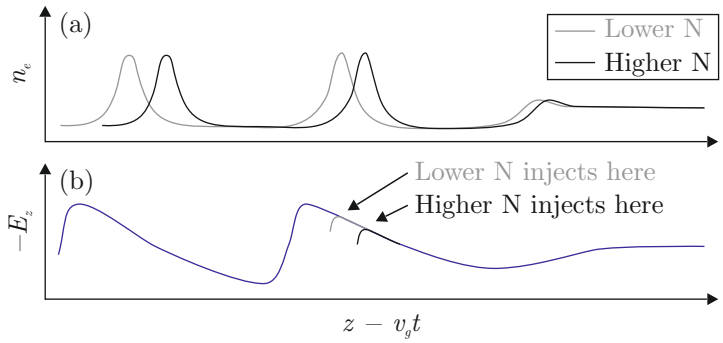

Figure 4.19: Schematic diagram showing the different injection position of electrons in a density ramp with higher (black) and lower (grey) peak densities. (a) Electron density distribution at different densities. (b) Unloaded electric field (blue) in the plateau region.

non-linear with larger changes in peak density [157].

Coupled plateau and peak density fluctuations

The density profiles used for simulation set II are shown in figure 4.20 along with the resulting wakefield phase velocity at $\zeta = \lambda_p$. The plateau density was varied according to σ_n, with the peak density following $N/n = 2.35$. These correspond to smaller peak density fluctuations than for simulation set I, $\Delta N = 0.82\sigma_N$. The electron beam deviations caused by these density fluctuations are summarised as the red triangles in figure 4.17.

Figure 4.17(a) shows an increase in injected charge at higher densities, though the

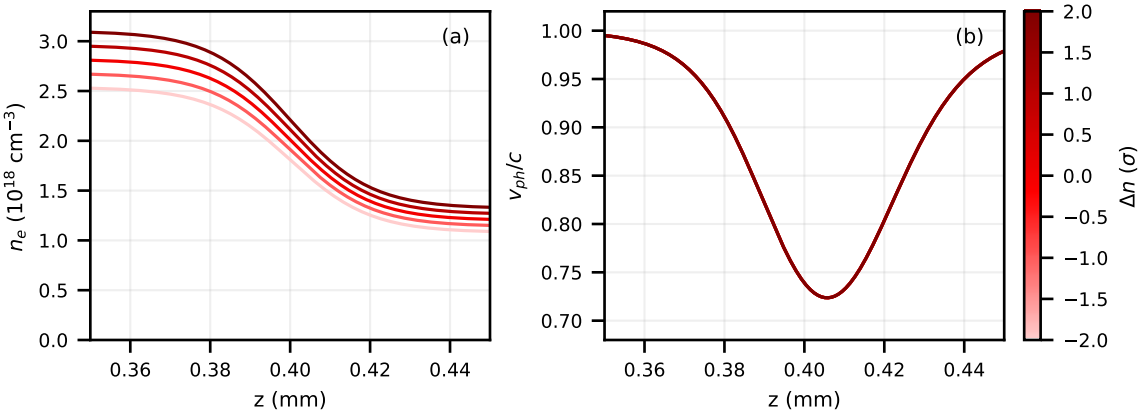

Figure 4.20: Simulations with peak and plateau densities varying at a constant ratio. (a) Simulated density profiles in the vicinity of the down-ramp. (b) Analytic evolution of the wakefield phase velocity at the back of the bubble.

deviations from the baseline are two times smaller than those obtained when varying the peak density only. In contrast to the case with constant plateau density, these ramps have a constant $n_e^{-1}\mathrm{d}n_e/\mathrm{d}z$, which results in an identical $v_p(z)$ at $\zeta = -\lambda_p$ as depicted in figure 4.20(b). Thus, the injection region is constant, and variations in injected charge are solely caused by the increased availability of particles at higher density.

Figure 4.21(a) shows the accelerating fields in these simulations after 4 ps. The leading high energy electrons, shown by the triangles, have a density-dependent ζ. This is because, while injection occurs at a constant z_{inj} in all density profiles, it takes place at the the back of the bubble, $\zeta = -\lambda_p$, and the plasma wavelength is density dependent. This means the injection time is different. In these density profiles, the similar evolution of the wake phase in the ramp ensures a constant duration electron bunch. This causes the ζ of the trailing electrons to have a similar spacing to those of the leading electrons for the different simulations, leading to the effective plasma wavelength being shorter at higher densities.

Coupled variations of peak and plateau densities result in an increasing trend of maximum electron beam energy with density, with 2σ density fluctuations causing $< 5\,\%$ deviations in E_{max}. As the plateau density is changed in proportion to the peak density, the acceleration dynamics also vary in these simulations. The variations in plateau density after injection are associated with changes to both the accelerating field strengths and the plasma wavelength in the acceleration region. The positive correlation of energy with density is consistent with the increased electric fields, $E_z \propto \sqrt{n_e}$, of the laser-driven wakefield. However, figure 4.21(a) presents consistent accelerating fields for the leading electrons. This is because of the different spatial position and phase of these electrons,

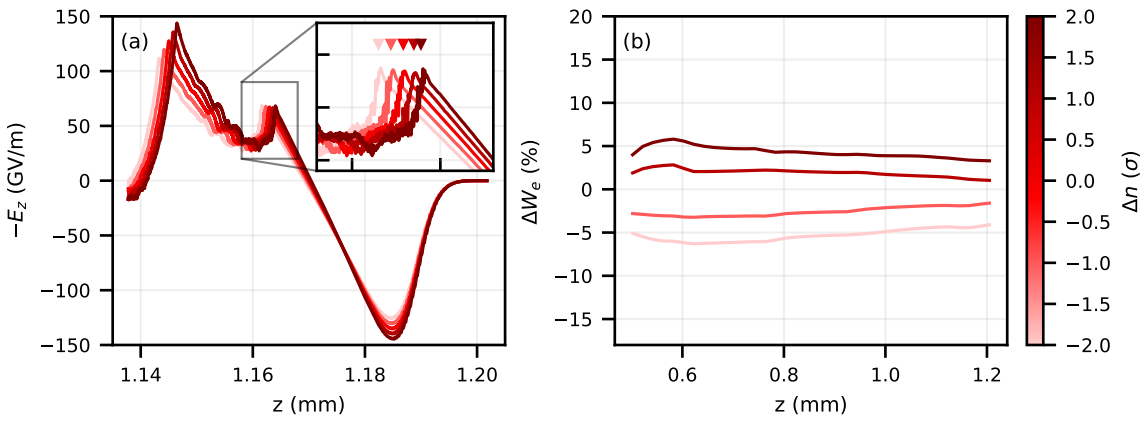

Figure 4.21: (a) Accelerating fields for simulations varying peak and plateau densities 4 ps. The inset shows the vicinity of the leading high energy electrons, whose position is shown by the triangles. (b) Deviations in the spatially integrated accelerating fields witnessed by the leading electrons.

which compensates for the change in wakefield amplitude. The result is more stable electron energies than obtained from peak density fluctuations independent of the plateau. Figure 4.21(b) presents the deviation of W_e throughout the simulation. The deviations of this quantity agree with the measured fluctuations of maximum electron energy after 4 ps, which reach 4 % and −3 % for -2σ and 2σ density variations, respectively.

The results show that the electron charge and maximum energy are very sensitive to variations in $n_e^{-1}\mathrm{d}n_e/\mathrm{d}z$, which cause changes in the injection dynamics. These variations are found to occur when the peak and plateau densities are changed independently, as would be caused by fluctuations of the blade position in the gas target. In contrast, fluctuations of the target backing pressure have a smaller impact on the electron fluctuations, as they keep the down-ramp, and therefore the injection dynamics, consistent.

Summary

- The injected charge is determined by the availability of electrons in the injection region; i.e. it depends on peak density.

- The injected charge also depends on the ratio of ramp steepness to local density, which is constant for coupled fluctuations of peak and plateau density. Therefore, the charge deviations are larger for fluctuations of peak density only.

- When only the peak density varies, the maximum electron beam energy is negatively correlated with peak density. This is because the injection position varies,

meaning that electrons end up in different phases of the wakefield, thereby witnessing different accelerating fields.

- When both the peak and plateau densities vary, the difference in electron injection position is compensated by a variation in plasma wavelength and wakefield amplitude in the plateau region. As a result, the accelerating fields are similar in all targets and the energy fluctuations are reduced.
- This suggests that fluctuations of the peak density independent of the plateau dominate the electron beam energy and charge fluctuations.

4.4.4 Sensitivity to longitudinal target fluctuations

Variations of the down-ramp position were simulated by moving the vacuum laser focus relative to the middle of the ramp as depicted in figure 4.22(a) for simulation set III. This enabled a study of the injection dynamics independent of the acceleration dynamics which would be dominated by the change in acceleration length. These variations are an order of magnitude smaller than the focusing geometry of the laser (Rayleigh range $z_r > 4.44\,\mathrm{mm}$) but represent different laser diameters at the beginning of the simulation. The laser widths at $z = 0$ are 32.6 µm, 32.8 µm, 33.1 µm, 33.5 µm and 34.1 µm which correspond to $-1.5\,\%$, $-0.9\,\%$, $1.2\,\%$ and $3.0\,\%$ variations from the baseline. The resulting injected charge and maximum electron beam energy deviations from the baseline simulation are shown in figure 4.23. $\Delta z_l = -\Delta z_r$ is defined here, such that motion of the ramp farther along the gas is equivalent to the laser focusing earlier.

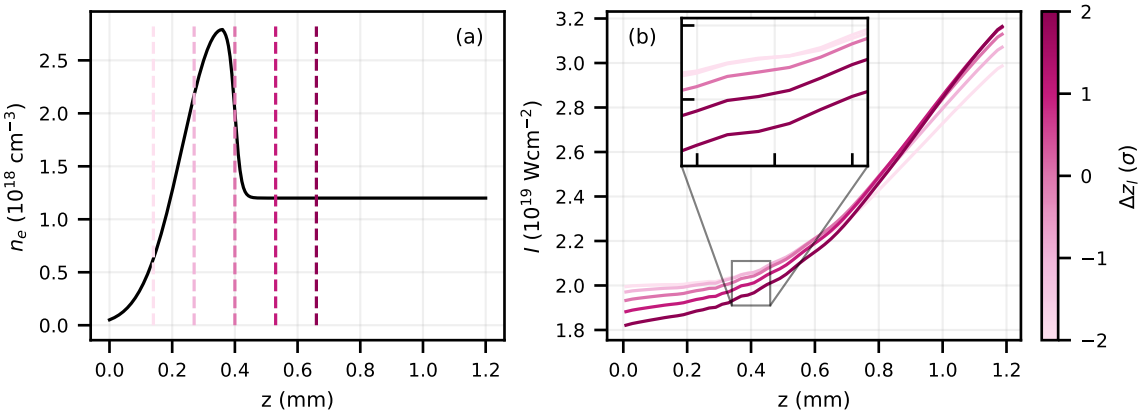

Figure 4.22: (a) Density profiles used for simulations III; the dashed lines show the position of vacuum laser focus. (b) Evolution of the laser intensity; the insets show the results within the density down-ramp.

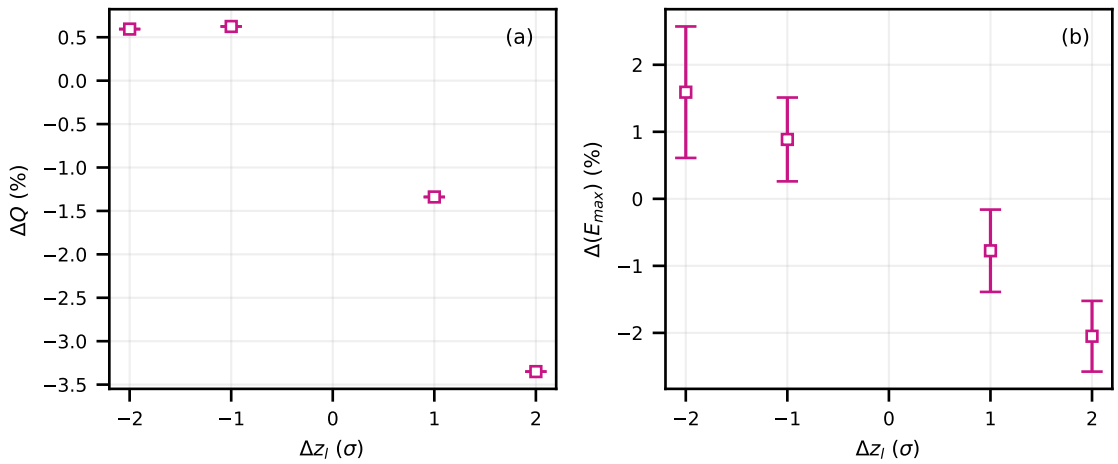

Figure 4.23: Results from the simulations of longitudinal target fluctuations in a tailored plasma target. Deviations of (a) injected charge and (b) maximum electron beam energy. The pink squares correspond to variations of the vacuum laser focus after 4 ps, while the green diamonds correspond to acceleration length variations at the end of the simulation.

The injected charge is observed to decrease when the ramp is positioned before the vacuum laser focus. The evolution of the laser wavelength throughout the interaction is indistinguishable for simulations with different laser focus positions (deviations $< 0.002\,\%$ throughout). This implies that the laser energy loss to the wakefield is comparable. However, the evolution of laser intensity does vary more significantly, as a result of the different rates of self-focusing and self-compression for different initial laser spot sizes. This is depicted in figure 4.22(b), which shows that the intensity in the ramp deviates by $-4\,\%$ and $-2\,\%$ from the baseline when the laser is set to focus 260 µm and 130 µm after the ramp, respectively. In contrast, setting the laser to focus before the ramp causes a $1\,\%$ deviation in laser intensity, which is very weakly dependent on the magnitude of the translation between 130 µm and 260 µm. The laser intensity determines the electron velocities reached during oscillation in the wakefield, thereby influencing the number of particles with $v_e > v_p$ that can inject. The observed charge deviations directly match the measured intensity variations in the ramp, suggesting a linear dependence of injected charge to local laser intensity despite the complex dynamics involved.

Variations of the ramp position relative to the vacuum laser focus result in fluctuations of the maximum electron beam energy of $\lesssim 2\,\%$. The energy is observed to increase as the vacuum laser focus is moved before the ramp. This suggests that the increased laser-plasma coupling early in the interaction taking place for $\Delta z_l < 0$ dominates the initial acceleration dynamics simulated. However, the reversal of the laser

intensity towards the end of the simulation indicates that the dynamics may complicate with longer propagation lengths. The accelerating fields at the end of the simulations are similar and show no identifiable trends with z_l.

The effect of laser focus position on density transition injection has been studied using a gas jet injector coupled to a capillary-discharge waveguide accelerator [146]. While this study suggests that precise matching of laser evolution to down-ramp position is important in order to optimise the electron beams obtained, the energy was reported to vary by 14 % for 2 mm changes in the focus position. This is consistent with the simulation results, assuming a linear trend of $\Delta(E_{\max})$ to Δz.

The results suggest that focusing the laser before the density transition is beneficial in terms of shot-to-shot charge stability, since the nonlinear dynamics will compensate an initial difference in intensity. Focusing on the other side does not have a similar compensating effect due to the decreased laser-plasma coupling.

Summary

- The variations in injected charge are correlated with deviations in laser intensity at the ramp position.
- The injected charge presents sub-percent deviations when the vacuum focus is set up to 520 µm before the down-ramp.
- The electron beam energy deviations reach 2 % for 2σ longitudinal fluctuations.

4.4.5 Simulations without a ramp

The baseline plateau simulation used a higher plasma density $n_p = 4 \times 10^{18}\,\mathrm{cm}^{-3}$. Injection occurs in the second period of the wakefield 0.8 mm into the plasma. The injection is observed to be transverse with the electrons undergoing substantial betatron oscillations. The total injected charge is approximately 1.3 times larger than in simulations with a tailored density profile, despite the 3.3 times higher densities. This demonstrates the lower injection efficiency when relying on self-injection. The electrons reach a maximum energy $\sim$ 75 MeV. The electron energy spectrum is smooth, which represents a gradual injection process. This causes large uncertainties in the measurements of maximum electron beam energy. In contrast, the sharp cut-off in the electron spectra obtained with the density ramp is indicative of a threshold process. Self-injection in this type of target is expected to depend on the length of the plasma channel due to the cumulative laser evolution during propagation. Thus, the results presented here, after 1.2 mm, represent a lower bound to the deviation of injected charge in a longer target.

Laser energy fluctuations

Variations of the laser energy from the baseline cause the deviations in electron beam parameters shown in black in figure 4.15. An increase in laser energy is associated with an increase in the injected charge, similarly to the case with the density ramp. However, the laser energy variations result in three times larger (fractional) charge fluctuations when self-injection is employed. In these simulations, the laser intensity at the injection point $z_{\text{inj}} = 0.8\,\text{mm}$ varies by $-9.54\,\%$, $-4.73\,\%$, $4.69\,\%$ and $9.31\,\%$ from the baseline of $3.65 \times 10^{18}\,\text{W}\,\text{cm}^{-2}$. These intensity variations are comparable to those in the tailored density profile at lower densities, but drive much larger fluctuations. This demonstrates the increased sensitivity of self-injection to laser fluctuations.

The increasing trend of maximum electron beam energy with laser energy is consistent with the increased pulse conditioning which drives stronger wakefields when the laser intensity is higher. While the fluctuations in electron beam energy are five times larger than those measured in simulations with a tailored target, this may be attributed to the higher densities required here, which result in higher acceleration gradients. Thus, these results may not be applicable to the longer targets used in the experiment, in which self-injection is observed at lower densities.

Plateau density fluctuations

The density was varied from the baseline $4 \times 10^{18}\,\text{cm}^{-3}$ according to $\sigma_n = 0.06 \times 10^{18}\,\text{cm}^{-3}$. These fluctuations represent a 3.3 times smaller fraction of the baseline than in the simulations with a tailored target. The resulting effects on the injected charge and maximum electron beam energy are shown as the black crosses in figure 4.17.

The injected charge is observed to increase with density due to the increased availability of particles. The charge deviations from the baseline are found to be larger than those obtained using a tailored density profile for density variations of the same magnitude. This evidences the sensitivity of self-injection to target conditions.

The maximum electron beam energy is observed to vary erratically with plasma density. 2σ fluctuations lead to energy deviations from the baseline that are of the same sign as the density change, which is consistent with the higher accelerating fields achieved at higher densities. However, 1σ fluctuations lead to energy deviations of opposite sign to the density change, which may be attributed to beam-loading or the positional effect discussed in section 4.4.3. These inconsistent results may arise from the random seed that initialises the particles in EPOCH simulations. The sensitivity of the results to this initialisation is further evidence for the lack of stability obtained without plasma density tailoring.

4.5 Discussion

Table 4.1 presents a summary of the fluctuations of electron beam parameters in a target with a tailored density profile as found in the simulations. Note that the values are measured at the same position, not at the dephasing length for each simulation. This was done in order to replicate the effect of the density fluctuations: these would not change the interaction length, which would be set in the experiment for optimum performance at the nominal conditions.

Fluctuating parameter	ΔQ (%)		$\Delta(E_{\max})$ (%)	
	-2σ	$+2\sigma$	-2σ	$+2\sigma$
Laser energy	−11.7	+10.3	−0.8	+0.4
Peak density	−8.7	+6.2	+15.3	−14.0
Plateau and peak densities	−4.2	+2.4	−3.8	+2.8
Down-ramp position	−3.4	+0.6	−2.0	+1.6

Table 4.1: Summary of electron beam fluctuations after 4 ps driven by laser and target fluctuations in a tailored density target.

Fluctuations of laser energy cause the largest differences in the injected charge, while having the lowest impact on the maximum electron beam energy.

Out of the target fluctuations, changes in the peak density independent of the plateau density dominate the variations of both the injected charge and maximum electron beam energy. The dependence of electron beam charge to density found in the simulations agrees with the experimental results of section 4.3, which reveal a strong correlation with peak density and weak correlation with plateau density. The experimental result that the charge is primarily set by the peak density is consistent with the findings that the injection dynamics are very sensitive to the profile of the density down-ramp. Note that while the simulations use a gentle density ramp, the dependence of charge on peak density is also expected for a sharp density transition. In this regime, the injected electrons originate in the high density region [104, 105] and the sudden increase in plasma wavelength means injection is approximated as occurring at a single point. Thus the charge is expected to be linear with peak density. This means that the effect of ramp length fluctuations in the experiment may be hidden in the correlation with peak density. This is explored further in section 4.6.

The experimental results show no correlation of maximum electron beam energy with plateau density, while the increasing trend with peak density contradicts the findings of the simulations. Due to the short propagation length in the simulations, which mainly captured the injection dynamics, the acceleration dynamics beyond 1.2 mm (reaching >

15 mm in the experiment) are not properly reproduced, and therefore disagreement with the experimental electron beam energy measurements is unsurprising. These dynamics are sensitive to the non-linear laser evolution in the plasma channel, as well as the non-uniformities observed in the plasma density profile after the ramp.

Maier *et al.* tested the quality of their data by performing a first-order parametrisation of the electron energy [30]. Their method is followed here to compare the measured and simulated fluctuations. Assuming that the electron beam energy and charge are described by the laser energy, peak density, plateau density and focus shift, the fluctuations in electron beam parameters can be approximated as

$$\Delta Q \approx \frac{\partial Q}{\partial n}\Delta n + \frac{\partial Q}{\partial N}\Delta N + \frac{\partial Q}{\partial z_l}\Delta z_l + \frac{\partial Q}{\partial E_l}\Delta E_l, \tag{4.5}$$

$$\Delta E_{\max} \approx \frac{\partial E}{\partial n}\Delta n + \frac{\partial E}{\partial N}\Delta N + \frac{\partial E}{\partial z_l}\Delta z_l + \frac{\partial E_{max}}{\partial E_l}\Delta E_l. \tag{4.6}$$

By estimating the partial derivatives from linear fits to the simulation results, this gives $\Delta Q = 24\,\%$ (13 % without E_l contribution) and $\Delta E_{\max} = 8\,\%$ for 1σ input fluctuations. These calculations assume the density fluctuations to be consistent (i.e. $\Delta N > 0$ and $\delta n > 0$), while the remaining input variations compound.

The variation of the injected charge observed in the experiment is $> 40\,\%$ at 1σ, while that of maximum energy is 18 %. These fluctuations are significantly larger than those predicted by the simulations.

The simulations used the shot-to-shot fluctuations of density parameters calculated in section 4.2.4, which considered the spread of values for different shots from the mean of the sample. This assumes that the value is known for every shot; however, there is an uncertainty in this value that is disregarded in calculations of the standard deviations. Figure 4.4 depicts the uncertainty on the density profile for a single shot. The uncertainty on n_e is determined by a combination of the noise in the interferometry data, $\sim 6\,\%$. and the z-dependent error on the Abel inversion (section 3.3.3). Averaging over z, these give a total uncertainty $\epsilon_i \sim 10\,\%$ for a single shot i. As the measurement uncertainties are similar to the spread of the values, the standard deviations calculated in section 4.2.4 may be underestimated. This can be quantified by assuming that a measurement is given by $X_i + Y_i$, where Y_i is a random variable from a distribution with standard deviation $\sigma_y = \epsilon_i$. Then, the standard deviation of the sample is $\sigma = \sqrt{\sigma_x^2 + \sigma_y^2}$, where σ_x is the standard deviation of the mean of the sample as calculated in section 4.2.4. Assuming $\sigma_x = \sigma_y$ on average, this results in $\sigma = \sqrt{2}\sigma_x$; i.e. the fluctuations are underestimated by around 40 %. The simulations of $\pm 2\sigma$ should suffice

to account for this underestimation.

The difference between the measured and predicted fluctuations suggests that the charge and maximum energy of the electron beam depend on additional parameters. Maier *et al.* found that the laser direction caused a significant fraction of the electron energy jitter when using ionisation injection [30]. With density transition injection, the laser pointing relative to the angle of the shock has been shown to be important in determining electron beam parameters due to refraction of the laser in a tilted shock [150]. In addition, a change in ramp length of order 10 µm, which is likely correlated with the peak density [153], is known to strongly affect the injected charge [154, 155]. Sensitivity studies of density transition injection to ramp length and angle variations would provide insights to further improve the stability of accelerated electrons. These would require the use of a high magnification interferometry diagnostic in experiment to obtain accurate measurements of the down-ramp.

4.6 Density transition lengths

While the gentle $L \gg \lambda_p$ and sharp $L \lesssim \lambda_p$ density transitions are fundamentally different regimes, as discussed in section 2.6.2, the lack of spatial resolution of the on-shot measured density profiles of centimetre-scale LWFA targets makes it difficult to identify the applicable regime. The thickness of a bow shock is of the order of the molecular mean free path, which is 1.7 µm for helium at $1 \times 10^{18}\,\mathrm{cm}^{-3}$ [101]. This is extended depending on the Mach number of the flow [168], to around 3.6 µm for the nozzle used in the experiment [159]. In contrast, FLASH simulations and high magnification shadowgraphy measurements of a blade-produced shock similar to that used in the experiment provide estimates of the ramp scale length of 50 µm to 60 µm [159]. This suggests the development of an intercepting shock instead [153]. The broad scans of blade position may even span the two regimes.

Further 2D simulations were performed to gain insights into the injection dynamics in ramps with different lengths. The target comprised a pre-ionised plasma peaking at a density $N_0 = 2.82 \times 10^{18}\,\mathrm{cm}^{-3}$ at $z = 0.36\,\mathrm{mm}$ followed by a $\tanh(z/r)$ down-ramp onto a plateau region at density $n_0 = 1.2 \times 10^{18}\,\mathrm{cm}^{-3}$, similar to the baseline simulation in section 4.4.1. The length scale of the down-ramp was varied so that $r = 0.2$ µm, 1 µm, 4 µm, 10 µm, 20 µm, 40 µm and 80 µm, ranging from the sharp to the gentle transition regime, as shown in figure 4.24. Note that r represents around 1/4 of the total effective length scale from N to n. All other simulation parameters were the same as in section 4.4. The vacuum laser focus was set to the middle of the down-ramp, which was different

for every ramp. An additional set of simulations with the vacuum laser focus set to the position of peak density, $f = 0.36\,\text{mm}$, was performed and compared to those with changing focus. The results were almost indistinguishable for $r \leq 20\,\mu\text{m}$ and presented $< 4\,\%$ differences for $r > 20\,\mu\text{m}$, revealing that the injection and acceleration dynamics are dominated by the density structure and not by variations in laser evolution. The analysis was restricted to the first period of the wakefield, and injection in this region was observed for all ramp lengths studied.

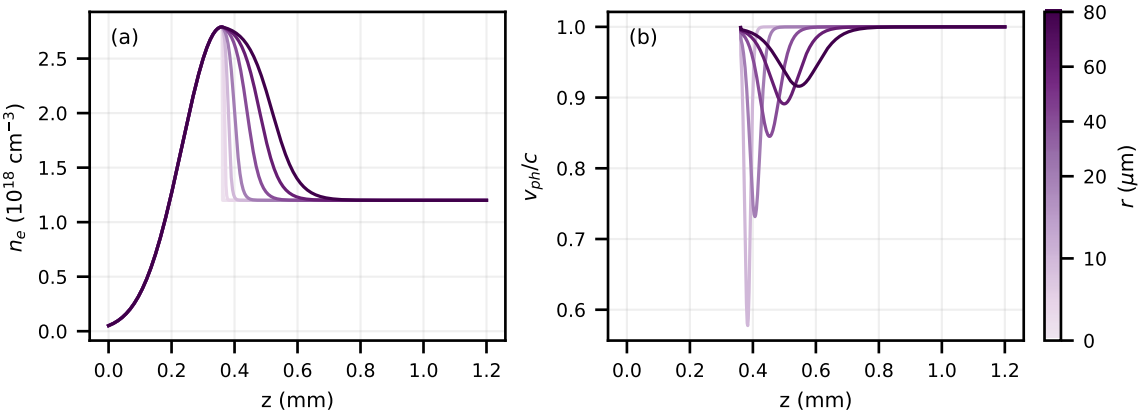

Figure 4.24: (a) Density profiles used for the simulations to study ramp length variations. (b) Analytic evolution of the wakefield phase velocity at the back of the bubble; the superluminal velocities reached in the rising edge are not shown.

The injected charge and maximum electron beam energies for the different simulations are presented in figure 4.25. The simulated plasma conditions form a wakefield with $\lambda_p = 30\,\mu\text{m}$ Therefore, ramps with $r = 0.2\,\mu\text{m},\ 1\,\mu\text{m},\ 4\,\mu\text{m}$ and $10\,\mu\text{m}$ correspond to the sharp regime. This regime change is evident in figure 4.25(a), where results for $r \leq 10\,\mu\text{m}$ follow different trends, suggesting that the injection mechanisms are fundamentally different in gentle and sharp density ramps. This contradicts 3D simulations by Samant *et al.*, which found that electron beam parameters, including charge and energy, vary monotonically with ramp length scale regardless of the regime [154].

4.6.1 Long density ramps

For $r \geq 20\,\mu\text{m}$, the injected charge decreases linearly with ramp length, while the maximum energy increases. The reduction in injected charge can be attributed to the phase velocity decrease of the wakefield in the ramp, shown in figure 4.24(b). In a gentle density ramp, v_p depends on $\zeta/n_e \times \mathrm{d}n_e/\mathrm{d}z_0$ as per (2.100). A longer ramp corresponds to a smaller density gradient, leading to a more gentle decrease of v_p and a higher

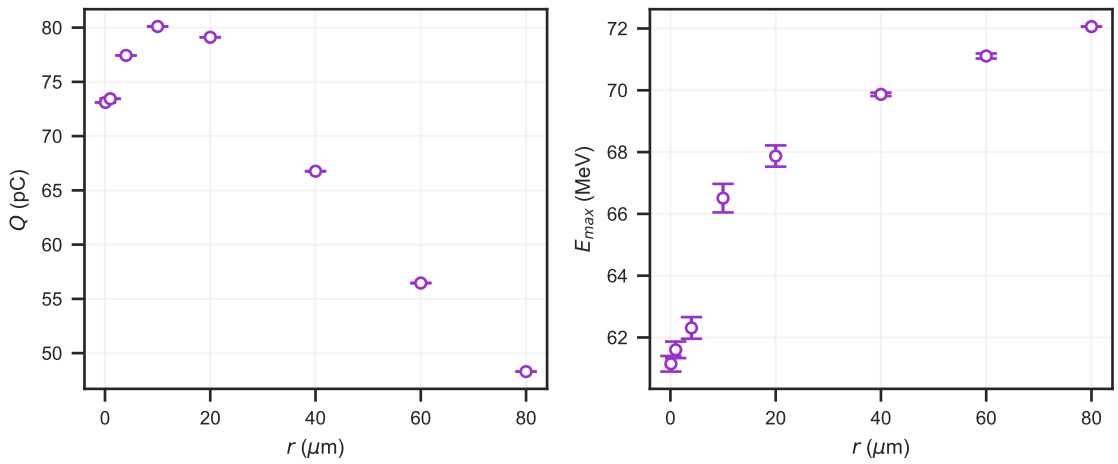

Figure 4.25: Results from the simulations of a ramp length scale parameter scan after 4 ps. (a) Injected charge. (b) Maximum electron beam energy.

minimum v_p. Therefore, fewer electrons satisfy the injection condition $v_e > v_p$. This is consistent with previous numerical studies [154–157].

The maximum energy of the electron beam increases with ramp length for both $r \lesssim \lambda_p$ and $r > \lambda_p$, as observed previously [154,155]. Injection occurs later for longer ramps, in line with the slower decrease of the wakefield phase velocity shown in figure 4.24(b). Acceleration in the remainder of the ramp occurs with higher fields due to the higher densities. However, this only partially compensates for the decrease in acceleration length, as the energies reached at the end of the ramp are still lower than for electrons injected with $r = 20\,\mu\text{m}$ at the same propagation distance. The different rates of energy gain in the plateau imply that the accelerating fields are stronger in targets with longer down-ramps, despite the constant plateau density. This suggests that the accelerating fields are diminished more strongly for targets with shorter ramps due to beam loading by the higher injected charge. The electron beam energies diverge as the propagation distance is extended (prior to dephasing).

4.6.2 Sharp density transitions

In contrast to long-scale density ramps, the injected charge is found to increase with ramp length in sharp density transitions in figure 4.25(a). This trend was also observed in supplementary 2D simulations with a constant high density and in 1D simulations. In the very sharp limit, $r \to 0$, the injected charge is expected to be determined solely by the availability of electrons in the high density region, as this determines the electron density peak that develops at $\zeta = -\lambda_{p1}$ (section 2.6.2). Such a constant trapped charge

for density transitions with lengths between 0 and $1/k_{p1}$ was found in numerical studies of particle-driven wakefields at densities $\sim 10^{13}\,\mathrm{cm}^{-3}$ [104]. However, simulations of laser-driven wakefield acceleration have presented different results. Brantov *et al.* observed a factor of two decrease in the injected charge between a density step and a ramp with length $0.6\lambda_p$ [102]; this took into account multiple periods of the wakefield. Samant *et al.* observed a monotonically decreasing injected charge for ramp lengths between 1 µm and 100 µm, with an 8 % decrease in charge from a ramp length of $0.04\lambda_p$ to $0.4\lambda_p$ [154]; this was restricted to the first wakefield period.

The present simulations model density transitions that occur over lengths that are not infinitesimally small. Figure 4.26 shows the $z - p_z$ electron spectrum for the $r = 1\,\mu\mathrm{m}$ and 10 µm simulation around 300 fs after injection. The spectra depict a localised bunch with large energy spread at the front (red), followed by low energy electrons in an extended region (blue). This extended injection region is observed to be similar for $r = 1\,\mu\mathrm{m}$ and 10 µm, suggesting its length is independent of the density transition length.

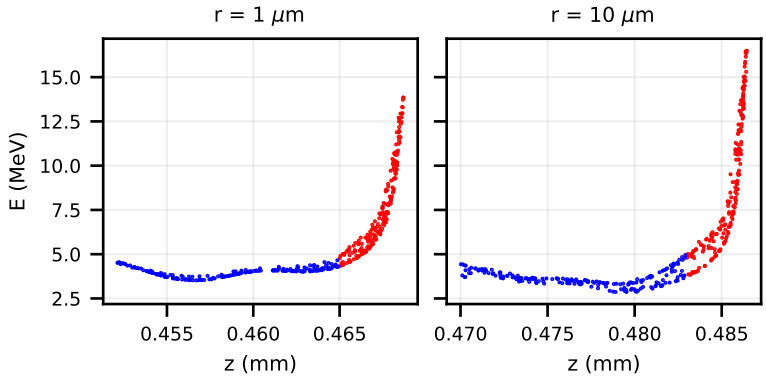

Figure 4.26: Longitudinal electron beam energy and position distribution during injection in (a) $r = 1\,\mu\mathrm{m}$ ramp and (b) $r = 10\,\mu\mathrm{m}$ ramp. Two electron distributions are identified as the leading (red) and trailing (blue) particles.

Particle tracking was performed in supplementary simulations with a constant high density and transitions centred at $z_r = 200\,\mu\mathrm{m}$ for $r = 1\,\mu\mathrm{m}$ and 10 µm. Two sets of particles were tracked. The results are shown in figure 4.27; the colours are consistent with figure 4.26. As the wakefield is non-linear, the oscillations are not coherent and electrons oscillate at a range of frequencies around ω_p. This means that electrons originating in a range of positions can end up in the same $\zeta = -\lambda_{p1}$ at a given time. The electrons that inject in the $r = 10\,\mu\mathrm{m}$ transition originate at earlier z than those which inject in the $r = 1\,\mu\mathrm{m}$ transition. This is because the longer transition begins earlier, meaning that electrons must have reached $\zeta = -\lambda_{p1}$ at an earlier time. Similarly, the

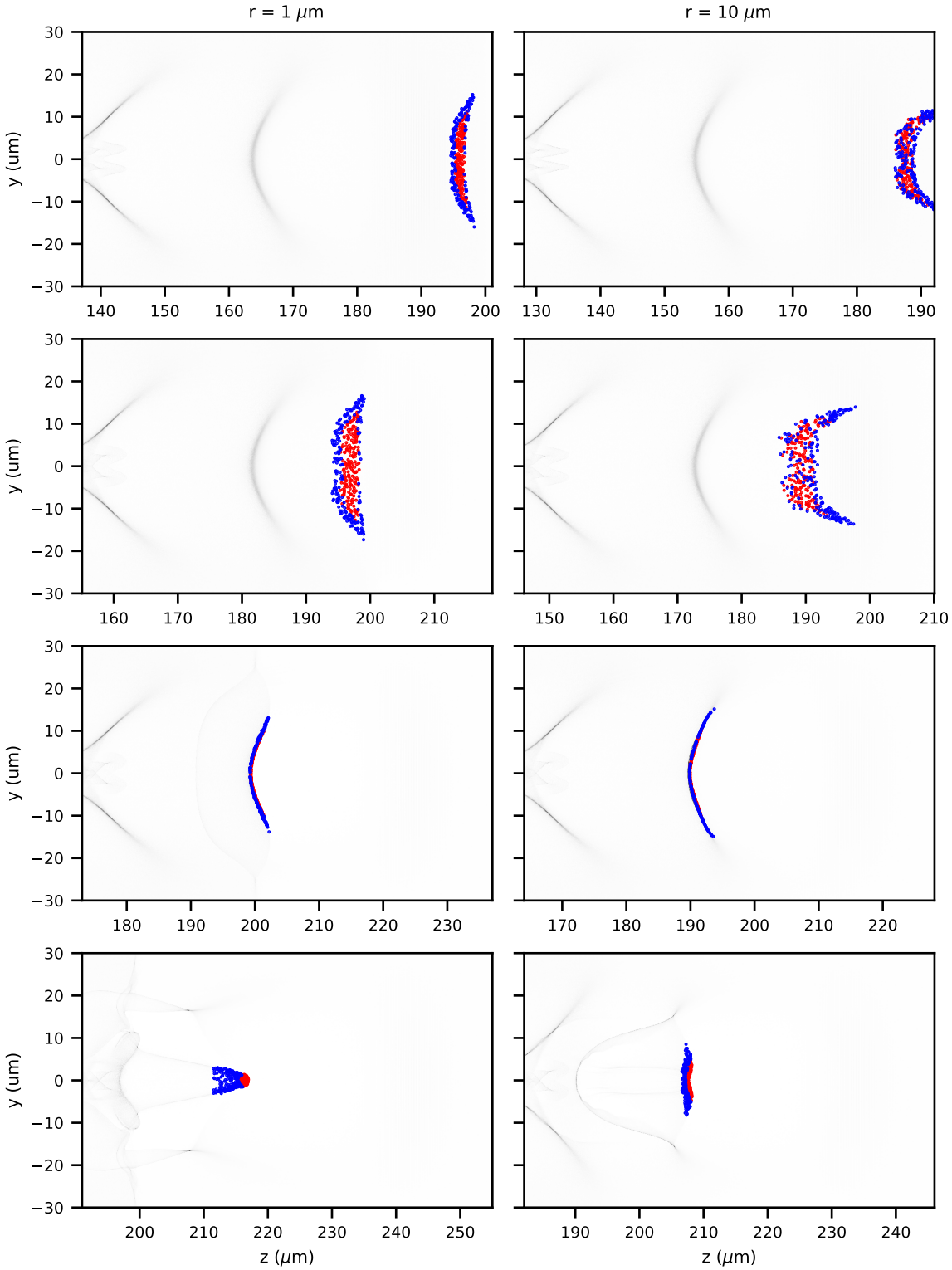

Figure 4.27: Electron density distribution showing the wakefield (greyscale) and two sets of 100 tracked pseudoparticles (red and blue) for the $r = 1\,\mu\text{m}$ simulation (left) and $r = 10\,\mu\text{m}$ simulation (right). Time progresses downwards and the frames are 30 fs apart.

injection process continues for a longer time for $r = 10\,\mu\text{m}$. This can be observed in the bottom row of figure 4.27, where the electrons in the right panel have not been fully focused and accelerated as in the left panel.

The electrons that inject are those which reach $\zeta = -\lambda_{p1}$ within the density transition, as shown in the third row of figure 4.27. The first row indicates that the longitudinal region in space in which the electrons that inject originate is larger for the $r = 10\,\mu\text{m}$ compared to the $r = 1\,\mu\text{m}$ target. This indicates that the initial conditions in six-dimensional phase space for electrons to inject are increasingly restrictive as $r \to 0$, causing a decrease in injected charge for shorter transitions. Moreover, the leading and trailing electrons appear to come from two distinct distributions in the $r = 1\,\mu\text{m}$ case. Because the position of the density transition is less well defined when $r = 10\,\mu\text{m}$, the injection is more complicated and electrons originating in very similar positions can end up in very different regions of phase space after injection. However, the two distributions are very clearly defined in the bottom right panel.

In both cases, the electrons that originate farthest from the laser axis and later in the plasma end up in the trailing bunch. This suggests that transverse effects are an important contribution to the injection dynamics.

Summary

- The particle tracking evidences differences in the injection dynamics even within the regime of sharp density transitions.
- Transverse injection is more significant in sharp ramps with longer length scales.

4.6.3 Electron beam energy spread

The electron $z - p_z$ distribution and accelerating fields for three representative simulations are shown in figure 4.28 after 4 ps. In all scenarios, the injected electron beam begins with a negative chirp. The energy spreads of the electron beams decrease with propagation distance due to phase space rotation as the rear electrons experience higher accelerating fields than the front. This effect has previously been relied on to obtain low energy spread electron beams from density ramp injection [28, 169], though using further density tailoring instead of the beam-loading occurring here.

The energy spread is largest when $4r \sim \lambda_p$ and decreases for shorter and longer ramps. This indicates a correlation of energy spread with injected charge, as previously highlighted [154]. While this suggests that longer ramps are preferred in terms of beam quality, two limitations can be noted. First, the decrease in charge may not be suitable

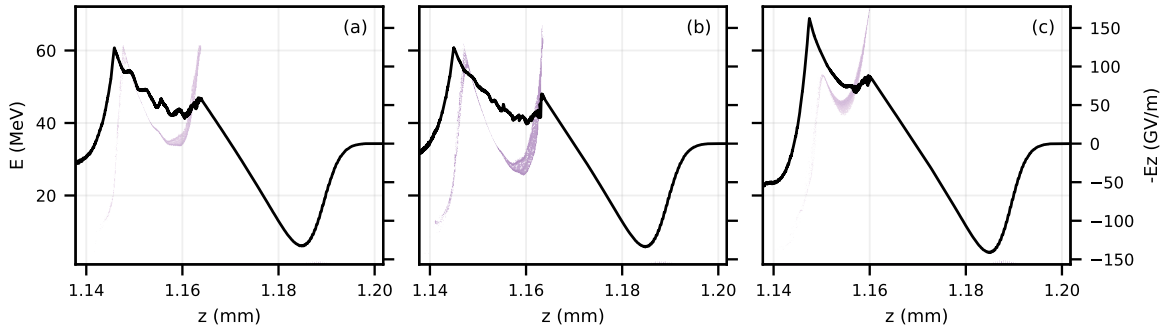

Figure 4.28: Longitudinal electron beam energy and position distribution (violet) and accelerating fields (black line) after 4 ps for three representative simulations: (a) $r = 1\,\mu\text{m}$, (b) $r = 10\,\mu\text{m}$, (c) $r = 60\,\mu\text{m}$.

for some applications, and there must be a limit for the density gradient which allows injection. This limit warrants further investigation. Secondly, the present study is restricted to the first wakefield period, but injection in subsequent periods is expected in gentle ramps [102]. This should result in more complex electron energy spectra, which may reverse any increase in spectral quality achieved through a gentler ramp.

4.6.4 Laser intensity effect

The vacuum laser intensity was reduced to $1 \times 10^{19}\,\text{W cm}^{-2}$ ($a_0 = 2.15$) and $5 \times 10^{18}\,\text{W cm}^{-2}$ ($a_0 = 1.52$) to study its effect on the injection dynamics. Three representative simulations were run with $r = 1\,\mu\text{m}$, $10\,\mu\text{m}$ and $60\,\mu\text{m}$. Due to the decreased non-linear plasma wavelength at these lower a_0, the second wakefield period was observed in the simulations, despite keeping the window size constant.

At the lowest intensity, injection is observed only in the second wakefield period for $r = 10\,\mu\text{m}$ and in neither the first or second periods for $r = 60\,\mu\text{m}$. Injection is also not observed in the $r = 60\,\mu\text{m}$ ramp at $1 \times 10^{19}\,\text{W cm}^{-2}$. In gentle density inhomogeneities, v_p decreases with time at a given z, meaning that injection becomes easier at farther periods behind the wakefield. Injection in subsequent wakefield buckets is an important consideration for experiments with low a_0. This will have physical limitations that need to be studied in further simulations.

Sharp density transitions

Figure 4.29 shows the longitudinal electron energy spectra and accelerating fields for the three laser intensities in the simulation with $r = 1\,\mu\text{m}$. The injected charge increases with increasing laser intensity. This can be attributed to the stronger, more non-linear

density spike at $\zeta = -\lambda_p$ that develops at higher a_0. The laser-driven wakefield is also stronger at higher intensities.

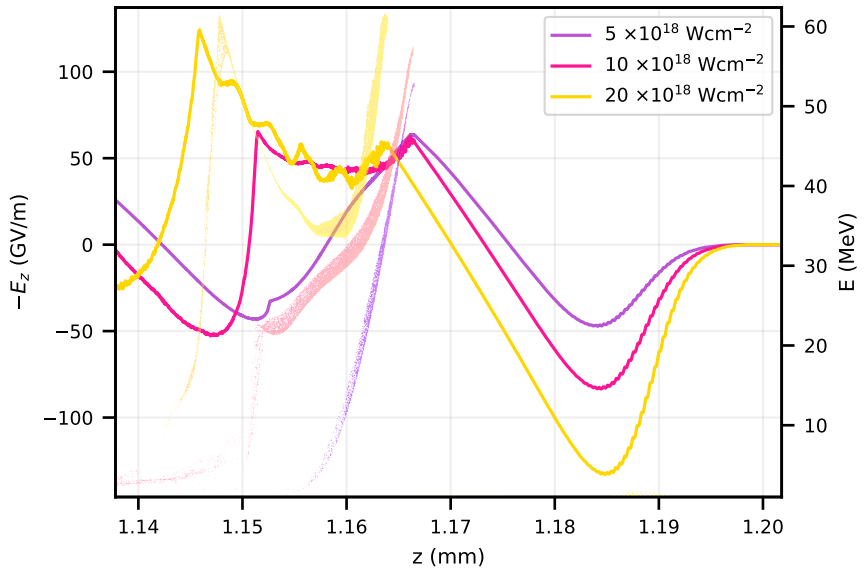

Figure 4.29: Accelerating fields (solid lines) and electron distributions in $z - p_z$ space (colour maps) for simulations with $r = 1\,\mu\text{m}$ ramp and varying laser intensity after 4 ps. The colours represent the laser intensity.

The energy spread of the electron beam decreases with increasing intensity, which can be attributed to the acceleration dynamics as depicted by the accelerating fields. These are affected by the changes in injected charge and wakefield strength, which cause differences in the beam-loading. At the lowest intensity (violet), the accelerating fields are higher for the leading electrons but decelerating at the rear of the beam. Such a structure is unsuitable for obtaining high quality electron beams as it worsens the negative chirp of the electron beam. At $1 \times 10^{19}\,\text{W cm}^{-2}$ (pink), the accelerating fields are similar for the entire electron beam, suggesting that the energy spread would remain similar throughout the interaction. The wakefield driven by the highest intensity laser (yellow) provides the most significant phase space rotation due to the high accelerating fields for the trailing electrons. This type of wakefield structure effectively reduces the energy spread of the electron beam for short propagation distances, but there is a limit to this as the electrons at the back will later reach higher energies than those at the front. This was also observed in 3D simulations in ref. [154].

The results suggest that driving a weakly non-linear wake in a target with a sharp density transition may not be desirable, as the beam-loading caused by the very sudden injection dominates over the laser-driven wakefield and counteracts the benefits of having highly localised injection.

Gentle density ramps

By changing the laser intensity, the strength of the non-linear wakefield can be controlled, which determines the velocity that can be reached by the electrons. Since injection occurs when the electron velocity exceeds the phase velocity of the wake, increasing the laser intensity causes a reduction in how much the wake needs to slow down in the ramp for injection to occur.

Figure 4.30(a) depicts the variation of the wakefield phase velocity at the back of the first period, $\zeta = -\lambda_p$ caused by density down-ramps with lengths $r > 10\,\mu\text{m}$, as calculated from (2.100). The minimum v_p increases logarithmically with r, while the position of minimum v_p relative to z_r increases linearly with r with a slope of 0.21. This change is small compared to the length scale of the ramp. For a given laser intensity, the maximum electron oscillation velocity is a function of the laser strength parameter $v_e = v_e(a_0)$. The injection threshold, $v_e > v_p$, can be represented by a given contour of figure 4.30(a), and the injection region corresponds to the distance in z enclosed by the contour at the relevant r. It can be seen that the injection region for a given laser intensity is not a monotonic function of r. Both shorter and longer ramps enable a narrower injection region; however, shorter ramps allow higher injected charge due to the lower minimum v_p reached.

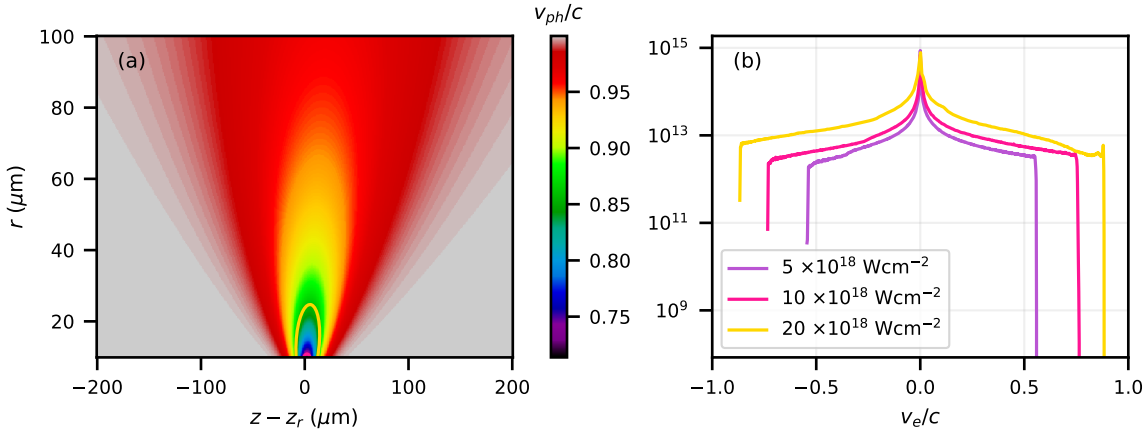

Figure 4.30: (a) Variation of the wakefield phase velocity in a $\tanh(z - z_r)/r$ density down-ramp for different ramp lengths. The contours (solid lines) correspond to the v_e measured in simulations. (b) Longitudinal electron velocity distribution at the position of peak density in simulations for three different laser intensities represented by the colour.

Figure 4.30(b) depicts the longitudinal electron momentum distribution at the position of peak density, $z = 0.36\,\text{mm}$, for the three simulated laser intensities. The dis-

tributions are characterised by velocities $v_e = 0.53c$, $0.73c$ and $0.86c$ (99th percentile) for increasing intensity, respectively. These are displayed as contours in 4.30(a). The contours suggest that v_p reaches $0.86c$ only for $r \lesssim 30\,\mu\text{m}$ and no injection in the first wakefield period should occur for longer ramps. In contrast, injection in the first period is observed in simulations up to $r = 80\,\mu\text{m}$.

The depicted variation of the wakefield v_p in figure 4.30(a) considers only the density inhomogeneity effect; however, laser evolution causes additional decreases in the phase velocity, as discussed in section 2.6.1. For $a_0 > 1$, the contribution of the laser evolution the wakefield phase velocity is given by (2.97). Then, taking the non-linear plasma wavelength $\lambda_{Np} = 2\pi c\sqrt{\gamma}/\omega_p$, the phase velocity decrease at the back of the first period, $\zeta_p = -\lambda_{Np}$, can be approximated as

$$\delta\beta_p \approx -\frac{2\pi}{\omega_p}\left(1 + \frac{a_0^2}{2}\right)^{-\frac{1}{2}} \frac{\partial a_0}{\partial t}\,. \tag{4.7}$$

Taking a_0 and $\partial a_0/\partial t$ from the simulations, the resulting deviations in wakefield phase velocity are shown in figure 4.31 for $r \geq 20\,\mu\text{m}$. The laser evolution is observed to cause small reductions in v_p, which are not sufficient to satisfy the injection condition for long density ramps.

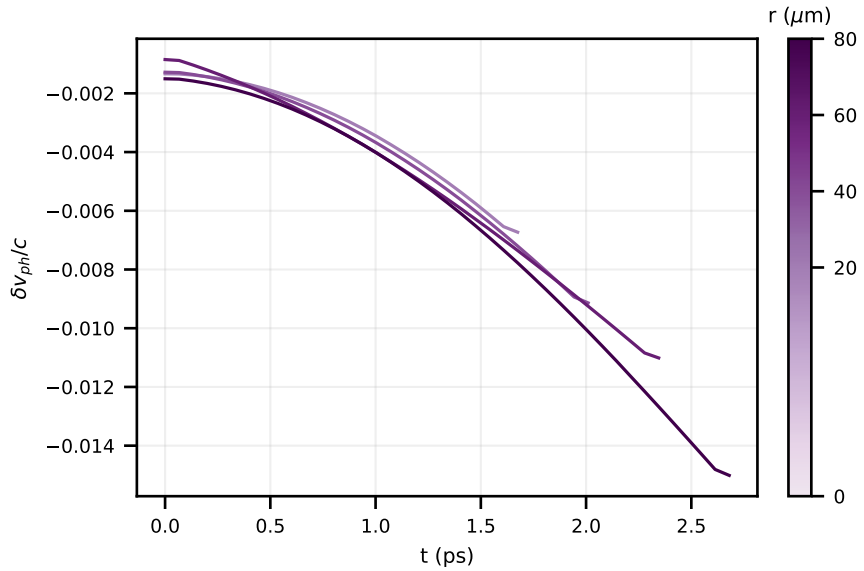

Figure 4.31: Variation of the wakefield phase velocity due to laser evolution effects, calculated from (4.7) using the simulation results, between the beginning of the simulation and the end of the density ramp.

The observed injection cannot be fully explained by the density ramp injection or

by laser evolution effects, both of which arise from one dimensional theory. A 1D simulation with $r = 60\,\mu\text{m}$ was run to assess whether two dimensional effects may be driving injection. The simulations show that a negligible charge of the order of $\text{fC}\,\mu\text{m}^{-2}$ was accelerated to 90 MeV. The results suggest that two dimensional effects, which are not captured by density transition injection theory, have a significant effect in the simulated non-linear regime. This transverse injection will require further investigation.

Summary

- In sharp density transitions, decreasing the laser intensity reduces the wakefield amplitude, while the injected charge remains high.
- This means that beam-loading is more significant at lower laser intensities, which worsens the phase space distribution of the accelerated electrons.
- The 1D model of injection in gentle density ramps is inconsistent with the simulation results, as it predicts injection only in ramp lengths shorter than $r = 30\,\mu\text{m}$. In contrast, the simulations show injection in ramps with r up to $80\,\mu\text{m}$.
- This inconsistency cannot be resolved by accounting for laser evolution, which suggests that transverse effects are significant for density ramp injection.
- The transverse injection taking place in both sharp and long scale regimes indicates variations in the electron beam emittance, which may be controlled and optimised for applications. This requires further investigation.

4.7 Conclusions

The results show that the electron charge and maximum energy are very sensitive to variations in $n_e^{-1}\mathrm{d}n_e/\mathrm{d}z$, which cause changes in the injection dynamics. These variations are found to occur when the peak and plateau densities are changed independently, as would be caused by fluctuations of the blade position in the gas target. Fluctuations in the ramp steepness would exacerbate this effect. In contrast, fluctuations of the target backing pressure have a smaller impact on the electron fluctuations, as they keep the down-ramp, and therefore the injection dynamics, consistent.

This strongly indicates that the fluctuations observed in the experimental data are more likely a result of a fluctuating blade rather than a variation in gas pressure. In addition to a more rigid obstruction to generate the down-ramp, the simulations suggest that focusing the laser before the density structure will likely reduce the fluctuations

observed in the electron beams generated. The results presented will enable future experimental campaigns to be designed to improve the stability of the accelerated electrons through target design and laser focal position. This should allow the effect of other variations (e.g. due to transverse effects) to be more clearly observed. The observation of transverse injection in simulations suggests that these $>$ 1D effects are very influential. Such a systematic approach to improved stability of LWFA electron beams presents a path to the stable electron beams required for future applications in particle physics, medicine and XFEL applications.

Chapter 5

Evolution of a wakefield acceleration laser driver

Determining the evolution of the laser is of vital importance to understand LWFA. The high intensity laser pulse is the driving force of the accelerated electrons, and the energy between them is coupled through the electron plasma wave. While the laser pulse affects the properties of the medium as it propagates, the laser itself is also modified during its interaction with the plasma wave. By characterising the laser pulse driving the acceleration, information about the acceleration dynamics can be obtained without needing to disturb the high-energy electron bunch. This has the potential to act as a diagnostic tool for the ultra-fast dynamics of laser-plasma interactions.

Many thorough studies of laser evolution have taken place at experimental conditions below the self-injection threshold in gas jets [134, 170, 171] and capillary waveguides [172–174]. These provide insights into the energy transfer of the laser to the plasma, which gives indirect information about the strength of the wakefields driven. However, the energy gain of electrons will depend on their injection position and phase, as illustrated in chapter 4. Therefore, it is important to investigate the laser evolution while driving electron injection and acceleration. More recent studies with ionisation injection have looked at the efficiency of laser energy transfer to electron acceleration through spectral measurements at different densities and acceleration lengths [175]. Spectral modifications of the laser driver have demonstrated redshifts up to the mid-IR [176], but the optimal conditions for electron acceleration and for laser spectrum extension have been found to differ [177]. Spectrum extension occurs along with pulse compression to few femtosecond durations [178,179] and a positive chirp for short propagation distances at low density [134].

In addition to temporal and spectral modifications, which result from the longitu-

dinal structure of the interaction, the laser pulse can evolve transversely in the plasma. Guiding of short pulses by the wakefield bubble [87] occurs over a length consistent with pump depletion [88]. The effect of self-focusing on ionisation injection has been studied extensively as a means of enhancing electron beam quality by preventing continuous injection. By relying on non-linear effects to reach high laser intensities, ionisation can become localised and peaked beams can be obtained [116,180]. Alternatively, the use of highly evolving laser pulses can suppress injection due to the non-linear evolution of the wakefield bubble, leading to low energy spread beams through self-truncated ionisation injection [117–119]. In tailored density profiles [111, 115], longitudinal laser variations have been highlighted as having a large effect on electron beam parameters [181, 182]. This is attributed to variations in the initial conditions leading to changes of the peak laser a_0, but detailed investigations into the effect of laser evolution throughout the interaction are still needed.

This chapter presents a detailed study of the transmitted optical spectra of a laser that drives wakefield acceleration in a tailored target using ionisation injection. Experimental measurements reveal correlations of post-interaction laser parameters with plasma conditions and electron beam characteristics. These are supported by extensive particle-in-cell simulations of the longitudinal and transverse laser evolution, which give insight into the observed electron beam parameters.

5.1 Experimental setup

An experiment was conducted at the Lund Laser Centre to study laser-plasma coupling in a laser-plasma injector as targeted by the EuPRAXIA project. The experimental setup is shown in figure 5.1. The laser delivered on average 740 mJ to the target in a 42 fs FWHM pulse duration with a central wavelength of 800 nm. An $f/20$ off-axis parabolic mirror focused the beam to a 12 µm (FWHM) focal spot in a custom-built gas cell target, achieving a peak intensity of $9.8 \times 10^{18}\,\mathrm{W\,cm^{-2}}$ ($a_0 = 2.15$). The target consisted of the electron injector for compact staged high energy accelerator (ELISA), which produced a tailored plasma density [183]. By varying the aperture and length of the entrance and exit cell facings, the plasma profile could be further modified. A density plateau is obtained in the inner part of the cell, surrounded by sharp gradients at the entrance and exit holes. At either side of these, smooth gradients inside the entrance and exit plates complete the transition to vacuum. The density profile used for the data in this thesis is shown in figure 5.1(b). The influence of changing the plates to vary the density tailoring on the accelerated electrons is discussed in ref. [182]. The

gas cell was filled with a gas mixture of 99.75 % hydrogen doped with 0.25 % nitrogen, following optimisation of the dopant concentration among 1 %, 0.5 % and 0.25 % during the experimental campaign. The entrance and exit plates were replaced weekly after sustaining $\sim$ 500 shots; there was evidence of laser ablation as the size of the holes increased. The requirements for EuPRAXIA mean that the targets should be able to sustain hundreds of thousands of shots at the nominal 20 Hz to 100 Hz repetition rate [49]. Therefore, further development of these gas cells is needed for their utility in practical machines.

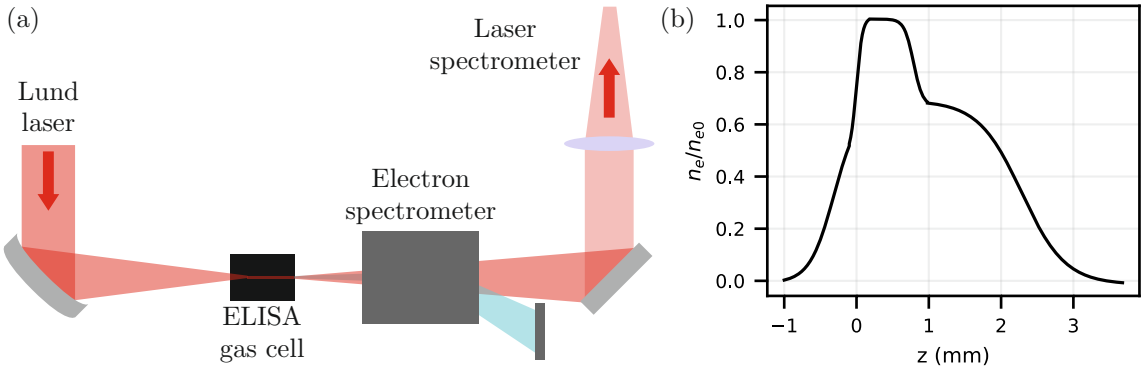

Figure 5.1: (a) Schematic diagram of the experimental setup. (b) Normalised density profile in the ELISA gas cell [182].

The accelerated electrons were measured using an electron spectrometer, which consisted of a dipole magnet of 0.83 T extending over 20 cm and a Lanex screen imaged by a 16 bit camera. The images were calibrated to give values of charge and detected electrons with energies between 11.3 MeV and 300 MeV. The analysis of the electron spectrometer images were performed by L. Dickson and are described in ref. [182, 184].

5.2 Post-interaction laser spectrum

The laser transmitted through the target was collected by a $f = 500$ mm lens and focused onto a spectrometer to analyse the post-interaction laser spectrum. The spectrometer (ORIEL MS257) used a grating with 300 lines per mm and a blaze of 475 nm to measure light between 650 nm and 900 nm and was calibrated using interference filters and a HgAr lamp. The data collection and calibration was performed by the team in ref. [182]. The laser transmission through vacuum is shown in grey in figure 5.2. The median laser wavelength is 800 nm and 96 % of the energy is found between $\lambda_0^{\text{min}} = 777$ nm and $\lambda_0^{\text{max}} = 831$ nm.

5.2.1 Pressure scan

The target density was modified by varying the pressure in the gas cell between 150 mbar and 210 mbar. This caused the density profile shown in figure 5.1(b) to be rescaled. While an online density diagnostic was unavailable for this experiment, the electron density in the ELISA gas cell was measured to vary linearly with pressure [185] in the follow-up experiment (section 5.5). Based on the offline measurement for this experiment of $n_{e0} \approx 7 \times 10^{18}\,\mathrm{cm}^{-3}$ at 182 mbar [182] and the linear trend from the pressure scan [185], n_{e0} varied from $5.7 \times 10^{18}\,\mathrm{cm}^{-3}$ to $8.2 \times 10^{18}\,\mathrm{cm}^{-3}$. This corresponds to plasma wavelengths between 15 µm and 19 µm, compared to the laser pulse length of 13 µm FWHM.

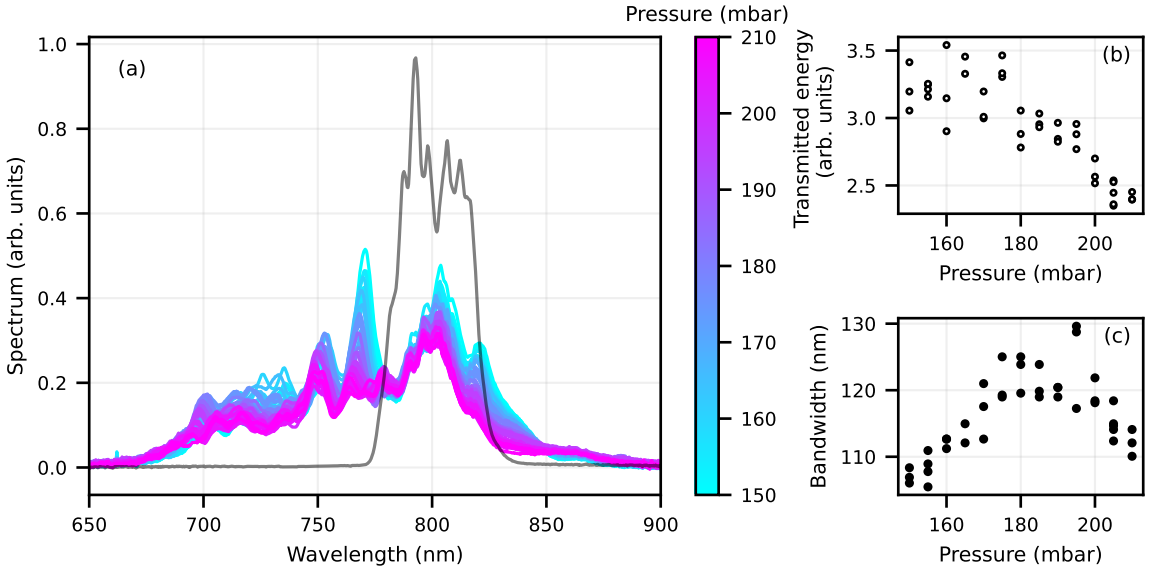

Figure 5.2: Post-interaction laser spectra; the colour bar represents the pressure in the gas cell. The spectra through vacuum is overlaid in grey; the line represents 10 shots.

Transmitted laser energy

Figure 5.2 shows the post-interaction laser spectra through the target under different cell pressures. While the overall shape of the spectra remains similar, the amplitude of the spectra decreases with increasing target density. In line with this, the laser energy transmitted through the plasma, which is given by the integrated spectra over the observed wavelength range, decreases with increasing target density as shown in figure 5.2(b). This indicates that the laser pulse is depleted more strongly at higher densities, in line with previous measurements [179]. Pump depletion at the front of the laser occurs at rate given by the pulse front etching velocity [76] $v_{\mathrm{etch}} = c\omega_p^2/\omega_0^2 \propto n_e$,

indicating that the laser energy from the front of the laser is absorbed into the plasma more quickly at higher densities, in line with observations.

As the energy from the etched region of the laser is transferred to the plasma, the laser energy loss can be calculated from v_{etch}. The extension of the etched region for the entire interaction can be estimated as $L_{\text{etch}} \approx v_{\text{etch}} t_{\text{int}} \approx v_{\text{etch}} z_{\text{int}}/c$, where t_{int} and z_{int} are the interaction time and length, respectively. From the target profile in figure 5.1(b), $z_{\text{int}} \approx 4\,\text{mm}$ is taken. Then, taking the average density over the interaction length as $0.45 n_{e0}$, it is found that L_{etch} ranges between $0.25 L_{\text{FWHM}}$ and $0.37 L_{\text{FWHM}}$, depending on n. This suggests that around 1/3 of the laser energy is absorbed into the plasma.

Spectral shifts

The spectra depict a reduced signal in the vacuum range, between λ_0^{min} and λ_0^{max}, with evidence of blueshifting. The spectra show $< 10\,\%$ of the laser energy above λ_0^{max}, which comprises very minimal, albeit non-negligible redshifting. However, a LWFA driver must lose energy to the plasma in driving a wakefield, which occurs via photon deceleration (section 2.5.1). The generation of a wakefield in these shots can be confirmed by the occurrence of electron beams with energies reaching 100 MeV to 200 MeV. This suggests that the strongly redshifted light that must be present was not collected by the spectrometer. Previous measurements of laser redshift have mainly been restricted to small shifts under 50 nm [134, 171, 172, 174, 179] for propagation lengths in the few millimetre scale. While stronger redshifts extending to the mid-infrared have also been measured, these used spectrometers sensitive to light above 1 µm [176] or 4 µm [177]. Streeter *et al.* measured transmitted laser spectra in the ranges 350 nm to 840 nm and 900 nm to 1700 nm and interpolated very weak signals between 840 nm and 900 nm, similar to the data in figure 5.2(a). Therefore, the weak redshift present in this data is not inconsistent with previous measurements. Instead, the expected strong redshifts likely lie outside the detector range, $\lambda > 900\,\text{nm}$. This is corroborated in the simulations of section 5.3, and encourages the use of spectrometers sensitive to these longer wavelengths in future experiments.

While the energy loss of the front of the laser pulse manifests itself as a strong redshifted signal, some of this energy can be re-gained by a laser component λ_p behind the driver [80] due to the opposite density gradient in this region. Due to the density dependence of the plasma wavelength, the fraction of the laser pulse in the region that causes photon acceleration increases at higher densities. At the same time, the stronger wakefield generated at higher densities causes stronger frequency shifts. Blueshift measurements like this have been extensively documented [170, 186–188], even with effective

electron acceleration [171] as in this experiment.

The blueshifted side of the spectrum appears to reach lower wavelengths at higher densities, albeit at lower intensities. This is consistent with previous results [170]. In addition, the main features in the spectra appear to shift to shorter wavelengths at increasing densities. The peak at around 770 nm stands out as it has a strong linear amplitude and position dependence on the cell pressure, as shown in figure 5.3.

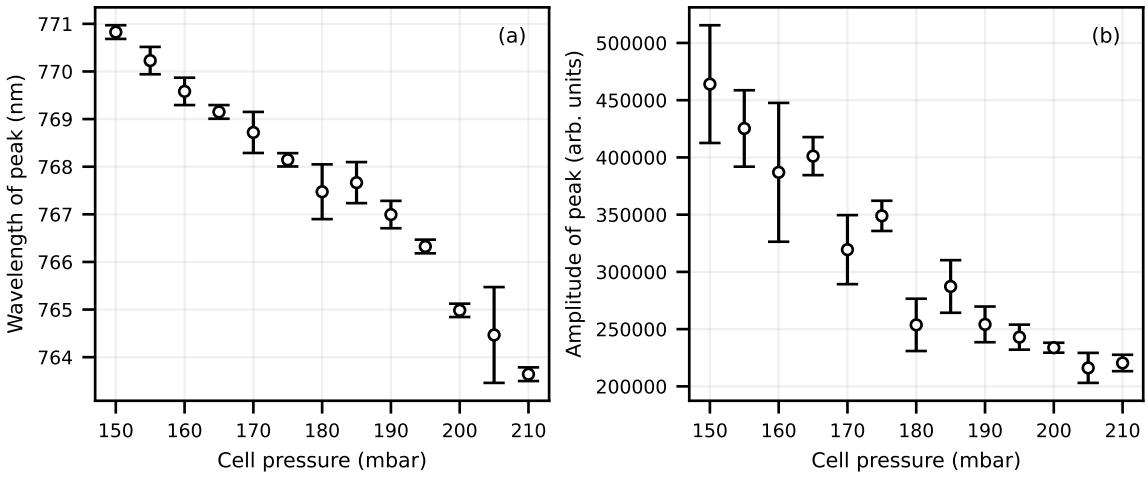

Figure 5.3: (a) Wavelength and (b) amplitude of one of the peaks in the transmitted spectrum as a function of gas cell pressure. Each point corresponds to the average of three to five shots at the same pressure and the error bars denote their range.

Peaks in the spectra are often attributed to stimulated Raman scattering in the literature [170]. This would mean that the peaks are separated by ω_p. Assuming that this is the source of the pressure-dependent wavelength of the peak shown in figure 5.3, the wavelength spacing of this peak relative to that at 800 nm should provide an estimate of the plasma density as

$$n_e = \frac{(\Delta\omega)^2 \gamma m_e \epsilon_0}{e^2} \,. \tag{5.1}$$

The results are shown in figure 5.4.

A linear trend of density with cell pressure is recovered, in line with interferometry [185] and wavefront sensor [184] measurements from the follow-up experiment. These measurements were made and analysed by F. Filippi and L. Dickson, respectively. The results obtained from the analysis of the transmitted spectra are lower than the interferometry measurements. However, the setup of the probe beam meant that the interferometry measured the high density plateau region only. As the laser propagates through the entire density profile, the density values obtained from the spectrum pro-

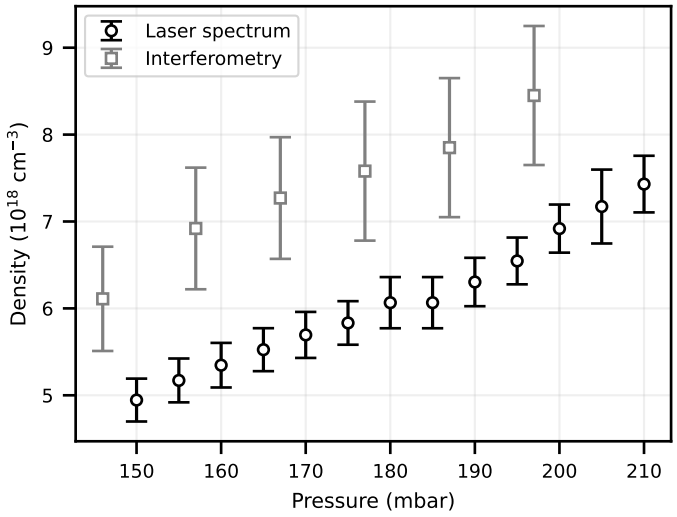

Figure 5.4: Plasma density as a function of cell pressure as calculated from the peaks in the laser spectrum (black circles). The results from interferometry measurements [185] are shown for comparison (grey squares).

vide a measure of the effective plasma density throughout the interaction. The plateau that is observed between 180 mbar and 185 mbar requires further investigation. This shows that post-interaction laser spectral data can provide information about the target, which may be used as an easy and non-invasive density stability diagnostic in future experiments.

5.2.2 Focus scan

The vacuum focus position of the laser was varied to investigate laser-plasma coupling. This has been highlighted as a very important parameter in experiments of ionisation injection with a tailored gas cell [182,183]. The zero position is defined at the beginning of the high density plateau region, as shown in figure 5.1(b). This was measured relative to the gas cell. The gas cell had an entrance hole of diameter 400 µm, meaning that the laser could pass through without significant interruption even when focused at $z = 1$ mm.

The post-interaction laser spectra for a focus scan is shown in figure 5.5(a). The results shown were taken at a gas cell pressure of 182 mbar, which corresponds to a plasma density with peak $n_{e0} \simeq 7 \times 10^{18}$ cm^{-3}, measured offline using Mach-Zehnder interferometry. The results at different plasma densities and initial laser temporal and spectral shapes follow similar trends. The shape of the spectrum changes significantly when the laser focus is moved, showing the difference in laser-plasma coupling. The

component of the spectra within the vacuum wavelength range, $\lambda_0^{\min}$ to $\lambda_0^{\max}$, represents the part of the laser that is unaffected by the plasma wave, meaning that it is not guided and therefore does not experience the longitudinal refractive index gradients that cause frequency shifts [141, 189]. Therefore, the coupling of laser energy to the plasma can be characterised by the fraction of laser energy frequency shifted outside of $\lambda_0^{\min}$ to $\lambda_0^{\max}$. For this data, this comprises mainly the blueshifted light while the redshifted component is not fully captured. Since $c\tau \lesssim \lambda_p$ in the high density plateau, spectral modulations are caused by the first wakefield period: the front of the laser undergoes photon deceleration while the back of the laser undergoes photon acceleration. Farther in the plasma, λ_p increases so that less of the laser is blueshifted. Any blueshifts necessitate redshifts to drive wakefields in the first place. Therefore, the fraction of laser energy blueshifted, as measured from the spectral data, is still a useful measurement of the spectral modifications and therefore laser-plasma coupling, albeit underestimated.

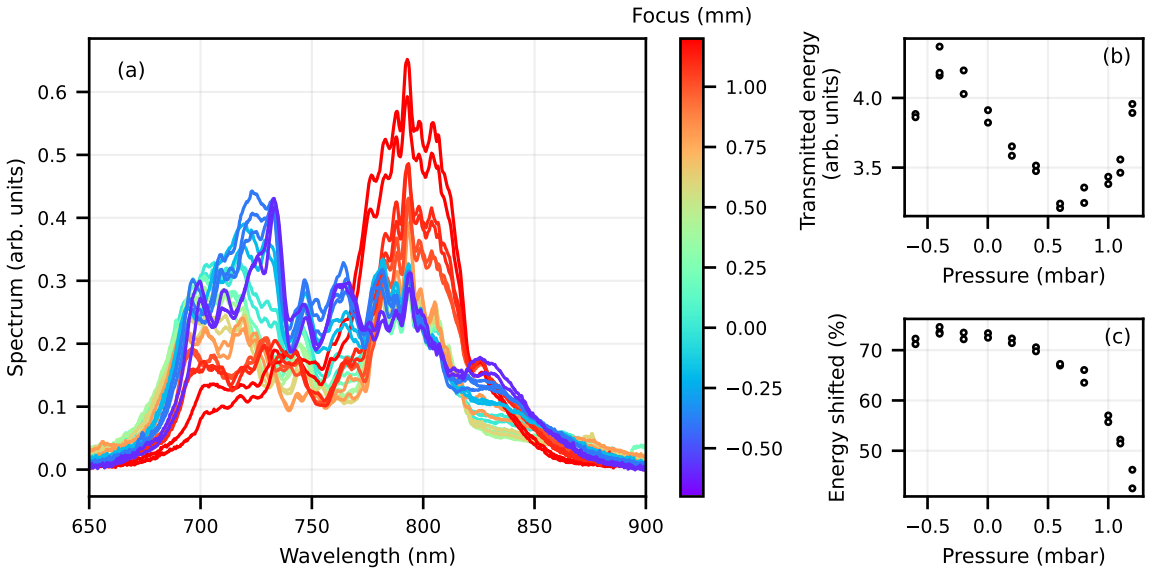

Figure 5.5: Post-interaction laser spectra; the colour bar represents the vacuum laser focus relative to the gas cell entrance. The gas pressure was 182 mbar.

Figure 5.5(b) shows the transmitted laser energy for the focus scan. The total counts on the spectrometer decrease as the laser focus is moved from −0.4 mm to 0.6 mm; the patterns invert outside this range. This intermediate focus range corresponds to highly symmetric transverse laser distributions with most of the energy in the central spot [182], as the Rayleigh range is $z_R \simeq 400\,\mu$m. Figure 5.5(a) shows that the decreasing trend here represents an approximately constant spectrum in the vacuum wavelength range, while the amount of blueshift increases with earlier focus. This implies that a similar fraction of the laser is guided for this range of focus positions, which is consistent with the focal

spot measurements [182]. The high transmission when focusing far into the plasma, which coincides with low spectral modifications, suggests that a significant fraction of the laser is not guided and the laser is ineffective in driving a strong wakefield in this regime. A low efficiency of electron acceleration is expected from this.

As depicted in figure 5.5(c), the fraction of laser energy shifted away from the vacuum range decreases with $f > 0.2\,\mathrm{mm}$, but remains approximately constant and high for earlier focusing. Increased blueshifting of light is observed when the laser is focused in the rising edge of the density profile. This is consistent with a small focal spot and high a_0 reached early in the interaction, which allows laser energy from the entire focal spot to be coupled into the plasma from the beginning of the target. In contrast, focusing 1 mm into the plateau region causes a significant fraction of the laser energy to remain between λ_0^{min} and λ_0^{max}. A late focus means that at the beginning of the target, the interaction takes place between the plasma and the laser in the mid-field. The laser energy distribution is not a pure Gaussian, but contains higher-order modes [182]. Thus, the transverse laser energy distribution away from the focal plane is more complex and asymmetric, with a modest fraction of energy contained outside a central spot. The features that appear away from the propagation axis are not captured by the self-focusing and do not drive strong wakefields [87,141,189]. As a result, a strong component of the laser remains in the initial wavelength range, and this is more significant at foci farther in due to the messier transverse distribution early in the interaction. These higher order modes can cause changes to the energy partition between longitudinal and transverse fields [174], causing a large effect on the transverse electron distribution as discussed in ref. [182].

Different regimes are found for $f < 0.6\,\mathrm{mm}$ and $f > 0.6\,\mathrm{mm}$. In the former, higher transmission correlates with significant frequency blueshifts. This suggests that the energy that the laser couples into the plasma by driving a wakefield is reabsorbed by the laser via photon acceleration. In the latter, the frequency blueshifts are negatively correlated with laser transmission.

Electron beam charge

Figure 5.6 shows the total electron beam charge measurements plotted against measured parameters of the post-interaction laser spectra. Each point corresponds to a single shot with the laser focus denoted by the colour and the different markers represent two separate runs at the same backing pressure but different laser pulse shape. The experiment used ionisation injection in a tailored density profile, so that the injected charge is determined by the region in which the laser pulse remains at high enough

intensity to further ionise the N^{5+} ions [181,182]. By introducing a density down-ramp, the self-focusing of the laser should weaken sufficiently to decrease the laser intensity and halt ionisation injection, generating electron beams with peaked energy spectra.

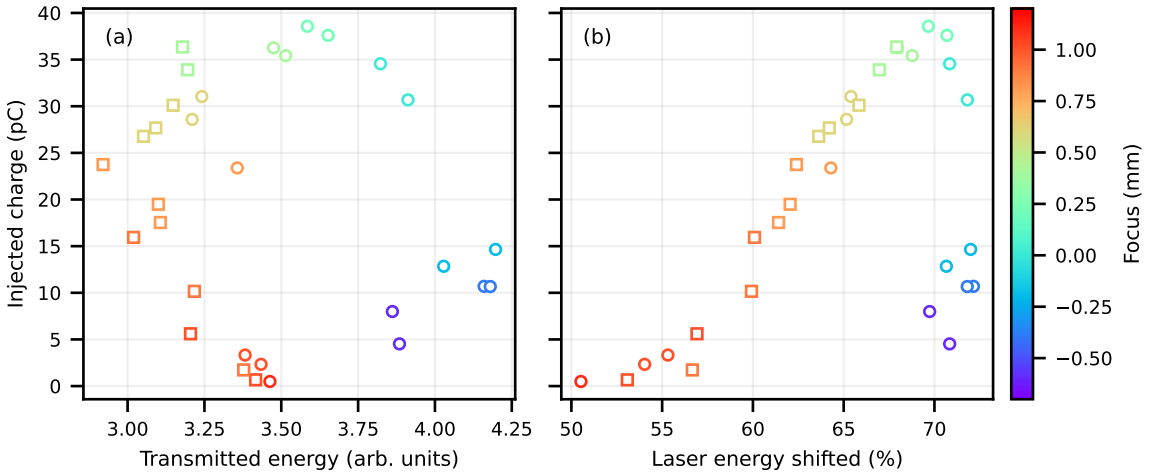

Figure 5.6: Total electron beam charge as a function of parameters of the post-interaction laser spectrum for a focus scan: (a) transmitted laser energy, (b) percentage of laser energy shifted away from the range $\lambda_0^{\min}$ to $\lambda_0^{\max}$. The circles and squares represent two runs with different initial laser temporal profile.

Figure 5.6(b) shows a clear dependence of total charge on the fraction of laser energy shifted away from the vacuum range. For $f > 0.4\,\mathrm{mm}$ (green to red), the injected charge increases with increased laser modifications. This suggests that the increased laser-plasma coupling enables the laser intensity to remain above the ionisation threshold over a larger volume, thereby driving more effective ionisation injection.

The injected charge is maximised for $f = 0.25\,\mathrm{mm}$, where around 70 % of the measured laser spectrum is shifted away from the vacuum range. When the laser is focused earlier than this, the spectral modifications to the pulse remain high at $\simeq 70\,\%$, but the injected charge decreases rapidly with decreasing f. This indicates that, while the laser transfers significant energy to the plasma, leading to strong spectral modifications, this is not correlated with a high laser intensity over an extended region where injection can occur. The strong wake driven in the rising edge of the target likely depletes the laser energy and restricts the intensities that can be reached later, where injection is allowed. Therefore, ionisation of N^{5+} in the plateau region is less likely. In summary, optimising charge relies on strong non-linear laser evolution but is ultimately limited by the density profile, as injection is forbidden in the rising edge.

Electron beam energy

The maximum energy of the electron beam is shown in figure 5.7 as a function of measured parameters of the transmitted laser spectra. In contrast to figure 5.6, where there was good agreement between the two runs displayed, the trends with maximum energy differ between the two runs for focal planes 1 mm into the plasma (red). There is good agreement for other focus positions. As the runs only differ by the laser spectral phase, this suggests that the different initial phase of the laser pulse has a more significant impact on the acceleration dynamics than on the injection dynamics. This is because ionisation of the electrons that inject is driven by the instantaneous laser field, which means that any changes to the laser may result in a difference in the phase of the injected electrons. Temporal pulse shape has been observed to change charge significantly for self-injection [190], but those results used more significant changes than the ones presented here. The sensitivity of laser energy transfer efficiency to temporal pulse shape has been observed in capillary waveguides though [174]. The observation of disagreement between the two runs only for focal planes deep into the plasma highlights the high sensitivity of this regime to initial conditions. This suggests that such a late focus is detrimental to the stability of the interaction.

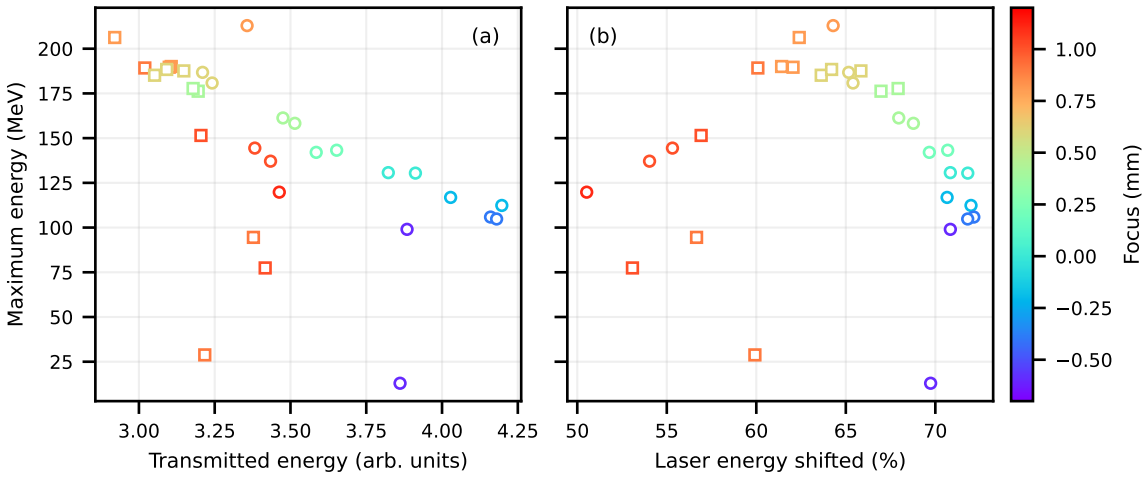

Figure 5.7: Maximum electron beam energy as a function of parameters of the post-interaction laser spectrum for two focus scans denoted by different markers: (a) transmitted laser energy, (b) percentage of laser energy shifted away from the range $\lambda_0^{\min}$ to $\lambda_0^{\max}$. The circles and squares represent two runs with different initial laser temporal profile.

The maximum electron beam energy is optimised around $f = 0.8$ mm, well into the high density plateau. This corresponds to beams with low charge. However, electron beams obtained with a later vacuum focal plane (higher f) contain both a lower charge

and a lower energy, suggesting that beam-loading is not the dominant effect. Instead, it is likely about a balance of the laser energy transferred to the plasma and that which is reabsorbed by the rear of the pulse. Figure 5.5(a) shows that the optimum (orange) corresponds to the transmitted spectra with the lowest amount of blueshift among the pulses with low transmission in the vacuum wavelength range. This translates to low overall transmitted energy as depicted in figure 5.7(a), which indicates a strong wakefield. Low transmission in the vacuum wavelength range indicates that most of the laser is guided, while low transmission below $\lambda_0^{\min}$ implies that the pulse does not gain significant energy back from the wakefield via photon acceleration. Instead, most of the energy that is transferred to the wakefield can be absorbed by the electrons, which leads to the high energies observed.

The maximum electron beam energy decreases with increasing laser transmission, as shown in figure 5.7(a). This is consistent with conservation of energy of the laser and electron beam together. The anomalous lower energies reached in shots with late focusing, $f \geq 1$ (red), can be explained by 5.7(b). The high transmission in the vacuum range represents less energy coupling to the plasma at late foci due to the messier transverse distribution. Therefore, there is less energy in the wakefield available to electrons. Figure 5.7(b) also shows that the maximum energy decreases with increasing laser energy shifted for $f \leq 0.6\,\mathrm{mm}$. This represents significant reabsorption of energy from the plasma, and the laser likely experiences phase space rotation. As the front of the laser redshifts, the low frequency photons move back due to the negative dispersion in a plasma, while photons at the back of the pulse blueshift and move forward. This means that the laser and wakefield propagate together without a significant net transfer of energy.

While the maximum electron beam energy is an insightful measure, a perhaps more useful metric is the total energy in the bunch. In the experiment, this was found to have a broad optimum in the range $0\,\mathrm{mm} < f \leq 0.6\,\mathrm{mm}$, with trends similar to figure 5.6. This shows that the vacuum focus position has varying effects in the acceleration and ionisation injection dynamics in a tailored density profile. The total electron bunch energy reached 2.8 mJ for this dataset. In comparison, the laser had an average pulse energy of 736 mJ. This suggests that 0.4 % of the laser energy was transferred to the electrons. This is lower than other measurements of LWFA efficiency in the literature which reach 10 % [26,27]. It is also very low compared to the 1/3 laser energy absorption estimated in section 5.2.1. This suggests that the wakefield is not efficiently accelerating the electrons.

5.3 Simulations of pulse modifications

2D simulations were performed using the particle-in-cell code EPOCH. The simulations were run in a window of size 64 µm × 112 µm in the laser propagation and transverse directions, respectively, which moved along the laser direction at the linear group velocity as calculated for the plateau density. The spatial resolution was 30 cells per wavelength in the longitudinal direction and 10 cells per wavelength in the transverse direction and 8 electrons per cell were used (see appendix A.2 for details of convergence). The laser pulse was polarised out of the plane of the window.

The laser pulse was modelled as a Gaussian with a FWHM duration of 42 fs, focused to a 12 µm FWHM focal spot and a peak intensity $I_0 = 9.8 \times 10^{18}\,\mathrm{W\,cm^{-2}}$. The target comprised a pre-ionised plasma with the density profile shown in figure 5.1(b) with maximum electron density $n_{e0} = 7 \times 10^{18}\,\mathrm{cm^{-3}}$ and a population of N^{5+} ions such that $n_{N^{5+}}/n_e = 0.0025$. This setup corresponds to the almost instantaneous ionisation of 99.75 % hydrogen and 0.25 % nitrogen (up to N^{5+}) by the leading edge of the laser, and significantly reduces computational costs compared to running the simulation with complete neutral populations. Given the temporal profile of the laser pulse and the intensity thresholds for barrier suppression ionisation (section 2.3), ionisation to N^{5+} should occur 64 fs (20 µm) before the peak of the laser pulse, while ionisation to H^+ should occur 84 fs (25 µm) earlier. The simulation window only views 20 µm in front of the peak of the laser pulse, so the assumption of a pre-ionised plasma is valid. Further ionisation of nitrogen was simulated by BSI and tunnelling ionisation using the ADK theory. These parameters are comparable to the experimental conditions. The vacuum laser focus f_{vac} was varied from −0.6 mm to 1.0 mm relative to the beginning of the high density plateau to investigate the effect of laser-plasma coupling and the influence of small longitudinal variations on ionisation injection and subsequent electron acceleration.

5.3.1 Wakefield formation

A preliminary simulation was run in a fully pre-ionised plasma with no nitrogen and the laser focused at $f_{\mathrm{vac}} = 0$ mm. No evidence of injection is observed at these densities and intensities, which implies that electron trapping in the simulations with mixed gas can be attributed to ionisation injection. The simulations with and without nitrogen ions produced almost identical laser evolution, with negligible differences in peak vector potential and transverse width and under 1 % deviations in average wavevector. This suggests that the concentration of nitrogen is sufficiently low that the ionisation of

N^{5+} causes a negligible effect on the laser pulse. In contrast, a measurable difference in blueshift was observed for a 10 % nitrogen mix compared to pure helium in ref. [108]. Similarly, the injected charge is low enough (~ 1 pC) that beam-loading does not significantly modify the wakefield structure; the differences in the plasma wavelength with and without injection are negligible and the peak accelerating fields vary by less than 5 %.

Laser focusing

As the laser pulse was polarised out of the plane of the 2D simulation, its properties were easy to extract independently of the fields from the wakefield. Performing a FFT on the laser electric field enabled measurement of the laser spectrum with respect to wavevector k. The fast oscillations in the electric field were removed by computing the analytic function using the Hilbert transform, which allowed measurements of the peak intensity and transverse size. Figure 5.8 shows the evolution of the average laser wavevector $\langle k \rangle$, transverse width w and peak vector potential a_0 throughout the simulations with different vacuum laser focus. In the following, w is used to represent the FWHM, not the $1/e^2$ width.

In the bubble regime, the laser undergoes guiding by the bubble at the matched spot size $w_m = r_b \approx 2\sqrt{a_0}/k_p$. This quantity is depicted by the dashed line in figure 5.8(b), where $k_p = k_p(n_e)$ was calculated for the density profile in figure 5.1(b) and the peak vacuum result $a_0 = 2.1$ was assumed as a first order approximation. For all simulations, the laser pulse width reaches a minimum within the high density plateau, between $z = 0$ mm and $z = 0.5$ mm. The minimum width $w_{\min}$ and its longitudinal position $z(w_{\min})$ are shown in figure 5.9. For early focusing, $f_{\text{vac}} \leq 0$, the minimum laser spot size is reached after f_{vac}, while for late focusing, $f_{\text{vac}} \geq 0.2$ it is reached before. Moreover, the minimum spot size appears to transition between 6.5 µm and 4.5 µm depending on f_{vac}. This can be understood through the balance of the laser's focusing geometry and guiding by the plasma. Consider the focusing geometry providing a focal plane farther into the plasma; e.g. $f_{\text{vac}} = 1$ mm (red in figure 5.8(b)). Guiding of the laser pulse becomes effective around $z \approx 0$ mm. As the laser spot size is larger than w_m here, the plasma guiding causes self-focusing, enhancing the focusing effect from the setup geometry. Conversely, consider the geometry which focuses the laser in the rising edge of the plasma; e.g. $f_{\text{vac}} = -0.6$ mm (blue in figure 5.8(b)). In this case, the blowout guiding only becomes effective after the vacuum focal plane, where the geometry causes diffraction of the laser. The geometric diffraction counteracts the blowout guiding, leading to a larger $w_{\min}$. Furthermore, earlier f_{vac} means the geometrical diffraction is

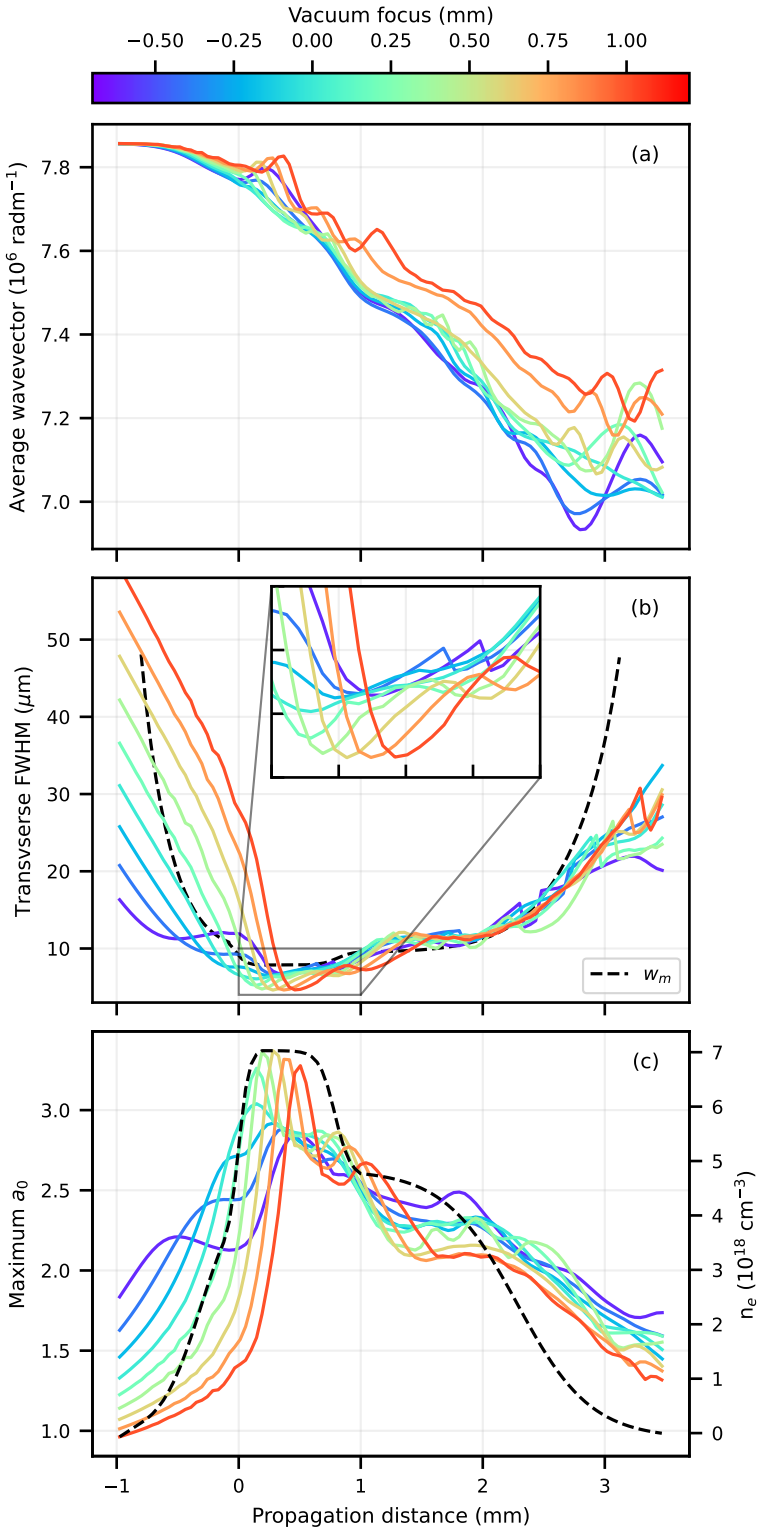

Figure 5.8: Simulated laser parameters a function of propagation distance for different vacuum focus. (a) Average wavevector. (b) FWHM pulse width; the dashed line represents the matched spot size $w_m = r_b$. (c) Peak vector potential; the density profile (dashed black) is displayed on the right axis.

stronger when blowout focusing becomes effective. Therefore, the evolution of the laser width is slower, and $w_{\min}$, representing the effective focus position, is reached later.

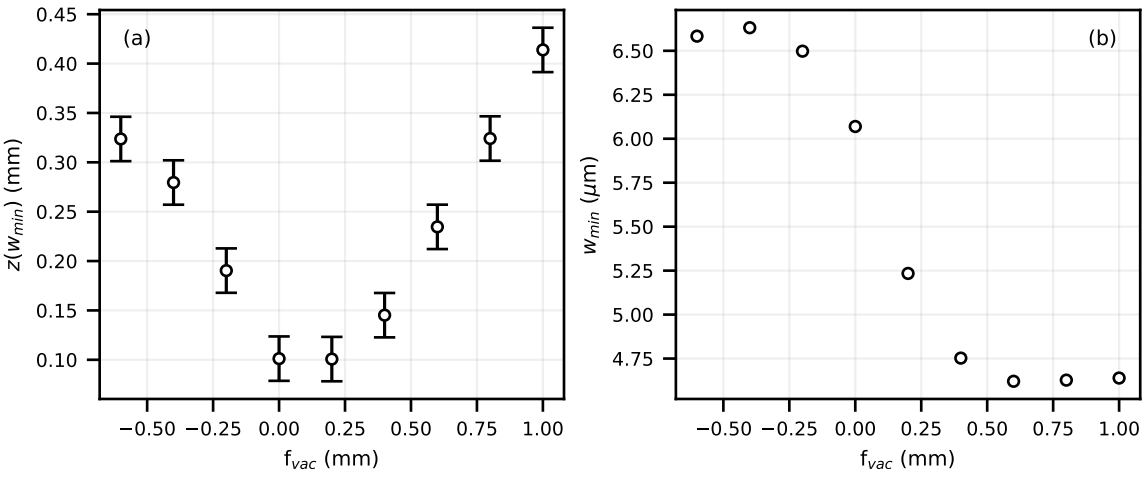

Figure 5.9: (a) Longitudinal position and (b) value of minimum transverse laser spot size for different vacuum focal planes.

In the simulations, $w_{\min}$ is not maintained, but increases again after $z(w_{\min})$. This suggests that the matched spot size is larger than $w_{\min}$, as the pulse width is known to oscillate around the matched value when the laser pulse is not perfectly matched to w_m [87]. Figure 5.8(b) shows this to be the case. In the falling edge of the plasma density, the simulations are consistent and closely follow the matched spot size, which is much closer to the laser's $w_0 = 12\,\mu\text{m}$. The measurements deviate from w_m at the end of the plasma target, where the driven wakefields weaken and guiding is no longer effective.

The peak laser a_0 throughout the simulation is shown in figure 5.8(c). As $a_0 \sim \lambda\sqrt{I} \sim (wk)^{-1}$, both the focusing and frequency shifts have comparable effects on the laser strength parameter. The variations of the peak laser a_0 closely follow the trends of the laser spot size up to $z \approx 1\,\text{mm}$. The maximum a_0 reached in the simulations occur at the same z as $w_{\min}$, indicating that they are determined mainly by the laser focusing dynamics and the balance described earlier. Simulations in a similar target profile also report a decreasing maximum a_0 when focusing later in the plasma, $f_{\text{vac}} > 0.15\,\mu\text{m}$ [181]. Although this is not explained, the interpretation presented here can also be applied to their results.

In the falling edge of the targets, the laser widths are similar. As a result, the laser spectrum evolution dominates the changes in laser strength parameter in this region. This is evidenced by the consistency between the differences in a_0 and the variations in average wavevector shown in figure 5.8(a).

Laser-plasma coupling

Energy from the laser is coupled into the plasma through photon deceleration, which can be measured from the laser spectrum. Figure 5.8(a) shows increased redshifting with earlier vacuum focus. This implies increased coupling of laser energy to the plasma at lower f_{vac}, and thus a stronger wakefield. The laser energy transfer to the plasma can be characterised by the strength of the driven wakefields, shown in figure 5.10. The measurements confirm that lasers with early foci excite strong wakefields in the rising edge of the plasma. They also confirm that the wakefields driven in the falling edge of the target weaken as f_{vac} is moved farther into the target. This is consistent with the lower redshifting observed when focusing deep into the target.

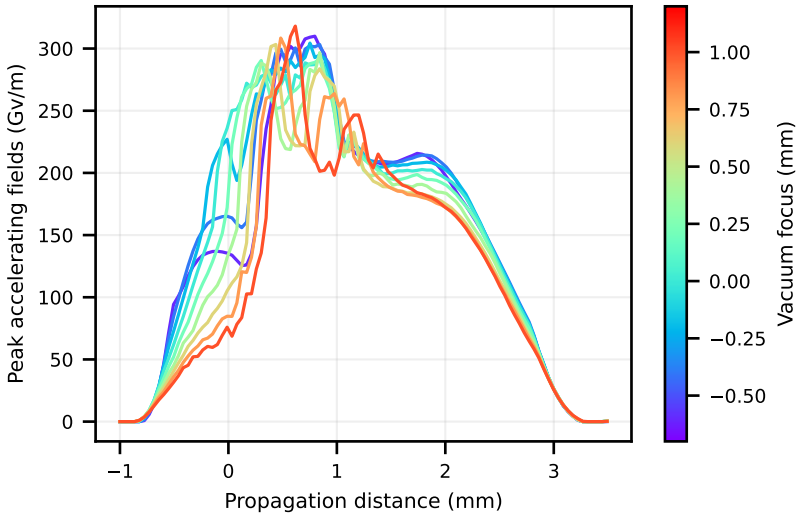

Figure 5.10: Evolution of the accelerating field strengths of the wakefield throughout the simulations. The colour bar represents the vacuum focus position of the laser.

In the bubble regime, the longitudinal field $E_z \sim \sqrt{a_0}$ so it is expected that the wakefield amplitudes vary in line with the a_0 variations depicted in figure 5.8(c). However, the wakefields driven in the high density plateau, $0\,\mathrm{mm} < z < 1\,\mathrm{mm}$, do not follow these trends. While the maximum a_0 are found to increase with foci farther into the plasma, the accelerating fields are weakest for an intermediate $f_{\mathrm{vac}} = 0.2\,\mathrm{mm}$ and increase for earlier and later focusing. Moreover, the early (blue) and late (red) focusing result in comparable peak accelerating fields despite the 20 % variations in their maximum laser a_0. This is because the relationship of the accelerating fields with laser strength parameter (section 2.4.3) assume a nonevolving laser driver. In reality, the laser with an early focus starts driving a wakefield earlier in the interaction. The density gradient associated with this wakefield causes the laser to undergo photon acceleration. This

means that more energy is transferred to the plasma so the wakefield strength increases. This cyclical reinforcement allows the peak wakefield amplitude to be high despite the lower peak a_0 reached. In contrast, the strong self-focusing of the laser with a late vacuum focus means that the wakefield has less time to grow before reaching its peak. The result is an approximately constant maximum wakefield amplitude. This suggests that it is not only the instantaneous a_0, but also its evolution, which determines the strength of the wakefield, thereby highlighting the importance of the laser evolution in the acceleration dynamics.

Figure 5.11 presents the Wigner transform of the laser electric field at four different timesteps for three representative simulations, labelled I, II and III, with $f_{\mathrm{vac}} = -0.6\,\mathrm{mm},\ 0.2\,\mathrm{mm}$ and $1.0\,\mathrm{mm}$, respectively. The Wigner transform is defined as

$$W(t,\omega) = \int_{-\infty}^{\infty} E\big(t - \frac{\tau}{2}\big) E\big(t + \frac{\tau}{2}\big) e^{-i\omega\tau}\,\mathrm{d}\tau\,, \tag{5.2}$$

and is a representation of the laser pulse distribution in the time-frequency domain. The Wigner transform benefits from providing the best possible resolution in both t and ω and its marginals correspond to the spectrum and intensity profile: $S(\omega) = \int W(t,\omega)\,\mathrm{d}t$ and $I(t) = \int W(t,\omega)\,\mathrm{d}\omega$. However, it is a non-linear transform and therefore exhibits additional artefacts from interference when the signal comprises more than one frequency component. These cross terms introduce negative values to the distribution which are not physically meaningful. In the simulations, z and k are considered in place of t and ω.

The evolution of the laser pulse shown in figure 5.11 can be explained by the electron density distribution with which the pulse interacts, which is depicted by the black lines. Simulations I and II, with laser foci at $-0.6\,\mathrm{mm}$ and $0.2\,\mathrm{mm}$, are qualitatively similar while simulation III, focused at $1\,\mathrm{mm}$, depicts clear differences. All lasers undergo photon acceleration at $\zeta < 0$ in the rising edge of the target (top row) due to the decreasing plasma density gradient associated with the back of the wakefield period. However, the slope of the positive chirp developed by the second timestep is largest for $f_{\mathrm{vac}} = 1\,\mu\mathrm{m}$. This is consistent with the electron density shown in the first timestep. As simulations I and II drive a non-linear wake early in the interaction, the back of the laser pulse interacts with a constant density which limits frequency shifts. In contrast, simulation III drives a lower amplitude wave for a longer time, which has a decreasing density gradient at the rear of the pulse. Moreover, while the lasers with earlier focusing develop a monotonic positive chirp at the back, the laser focused at $1\,\mathrm{mm}$ develops more structure in the blueshift. This is evident in the second timestep around $\zeta = -10\,\mu\mathrm{m}$.

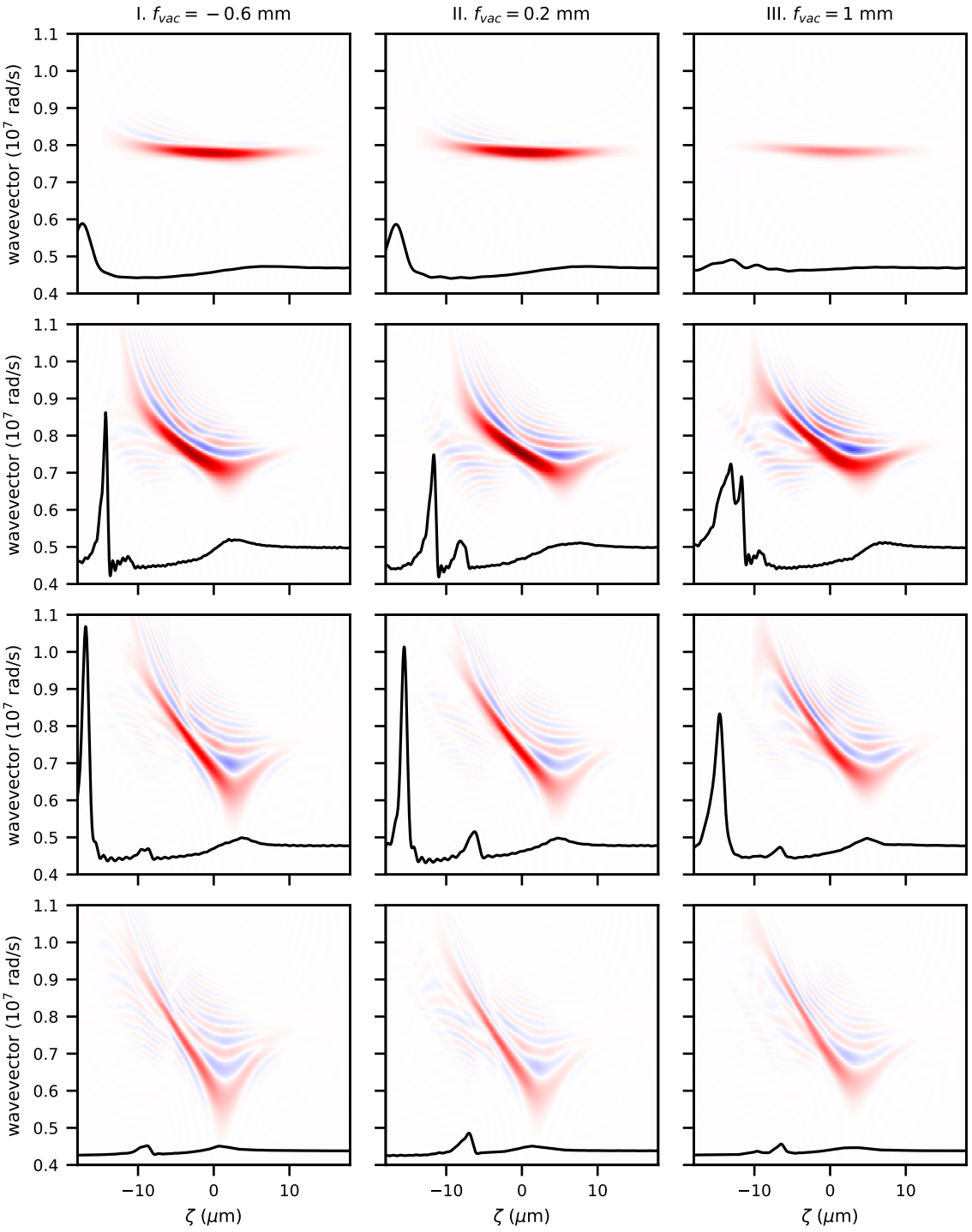

Figure 5.11: Time evolution of the Wigner transform of the laser with $f_{\mathrm{vac}} = -0.6\,\mathrm{mm}$ (simulation I, left column), $f_{\mathrm{vac}} = 0.2\,\mathrm{mm}$ (simulation II, middle column) and $f_{\mathrm{vac}} = 1.0\,\mathrm{mm}$ (simulation III, right column). Time progresses downwards and the frames are 3 ps apart. The density profile of the wakefield is overlaid in black.

This feature can also be attributed to the weaker wakefield driven. As the wakefield develops an electron density peak farther forward, the back of the laser interacts with both positive and negative density gradients. This results in both photon acceleration and deceleration.

Photon acceleration appears to stop after the third timestep. This is consistent with the growing plasma wavelength in the trailing edge of the plasma target, which causes the pulse to interact primarily with the increasing density gradient at the front of the wakefield. This causes the laser to undergo an overall redshift in the third and fourth timesteps. This occurs along with an increase of the laser chirp due to photon deceleration occurring preferentially around $\zeta = 0$, but more weakly at the back of the pulse. The last row of figure 5.11 shows that simulation III undergoes the least redshift in the latter half of the interaction despite developing the strongest chirp. This indicates strong photon acceleration and therefore lower net energy transfer to the plasma.

Summary

- The effective focal plane of the laser, i.e. the position where it reaches its minimum width, varies non-monotonically with vacuum position.
- This is because the self-focusing in the plasma can either enhance (for early f_{vac}) or counteract (for late f_{vac}) the geometric focusing.
- The strength of the wakefield at a given time is determined by the time evolution of the laser a_0 and not the instantaneous a_0. Therefore, the laser redshift is a better indicator of the accelerating fields than the peak laser a_0 as determined by the focusing dynamics.

5.3.2 Electron acceleration

Electron injection

The rate of electron injection as a function of propagation distance is shown in figure 5.12 for three representative simulations, along with the evolution of the peak laser intensity. The BSI intensity thresholds I_{th} for N^{6+} and N^{7+} are denoted by the horizontal dashed lines. Injection is prevented in the rising edge of the target, $z < 0$, due to bubble compression [111, 114], as seen in figure 5.12(a). Only lasers with $f_{\mathrm{vac}} < 0$ caused ionisation in this region, which implies that an early vacuum focusing is less efficient in driving injection.

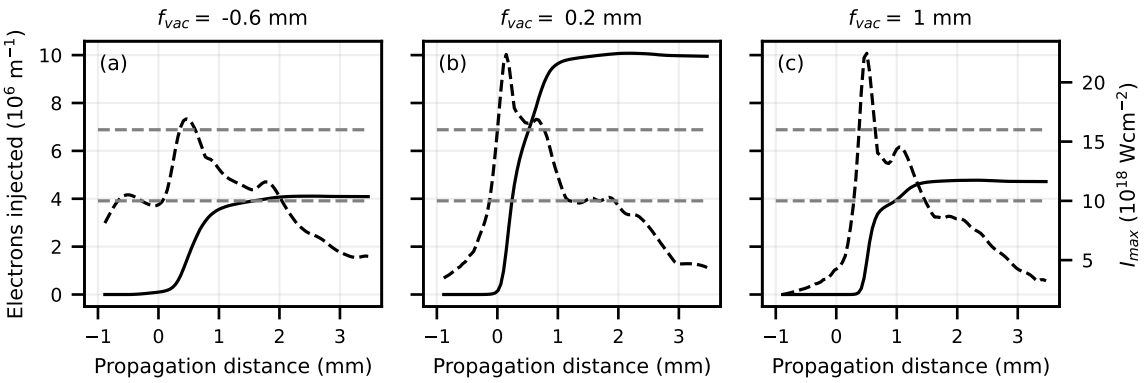

Figure 5.12: Injected charge as a function of propagation distance for vacuum laser focus at (a) −0.6 mm (b) 0.2 mm and (c) 1.0 mm. The dashed line (right axis) shows the evolution of the peak laser intensity and the horizontal grey lines denote the BSI threshold intensities for N^{6+} and N^{7+}.

For all simulations, all of the electrons ionised from N^{5+} in $z > 0$ are injected into the wakefield, implying that the injection condition $\Delta\phi > 1$ (section 2.6.3) is automatically satisfied here. This is consistent with the requirement $a_0 \gtrsim 1.6$ [108] being always fulfilled for the ionisation thresholds of N^{6+} and N^{7+}. However, previous studies of ionisation injection driven by highly evolving laser pulses indicate that the non-linear bubble evolution at higher a_0 can halt the injection condition while ionisation continues [117–119]. This self-truncated ionisation injection (STII) regime is characterised by injection suppression at high a_0, whereas figure 5.12 depicts an increase in injected charge consistent with increases in $I_{\max}$ reaching I_{th}. This indicates that the interaction presented here is not in the STII regime.

The slower laser evolution for $f_{\text{vac}} < 0$ results in a longer injection region than the aggressive increase in $I_{\max}$ for $f_{\text{vac}} > 0$ that occurs due to the enhanced focusing. However, the presence of multiple peaks in $I_{\max}$ above I_{th} for all simulations causes the rate of injection to vary, as seen most clearly in figure 5.12(c) around $z = 1$ mm. As the intensities follow the evolution of a_0 shown in figure 5.8(c), this is consistent with previous findings that the focal plane changes the maximum value of a_0 [174], which affects the longitudinal injection position [183] and the injected volume in phase space [115]. However, the results show that it is not only the peak a_0, but also its evolution through the plasma, which determines the injected charge, as previously observed in simulations with different laser intensities [116]. This demonstrates the sensitivity of ionisation injection to variations in laser focusing, especially when relying on laser evolution to control the injection region. The results are consistent with stability studies which found correlations of electron beam parameters with laser fluctuations [30].

Simulations of ionisation injection in the tailored target resulted in peaked electron energy spectra, with energy spreads ranging from 60 MeV to 100 MeV (FWHM). The total charge of the electron beam is plotted in figure 5.13 as a function of two parameters of the laser a_0 evolution shown in 5.8(c): the maximum value reached and its position. The charge is optimised for $f_{\text{vac}} = 0.2\,\text{mm}$ and decreases linearly away from this value, in line with previous observations [181]. This corresponds to the simulation where the laser reaches its peak a_0 and minimum pulse width the earliest, and not that which reaches the highest a_0. While the maximum a_0 is reached for $f_{\text{vac}} = 0.6\,\text{mm}$ at $z = 0.24\,\text{mm}$, for $f_{\text{vac}} = 0.2\,\text{mm}$ it is reached at $z = 0.1\,\text{mm}$, at the beginning of the plateau. By reaching its peak a_0 earlier in the plasma, the laser is able to ionise electrons in a longer region within the high density plateau, $0 \geq z \geq 1\,\text{mm}$, leading to a higher injected charge.

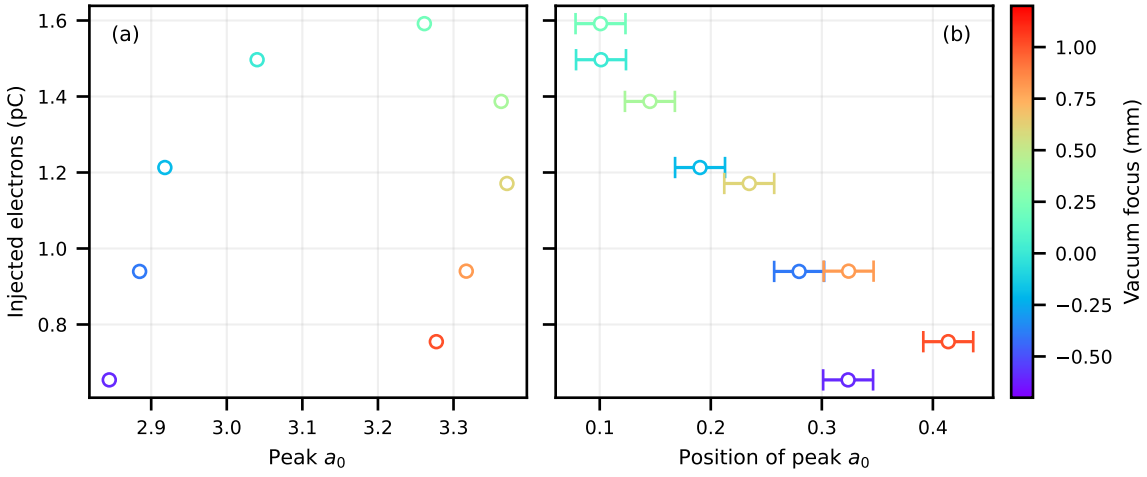

Figure 5.13: Total charge of the accelerated electron beam as a function of (a) peak laser a_0 reached in the simulations and (b) longitudinal position at which the peak a_0 is reached.

Electron acceleration

The maximum energy of the accelerated electron beams was calculated as the 99$^{\text{th}}$ percentile of their energy distribution. The value at the end of the simulation is shown in figure 5.14, as a function of laser parameters: $\int a_0\,\mathrm{d}z$ and average wavevector. The maximum electron beam energy is optimised for $f_{\text{vac}} = -0.2\,\text{mm}$ and found to decrease with earlier and later foci. As discussed in section 5.3.1, the instantaneous laser a_0 is not the best indicator of the strength of the driven wakefields; however, 5.14(a) shows that the integrated a_0 is a good measure of the electron energies, as it takes into account the build up of the wakefield throughout the interaction. Figure 5.14(b) depicts

a decrease of the transmitted laser wavevector when the electron energies are higher. This is consistent with increased energy transfer to the wakefield. The integrated a_0 is found to be directly correlated with the maximum laser wavelength. The results imply that the transmitted wavevector is well correlated with the integrated a_0, meaning that the spectral modifications can provide a good indication of the energies reached by the accelerated electrons.

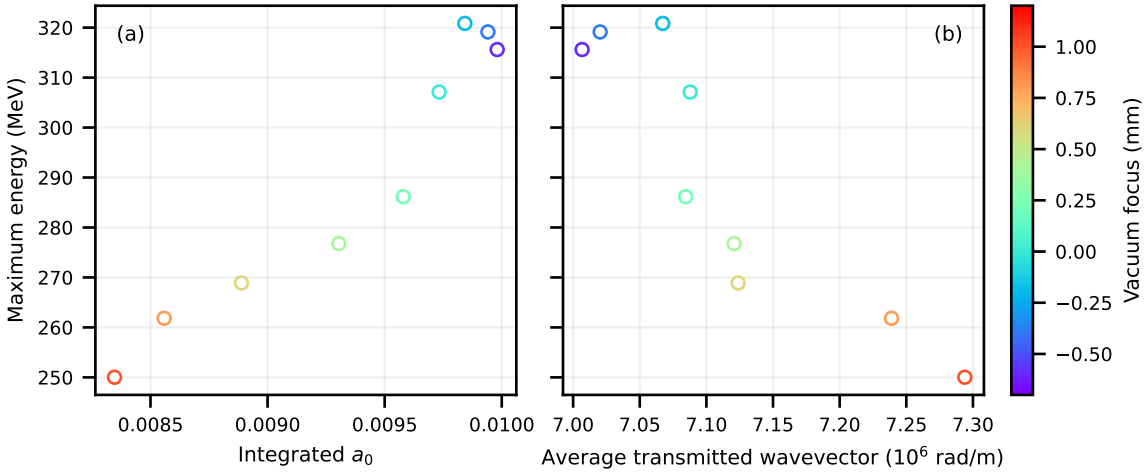

Figure 5.14: Maximum electron beam energy as a function of (a) integrated laser a_0 with respect to propagation distance and (b) average transmitted wavevector at the end of the simulations. The wavevectors were calculated from a parabolic fit to the simulation results to reduce noise.

Simulations with lasers set to focus earlier than −0.2 mm reach lower energies, but only 3 % below the optimum. This suggests that the acceleration dynamics are more stable when focusing early in the target. These simulations with very early focus do not follow the trends with integrated a_0 or average wavevector because the electrons are unaffected by the wakefield dynamics in the leading edge of the target, which are captured by these laser parameters.

As the transfer of laser energy to the plasma can be characterised by the redshifting of the laser, combining measurements of the laser spectrum with the energy gain of the injected electrons enables the efficiency of the wakefield accelerator to be calculated. Streeter *et al.* determine that the instantaneous energy extraction efficiency can be found as [175]

$$\tilde{\eta}_e = -\frac{N_e m_e c^2 \omega_0}{W_{L0}} \left(\frac{\mathrm{d}\langle\gamma\rangle}{\mathrm{d}z} \right) \left(\frac{\mathrm{d}\langle\omega\rangle}{\mathrm{d}z} \right)^{-1} \tag{5.3}$$

where N_e is the number of accelerated electrons, ω_0 and W_{L0} are the initial laser frequency and energy, respectively, $\langle\omega\rangle$ is the average angular frequency of the laser and

$\langle\gamma\rangle$ is the average Lorentz factor of the beam. The latter is a measure of the electron beam energy and can be characterised from the electron energy spectrum $S(\gamma)$ as $\langle\gamma\rangle = \int S(\gamma)\,\mathrm{d}\gamma/N_e$.

As the simulation outputs the laser wavevector $k = \omega/c$, this was used for the efficiency calculations. The presence of turning points in $\langle k\rangle$ shown in figure 5.8(a) is problematic for the calculation of the efficiency using (5.3). While the increase in average wavevector that occurs around $z = 0.3\,\mathrm{mm}$ is likely physical, as there is significant photon acceleration in this region, subsequent oscillations may be noise. As the analysis was performed on a single lineout of the laser electric field along the laser axis rather than on the entire pulse, $\langle k\rangle$ may be more sensitive to the varying focusing and defocusing of different frequency components. Therefore, a quadratic fit was used on the simulation results as a smooth approximation to the average laser wavevector between $z = -1\,\mathrm{mm}$ and $2.5\,\mathrm{mm}$, which resulted in a constant $\mathrm{d}\langle k\rangle/\mathrm{d}z$. The energy gradients, $\mathrm{d}\langle\gamma\rangle/\mathrm{d}z$ and $\mathrm{d}\langle k\rangle/\mathrm{d}z$, were then calculated from the simulation results. The calculated efficiency is depicted in figure 5.15, along with an average efficiency value for each simulation. The average efficiency was calculated using the values at the end of the simulation as $\eta_e = -W_e/\Delta W_L$, where W_e is the total electron beam energy and $\Delta W_L = N_{\mathrm{ph}}\hbar\Delta k/c$ is the total laser energy loss. For this, the number of photons $N_{\mathrm{ph}} = W_{L0}/\hbar\omega_0$ was assumed to be conserved throughout the interaction [79].

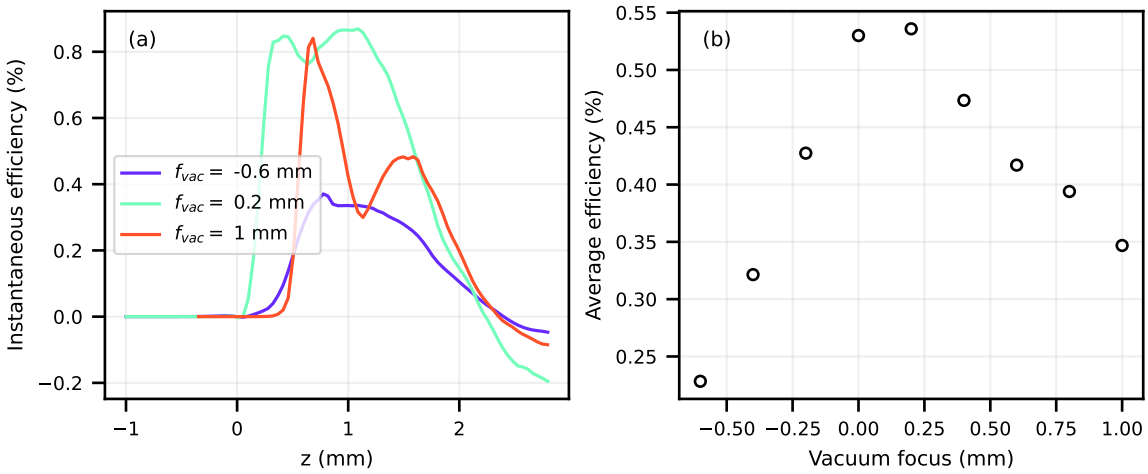

Figure 5.15: (a) Instantaneous extraction efficiency as a function of propagation distance for three representative simulations. (b) Average efficiency calculated at the end of the simulations for different vacuum laser focus.

The extraction efficiency varies throughout the interaction as a result of dephasing, drive laser evolution, injection and loss of electrons [175]. Figure 5.15(a) shows that, early in the interaction, the instantaneous efficiency rises along with the injected charge

depicted in figure 5.12. This is because the instantaneous efficiency is only meaningful after injection. As a result, the region in which $\tilde{\eta}_e > 0$ depends on the position where injection begins, and is therefore influenced by the focusing dynamics.

After $z = 1\,\mathrm{mm}$, the number of electrons in the beam is constant so the trends in the efficiency are dominated by the acceleration dynamics. The rate of electron energy gain decreases with propagation distance as a result of dephasing and depletion, as previously observed [175]. The peak instantaneous efficiency is lowest (among all f_{vac}, not just those shown) for the early $f_{\mathrm{vac}} = -0.6\,\mathrm{mm}$ focus, despite the higher average and maximum energies reached in this simulation. In contrast, the peak instantaneous efficiency is higher when the vacuum focus is in the high density plateau. This corresponds to the electron beams with the highest charge, suggesting that N_e is the dominant contribution to $\tilde{\eta}_e$. The negative efficiencies reached by the $f_{\mathrm{vac}} = 0.2\,\mathrm{mm}$ and $1\,\mathrm{mm}$ in the falling edge of the target are due to decreases in the average electron energy. There is evidence of the electrons driving their own wakefield at this point. These trends are captured effectively by the average efficiency shown in figure 5.15(b). The most efficient accelerators are those which accelerate the most charge. While an early focus is the least efficient, it may be convenient for reaching higher electron beam energies at the expense of a lower charge.

Summary

- The injected charge is not only determined by the peak laser a_0, but also its evolution through the plasma.
- The injected charge is highest when the laser reaches its peak a_0 earlier in the plasma, due to the longer region of N^{5+} and N^{6+} ionisation.
- This shows that ionisation injection is highly sensitive to variations in laser focusing, especially when relying on laser evolution to control the injection region.
- The electron energies are correlated with the integrated laser a_0 and the laser redshift, so spectral modifications provide a good indication of acceleration dynamics.
- The maximum electron energies are more consistent when the laser focus is set early in the target.

5.4 Discussion

The experimental measurements of the post-interaction spectra have some limitations. Figure 5.16 shows the laser spectra at the end of the simulations, where the inset shows the spectral range that could be measured in the experiment, corrected for the spectrometer response [191]. While the simulations show that redshifted light dominates the spectrum and provides information about the efficiency of wakefield excitation, the main redshifted component was not captured by the detector in the experiment. The blueshifted light shares similarities with the experiment, where the signal between 700 nm to 750 nm is stronger for $f_{\mathrm{vac}} < 1$ than for late focusing. However, the most clear trends are found outside the sensitivity range of the spectrometer. This suggests that the most useful redshifts require measuring the transmitted laser spectra above 900 nm, which should inform future experimental design.

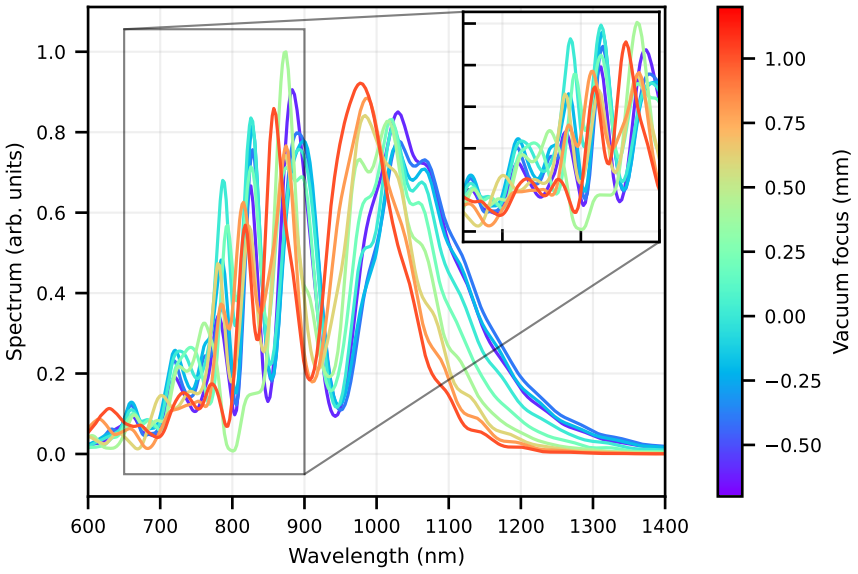

Figure 5.16: Laser spectra at the end of the simulation. The colour bar represents the vacuum focus position of the laser. The insets display the spectrum in the range captured by the spectrometer used in the experiment.

Nevertheless, the transmitted spectra was found to provide useful information about the laser-plasma interaction. The development of secondary peaks can work as a secondary density diagnostic, while the captured transmitted energy in the low wavelength range gives information about the energy remaining in the laser pulse, and therefore the laser-plasma coupling. The spectra revealed that a very late laser focus resulted in a significant fraction of the laser which remained unguided and this was correlated with low electron beam energies. However, lasers with early to intermediate focus reabsorbed

some energy from the wakefield, which also led to less electron acceleration. In addition, linear trends were found between the laser energy shifted away from the vacuum range and the injected charge, and between the transmission and maximum electron beam energy, within certain ranges of vacuum laser focus. These reveal that a very late focus, $> 1\,\mathrm{mm}$ after the beginning of the density plateau, is detrimental to the stability of the acceleration dynamics.

Figure 5.17 compares the experimental and simulation results for the injected charge and maximum electron beam energy. The simulations generated 15 times lower charge than measured in the experiment. This may be a dimensionality problem; the 2D simulations capture the transverse evolution of the pulse at a slower rate [96, 192], which may lead to lower intensities and therefore less injection than in experiment. It is unfeasible to run a 3D simulation to verify this due to the prohibitively expensive computational costs required. However, an increase in injected charge is observed in the 2D simulations compared to a 1D simulation which does not capture the self-focusing dynamics. Extrapolating this suggests an even higher charge in 3D. Despite these issues, the trends observed are still insightful and aid in the interpretation of the experimental results. The low simulated charge resulted in an underestimated beam-loading, which may partly explain the higher energies reached compared to the experiment.

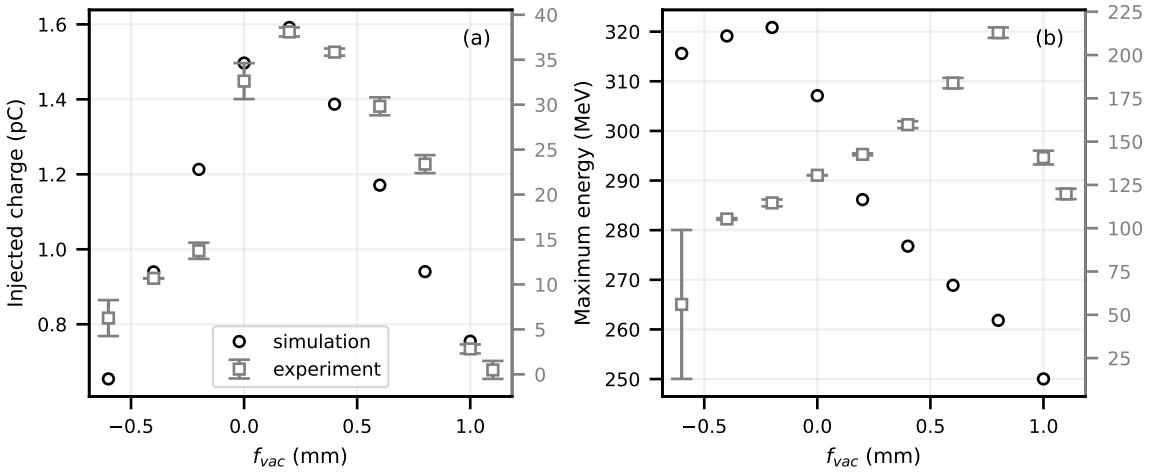

Figure 5.17: Comparison of the simulated and experimentally measured (a) total electron beam charge and (b) maximum electron beam energy for different vacuum laser focus. The experimental results are an average of two shots with the same focus, with the error bars delimiting their range.

The simulations and experiment present similar trends of injected charge with vacuum laser focus, as depicted in figure 5.17(a). In both cases the optimum charge is found at $f_{\mathrm{vac}} = 0.2\,\mathrm{mm}$, which the simulations reveal corresponds to the earliest effective fo-

cus. This suggests that trends in the self-focusing dynamics are well represented despite the use of 2D simulations. While stronger self-focusing is expected in the experiment, the position of minimum width will still be determined by the balance of this and the geometric diffraction.

The vacuum laser focus which optimises the maximum electron beam energy is very different in simulations and experiment. However, the trends with f_{vac} away from this optimum are similar, with a steeper decrease when focusing farther into the target and a more gentle decrease when focusing earlier. In the experiment, the electron energy is lower at late focus because a significant portion of the laser is not guided and therefore does not couple to the plasma. The laser-plasma coupling is similar for earlier foci, but the laser reabsorbs some of the energy from the wakefield, meaning that it is unavailable to the electrons. The highest electron energies are obtained where these two effects are balanced. In the simulations, the electron energy is lower at early focus because of pump depletion in the rising edge of the target. At later foci, the spectral modifications show a gradual decrease in laser energy coupling to the plasma. These explanations suggest that the differences between simulation and experiment arise from varying laser-plasma coupling. This may be explained by the transverse distribution of laser energy, which is presented in figure 5.18 for the experiment and simulation. Despite the emergence of broad halos away from focus in the experiment, the central laser spot does not vary significantly in size within 0.5 mm from the focus. Conversely, the profile of the simulated Gaussian laser is defined to vary smoothly over z. By maintaining a similar central spot over a range of z, lasers with a range of f can drive similar wakefields, leading to more consistent levels of depletion. The effect of this would be that the negative slope obtained in the simulations in figure 5.17(b) would only start at f_{vac} sufficiently large that a significant portion of the laser is not guided. The difference in simulated and experimental laser distributions has a lower impact on the injected charge because this is still determined by the balance of geometric diffraction and self-focusing. These are determined by the vacuum focus position and laser power, respectively, and are therefore weakly influenced by transverse laser variations.

More accurate modelling of the transverse laser profile could be achieved by simulating a laser pulse comprised of multiple Gaussian modes. This should result in lower overall laser energy coupling to the plasma, which would reduce the simulated electron beam energies to be more consistent with the experimental results.

The study was limited to the maximum energy and total charge of the electron beam. However, EuPRAXIA also has strict requirements on the energy spread, which must be $< 5\,\%$. Analysis of the energy spread done in refs. [182, 184] found a clear optimum in

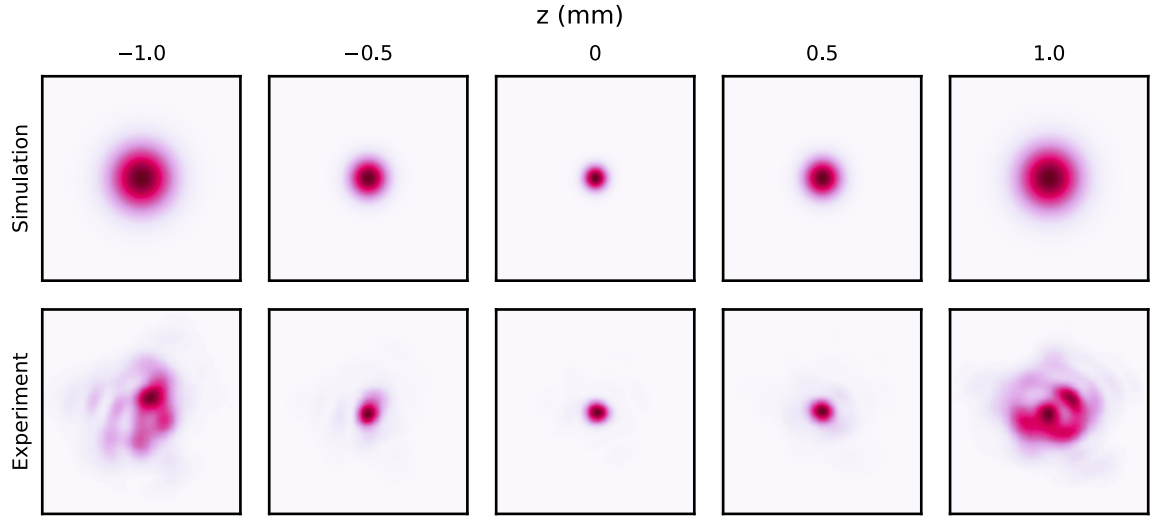

Figure 5.18: Normalised laser energy distribution in the transverse plane for simulation (top) and experiment (bottom) as a function of z position from focus. The experimental results were taken from ref. [182].

the experiment which was different to the optimum for the beam energy and charge. However, in the simulations, the accelerated electron beams had similar peaked spectra for all f_{vac}. This suggests that the simulated dynamics are simplified compared to the experiment.

5.5 Transmitted pulse shape measurements

A follow-up experiment was conducted at the Lund Laser Centre to further develop the laser-plasma injector for the EuPRAXIA project. The experimental setup was similar to that described in section 5.1. Upgrades to the laser system changed the pulse duration to 38 fs (FWHM) and the focal spot to 16 µm; the pulse energy increased from 0.7 J to 1 J. This resulted in an $a_0 = 2.02$. Moreover, an online Mach-Zehnder interferometer was added and changes were made to the post-interaction laser diagnostics. Two wedges were placed in front of a $f = 700$ mm lens to collect the laser after the interaction. A pick-off mirror transported the centre of the collimated beam onto a Swamp Optics Grenouille, which measured the FROG trace in a single shot to obtain the full temporal and spectral information of the laser. The FROG comprises a progression from the spectrometer used in the previous campaign, as it is expected to reveal the spectral modifications undergone by different regions of the laser pulse. This was found to be informative in simulations.

The Grenouille data was captured by a low dynamic range 8 bit camera. This resulted in noisy data. As the FROG trace has N^2 data points that are used to calculate $2N$ phase points of $E(t)$, there is an over-determination of the pulse shape and phase. This, in conjunction with the fact that the noise does not follow the mathematical constraint of the SHG FROG (section 3.5.2), enables the retrieval algorithm to reproduce a pulse that is more accurate than the original noisy trace. As a result, the retrieved intensity and phase can achieve 1 % RMS errors [132]. However, many shots presented low laser transmission, which was exacerbated in the FROG measurements by the SHG crystal. The very low signal to noise ratio in the FROG trace for these shots meant that the measurements were unsuitable for further analysis.

5.5.1 FROG trace processing

A systematic artefact was identified in the FROG measurements, as shown in figure 5.19(a). The artefact appeared in the same region of the image independent of the laser transmission, the initial pulse shape and spectral modifications; however, its structure did vary from shot to shot. As the Grenouille was fully enclosed, this artefact was attributed to stray reflection inside the diagnostic. Its high signal even when the FROG trace was very faint suggests that it was light at the fundamental frequency.

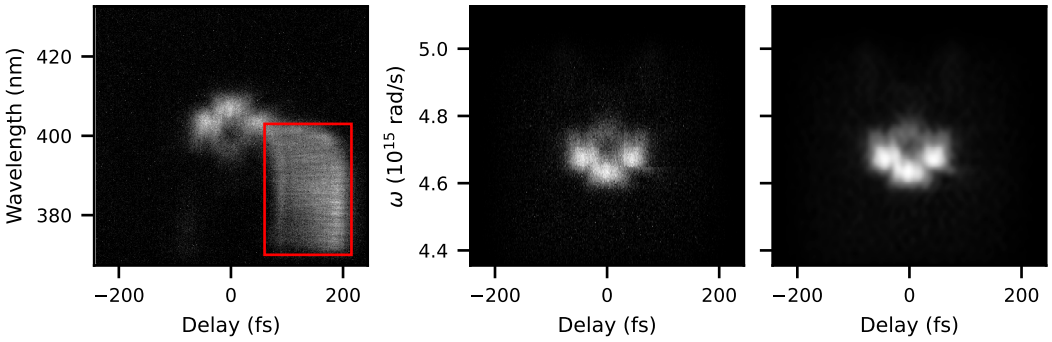

Figure 5.19: Image processing of a FROG trace. (a) Raw measurement, showing a bright artefact. (b) The pixels in the region of the artefact are replaced by those at the equivalent negative delays. (c) A low pass filter is employed to delete hot pixels and reduce noise.

Processing of the measured FROG traces was done to disregard the unphysical artefact so that the pulse retrieval could be performed. The region affected by the artefact was identified from high pressure shots whose FROG traces otherwise had very little signal. As the structure within the artefact varied between shots and days, it could not always be successfully removed by background subtraction. Instead, a mirroring of

the FROG trace was performed only within the region affected by the artefact. The result of this is shown in figure 5.19(b). This required an accurate identification of the symmetry axis. While the Grenouille is aligned so that the FROG trace is centred on the camera, this was not always the case for the data, meaning that the laser had some pulse front tilt.

Further image processing techniques could be used to improve the signal to noise ratio, and therefore the quality of the retrieved pulse. A background subtraction was performed, where the background value was taken to be the average of pixels at large delay. This removed contributions of incoherently scattered light. Then, a 2D low pass filter was implemented. This suppressed the high spatial frequencies, thereby smoothing the data. The low pass filter presents an advantage over the median filter of not broadening the FROG signal, which would produce unphysical traces. Though not necessary for every trace, as the retrieval algorithm can deal with noise, the low pass filter was useful for low signal shots. An example of its effect is shown in figure 5.19(c).

5.5.2 Vacuum results

A few FROG measurements were taken with the laser propagating through vacuum. These enabled characterisation of the laser pulse before the interaction, as a dedicated pre-interaction FROG diagnostic was not available. The FROG traces in vacuum were saturated by the high transmission. The saturation was compensated by performing two Gaussian fits to the horizontal and vertical lineouts of the FROG trace at $\tau = 0$ and $\Delta\omega = 0$ and substituting the pixel values $> 95\,\%$ of the maximum by the results from the fits. The resulting processed image is shown in figure 5.20(a), with the FROG reconstruction in (b) and retrieved laser pulse in (c).

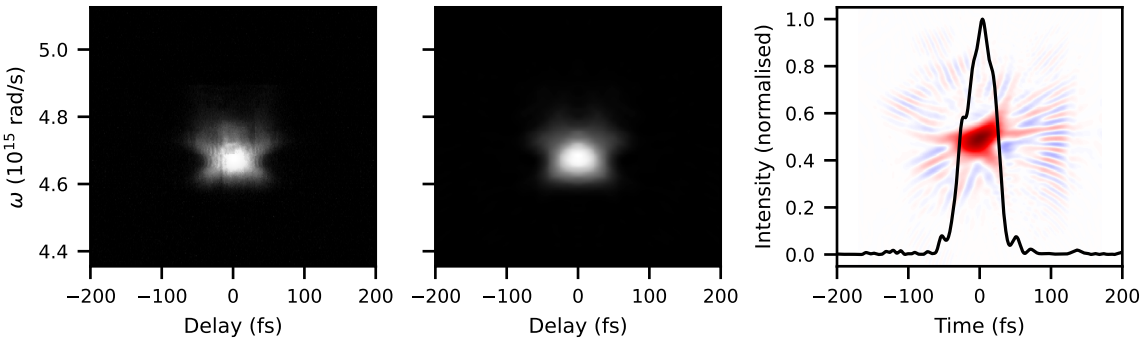

Figure 5.20: FROG measurement (a) reconstruction (b) with $< 1.5\,\%$ error and retrieved laser intensity and phase (c) from a vacuum shot.

The reconstruction algorithm successfully converged within 200 iterations. The re-

trieved pulse is measured to have a FWHM duration of 50 fs and a quadratic phase. As the transmitted laser pulse travels through a lens and the chamber window on its way to the Grenouille, it suffers from group delay dispersion (GDD), which is characterised by a second order spectral phase (section 2.2.1). Assuming that the input laser had optimal compression, $\tau_{\mathrm{FWHM}} = 38\,\mathrm{fs}$ with a flat spectral phase, the retrieval can be used to determine the the effect of the optics on the pulse.

Consider adding a GDD, $\varphi(\omega) = \beta\omega^2$, to a laser pulse defined in the frequency domain (2.35),

$$\tilde{E}(\omega) = E_0\sqrt{\frac{\pi}{a}}\exp\left(-\frac{\omega^2}{4a} + i\beta\omega^2\right), \tag{5.4}$$

where $a = \tau_{1/e}^{-2}$ with $\tau_{1/e}$ the $1/e^2$ pulse duration at optimal compression. Then the time representation can be computed through the inverse Fourier transform of (5.4), giving a pulse with amplitude

$$\begin{aligned} E(t) &= E_0\sqrt{\frac{\pi}{a}}\frac{1}{2\pi}\int_{-\infty}^{\infty}\exp\left(-\frac{\omega^2}{4a} + \beta\omega^2 + i\omega t\right)\mathrm{d}\omega \\ |E(t)| &\propto \exp\left(-\frac{at^2}{1+16a^2\beta^2}\right). \end{aligned} \tag{5.5}$$

This means that the pulse duration is extended to

$$\tau'_{1/e} = \tau_{1/e}\sqrt{1+\left(\frac{4\beta}{\tau_{1/e}^2}\right)^2}. \tag{5.6}$$

Rearranging (5.6) for β and using the pulse duration at optimal compression as τ and the measured pulse duration as τ' gives a GDD of $\beta \approx 450\,\mathrm{fs}^2$. This figure is consistent with laser transmission through the 8 mm thick N-BK7 lens and the 3 mm thick fused silica window, which give a combined GDD of $468\,\mathrm{fs}^2$ [193]. Using this, the GDD imparted by the post-interaction optics could be undone multiplying the retrieved pulse electric field in the frequency domain by $\exp(-i\beta\omega^2)$.

5.5.3 Density scan

Figure 5.21 shows the measured FROG traces for the pulse after interacting with plasma at different densities. At the lowest density, the FROG trace comprises a narrow bandwidth signal centred approximately at the second harmonic frequency of the input laser. No electrons were measured for this shot which suggests that self-focusing has not taken place to enable the laser intensity to exceed the ionisation threshold for N^{5+}. This is consistent with the n_e^{-2} dependence of the critical power for relativistic self focusing. Sig-

nals at higher frequencies emerge at $1.9 \times 10^{18}\,\mathrm{cm}^{-2}$ and $2.8 \times 10^{19}\,\mathrm{cm}^{-2}$, which suggests that photon acceleration is taking place. This indicates that a wakefield is driven with a plasma wavelength $\lesssim c\tau$. Accelerated electrons are measured from $2.8 \times 10^{18}\,\mathrm{cm}^{-2}$. By $3.9 \times 10^{18}\,\mathrm{cm}^{-2}$, the redshifts are significant enough that the FROG signal approaches the long wavelength limit of the diagnostic, implying significant laser energy transfer to the plasma. Stronger pump depletion at higher densities meant that the full pulse was not captured by the diagnostic. As a result, the FROG retrieval could not be accurately performed for shots at high densities.

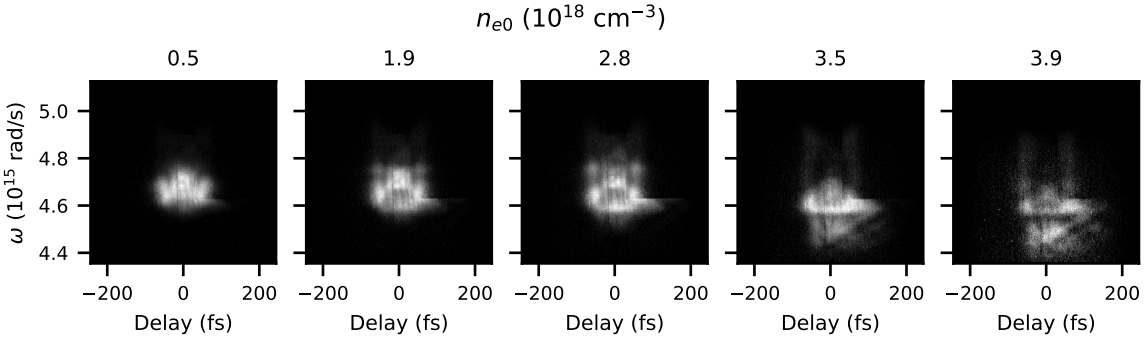

Figure 5.21: Normalised FROG measurements after image processing for five shots under different plasma densities.

In an attempt to retrieve information from the FROG measurements even when the reconstructions failed due to an incomplete pulse, the total counts on the FROG and a measure of the spectral width were obtained from the processed FROG traces. The results for a pressure scan are plotted in figure 5.22 against the measured electron beam charge and energy for every shot. The spectral width was calculated as the 5^{th} to 95^{th} percentile of the FROG delay marginal and is a measure of laser modifications. Analysis of the electron spectrometer data was performed by L. Dickson and described in ref. [184]. Here the maximum energy is defined as the energy at which the spectra $\mathrm{d}Q/\mathrm{d}E$ decreased to 10 % of its peak value.

Stronger spectral modulations are correlated with increased electron charge as shown in figure 5.22(a). However, this relationship is not necessarily causal. The higher injected charge is obtained at higher densities, which is likely a combination of the increased electron availability and the increased rates of self-focusing. At the same time, pump depletion is stronger at higher densities due to the increased density gradients leading to significant redshifting, while the decreasing plasma wavelength allows for increased photon acceleration as the back of the laser reaches a decreasing plasma density gradient. A similar positive trend is retrieved between the maximum energy and spectral

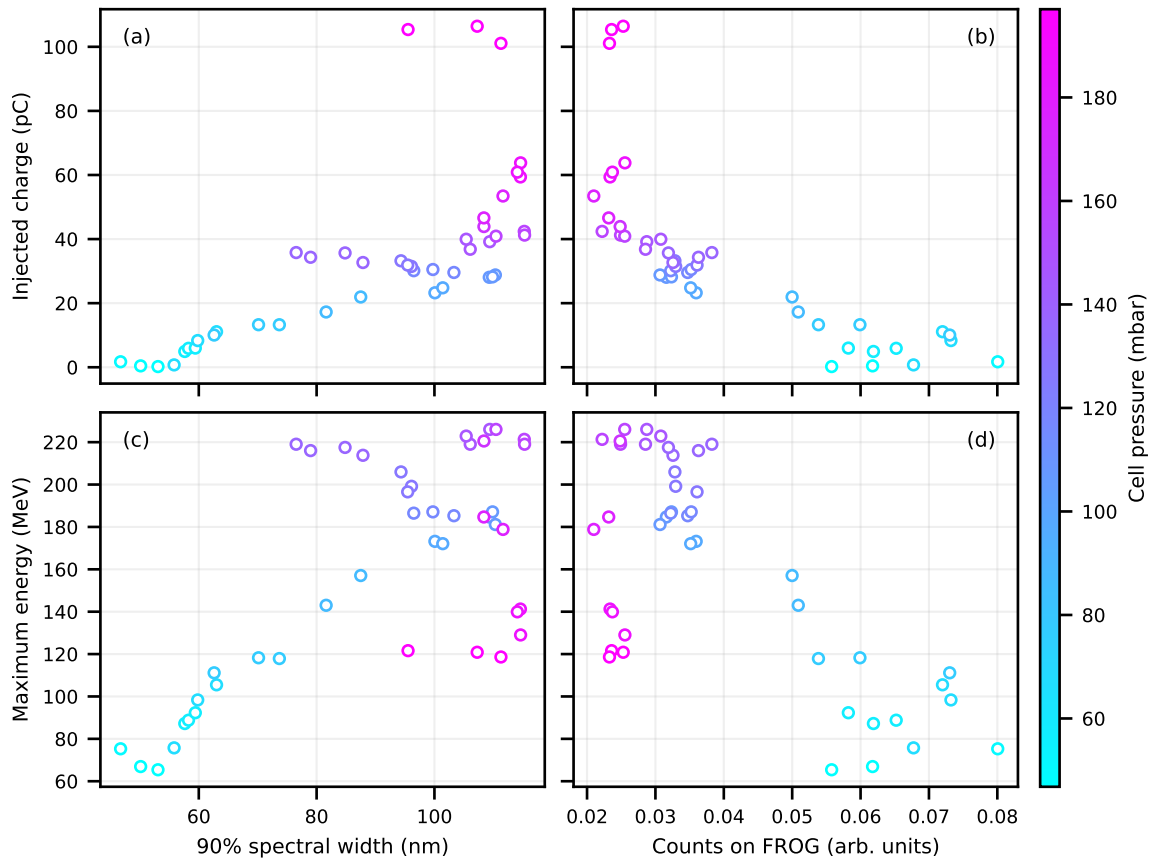

Figure 5.22: Correlations of post-interaction laser measurements obtained from the FROG trace with electron beam charge (top) and maximum electron beam energy (bottom).

width in figure 5.22(c), though with many outliers. There is a maximum to the spectral width that can be measured, which is $\approx 120\,\text{nm}$. Therefore, lasers which undergo more photon acceleration will be incorrectly characterised by this metric, as observed at high densities (magenta). The trends of electron beam parameters with counts on the FROG shown in figure 5.22(b) and (d) also show strong dependences. Similarly to the results from the previous experiment presented in section 5.2, low transmission is correlated with higher maximum energies. Here there is also a minimum transmission value. In contrast to the spectral data for the focus scan, the charge presents a clear linear trend with transmission, excluding the highest density data. The results suggest that the observed transmission and spectral modifications are likely dominated by the increased depletion at higher densities. While not very informative about the differences in the dynamics at every shot, this is further evidence for the use of transmitted laser data as a measure of density.

5.5.4 Discussion

The data presented here comprises a small selection of FROG measurements that could reveal some information about the interaction in the experiment. In general, the FROG measurements were found to have severe limitations. The low dynamic range of the camera resulted in noisy images with little detail when the laser transmission was low. As low transmission in the wavelength range captured is found to be a sign of efficient acceleration, this meant that the data for shots with the most interesting dynamics were unavailable.

As seen in the pressure scan, the FROG measurement was clipped by the diagnostic at densities $\gtrsim 4 \times 10^{18}\,\mathrm{cm}^{-2}$. The FROG captured a wavelength range equivalent to 735 nm to 865 nm in the fundamental harmonic. This is smaller than the range of the spectrometer used in the previous experiment. In comparison, the simulations of section 5.3 show that the laser undergoes redshifts up to 900 nm on average, with the longest wavelength components of the spectrum reaching wavelengths beyond 1 µm. This meant that the wavelength range spanned by the Grenouille was too small to capture the frequency shifts achieved in the experiment. In contrast, successful FROG measurements of the post-interaction laser in a wakefield accelerator have measured frequency shifts up to 880 µm in low plasma densities $\lesssim 1 \times 10^{18}\,\mathrm{cm}^{-3}$ [134, 179], where no electrons were accelerated. The narrow wavelength range of the Grenouille is likely a result of the strict phase-matching requirements of the SHG crystal [132]. The large bandwidth of the transmitted laser evidenced in simulations is unlikely to fulfil this condition, which means that FROG may not be the most appropriate diagnostic for strongly modified laser pulses.

The implementation of a post-interaction laser spectrometer in addition to the FROG would be beneficial. By comparing the calculated frequency marginal of the retrieved pulse to its known functional form for SHG FROG (section 3.5.1), the spectrum can help uncover systematic errors. In addition, the spectrum enables these systematic errors to be corrected in the post-processing of the measured traces [132]. This is crucial for SHG FROG, as, unlike other FROG geometries, convergence of the retrieval algorithm does not necessarily indicate a correct pulse measurement. This is because of the time ambiguity and symmetry. The study would also benefit from a pre-interaction FROG diagnostic for reference so that the pulse modifications occurring during the interaction can be isolated from deliberate changes to the incoming laser pulse.

In summary, using FROG to diagnose a laser driving wakefield acceleration can provide some useful information about the depletion of the laser and the strength of the driven wakefields, which are found to be correlated with electron beam parameters.

However, practical use of the diagnostic presents many difficulties which prevented its full exploitation in retrieving the complete laser profile. In particular, it appears to be unsuitable for pulses with large bandwidth. As a result, the FROG measurements provided similar information as the transmitted spectra measurements discussed in section 5.2. This suggests that a simpler laser spectrometer may be sufficient to characterise the modifications to a wakefield accelerator laser driver, as it was not possible to take advantage of the benefits provided by FROG. Further consideration and testing of the experimental setup may be needed for successful use of FROG. Demonstrating the power of this optical diagnostic would likely require a dedicated experiment.

Chapter 6

Conclusions

Laser wakefield acceleration is a complex process that is highly sensitive to the the plasma target conditions and the evolution of the laser driver. The work presented in this thesis adds to the understanding of electron injection and acceleration dynamics under conditions that are relevant for applications in particle physics, medicine and XFELs. This is achieved by examining the effect of target fluctuations and studying the evolution of a laser as it drives a plasma wakefield. These studies are necessary to accelerate the development of these novel sources and present a path towards the stable electron beams required for future applications.

6.1 Stability of density transition injected electron beams

Controlling injection enables improved shot-to-shot stability of the electron beams generated through laser wakefield acceleration. However, large shot to shot fluctuations of electron beam parameters were observed in an experiment using density transition injection. This suggested that further study into the stability of these dynamics was necessary.

The experiment used a razor blade positioned in a supersonic gas jet to produce a tailored target with a decreasing density gradient. Interferometry measurements of the target density revealed that correlated peak and plateau densities are indicative of a change in gas backing pressure, while a lack of correlation between the densities implies motion of the blade in the gas. The target fluctuations were characterised for the plateau density, peak density and ramp position. While the experiment was not designed as a stability study, the data provides accurate estimates of the shot-to-shot

target fluctuations that are relevant to a wide range of target profiles used in LWFA. Therefore, this type of analysis could be repeated for any LWFA experiment to improve understanding of target stability.

A sensitivity study to the experimentally measured shot-to-shot target fluctuations using PIC simulations revealed that the electron charge and maximum energy are very sensitive to variations in $n_e^{-1}\mathrm{d}n_e/\mathrm{d}z$, which cause changes in the injection dynamics. As a result, changes in the peak density independent of the plateau density dominate the variations of both the injected charge and maximum electron beam energy. These variations would be caused by fluctuations of the blade position in the gas target. Variations in the ramp steepness exacerbate this effect.

In contrast, correlated changes of the peak and plateau densities result in equal reduction of the wakefield phase velocity, meaning that the injection dynamics are consistent. The simultaneous increased wakefield amplitude and decreased plasma wavelength occurring at higher plateau densities offset the injection occurring farther forward due to higher peak densities. This results in the electrons witnessing very similar accelerating fields despite the density fluctuations. As this type of target variation occurs due to fluctuations in the target backing pressure, this strongly indicates that the fluctuations observed in the experimental data are more likely a result of a fluctuating blade rather than a variation in gas pressure. Therefore, the use of a more rigid obstruction to generate the down-ramp would be beneficial for the stability of the accelerator.

Variations in the length of the density down-ramp cause different effects on the injected charge depending on the regime involved. The decrease in injected charge with increasing length for long-scale ramps is described by the 1D evolution of the wakefield phase velocity in the ramp. However, this theoretical variation prevents injection in ramps where injection is observed in simulation. While the laser evolution causes further reduction of the phase velocity, it is insufficient to account for the injection observed. The results suggest that two dimensional effects such as transverse injection have a significant effect in the simulated non-linear regime. This will require further investigation.

In contrast to long-scale density ramps, the injected charge is found to increase with ramp length in sharp density transitions. This is because the initial conditions for electrons to inject are increasingly restrictive as the transition length $\to 0$. In addition, the injection dynamics are more complicated in sharp transitions with a longer length scale. As the position of the density transition is less well defined, electrons originating in very similar regions of phase space can end up in a highly organised distribution over an extended region after injection. This new evidence of the behaviour and acceleration of

electrons injected in very short ramp suggests potential for further tunability of electron beam energy and emittance through precise control of the target profile.

The strong beam-loading caused by the sudden injection in sharp transitions counteracts the benefits of having highly localised injection. This is exacerbated for lower laser intensities, where beam-loading dominates over the laser-driven wakefield. Therefore, driving a weakly non-linear wake in a target with a sharp density transition may not be desirable. Instead, long-scale density ramps are preferred in terms of beam spectral quality. However, the analysis neglects injection in further periods of the wakefield, which may be undesirable.

6.2 Evolution of a wakefield acceleration laser driver

The post-interaction laser spectrum was found to provide useful information about the laser-plasma interaction, which could indicate trends in the injected charge and electron beam energy. An empirical relation between the wavelength and amplitude of secondary peaks with density enables the transmitted spectra to work as a secondary density diagnostic. This could be particularly useful for stability measurements. Moreover, the laser transmission at low wavelengths gives an indication of the laser energy that is not coupled to the plasma due to a lack of guiding, as well as the energy that the laser takes back from the wakefield via photon acceleration. The transmitted laser energy below 900 nm is negatively correlated with maximum electron beam energy in a focus scan and with injected charge in a cell pressure scan.

The experiments show that obtaining the electron beams with the highest energies requires a balance between coupling laser energy into the plasma and taking energy back from the plasma via photon acceleration. These effects can be measured through diagnosis of the transmitted laser pulse. When part of the laser is not guided, the post-interaction spectrum shows a large component in the wavelength range that matches the pre-interaction laser. This corresponds to energy that is not transferred to the plasma, and is observed when focusing too far into the target. However, when driving a strong wakefield with $c\tau \sim \lambda_p$, photon acceleration can occur which manifests itself as a strong blueshifted signal. While the unshifted and blueshifted components proved to be informative, the simulations revealed that the strongly redshifted light is the best indicator of the acceleration dynamics. Measuring this in experiment requires the use of spectrometers sensitive to wavelengths above 900 nm.

The simulations provide insights into the relation between laser parameters and electron beam parameters. The self-focusing of the laser was shown to be crucial in

determining the ionisation injection dynamics in a tailored target at moderate intensities. While relying on laser evolution to control the injection region allows peaked electron spectra to be obtained, the dynamics are very sensitive to laser focusing. The geometric diffraction determined by the vacuum focus position must be balanced by the self-focusing determined by the laser power. The dynamics which cause the laser to reach its peak a_0 and minimum width the earliest result in the highest injected charge, even if a different setup reaches a higher peak a_0.

Similarly, the peak a_0 is not the best indicator of the strength of the driven wakefields, as it does not take into account the buildup of the wakefield strength throughout the interaction. Instead, the electrons with the highest energies were obtained where the laser a_0 remained high over the longest region after injection, demonstrating that it is the laser evolution, and not any instantaneous value, which determines the acceleration dynamics. This was influenced by wakefield guiding of the laser, which closely followed the matched spot size in the latter half of the interaction.

6.3 Influence of laser focusing

The two results chapters present different aspects of LWFA. While chapter 4 studies the fluctuations of a gas jet and blade target driving density transition injection, chapter 5 examines the laser evolution driving ionisation injection in a tailored gas cell. However, the studies have in common the complex interplay between the laser dynamics and the tailored density profile. This has been shown to be critical to the injection and acceleration dynamics in both studies.

Both longitudinal and transverse motion of the blade in the gas jet cause variations in the longitudinal position of the density ramp, which is equivalent to changes in the vacuum laser focus position. Simulations of these variations reveal an asymmetry to the deviations of injected charge when the laser is focused before and after the density transition. These charge variations are comparable to the intensity deviations at the ramp, which indicates that they are caused by differences in the laser evolution. The fluctuations are reduced when the laser is focused before the density ramp because differences in the initial intensity are compensated by self-focusing.

These findings are consistent with the measurements of the transmitted laser in the study of ionisation injection. When the laser is set to focus too far into the target, the plasma guiding adds to the geometric focusing to over-focus the laser, which leads to severe variations in the pulse width and a_0 over the interaction region. An earlier vacuum focus allows more gradual effective focusing which results in a more stable a_0

as the pulse gets close to the matching condition. This means that the laser reaches similar a_0 with the $f_{\text{vac}} \leq 0$, but the results are more variable for the different f_{vac} with late focusing, thereby explaining the results from the target sensitivity study.

The lack of stability when focusing later in the target was also observed, as the electron beam energies obtained in two runs with different laser spectral phase disagreed only for these foci. However, experimental results with the laser set to focus very early in the target presented significant shot-to-shot fluctuations of the maximum electron beam energy. This suggests that there is a limit to the improved stability achieved at early foci that was found in the density sensitivity study. Due to the difference in target profile and injection mechanism for the two studies, further work is required to identify this limit for the target produced by a blade in a gas jet.

6.4 Laser wakefield acceleration performance

Present laser wakefield accelerators can generate nanocoulomb-level electron beams with multi-gigaelectronvolt energies and sub-percent energy spread. These parameters are becoming comparable to state-of-the art RF accelerators, which has driven the interest in user facilities for compact plasma-based radiation sources and the potential for linear particle colliders. However, these applications are hindered by the difficulty in achieving all of the optimal parameters simultaneously with LWFA. This indicates that stability remains an outstanding challenge.

The work in this thesis contributes to the performance requirements of LWFA by performing dedicated studies of stability and the sources of fluctuation. These types of sensitivity studies are lacking, despite being crucial to define the required level of control and acceptable tolerances for a reliable accelerator. Therefore, this work addresses the need for improved understanding of fluctuations, which enables the identification of the dominant sources of instability and of regimes of improved stability.

For the density ramp injection setup considered in chapter 4, the sources of experimental density fluctuations were identified as the variable gas jet pressure and the variations of blade position from shot to shot. The magnitude of these density fluctuations were measured as $\sim 10\,\%$ from a dataset with few repeats for the first time. This characterisation was used in a systematic stability study of the effect of plasma density on electron beam parameters. The injected charge and maximum electron beam energy were found to vary by up to $9\,\%$ and $15\,\%$, respectively. The current performance is sufficient for betatron x-ray and radiobiology applications but will require improved stability for free electron lasers.

The study revealed that a more robust method of producing the density ramp could improve the charge stability by a factor of 2 and the energy stability by a factor of 3. For density stability limited by gas pressure variations, obtaining sub-percent level fluctuations in the electron beam parameters would require improvements of fluctuations in the gas system to be below 2 %. The stability of various gas systems needs to be measured to determine if these performance requirements are met. These considerations will help define the parameters of operation of future facilities.

The studies also show that density ramp injection successfully decouples laser energy fluctuations from electron beam energy, but these need to be < 1 % to obtain sub-percent charge stability. Such laser energy stability is expected for the EuPRAXIA facility owing to ongoing laser development [49]; currently < 2 % laser energy fluctuations have been reported at multiple facilities [30, 194].

6.5 Future work

The injection and acceleration dynamics of electrons injected through density transition injection have been shown to be very sensitive to the precise density profile of the target. The low magnification interferometry used in the experiment was unable to provide an accurate representation of the density ramp. Using a higher magnification diagnostic on shot would provide a better idea of the density ramp regime that is used and improve sensitivity at low densities. This could be combined with offline tomographic reconstruction of the density ramp to provide a complete 3D description of the target. Tomography would reveal additional target parameters such as ramp length and angle, whose fluctuations could then be characterised and used in further PIC simulations for additional target sensitivity studies. The use of tomography would present benefits over fluid simulations, which have limitations when the gas is expanding into vacuum.

In addition, the setup used to produce the density transition needs to be optimised. Offline characterisation of blade motion and damage using the present setup should inform future designs so as to be more robust. Alternatively, a setup with no moving parts could be conceived, as oblique shocks can be produced in supersonic nozzles by introducing sharp features and breaking the cylindrical symmetry [195]. A density profile suitable for density transition injection has been demonstrated using a shocked nozzle with a 300 µm opening [54], but a millimetre-scale design has not been proposed. Improved gas nozzle design, in conjunction with a robust density tailoring setup, should produce measurable improvements in the stability of the density profiles and therefore

in the reproducibility of the accelerated electron beams.

Transverse injection in decreasing density ramps requires further study, as the current 1D theory cannot fully describe the observations from simulations. The conditions for enhanced transverse injection need to be identified for both sharp and long-scale transitions. This may enable control over the electron beam emittance and the ability to optimise betatron emission, which would be of interest for future applications.

The measurements of laser pulse modifications while driving wakefield acceleration have been shown to provide useful information about laser-plasma coupling and comprise a good indicator for the electron beam parameters. However, the use of FROG to learn about the pulse shape and chirp was unsuccessful. This can be attributed to the strict phase-matching conditions in the SHG crystal, which limit the bandwidth that can be diagnosed. Instead, the transmitted spectra is found to be a more effective diagnostic. However, the spectral range of the spectrometer needs to be extended to enable a more direct measurement of laser-plasma coupling. This would allow the features of the laser that contribute most to pump depletion and those which take energy back from the wakefield to be identified.

Further consideration and testing of the experimental setup is needed for successful use of FROG, for example by using multiple devices across the transmitted laser bandwidth. A camera with higher dynamic range should enable more accurate retrieval even for shots with low transmission. This would reveal the laser modifications associated with the most useful electron beams. Moreover, the implementation of a post-interaction laser spectrometer in addition to the FROG would allow for systematic errors to be identified and corrected. The study would also benefit from a pre-interaction FROG diagnostic. This would provide a reference so that the pulse modifications that take place during the interaction can be isolated from deliberate changes to the incoming laser pulse, which are known to subtly affect the interaction dynamics. This all indicates that demonstrating the power of optical diagnostics would likely require a dedicated experiment.

Appendix A

Appendices

A.1 Gaussian beam focusing

The following derivation of Gaussian optics follows the standard approach as given in [196].

The wave equation can be obtained from Maxwell's equations by computing $\nabla \times \nabla \times \vec{E}$ to obtain

$$\nabla^2 \vec{E} - \frac{n^2}{c^2} \frac{\partial^2 \vec{E}}{\partial t^2} = 0, \tag{A.1}$$

where n is the refractive index of the medium and c is the speed of light. Assuming a wave propagating in the z direction of the form

$$E(x, y, z, t) = E_0 \Psi(x, y, z) \exp\big(i(\omega t - kz)\big) \tag{A.2}$$

yields the Helmholtz wave equation,

$$\nabla_T^2 \Psi - 2ik \frac{\partial \Psi}{\partial z} + \frac{\partial^2 \Psi}{\partial z^2} = 0, \tag{A.3}$$

where ∇_T^2 is the transverse Laplacian operator. In the paraxial approximation, the smallest term $\frac{\partial^2 \Psi}{\partial z^2}$ is neglected to obtain

$$\frac{1}{r} \frac{\partial}{\partial r} \left(r \frac{\partial \Psi}{\partial r} \right) - 2ik \frac{\partial \Psi}{\partial z} = 0 \tag{A.4}$$

in cylindrical coordinates.

The Gaussian solutions to (A.4) take the form:

$$\Psi = \exp\left(-i\left(P(z) + \frac{kr^2}{2q(z)} \right) \right), \tag{A.5}$$

where $q(z)$ is allowed to be a complex variable to account for both the Gaussian envelope and the curvature of the wavefronts, and $P(z)$ is an additional longitudinal phase.

Substituting the solution (A.5) into the wave equation (A.4) gives an equation for $P(z)$ and $q(z)$,

$$\left[\left(\frac{k^2}{q^2(z)} (q'(z) - 1) \right) r^2 - 2k \left(P'(z) + \frac{i}{q(z)} \right) \right] \Psi = 0, \tag{A.6}$$

where both terms in brackets must be solved independently for the equation to hold for all r. Solving the first term gives

$$q(z) = z + iz_R, \tag{A.7}$$

such that the $z = 0$ solution has the required Gaussian form $\exp(-kr^2/2z_R)$. Through the $z = 0$ solution, z_R can be related to the physical parameter w_0, which is the spot size of the laser beam, via

$$z_R = \frac{n\pi w_0^2}{\lambda}. \tag{A.8}$$

z_R is known as the Rayleigh range, which is the distance from the focus over which the laser's electric field amplitude decreases to a factor of $1/e$ of the peak. Equivalently, it is the distance over which the area of the beam doubles compared to the waist at $z = 0$.

By considering the inverse of $q(z)$,

$$\frac{1}{q(z)} = \frac{z}{z_0^2 + z^2} - i\frac{z_0}{z^2 + z_0^2}, \tag{A.9}$$

Ψ can be retrieved as

$$\Psi(r, z) = \exp\left(-\frac{kr^2 z_R}{2(z^2 + z_R^2)} \right) \exp\left(-i\frac{kr^2 z}{2(z^2 + z_R^2)} \right) \exp(-iP(z)). \tag{A.10}$$

The first term in (A.10) is a Gaussian in r with a $1/e$ half-width $w(z)$ given by

$$\begin{aligned} w^2(z) &= \frac{2(z^2 + z_R^2)}{kz_R}, \\ &= w_0^2 \left[1 + \left(\frac{z}{z_R} \right)^2 \right]. \end{aligned} \tag{A.11}$$

The second term in (A.10) constitutes an additional phase (recall that the plane wave phase kz appears in the full solution of E in (A.2)). It corresponds to the wave picking up more phase further off axis, which results in the wavefronts being curved parabolically. Thus, a radius of curvature $R(z)$ can be defined as

$$R(z) = z\left[1 + \left(\frac{z_R}{z}\right)^2\right]. \tag{A.12}$$

At $z = 0$, which corresponds to the focus, $R(z = 0) = \infty$ and a plane wave is retrieved. At very large z, again $R \to \infty$, as the beam expands and the wavefronts appear locally planar.

The expression for $R(z)$ can be used to rewrite $q(z)$ as

$$\frac{1}{q(z)} = \frac{1}{R(z)} - i\frac{\lambda}{n\pi w^2(z)}, \tag{A.13}$$

which can be used to obtain local information about the laser at any z, while q can provide information about the laser's focus.

Now that $q(z)$ is known, solving for $P(z)$ in (A.6) gives

$$\begin{aligned} P(z) &= \ln\left(1 - i\frac{z}{z_0}\right), \\ &= \ln\sqrt{1 + \left(\frac{z}{z_0}\right)^2} - i\arctan\left(\frac{z}{z_0}\right), \end{aligned} \tag{A.14}$$

and

$$\exp\left(-iP(z)\right) = \frac{w(z)}{w_0}\exp\left(-i\arctan\left(\frac{z}{z_0}\right)\right). \tag{A.15}$$

The resulting amplitude term describes how the electric field decreases as the beam spreads, consistent with the definition of the Rayleigh range as the $1/e$ beam half-width in z. The exponential term corresponds to a longitudinal phase known as the Gouy phase. It describes a real wave picking up π more phase than a plane wave as it passes through focus due to its finite radial extent.

The full expression for the electric field of a Gaussian mode is then:

$$\begin{aligned} E(r,z,t) = E_0 \frac{w_0}{w(z)} \exp\left(-\frac{r^2}{w^2(z)}\right) \\ \times \exp\left(-i\frac{kr^2}{2R(z)}\right) \\ \times \exp\left(-i\left[kz + \arctan\left(\frac{z}{z_R}\right)\right]\right) \\ \times \exp\left(i\omega t\right), \end{aligned} \tag{A.16}$$

where each line corresponds to the amplitude, radial phase, longitudinal phase and temporal phase, respectively.

A.2 Convergence testing

The ratio of longitudinal to transverse spectral resolutions determines dispersion in PIC codes, as discussed in section 3.6.1. However, running 4 mm simulations at 60×20 cells per wavelength is unfeasible. Thus, multiple 2D EPOCH simulations were performed in order to determine the resolution requirements to sufficiently capture the laser propagation and electron acceleration dynamics. Simulations were run with $\lambda_0/\Delta x \times \lambda_0/\Delta y$ of 30×10, 40×10 and 60×20, all of which have $|v_g/c - 1| < 2 \times 10^{-3}$. The CLF condition is satisfied with $\Delta x = 0.95\Delta t$, which is the standard for EPOCH.

The simulations were run with a $I_0 = 9.8 \times 10^{18}\,\mathrm{W\,cm^{-2}}$, 12 µm and 42 fs laser propagating through a $n_e = 7 \times 10^{18}\,\mathrm{cm^{-3}}$ plasma, as in section 5.3. Figures A.1 and A.2 show the laser profile and spectrum, respectively, as a function of propagation distance. The evolution of the maximum laser intensity and laser width are also shown, as well as the laser spectra after exiting the plasma. Both the laser focusing and the structure of the spectra are well represented for all simulations. The lowest resolution simulation, 30×10, deviates from the highest resolution simulation, 60×20, by $-2\,\%$ in w and $-11\,\%$ in I_{max} by $z = 2.5$ mm. The intensity deviations are only evident in the latter half of the simulation, where they are not expected to influence the injection dynamics. While the details of the spectra vary, the 30×10 resolution appears to be sufficient to obtain qualitative insights.

The electron distribution in longitudinal position - longitudinal momentum space is shown in figure A.3, along with their spatially-integrated energy spectra after exiting the plasma. While the shape of the electron distribution is similar, lower average energies are reached in the higher resolution simulations. The lowest resolution deviates from the

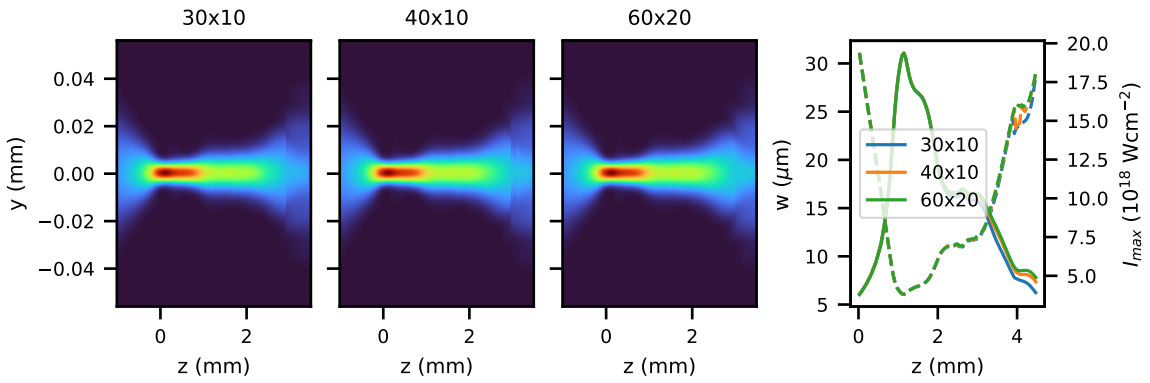

Figure A.1: Spatial laser distribution (normalised) as a function of propagation distance throughout the simulations. The right panel shows the maximum laser intensity and laser width throughout the simulation.

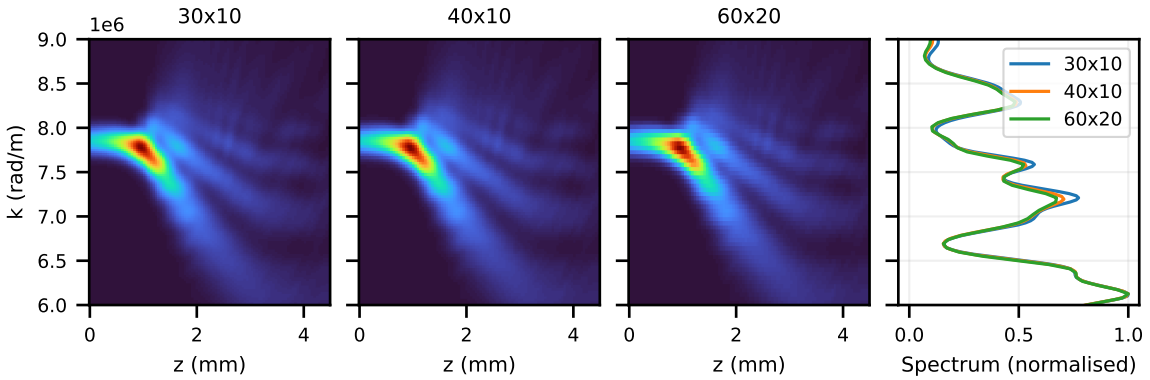

Figure A.2: Laser spectrum (normalised) as a function of propagation distance throughout the simulations. The right panel shows the laser spectra at the end of the simulation.

highest resolution simulation by 3 % in maximum energy and −4 % in injected charge. This shows that the 11 % intensity deviation in the lowest resolution simulation does not significantly affect the acceleration dynamics. Therefore, the 30 × 10 simulation is suitable to study the interaction.

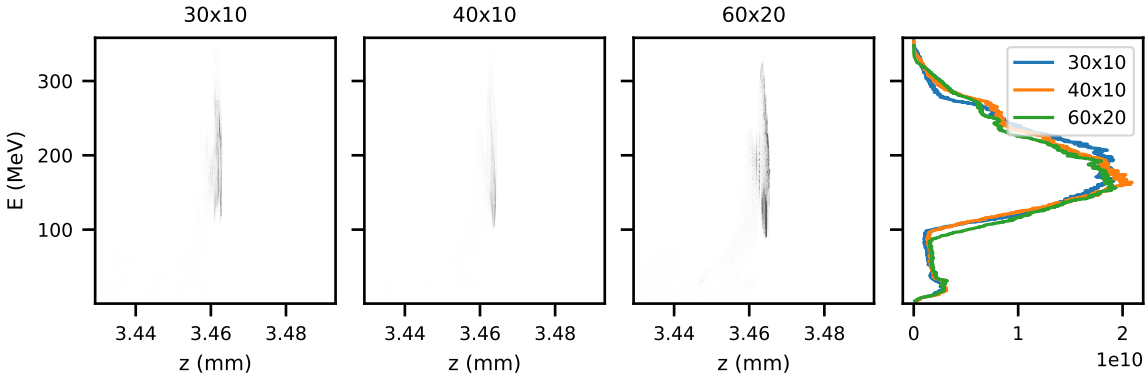

Figure A.3: Electron longitudinal position-energy distribution at the end of the simulations. The right panel shows the spatially-integrated energy spectra.

Bibliography

[1] T. Tajima and J. M. Dawson. Laser electron accelerator. *Phys. Rev. Lett.*, 43:267–270, 1979.

[2] J. M. Cole, K. T. Behm, E. Gerstmayr, T. G. Blackburn, J. C. Wood, C. D. Baird, et al. Experimental evidence of radiation reaction in the collision of a high-intensity laser pulse with a laser-wakefield accelerated electron beam. *Phys. Rev. X*, 8:011020, 2018.

[3] S. Kneip, C. McGuffey, F. Dollar, M. S. Bloom, V. Chvykov, G. Kalintchenko, et al. X-ray phase contrast imaging of biological specimens with femtosecond pulses of betatron radiation from a compact laser plasma wakefield accelerator. *Applied Physics Letters*, 99(9):093701, 2011.

[4] F. Albert, M. E. Couprie, A. Debus, M. C. Downer, J. Faure, A. Flacco, et al. 2020 roadmap on plasma accelerators. *New Journal of Physics*, 23(3):031101, 2021.

[5] E. Rutherford. LXXIX. the scattering of αand βparticles by matter and the structure of the atom. *The London, Edinburgh, and Dublin Philosophical Magazine and Journal of Science*, 21(125):669–688, 1911.

[6] ATLAS Collaboration. Observation of a new particle in the search for the standard model higgs boson with the atlas detector at the lhc. *Physics Letters B*, 716(1):1–29, 2012.

[7] A. Momose, T. Takeda, Y. Itai, and K. Hirano. Phase–contrast x–ray computed tomography for observing biological soft tissues. *Nature medicine*, 2(4):473–475, 1996.

[8] P. F. Fewster. *X-Ray Scattering from Semiconductors*. Imperial College Press, 2nd edition, 2003.

[9] United States Geological Survey. Stanford linear accelerator, 2004. Accessed: 06/12/2023.

[10] V. I. Veksler. Coherent principle of acceleration of charged particles. In *CERN Symposium on High-Energy Accelerators and Pion Physics*, 1956.

[11] M. N. Rosenbluth and C. S. Liu. Excitation of plasma waves by two laser beams. *Phys. Rev. Lett.*, 29:701–705, 1972.

[12] C. E. Clayton, C. Joshi, C. Darrow, and D. Umstadter. Relativistic plasma-wave excitation by collinear optical mixing. *Phys. Rev. Lett.*, 54:2343–2346, 1985.

[13] C. E. Clayton, K. A. Marsh, A. Dyson, M. Everett, A. Lal, W. P. Leemans, et al. Ultrahigh-gradient acceleration of injected electrons by laser-excited relativistic electron plasma waves. *Phys. Rev. Lett.*, 70:37–40, 1993.

[14] N. E. Andreev, L. Gorbunov, V. Kirsanov, A. A. Pogosova, and R. Ramazashvili. Resonant excitation of wakefields by a laser pulse in a plasma. *Jetp Letters - JETP LETT-ENGL TR*, 55, 1992.

[15] E. Esarey, J. Krall, and P. Sprangle. Envelope analysis of intense laser pulse self-modulation in plasmas. *Phys. Rev. Lett.*, 72:2887–2890, 1994.

[16] A. Modena, Z. Najmudin, A. E. Dangor, C. E. Clayton, K. A. Marsh, C. Joshi, et al. Electron acceleration from the breaking of relativistic plasma waves. *Nature*, 377:606 – 608, 1995.

[17] D. Strickland and G. Mourou. Compression of amplified chirped optical pulses. *Optics Communications*, 55(6):447 – 449, 1985.

[18] J. Faure, Y. Glinec, A. Pukhov, S. Kiselev, S. Gordienko, E. Lefebvre, et al. A laser–plasma accelerator producing monoenergetic electron beams. *Nature*, 431:541–544, 2004.

[19] C. G. R. Geddes, Cs. Toth, J. van Tilborg, E. Esarey, C. B. Schroeder, D. Bruhwiler, et al. High-quality electron beams from a laser wakefield accelerator using plasma-channel guiding. *Nature*, 431:538–541, 2004.

[20] S. P. D. Mangles, C. D. Murphy, Z. Najmudin, A. G. R. Thomas, J. L. Collier, A. E. Dangor, et al. Monoenergetic beams of relativistic electrons from intense laser-plasma interactions. *Nature*, 431:535–538, 2004.

[21] J. Couperus Cabadağ, R. Pausch, A. Köhler, O. Zarini, J. Krämer, M. Garten, et al. Demonstration of a beam loaded nanocoulomb-class laser wakefield accelerator. *Nature Communications*, 8:487, 2017.

[22] A. J. Gonsalves, K. Nakamura, J. Daniels, C. Benedetti, C. Pieronek, T. C. H. de Raadt, et al. Petawatt laser guiding and electron beam acceleration to 8 gev in a laser-heated capillary discharge waveguide. *Phys. Rev. Lett.*, 122:084801, 2019.

[23] S. P. D. Mangles, A. G. R. Thomas, M. C. Kaluza, O. Lundh, F. Lindau, A. Persson, et al. Laser-wakefield acceleration of monoenergetic electron beams in the first plasma-wave period. *Phys. Rev. Lett.*, 96:215001, 2006.

[24] A. D. Debus, M. Bussmann, U. Schramm, R. Sauerbrey, C. D. Murphy, Zs. Major, et al. Electron bunch length measurements from laser-accelerated electrons using single-shot thz time-domain interferometry. *Phys. Rev. Lett.*, 104:084802, 2010.

[25] O. Lundh, J. Lim, C. Rechatin, L. Ammoura, A. Ben-Ismaïl, X. Davoine, et al. Few femtosecond, few kiloampere electron bunch produced by a laser-plasma accelerator. *Nature Physics*, 7(3):219–222, 2011.

[26] J. Götzfried, A. Döpp, M. F. Gilljohann, F. M. Foerster, H. Ding, S. Schindler, G. Schilling, A. Buck, L. Veisz, and S. Karsch. Physics of high-charge electron beams in laser-plasma wakefields. *Phys. Rev. X*, 10:041015, 2020.

[27] J. Shaw, M. Romo-Gonzalez, N. Lemos, P. King, G. Bruhaug, K. Miller, et al. Micro-coulomb ($0.7 \pm 0.40.2$ µC) laser plasma accelerator on OMEGA EP. *Scientific Reports*, 11:7498, 2021.

[28] L. T. Ke, K. Feng, W. T. Wang, Z. Y. Qin, C. H. Yu, Y. Wu, et al. Near-GeV electron beams at a few per-mille level from a laser wakefield accelerator via density-tailored plasma. *Phys. Rev. Lett.*, 126:214801, 2021.

[29] R. Weingartner, S. Raith, A. Popp, S. Chou, J. Wenz, K. Khrennikov, et al. Ultralow emittance electron beams from a laser-wakefield accelerator. *Phys. Rev. ST Accel. Beams*, 15:111302, 2012.

[30] A. R. Maier, N. M. Delbos, T. Eichner, L. Hübner, S. Jalas, L. Jeppe, et al. Decoding sources of energy variability in a laser-plasma accelerator. *Phys. Rev. X*, 10:031039, 2020.

[31] F. Salehi, M. Le, L. Railing, M. Kolesik, and H. M. Milchberg. Laser-accelerated, low-divergence 15-MeV quasimonoenergetic electron bunches at 1 khz. *Phys. Rev. X*, 11:021055, 2021.

[32] M. Fuchs, G. Andonian, O. Apsimon, M. Büscher, M. C. Downer, D. Filippetto, A. Lehrach, C. B. Schroeder, B.A. Shadwick, A. G. R. Thomas, N. Vafaei-Najafabadi, and G. Xia. Plasma-based particle sources. *Journal of Instrumentation*, 19(01):T01004, 2024.

[33] E. Schneidmiller and M.V. Yurkov. Baseline Parameters of the European XFEL. In *Proc. of International Free Electron Laser Conference (FEL'17), Santa Fe, NM, USA,*

August 20-25, 2017, number 38 in International Free Electron Laser Conference, pages 109–112, Geneva, Switzerland, 2018. JACoW.

[34] K. Poder, M. Tamburini, G. Sarri, A. Di Piazza, S. Kuschel, C. D. Baird, et al. Experimental signatures of the quantum nature of radiation reaction in the field of an ultraintense laser. *Phys. Rev. X*, 8:031004, 2018.

[35] C. B. Schroeder, F. Albert, C. Benedetti, J. Bromage, D. Bruhwiler, S. S. Bulanov, et al. Linear colliders based on laser-plasma accelerators. *Journal of Instrumentation*, 18(06):T06001, 2023.

[36] Z. H. He, B. Beaurepaire, J. A. Nees, G. Gallé, S. A. Scott, J. R. Sánchez Pérez, M. G. Lagally, K. Krushelnick, A. G. R. Thomas, and J. Faure. Capturing structural dynamics in crystalline silicon using chirped electrons from a laser wakefield accelerator. *Scientific Reports*, 6(1):36224, 2016.

[37] G. Sarri, D. J. Corvan, W. Schumaker, J. M. Cole, A. Di Piazza, H. Ahmed, et al. Ultrahigh brilliance multi-mev γ-ray beams from nonlinear relativistic thomson scattering. *Phys. Rev. Lett.*, 113:224801, 2014.

[38] G. Sarri, W. Schumaker, A. Di Piazza, M. Vargas, B. Dromey, M. E. Dieckmann, et al. Table-top laser-based source of femtosecond, collimated, ultrarelativistic positron beams. *Phys. Rev. Lett.*, 110:255002, 2013.

[39] S. Kneip, C. Mcguffey, J. Martins, S. Martins, C. Bellei, V. Chvykov, et al. A bright spatially-coherent compact x-ray synchrotron source. *Nature Phys*, 6:980–983, 2010.

[40] J. Wenz, S. Schleede, K. Khrennikov, M. Bech, P. Thibault, M. Heigoldt, F Pfeiffer, and S Karsch. Quantitative x-ray phase-contrast microtomography from a compact laser-driven betatron source. *Nature Communications*, 6, 2015.

[41] N. D. Powers, I. Ghebregziabher, G. Golovin, C. Liu, S. Chen, S. Banerjee, J. Zhang, and D. P. Umstadter. Quasi-monoenergetic and tunable x-rays from a laser-driven compton light source. *Nature Photonics*, 8(1):28–31, 2014.

[42] W. Wang, K. Feng, K. Lintong, C. Yu, Y. Xu, R. Qi, et al. Free-electron lasing at 27 nanometres based on a laser wakefield accelerator. *Nature*, 595:516–520, 2021.

[43] M. Labat, J. Couperus Cabadağ, A. Ghaith, A. Irman, A. Berlioux, P. Berteaud, et al. Seeded free-electron laser driven by a compact laser plasma accelerator. *Nature Photonics*, 17:1–7, 2022.

[44] P. Muggli, M. Ferrario, J. Osterhoff, and B. Cros. European facilities for advanced accelerators development. *Journal of Instrumentation*, 17(05):T05008, 2022.

[45] S. Steinke, J. van Tilborg, C. Benedetti, C. G. R. Geddes, C. B. Schroeder, J. Daniels, et al. Multistage coupling of independent laser-plasma accelerators. *Nature*, 530(7589):190—193, 2016.

[46] C. A. Lindstrøm. Staging of plasma-wakefield accelerators. *Phys. Rev. Accel. Beams*, 24:014801, 2021.

[47] V. Shiltsev and F. Zimmermann. Modern and future colliders. *Rev. Mod. Phys.*, 93:015006, 2021.

[48] C. Emma, J. Van Tilborg, R. Assmann, S. Barber, A. Cianchi, S. Corde, et al. Free electron lasers driven by plasma accelerators: status and near-term prospects. *High Power Laser Science and Engineering*, 9:e57, 2021.

[49] R. W. Assmann et al. EuPRAXIA conceptual design report. *European Physical Journal - Special Topics*, 229(24):3675–4284, 2020.

[50] C. Pellegrini. The history of x-ray free-electron lasers. *The European Physical Journal H*, 37, 2012.

[51] F. Albert and A. G. R. Thomas. Applications of laser wakefield accelerator-based light sources. *Plasma Physics and Controlled Fusion*, 58(10):103001, 2016.

[52] S. Cipiccia, S. M. Wiggins, R. P. Shanks, M. R. Islam, G. Vieux, R. C. Issac, and Bothers. A tuneable ultra-compact high-power, ultra-short pulsed, bright gamma-ray source based on bremsstrahlung radiation from laser-plasma accelerated electrons. *Journal of Applied Physics*, 111(6):063302, 2012.

[53] V. Senthilkumaran, D. Bailie, K. Behm, J. Warwick, G. M. Samarin, A. Maksimchuk, et al. Intense gamma-ray source based on focused electron beams from a laser wakefield accelerator. *Applied Physics Letters*, 120(26):264103, 2022.

[54] L. Rovige, J. Huijts, I. Andriyash, A. Vernier, V. Tomkus, V. Girdauskas, et al. Demonstration of stable long-term operation of a kilohertz laser-plasma accelerator. *Phys. Rev. Accel. Beams*, 23:093401, 2020.

[55] B. Guo, X. Zhang, J. Zhang, J. Hua, C.-H. Pai, C. Zhang, et al. High-resolution phase-contrast imaging of biological specimens using a stable betatron x-ray source in the multiple-exposure mode. *Scientific Reports*, 9, 2019.

[56] S. Corde, K. Ta Phuoc, G. Lambert, R. Fitour, V. Malka, A. Rousse, A. Beck, and E. Lefebvre. Femtosecond x rays from laser-plasma accelerators. *Rev. Mod. Phys.*, 85:1–48, 2013.

[57] F. Albert. Laser plasma accelerators: Next generation x-ray light sources. In *Frontiers in Optics + Laser Science 2023 (FiO, LS)*, page LTu2B.1. Optica Publishing Group, 2023.

[58] J. Cole, J. Wood, N. Lopes, K. Poder, R. Abel, S. Alatabi, et al. Laser-wakefield accelerators as hard x-ray sources for 3d medical imaging of human bone. *Scientific reports*, 5:13244, 2015.

[59] J. Wood, D. Chapman, K. Poder, N. Lopes, M. Rutherford, T. White, et al. Ultrafast imaging of laser driven shock waves using betatron x-rays from a laser wakefield accelerator. *Scientific Reports*, 8, 2018.

[60] CLF EPAC. `https://www.clf.stfc.ac.uk/Pages/EPAC.aspx/`. Accessed: 01/12/2023.

[61] Major boost to European plasma accelerator facility . `https://www.eupraxia-facility.org/post/major-boost-to-european-plasma-accelerator-facility`. Accessed: 01/12/2023.

[62] F.G. Desforges, M. Hansson, J. Ju, L. Senje, T.L. Audet, S. Dobosz-Dufrénoy, A. Persson, O. Lundh, C.-G. Wahlström, and B. Cros. Reproducibility of electron beams from laser wakefield acceleration in capillary tubes. *Nuclear Instruments and Methods in Physics Research Section A: Accelerators, Spectrometers, Detectors and Associated Equipment*, 740:54–59, 2014. Proceedings of the first European Advanced Accelerator Concepts Workshop 2013.

[63] P. A. P. Nghiem, D. Alesini, A. Aschikhin, R. W. Assmann, T. Audet, A. Beck, et al. Eupraxia, a step toward a plasma-wakefield based accelerator with high beam quality. *Journal of Physics: Conference Series*, 1350(1):012068, 2019.

[64] W. Kruer. *The Physics Of Laser Plasma Interactions (1st ed.)*. CRC Press, Boca Raton, 2003.

[65] B. Quesnel and P. Mora. Theory and simulation of the interaction of ultraintense laser pulses with electrons in vacuum. *Phys. Rev. E*, 58:3719–3732, 1998.

[66] S. Augst, D. Strickland, D. D. Meyerhofer, S. L. Chin, and J. H. Eberly. Tunneling ionization of noble gases in a high-intensity laser field. *Phys. Rev. Lett.*, 63:2212–2215, 1989.

[67] A. Kramida et al. Atomic spectra database, Oct 2022.

[68] M. V Ammosov, N. B. Delone, and V. P. Krainov. Tunnel ionization of complex atoms and of atomic ions in an alternating electromagnetic field. *Soviet Journal of Experimental and Theoretical Physics*, 64(6):1191, 1986.

[69] J. M. Dawson. Nonlinear electron oscillations in a cold plasma. *Phys. Rev.*, 113:383–387, 1959.

[70] V. I. Berezhiani and I. G. Murusidze. Relativistic wake-field generation by an intense laser pulse in a plasma. *Physics Letters A*, 148(6):338–340, 1990.

[71] E. Esarey, C. B. Schroeder, and W. P. Leemans. Physics of laser-driven plasma-based electron accelerators. *Rev. Mod. Phys.*, 81:1229–1285, 2009.

[72] A. Pukhov and J. Meyer-ter Vehn. Laser wake field acceleration: The highly non-linear broken-wave regime. *Applied Physics B-Lasers and Optics, v.74, 355-361 (2002)*, 74, 2002.

[73] I. Kostyukov, A. Pukhov, and S. Kiselev. Phenomenological theory of laser-plasma interaction in "bubble" regime. *Physics of Plasmas*, 11(11):5256–5264, 2004.

[74] W. Lu, M. Tzoufras, C. Joshi, F. S. Tsung, W. B. Mori, J. Vieira, R. A. Fonseca, and L. O. Silva. Generating multi-gev electron bunches using single stage laser wakefield acceleration in a 3d nonlinear regime. *Phys. Rev. ST Accel. Beams*, 10:061301, 2007.

[75] E. Esarey and M. Pilloff. Trapping and acceleration in nonlinear plasma waves. *Physics of Plasmas*, 2(5):1432–1436, 1995.

[76] C. D. Decker, W. B. Mori, K.-C. Tzeng, and T. Katsouleas. The evolution of ultra-intense, short-pulse lasers in underdense plasmas. *Physics of Plasmas*, 3(5):2047–2056, 1996.

[77] T. C. Katsouleas, S. Wilks, P. Chen, J. M. Dawson, and J. J. Su. Beam Loading in Plasma Accelerators. *Part. Accel.*, 22:81–99, 1987.

[78] C. Rechatin, X. Davoine, A. Lifschitz, A. Ben Ismail, J. Lim, E. Lefebvre, J. Faure, and V. Malka. Observation of beam loading in a laser-plasma accelerator. *Phys. Rev. Lett.*, 103:194804, 2009.

[79] W. B. Mori. The physics of the nonlinear optics of plasmas at relativistic intensities for short-pulse lasers. *IEEE Journal of Quantum Electronics*, 33(11):1942–1953, 1997.

[80] S. C. Wilks, J. M. Dawson, W. B. Mori, T. Katsouleas, and M. E. Jones. Photon accelerator. *Phys. Rev. Lett.*, 62:2600–2603, 1989.

[81] W. B. Mori. Generation of tunable radiation using an underdense ionization front. *Phys. Rev. A*, 44:5118–5121, 1991.

[82] E. Esarey, G. Joyce, and P. Sprangle. Frequency up-shifting of laser pulses by copropagating ionization fronts. *Phys. Rev. A*, 44:3908–3911, 1991.

[83] J. Vieira, F. Fiúza, L. O. Silva, M. Tzoufras, and W. B. Mori. Onset of self-steepening of intense laser pulses in plasmas. *New Journal of Physics*, 12(4):045025, 2010.

[84] P. Sprangle, C.-M. Tang, and E. Esarey. Relativistic self-focusing of short-pulse radiation beams in plasmas. *IEEE Transactions on Plasma Science*, 15(2):145–153, 1987.

[85] E. Esarey, P. Sprangle, J. Krall, and A. Ting. Self-focusing and guiding of short laser pulses in ionizing gases and plasmas. *IEEE Journal of Quantum Electronics*, 33(11):1879–1914, 1997.

[86] P. Sprangle, E. Esarey, and A. Ting. Nonlinear interaction of intense laser pulses in plasmas. *Phys. Rev. A*, 41:4463–4469, 1990.

[87] A. G. R. Thomas, Z. Najmudin, S. P. D. Mangles, C. D. Murphy, A. E. Dangor, C. Kamperidis, et al. Effect of laser-focusing conditions on propagation and monoenergetic electron production in laser-wakefield accelerators. *Phys. Rev. Lett.*, 98:095004, 2007.

[88] J. E. Ralph, K. A. Marsh, A. E. Pak, W. Lu, C. E. Clayton, F. Fang, W. B. Mori, and C. Joshi. Self-guiding of ultrashort, relativistically intense laser pulses through underdense plasmas in the blowout regime. *Phys. Rev. Lett.*, 102:175003, 2009.

[89] A. Zigler, Y. Ehrlich, C. Cohen, J. Krall, and P. Sprangle. Optical guiding of high-intensity laser pulses in a long plasma channel formed by a slow capillary discharge. *J. Opt. Soc. Am. B*, 13(1):68–71, 1996.

[90] C. G. Durfee and H. M. Milchberg. Light pipe for high intensity laser pulses. *Phys. Rev. Lett.*, 71:2409–2412, 1993.

[91] R. J. Shalloo, C. Arran, L. Corner, J. Holloway, J. Jonnerby, R. Walczak, H. M. Milchberg, and S. M. Hooker. Hydrodynamic optical-field-ionized plasma channels. *Phys. Rev. E*, 97:053203, 2018.

[92] A. Picksley, J. Chappell, E. Archer, N. Bourgeois, J. Cowley, D. R. Emerson, et al. All-optical gev electron bunch generation in a laser-plasma accelerator via truncated-channel injection. *Phys. Rev. Lett.*, 131:245001, 2023.

[93] S. Bulanov, N. Naumova, F. Pegoraro, and J. Sakai. Particle injection into the wave acceleration phase due to nonlinear wake wave breaking. *Phys. Rev. E*, 58:R5257–R5260, 1998.

[94] A. Bergmann and P. Mulser. Breaking of resonantly excited electron plasma waves. *Phys. Rev. E*, 47:3585–3589, 1993.

[95] S. V. Bulanov, F. Pegoraro, A. M. Pukhov, and A. S. Sakharov. Transverse-wake wave breaking. *Phys. Rev. Lett.*, 78:4205–4208, 1997.

[96] F. S. Tsung, R. Narang, W. B. Mori, C. Joshi, R. A. Fonseca, and L. O. Silva. Near-gev-energy laser-wakefield acceleration of self-injected electrons in a centimeter-scale plasma channel. *Phys. Rev. Lett.*, 93:185002, 2004.

[97] S. P. D. Mangles, A. G. R. Thomas, C. Bellei, A. E. Dangor, C. Kamperidis, S. Kneip, S. R. Nagel, L. Willingale, and Z. Najmudin. Self-guided wakefield experiments driven by petawatt-class ultrashort laser pulses. *IEEE Transactions on Plasma Science*, 36(4):1715–1721, 2008.

[98] S. Kalmykov, S. A. Yi, V. Khudik, and G. Shvets. Electron self-injection and trapping into an evolving plasma bubble. *Phys. Rev. Lett.*, 103:135004, 2009.

[99] C. B. Schroeder, C. Benedetti, E. Esarey, and W. P. Leemans. Nonlinear pulse propagation and phase velocity of laser-driven plasma waves. *Phys. Rev. Lett.*, 106:135002, 2011.

[100] H. Suk, N. Barov, J. B. Rosenzweig, and E. Esarey. Plasma electron trapping and acceleration in a plasma wake field using a density transition. *Phys. Rev. Lett.*, 86:1011–1014, 2001.

[101] K. Schmid, A. Buck, C. M. S. Sears, J. M. Mikhailova, R. Tautz, D. Herrmann, M. Geissler, F. Krausz, and L. Veisz. Density-transition based electron injector for laser driven wakefield accelerators. *Phys. Rev. ST Accel. Beams*, 13:091301, 2010.

[102] A. V. Brantov, T. Zh. Esirkepov, M. Kando, H. Kotaki, V. Yu. Bychenkov, and S. V. Bulanov. Controlled electron injection into the wake wave using plasma density inhomogeneity. *Physics of Plasmas*, 15(7):073111, 2008.

[103] A. Martinez de la Ossa, Z. Hu, M. J. V. Streeter, T. J. Mehrling, O. Kononenko, B. Sheeran, and J. Osterhoff. Optimizing density down-ramp injection for beam-driven plasma wakefield accelerators. *Phys. Rev. Accel. Beams*, 20:091301, 2017.

[104] M. C. Thompson, J. B. Rosenzweig, and H. Suk. Plasma density transition trapping as a possible high-brightness electron beam source. *Phys. Rev. ST Accel. Beams*, 7:011301, 2004.

[105] A. Buck, J. Wenz, J. Xu, K. Khrennikov, K. Schmid, M. Heigoldt, et al. Shock-front injector for high-quality laser-plasma acceleration. *Phys. Rev. Lett.*, 110:185006, 2013.

[106] D. Umstadter, J. K. Kim, and E. Dodd. Laser injection of ultrashort electron pulses into wakefield plasma waves. *Phys. Rev. Lett.*, 76:2073–2076, 1996.

[107] M. Chen, Z.-M. Sheng, Y.-Y. Ma, and J. Zhang. Electron injection and trapping in a laser wakefield by field ionization to high-charge states of gases. *Journal of Applied Physics*, 99(5):056109, 2006.

[108] A. Pak, K. A. Marsh, S. F. Martins, W. Lu, W. B. Mori, and C. Joshi. Injection and trapping of tunnel-ionized electrons into laser-produced wakes. *Phys. Rev. Lett.*, 104:025003, 2010.

[109] C. McGuffey, A. G. R. Thomas, W. Schumaker, T. Matsuoka, V. Chvykov, F. J. Dollar, et al. Ionization induced trapping in a laser wakefield accelerator. *Phys. Rev. Lett.*, 104:025004, 2010.

[110] M. Chen, E. Esarey, C. B. Schroeder, C. G. R. Geddes, and W. P. Leemans. Theory of ionization-induced trapping in laser-plasma accelerators. *Physics of Plasmas*, 19(3):033101, 2012.

[111] M. Zeng, N. A. M. Hafz, K. Nakajima, L.-M. Chen, W. Lu, W. B. Mori, Z.-M. Sheng, and J. Zang. Controlled ionization-induced injection by tailoring the gas-density profile in laser wakefield acceleration. *Journal of Plasma Physics*, 78(4):363–371, 2012.

[112] J. S. Liu, C. Q. Xia, W. T. Wang, H. Y. Lu, Ch. Wang, A. H. Deng, et al. All-optical cascaded laser wakefield accelerator using ionization-induced injection. *Phys. Rev. Lett.*, 107:035001, 2011.

[113] B. B. Pollock, C. E. Clayton, J. E. Ralph, F. Albert, A. Davidson, L. Divol, et al. Demonstration of a narrow energy spread, ~ 0.5 GeV electron beam from a two-stage laser wakefield accelerator. *Phys. Rev. Lett.*, 107:045001, 2011.

[114] G. Golovin, S. Chen, N. Powers, C. Liu, S. Banerjee, J. Zhang, M. Zeng, Z. Sheng, and D. Umstadter. Tunable monoenergetic electron beams from independently controllable laser-wakefield acceleration and injection. *Phys. Rev. ST Accel. Beams*, 18:011301, 2015.

[115] C. Thaury, E. Guillaume, A. Lifschitz, K. Ta Phuoc, M. Hansson, G. Grittani, et al. Shock assisted ionization injection in laser-plasma accelerators. *Scientific Reports*, 5, 2015.

[116] C. Xia, J. Liu, W. Wang, H. Lu, W. Cheng, A. Deng, et al. Effects of self-focusing on tunnel-ionization-induced injection in a laser wakefield accelerator. *Physics of Plasmas*, 18(11):113101, 2011.

[117] M. Zeng, M. Chen, Z.-M. Sheng, W. B. Mori, and J. Zhang. Self-truncated ionization injection and consequent monoenergetic electron bunches in laser wakefield acceleration. *Physics of Plasmas*, 21(3):030701, 2014.

[118] M. Mirzaie, S. Li, M. Zeng, N. A. M. Hafz, G. Y. Li, Q. J. Zhu, et al. Demonstration of self-truncated ionization injection for gev electron beams. *Scientific Reports*, 5, 2015.

[119] A. Irman, J. P. Couperus, A. Debus, A. Köhler, J. M. Krämer, R. Pausch, O. Zarini, and U. Schramm. Improved performance of laser wakefield acceleration by tailored self-truncated ionization injection. *Plasma Physics and Controlled Fusion*, 60(4):044015, 2018.

[120] C. J. Hooker, J. L. Collier, O. Chekhlov, R. J. Clarke, E. J. Divall, K. Ertel, et al. The Astra Gemini Petawatt Ti:Sapphire Laser. *The Review of Laser Engineering*, 37(6):443–448, 2009.

[121] K. Svendsen. *Applications of Laser-Plasma Acceleration*. PhD Thesis, Lund University, 2022.

[122] J. M. Cole. *Diagnosis and application of laser wakefield accelerators*. PhD Thesis, Imperial College London, 2015.

[123] M. Takeda, H. Ina, and S. Kobayashi. Fourier-transform method of fringe-pattern analysis for computer-based topography and interferometry. *J. Opt. Soc. Am.*, 72(1):156–160, 1982.

[124] K. Chauhan, H. C. H. Ng, and I. Marusic. Empirical mode decomposition and hilbert transforms for analysis of oil-film interferograms. *Measurement Science and Technology*, 21(10):105405, 2010.

[125] M. Arevallilo Herráez, D. R. Burton, M. J. Lalor, and M. A. Gdeisat. Fast two-dimensional phase-unwrapping algorithm based on sorting by reliability following a non-continuous path. *Appl. Opt.*, 41(35):7437–7444, 2002.

[126] R. Azambuja, M. Eloy, G. Figueira, and D. Neely. Three-dimensional characterization of high-density non-cylindrical pulsed gas jets. *Journal of Physics D: Applied Physics*, 32(8):L35, 1999.

[127] G. Golovin, S. Banerjee, J. Zhang, S. Chen, C. Liu, B. Zhao, J. Mills, K. Brown, C. Petersen, and D. Umstadter. Tomographic imaging of nonsymmetric multicomponent tailored supersonic flows from structured gas nozzles. *Appl. Opt.*, 54(11):3491–3497, 2015.

[128] R. N. Bracewell. *The Fourier Transform & Its Applications*. McGraw-Hill, New York, 1986.

[129] R. Yurchak. *Experimental and numerical study of accretion-ejection mechanisms in laboratory astrophysics*. Phd thesis, Ecole Polytechnique (EDX), 2015.

[130] A. Buck, K. Zeil, A. Popp, K. Schmid, A. Jochmann, S. D. Kraft, et al. Absolute charge calibration of scintillating screens for relativistic electron detection. *Review of Scientific Instruments*, 81(3):033301, 2010.

[131] Y. Glinec, J. Faure, A. Guemnie-Tafo, V. Malka, H. Monard, J. P. Larbre, V. De Waele, J. L. Marignier, and M. Mostafavi. Absolute calibration for a broad range single shot electron spectrometer. *Review of Scientific Instruments*, 77(10):103301, 2006.

[132] R. Trebino. *Frequency-Resolved Optical Gating: The Measurement of Ultrashort Laser Pulses.* Springer, 2000.

[133] K. W. DeLong, R. Trebino, and D. J. Kane. Comparison of ultrashort-pulse frequency-resolved-optical-gating traces for three common beam geometries. *J. Opt. Soc. Am. B*, 11(9):1595–1608, 1994.

[134] J. Schreiber, C. Bellei, S. P. D. Mangles, C. Kamperidis, S. Kneip, S. R. Nagel, C. A. J. Palmer, P. P. Rajeev, M. J. V. Streeter, and Z. Najmudin. Complete temporal characterization of asymmetric pulse compression in a laser wakefield. *Phys. Rev. Lett.*, 105:235003, 2010.

[135] R. Trebino and D. J. Kane. Using phase retrieval to measure the intensity and phase of ultrashort pulses: frequency-resolved optical gating. *J. Opt. Soc. Am. A*, 10(5):1101–1111, 1993.

[136] D. J. Kane. Real-time measurement of ultrashort laser pulses using principal component generalized projections. *IEEE Journal of Selected Topics in Quantum Electronics*, 4(2):278–284, 1998.

[137] D.J. Kane. Recent progress toward real-time measurement of ultrashort laser pulses. *IEEE Journal of Quantum Electronics*, 35(4):421–431, 1999.

[138] T. D. Arber, K. Bennett, C. S. Brady, A. Lawrence-Douglas, M. G. Ramsay, et al. Contemporary particle-in-cell approach to laser-plasma modelling. *Plasma Physics and Controlled Fusion*, 57(11):1–26, 2015.

[139] C. K. Birdsall and A. B Langdon. *Plasma Physics via Computer Simulation.* CRC Press, Boca Raton, 1991.

[140] J. Osterhoff, A. Popp, Zs. Major, B. Marx, T. P. Rowlands-Rees, M. Fuchs, et al. Generation of stable, low-divergence electron beams by laser-wakefield acceleration in a steady-state-flow gas cell. *Phys. Rev. Lett.*, 101:085002, 2008.

[141] J. Vieira, S. F. Martins, F. Fiúza, C. K. Huang, W. B. Mori, S. P. D. Mangles, S. Kneip, S. Nagel, Z. Najmudin, and L. O. Silva. Influence of realistic parameters on state-of-the-art laser wakefield accelerator experiments. *Plasma Physics and Controlled Fusion*, 54(5):055010, 2012.

[142] J. Faure, C. Rechatin, A. Norlin, A. Lifschitz, Y. Glinec, and V. Malka. Controlled injection and acceleration of electrons in plasma wakefields by colliding laser pulses. *Nature*, 444:737–9, 2006.

[143] S. Bohlen, J. C. Wood, T. Brümmer, F. Grüner, C. A. Lindstrøm, M. Meisel, T. Staufer, R. D'Arcy, K. Põder, and J. Osterhoff. Stability of ionization-injection-based laser-plasma accelerators. *Phys. Rev. Accel. Beams*, 25:031301, 2022.

[144] C. G. R. Geddes, K. Nakamura, G. R. Plateau, Cs. Toth, E. Cormier-Michel, E. Esarey, C. B. Schroeder, J. R. Cary, and W. P. Leemans. Plasma-density-gradient injection of low absolute-momentum-spread electron bunches. *Phys. Rev. Lett.*, 100:215004, 2008.

[145] P. Tomassini, M. Galimberti, A. Giulietti, D. Giulietti, L. A. Gizzi, L. Labate, and F. Pegoraro. Production of high-quality electron beams in numerical experiments of laser wakefield acceleration with longitudinal wave breaking. *Phys. Rev. ST Accel. Beams*, 6:121301, 2003.

[146] A. Gonsalves, K. Nakamura, C. Lin, S. Shiraishi, T. Sokollik, C. Benedetti, et al. Tunable laser plasma accelerator based on longitudinal density tailoring. *Nature Physics*, 7:862–866, 2011.

[147] M. Hansson, B. Aurand, X. Davoine, H. Ekerfelt, K. Svensson, A. Persson, C.-G. Wahlström, and O. Lundh. Down-ramp injection and independently controlled acceleration of electrons in a tailored laser wakefield accelerator. *Phys. Rev. ST Accel. Beams*, 18:071303, 2015.

[148] M. Burza, A. Gonoskov, K. Svensson, F. Wojda, A. Persson, M. Hansson, G. Genoud, M. Marklund, C.-G. Wahlström, and O. Lundh. Laser wakefield acceleration using wire produced double density ramps. *Phys. Rev. ST Accel. Beams*, 16:011301, 2013.

[149] K. K. Swanson, H.-E. Tsai, S. K. Barber, R. Lehe, H.-S. Mao, S. Steinke, et al. Control of tunable, monoenergetic laser-plasma-accelerated electron beams using a shock-induced density downramp injector. *Phys. Rev. Accel. Beams*, 20:051301, 2017.

[150] H.-E. Tsai, K. K. Swanson, S. K. Barber, R. Lehe, H.-S. Mao, D. E. Mittelberger, et al. Control of quasi-monoenergetic electron beams from laser-plasma accelerators with adjustable shock density profile. *Physics of Plasmas*, 25(4):043107, 2018.

[151] K. N. Kim, Y. Hwangbo, S.-g. Jeon, and J. Kim. Characteristics of the Shock Structure for Transition Injection in Laser Wakefield Acceleration. *Journal of Korean Physical Society*, 73(5):561–566, 2018.

[152] M. Fang, Z. Zhang, W. Wang, J. Liu, and R. Li. Sharp plasma pinnacle structure based on shockwave for an improved laser wakefield accelerator. *Plasma Physics and Controlled Fusion*, 60(7):075008, 2018.

[153] L. Fan-Chiang, H.-S. Mao, H.-E. Tsai, T. Ostermayr, K. K. Swanson, S. K. Barber, S. Steinke, J. van Tilborg, C. G. R. Geddes, and W. P. Leemans. Gas density structure of supersonic flows impinged on by thin blades for laser–plasma accelerator targets. *Physics of Fluids*, 32(6):066108, 2020.

[154] S. A. Samant, A. K. Upadhyay, and S. Krishnagopal. High brightness electron beams from density transition laser wakefield acceleration for short-wavelength free-electron lasers. *Plasma Physics and Controlled Fusion*, 56(9):095003, 2014.

[155] F. Massimo, A. F. Lifschitz, C. Thaury, and V. Malka. Numerical studies of density transition injection in laser wakefield acceleration. *Plasma Physics and Controlled Fusion*, 59(8):085004, 2017.

[156] F. Massimo, A. F. Lifschitz, C. Thaury, and V. Malka. Numerical study of laser energy effects on density transition injection in laser wakefield acceleration. *Plasma Physics and Controlled Fusion*, 60(3):034005, 2018.

[157] H. Ekerfelt, M. Hansson, I. Gallardo González, X. Davoine, and O. Lundh. A tunable electron beam source using trapping of electrons in a density down-ramp in laser wakefield acceleration. *Sci. Rep.*, 7(1):12229, 2017.

[158] S. Semushin and V. Malka. High density gas jet nozzle design for laser target production. *Review of Scientific Instruments*, 72(7):2961–2965, 2001.

[159] C. G. W. D. Colgan. *Laser-plasma interactions as tools for studying processes in quantum electrodynamics*. PhD Thesis, Imperial College London, 2022.

[160] J. D. Anderson. *Modern Compressible Flow with Historical Perspective of Aeronautical and Aerospace Engineering*. McGraw-Hill, New York, 1990.

[161] K. Schmid and L. Veisz. Supersonic gas jets for laser-plasma experiments. *Review of Scientific Instruments*, 83(5):053304, 2012.

[162] V. Malka, C. Coulaud, J. P. Geindre, V. Lopez, Z. Najmudin, D. Neely, et al. Characterization of neutral density profile in a wide range of pressure of cylindrical pulsed gas jets. *Review of Scientific Instruments*, 71(6):2329–2333, 2000.

[163] N. Lemos, N. Lopes, J. M. Dias, and F. Viola. Design and characterization of supersonic nozzles for wide focus laser-plasma interactions. *Review of Scientific Instruments*, 80(10):103301, 2009.

[164] H.-S. Mao, K. K. Swanson, H.-E. Tsai, S. K. Barber, S. Steinke, J. van Tilborg, C. G. R. Geddes, and W. P. Leemans. Gas density structure of supersonic flows impinged on by thin blades for laser-plasma accelerators. *AIP Conference Proceedings*, 1812(1), 2017. 040007.

[165] C. Zhang, C.-K. Huang, K. A. Marsh, X. L. Xu, F. Li, M. Hogan, V. Yakimenko, S. Corde, W. B. Mori, and C. Joshi. Effect of fluctuations in the down ramp plasma source profile on the emittance and current profile of the self-injected beam in a plasma wakefield accelerator. *Phys. Rev. Accel. Beams*, 22:111301, 2019.

[166] M. P. Tooley, B. Ersfeld, S. R. Yoffe, A. Noble, E. Brunetti, Z. M. Sheng, M. R. Islam, and D. A. Jaroszynski. Towards attosecond high-energy electron bunches: Controlling self-injection in laser-wakefield accelerators through plasma-density modulation. *Phys. Rev. Lett.*, 119:044801, 2017.

[167] S. Kuschel, M. B. Schwab, M. Yeung, D. Hollatz, A. Seidel, W. Ziegler, A. Sävert, M. C. Kaluza, and M. Zepf. Controlling the self-injection threshold in laser wakefield accelerators. *Phys. Rev. Lett.*, 121:154801, 2018.

[168] H. M. Mott-Smith. The solution of the Boltzmann equation for a shock wave. *Phys. Rev.*, 82:885–892, 1951.

[169] A. Döpp, C. Thaury, E. Guillaume, F. Massimo, A. Lifschitz, I. Andriyash, J.-P. Goddet, A. Tazfi, K. Ta Phuoc, and V. Malka. Energy-chirp compensation in a laser wakefield accelerator. *Phys. Rev. Lett.*, 121:074802, 2018.

[170] C. D. Murphy, R. Trines, J. Vieira, A. J. W. Reitsma, R. Bingham, J. L. Collier, et al. Evidence of photon acceleration by laser wake fields. *Physics of Plasmas*, 13(3):033108, 2006.

[171] S. Karsch, J. Osterhoff, A. Popp, T. P. Rowlands-Rees, Zs. Major, M. Fuchs, et al. Gev-scale electron acceleration in a gas-filled capillary discharge waveguide. *New Journal of Physics*, 9(11):415, 2007.

[172] N. E. Andreev, K. Cassou, F. Wojda, G. Genoud, M. Burza, O. Lundh, A. Persson, B. Cros, V. E. Fortov, and C.-G. Wahlstrom. Analysis of laser wakefield dynamics in capillary tubes. *New Journal of Physics*, 12(4):045024, 2010.

[173] T. P. A. Ibbotson, N. Bourgeois, T. P. Rowlands-Rees, L. S. Caballero, S. I. Bajlekov, P. A. Walker, et al. Investigation of the role of plasma channels as waveguides for laser-wakefield accelerators. *New Journal of Physics*, 12(4):045008, 2010.

[174] S. Shiraishi, C. Benedetti, A. J. Gonsalves, K. Nakamura, B. H. Shaw, T. Sokollik, et al. Laser red shifting based characterization of wakefield excitation in a laser-plasma accelerator. *Physics of Plasmas*, 20(6):063103, 2013.

[175] M. J. V. Streeter, Y. Ma, B. Kettle, S. J. D. Dann, E. Gerstmayr, F. Albert, et al. Characterization of laser wakefield acceleration efficiency with octave spanning near-ir spectrum measurements. *Phys. Rev. Accel. Beams*, 25:101302, 2022.

[176] A. E. Hussein, J. D. Ludwig, Y. Ma, P.-E. Masson-Laborde, P. J. Skrodzki, J. Hinojosa, et al. Direct spectral measurements of midinfrared radiation from a laser wakefield accelerator. *Phys. Rev. A*, 106:063505, 2022.

[177] C.-H. Pai, Y.-Y. Chang, L.-C. Ha, Z.-H. Xie, M.-W. Lin, J.-M. Lin, et al. Generation of intense ultrashort midinfrared pulses by laser-plasma interaction in the bubble regime. *Phys. Rev. A*, 82:063804, 2010.

[178] J. Faure, Y. Glinec, J. J. Santos, F. Ewald, J.-P. Rousseau, S. Kiselev, A. Pukhov, T. Hosokai, and V. Malka. Observation of laser-pulse shortening in nonlinear plasma waves. *Phys. Rev. Lett.*, 95:205003, 2005.

[179] M. J. V. Streeter, S. Kneip, M. S. Bloom, R. A. Bendoyro, O. Chekhlov, A. E. Dangor, et al. Observation of laser power amplification in a self-injecting laser wakefield accelerator. *Phys. Rev. Lett.*, 120:254801, 2018.

[180] C. Kamperidis, V. Dimitriou, S. P. D. Mangles, A. E. Dangor, and Z. Najmudin. Low energy spread electron beams from ionization injection in a weakly relativistic laser wakefield accelerator. *Plasma Physics and Controlled Fusion*, 56(8):084007, 2014.

[181] T. L. Audet, M. Hansson, P. Lee, F. G. Desforges, G. Maynard, S. Dobosz Dufrénoy, et al. Investigation of ionization-induced electron injection in a wakefield driven by laser inside a gas cell. *Physics of Plasmas*, 23(2):023110, 2016.

[182] L. T. Dickson, C. I. D. Underwood, F. Filippi, R. J. Shalloo, J. Björklund Svensson, D. Guénot, et al. Mechanisms to control laser-plasma coupling in laser wakefield electron acceleration. *Phys. Rev. Accel. Beams*, 25:101301, 2022.

[183] T. L. Audet, F. G. Desforges, A. Maitrallain, S. Dobosz Dufrénoy, M. Bougeard, G. Maynard, et al. Electron injector for compact staged high energy accelerator. *Nuclear Instruments and Methods in Physics Research Section A: Accelerators, Spectrometers, Detectors and Associated Equipment*, 829:304–308, 2016. 2nd European Advanced Accelerator Concepts Workshop - EAAC 2015.

[184] L. Dickson. *Laser wakefield acceleration of electrons.* PhD Thesis, Université Paris-Saclay, 2023.

[185] F. Filippi, L. T. Dickson, M. Backhouse, P. Forestier-Colleoni, C. Gustafsson, C. Cobo, et al. Plasma density profile reconstruction of a gas cell for ionization induced laser wakefield acceleration. *Journal of Instrumentation*, 18(05):C05013, 2023.

[186] R. M. G. M. Trines, C. D. Murphy, K. L. Lancaster, O. Chekhlov, P. A. Norreys, R. Bingham, et al. Photon acceleration and modulational instability during wakefield

excitation using long laser pulses. *Plasma Physics and Controlled Fusion*, 51(2):024008, 2009.

[187] V. Eremin, Yu. Malkov, V. Korolikhin, A. Kiselev, S. Skobelev, A. Stepanov, and N. Andreev. Study of the plasma wave excited by intense femtosecond laser pulses in a dielectric capillary. *Physics of Plasmas*, 19(9):093121, 2012.

[188] H. Kotaki, Y. Hayashi, M. Mori, M. Kando, J. K. Koga, and S. V. Bulanov. Limitation of the plasma channel due to the frequency blueshift. *Journal of Physics: Conference Series*, 688(1):012054, 2016.

[189] G. Genoud, M. S. Bloom, J. Vieira, M. Burza, Z. Najmudin, A. Persson, L. O. Silva, K. Svensson, C.-G. Wahlström, and S. P. D. Mangles. Increasing energy coupling into plasma waves by tailoring the laser radial focal spot distribution in a laser wakefield accelerator. *Physics of Plasmas*, 20(6):064501, 2013.

[190] W. P. Leemans, P. Catravas, E. Esarey, C. G. R. Geddes, C. Toth, R. Trines, C. B. Schroeder, B. A. Shadwick, J. van Tilborg, and J. Faure. Electron-yield enhancement in a laser-wakefield accelerator driven by asymmetric laser pulses. *Phys. Rev. Lett.*, 89:174802, 2002.

[191] Newport Corporation, Irvine, CA. *Oriel Legacy MS257 Monochromator User Manual*, 2012. Available at `https://www.newport.com/f/ms257-1_4-m-imaging-spectrograph`.

[192] F. S. Tsung, W. Lu, M. Tzoufras, W. B. Mori, C. Joshi, J. M. Vieira, L. O. Silva, and R. A. Fonseca. Simulation of monoenergetic electron generation via laser wakefield accelerators for 5–25TW lasersa). *Physics of Plasmas*, 13(5):056708, 2006.

[193] M. Polyanskiy. Refractiveindex.info database of optical constants. *Scientific Data*, 11, 01 2024.

[194] M. Hansson, L. Senje, A. Persson, O. Lundh, C.-G. Wahlström, F. G. Desforges, et al. Enhanced stability of laser wakefield acceleration using dielectric capillary tubes. *Phys. Rev. ST Accel. Beams*, 17:031303, 2014.

[195] C. I. D. Underwood. *Optimising Production of High Energy Radiation Using Laser Wakefield Acceleration*. PhD Thesis, University of York, 2020.

[196] H. Kogelnik and T. Li. Laser beams and resonators. *Proceedings of the IEEE*, 54(10):1312–1329, 1966.